Applications of Gravitational Lensing: Revealing the Structure of Quasars

Carina Fian
Instituto de Astrofísica de Canarias

A thesis submitted for the degree of
Doctor
by the
Universidad de La Laguna

2018

Examination date: September, 2018
Thesis supervisor: Dr. Evencio Mediavilla Gradolph

Some of the material included in this document has already been published in *The Astrophysical Journal*, in the *Open Access Publikationsserver* of the University of Graz and in the annual report of the *International Scientific Committee*.

Acknowledgment

I am still confused, but on a higher level.
Enrico Fermi

Above all, I would like to express my appreciation and thanks to my supervisor Evencio Mediavilla for his support and engagement through the learning process of my PhD. He always found time to explain me everything and taught me most of what I know about gravitational lensing. I would like to thank for encouraging my research, for teaching me how to write scientific papers, for his vast contribution to all the publications and for his funny comments.

Special thanks are given to Verónica Motta and Arnold Hanslmeier for the useful and instructive stays in Chile/Austria. Many thanks to Jorge Jiménez-Vicente and Jose Muñoz for helpful comments and advices. Thanks to the collaborators (Eduardo Guerras, Emilio Falco, Alex Oscoz and Karina Rojas) I met/worked with during my PhD and to my friends and colleagues at the IAC (Nikolay, Hannu, Francesca, Jorge are many more) for the friendly environment. I have a special appreciation for my Canary friend Marta, for her patience with me learning/speaking Spanish and always being there and helping.

Last but not least important, I owe more than thanks to my family members which includes my parents, grandmother and my twin brother and his fiancée, for their encouragement throughout my life.

Carina Fian
La Laguna, May 2018

Abstract

Since its first observational evidence, gravitational lensing – the deflection of light by mass – has become an established astrophysical tool than can be used to study the physical properties and environments of the lens galaxies and to reveal the structure of the lensed quasars. This thesis combines theoretical and observational results of a sample of gravitationally lensed quasars to study the structure of the broad-line region (BLR), the size of the accretion disk and the mass of the central Super Massive Black Hole (SMBH). We start with a general introduction and a theoretical description of the basics of lensing (Chapter 1) followed by a short motivation statement (Chapter 2). In the third chapter a summary of the observations, data reduction and lens database is provided. This chapter also includes a description of the analysis tools and methods used in this thesis. We continue with the study of microlensing variations in the light curves of the wide-separation lensed quasar SDSS J1004+4112 and the cross-shaped lensed quasar HE 0435-1223 to infer the size of their accretion disks (Section 4.1). The main conclusion is that the accretion disks are greater than expected according to the standard Shakura-Sunyaev disk model. In Section 4.2 we analyze the impact of intrinsic variability and microlensing in the objects of our spectroscopic database concluding the existence of two different regions in the BLR, one that is insensitive to microlensing (of size ≥50 light-days and kinematics not confined to a plane) and another (of size of a few light-days, comparable to the accretion disk) that shows up only when it is magnified by microlensing. The strong microlensing of some spectral features indicates that they could arise from the inner parts of the disk. This may be the case of the Fe III UV blend, a feature which we found systematically redshifted. Under the gravitational redshift hypothesis, this feature could be used to estimate, in a way independent of the geometry of the system, the mass of the central SMBH (Section 4.3). Finally (Chapter 5), we summarize the main conclusions of the thesis and emphasize the work in progress and future prospects.

This thesis was carried out at the Instituto de Astrofísica de Canarias (IAC) under the supervision of Evencio Mediavilla from October 2015 to June 2018 and was funded through a La Caixa fellowship. The thesis includes five scientific papers published (2)/accepted (1) in or submitted (1) to the *Astrophysical Journal*.

Resumen

Desde su confirmación observacional, el efecto lente gravitatoria – la desviación de la luz por la materia – se ha convertido en una herramienta astrofísica que se puede usar para estudiar las propiedades físicas y los entornos de las galaxias lente y revelar la estructura de los cuásares sometidos a este efecto. Esta tesis combina resultados teóricos y observacionales de una muestra de cuásares en sistemas lente para estudiar la estructura de la región de líneas anchas (BLR), el tamaño del disco de acreción y la masa del agujero negro supermasivo central (SMBH). Comenzamos con una introducción general y una descripción teórica de los conceptos básicos del efecto lente gravitatoria (Capítulo 1). A continuación se presentan la motivación y los objetivos de la tesis (Capítulo 2). En el tercer capítulo se proporciona un resumen de las observaciones, la reducción de datos y la base de datos de lentes. En este capítulo también se describen las herramientas y los métodos de análisis utilizados en la tesis. Continuamos con el estudio de las variaciones inducidas por el efecto microlente en las curvas de luz del sistema lente de gran tamaño SDSS J1004+4112 y del sistema lente con forma de cruz HE 0435-1223 para inferir el tamaño de sus discos de acreción (Sección 4.1). La principal conclusión es que los discos de acreción son mas grandes de lo esperado según el modelo de disco estándar de Shakura-Sunyaev. En la Sección 4.2 analizamos el impacto de la variabilidad intrínseca y del efecto microlente en los objetos de nuestra base de datos espectroscópicos, concluyendo que existen dos regiones diferentes en la BLR, una que es insensible a microlensing (de tamaño $\geq$ 50 días de luz y cinemática no confinada a un plano) y otra (de un tamaño de unos pocos días de luz, comparable al disco de acreción) que aparece solo cuando se amplifica por el efecto microlente. Las fuertes amplificaciones debidas a microlensing de algunas características espectrales indican que podrían tener su origen en las partes internas del disco de acreción. Este puede ser el caso de Fe III UV 'blend', una característica que encontramos sistemáticamente desplazada al rojo. Bajo la hipótesis de un desplazamiento al rojo gravitatorio, esta característica se podría utilizar para estimar, de una manera independiente de la geometría del sistema, la masa del SMBH central. Finalmente, en el Capítulo 5 resumimos las principales conclusiones de la tesis y presentamos el trabajo en progreso y las perspectivas de futuro.

Esta tesis se llevó a cabo en el Instituto de Astrofísica de Canarias (IAC) bajo la supervisión de Evencio Mediavilla de Octubre 2015 a Junio 2018 y fue financiada a través de una beca de La Caixa. La tesis incluye cinco artículos científicos publicados (2)/aceptados (1) en o enviados (1) al *Astrophysical Journal*.

Contents

[1] see Sections 4.1.3 and 4.1.4
[2] see Section A

1

Introduction

The field of gravitational lensing has evolved from a theoretical idea to a robust astrophysical and cosmological tool in the past few decades and offers the best, and sometimes the only (due to the amplification effect gravitational lensing is capable of discovering celestial objects at great distances from the Earth, like exoplanets or quasars, which would otherwise be too faint to be detected with present telescopes), means of tackling key problems in many fields. According to Einstein's *General Theory of Relativity*, mass curves the space-time and the basic phenomena of gravitational lensing - light deflection and time dilation by gravitational fields - are two essential predictions by this theory. Since gravitational lensing is independent of the nature and the state of matter, and in particular is equally sensitive to luminous and dark matter, it provides a unique tool for mapping and analyzing the distribution of mass in the Universe. In recent years, gravitational lensing has significantly improved our knowledge of many astrophysical phenomena, such as exoplanets, active galactic nuclei, quasars, galaxies and clusters of galaxies, dark matter, large-scale structure and cosmology (Eigenbrod 2011; Suyu 2016).

Gravitational lensing happens on all scales - light rays are bend by the gravitational fields of massive objects (for instance galaxies or cluster of galaxies) but also smaller objects like stars and planets affect the path of the light. To be precise, anything that has a mass - even the mass of our own body - lenses passing light rays, although this effect cannot be measured for low masses. The most extreme bending of light rays occurs when the lens is a massive object and light rays pass close to it. In this case, light can take different paths to the observer and multiple images of the background source are formed. If the source varies with time, the generated multiple images will also vary with time and since the light rays of the source do not travel the same distance to each image, there will

be time delays for these changes between the images (Eigenbrod 2011).

The present thesis focuses on applications related to a particular kind of gravitational lenses, namely gravitationally lensed quasars. Quasars are the most luminous subclass among active galactic nuclei and are the brightest objects known in the Universe, far outshining the total starlight of their host galaxies (Berkeley 2011). Although they appear to be distributed everywhere in the Universe over a wide range of redshifts, only a small fraction of them happen to be gravitationally lensed into multiple images. However, up to now several examples of galaxies which contain gravitationally lensed quasars have been discovered (More et al. 2016; Lemon et al. 2018).

The small sizes of the emitting regions of quasars, together with the large distances involved, makes it impossible to resolve quasars spatially even with the largest available optical telescopes. Compact objects such as stars in the lens galaxy induce uncorrelated changes in the flux of the images - this microlensing effect can help us overcoming these difficulties as it is sensitive to the size of the emitting region and thus, can be used to extract information about both the source and the lens.

In this chapter, we introduce the principles of gravitational lensing in Section 1.1. We briefly recount the history of lensing in Section 1.2. We continue with the theory of lensing in Section 1.3 and describe the different fields of lensing in Section 1.4. Section 1.5 and 1.6 are devoted to the lensing phenomena and applications of lensing. Finally, in Section 1.7, we give an overview of active galactic nuclei with a special focus on quasars.

1.1 Principle of Lensing

Massive objects, for instance galaxies or cluster of galaxies which are located between an observer and a distant light source, cause high curvatures in the space-time. Light is following these curvatures and as a consequence, light rays passing near massive objects are deflected. This phenomenon is called *gravitational lensing* and is an effect of Einstein's theory of general relativity. As a result, a celestial object can hide itself behind a galaxy and then paradoxically becomes much more visible, magnified in both size and flux (Eigenbrod 2011; Wambsganss 1998).

A galaxy located on the line-of-sight of a distant background source produces magnified multiple images of the source. The light rays of these images follow different paths and intrinsic variations of the emitting source can be observed at different times in each image. The principles of gravitational lensing are easy to explain due to its being a geometrical effect. In some cases gravitational lensing can be described in analogy to the deflection of light by glass lenses in optics.

In Figure 1.1 one can see the principle of gravitational lensing: light from a distant background source (here a galaxy) is passing close to a cluster of galaxies and is bent towards the galaxy cluster due to the curvature of the space-time (caused by the cluster) during its way to the Earth. From the point of view of an observer on the Earth it looks as if two (or more) light rays have traveled along straight lines from different parts of the universe. As a consequence, we are able to observe multiple distorted images of the background source which otherwise would not be visible. The orange-colored light curves symbolize the two lensed images of the same galaxy, the white-colored light curves do not hit the Earth and therefore cannot be observed (Eigenbrod 2011; Grocutt 2014; Wambsganss 1998).

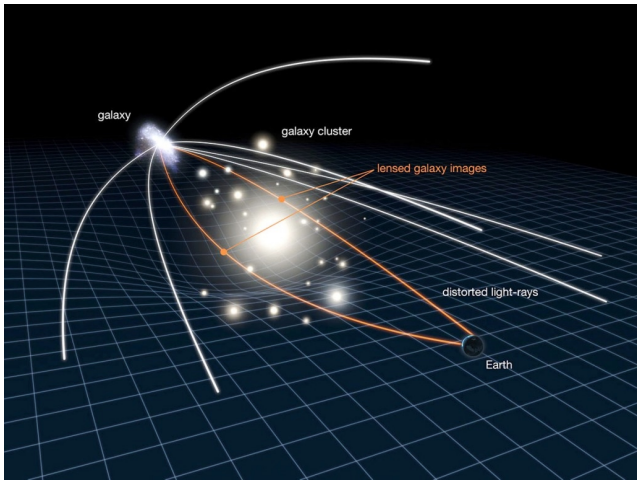

Figure 1.1: Principle of gravitational lensing. Two images of the background source can be detected (orange-colored lines) whereas the white-colored lines do no hit the Earth (from: NASA/ESA).

1.2 Historical Background

The idea of the deflection of light rays passing close to a mass was already mentioned by Isaac Newton in 1704 based on his corpuscular theory of light. More than two centuries later, in 1916, Albert Einstein was the first one to explain accurately the way light is affected by mass and the first calculations related to gravitational lensing were found in some unpublished notes (Renn et al. 1997), where he considered a star perfectly aligned with a foreground mass. He concluded that in case of a perfect alignment the source would be imaged as a ring (such a configuration is called "Einstein ring") around the deflecting mass. If the alignment between a background source and a foreground mass is not perfect, two images of the background source are visible on either side of the lens. A consistent theoretical description of the phenomenon of gravitational lensing was possible with his completion of the *General Theory of Relativity* in 1936. He described the major characteristics of gravitational lensing and computed the typical separation of lensed images. Since this separation would be very small (a few milli-arcseconds), he concluded that "there is no great chance of observing this phenomenon" (Einstein 1936).

It was the astronomer Fritz Zwicky who realized in 1937 that gravitationally induced Einstein rings would be still resolvable with optical telescopes if whole galaxies at cosmological distances would be considered instead of stars in our galaxy. He estimated the image separation of a lensed background source to be of order ∼10 arcseconds (Zwicky 1937). Despite this encouraging prediction, the field of gravitational lensing remained quiet until the beginning of the 1960s, when the subject was reopened by Sjur Refsdal (Refsdal 1964a,c). In 1963, the first quasar was identified by Maarten Schmidt and it took another 16 years and several technical developments until the first detection to happen (Walsh et al. 1979): a galaxy at z=0.36 nearly perfect aligned with the quasar Q0957+561 at z=1.41 produces two images with the same spectral fingerprint of the background object. Many other detections have followed, with the lenses typically being a galaxy or a cluster of galaxies and the background objects usually being galaxies and quasars. Since the beginning of the twentieth century, gravitational lensing became more popular and has evolved to a powerful tool in astronomy, addressing many astrophysical and cosmological questions. Although lensing is a very rare phenomenon (only one in ∼500 quasars is gravitationally lensed), approximately 200 lensed quasars have been discovered up to now (Abdo 2013; Eigenbrod 2011; Eulaers 2012).

1.3 Theoretical Background

In this section we discuss the *lens equation*, which is the fundamental equation in studying gravitational lensing. The simplest model of a lens (Schwarzschild lens) is introduced, followed by a short description of the surface mass density. Next, the magnification and distortion of source images are discussed and critical curves/caustics are explained. We continue with a description of the time delays between the observed images and an explanation based on Fermat's principle is given. All equations derived in Sections 1.3.1–1.3.6 are based on the description by Eigenbrod (2011).

1.3.1 Lens Equation

There exist many approaches to derive the lens equation, in most cases of strong gravitational lensing the *thin lens approximation* is used. In this approximation, the light deflections take place within a very small distance compared to the distance between the source and the observer. The two- and three-dimensional geometry of a gravitational lens system is illustrated in Figure 1.2.

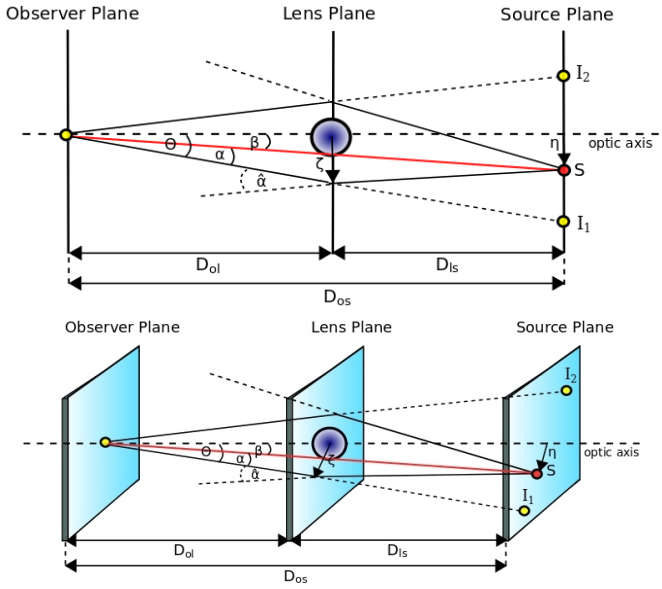

Figure 1.2: Lensing system in 2D (upper panel) and 3D (lower panel).

Let's consider a light source, *S*, seen by an observer *O* through an intervening mass distribution. For simplification, we assume that this mass distribution is located in one single plane (lens plane) orthogonal to the line-of-sight between the source and the observer. This assumption is not unreasonable since the thickness of the lens (even if the lens is a galaxy or a cluster of galaxies) is negligible relative to the large spatial distances involved.

Light rays from a source *S* located at the distance D_{os} from the observer *O* are passing the mass concentration (lens plane) at the distance D_{ol} and cross the lens plane at position ζ. This is the so-called *impact parameter*, defined as the perpendicular extrapolated distance between the path of the light ray and the center of the gravitational field created by the lens. The corresponding two-dimensional angular position of the source is $\Theta = \zeta/D_{ol}$. The true position of the source in the source plane is denominated as η with the corresponding angular position being $\beta = \eta/D_{os}$. In the absence of any deflecting mass we would observe the source at this position. The lens equation is obtained from the projection of the three angles β, $\hat{\alpha}$ (deflection angle) and Θ on the source plane. Simple geometric relations between three angles lead to the *lens equation*:

$$\beta = \Theta - \alpha(\Theta). \tag{1.1}$$

β ..... true angular position of the source
Θ ..... observed angular position of the source
α ..... difference true/observed angular position of the source

If we assume small angles, we can say that $\Theta = \zeta/D_{ol}$, and we can express α as:

$$\alpha(\Theta) = -\frac{D_{ls}}{D_{os}}\,\hat{\alpha}(\zeta). \tag{1.2}$$

$\hat{\alpha}$ ..... deflection angle

If we insert Eq. 1.2 in Eq. 1.1, the geometrical condition for a light ray to reach the observer is:

$$\beta = \Theta + \frac{D_{ls}}{D_{os}}\,\hat{\alpha}(\zeta). \tag{1.3}$$

D_{os} ..... distance observer-source
D_{ol} ..... distance observer-lens
D_{ls} ..... distance lens-source
ζ ..... impact parameter

This equation is also referred to as *lens* or *ray tracing equation*. A given image position always corresponds to a specific source position. In order to find all image positions for a given source it is necessary to invert the lens equation.

Sometimes it is useful to rewrite the lens equation in a dimensionless form: we can define a characteristic length ζ_0 in the lens plane and a corresponding length η_0 in the source plane $\eta_0 = \zeta_0 \cdot D_{os}/D_{ol}$.

The dimensionless vectors in each plane then are:

$$x = \frac{\zeta}{\zeta_0}, \tag{1.4}$$

$$y = \frac{\eta}{\eta_0} \tag{1.5}$$

With these definitions the dimensionless lens equation can be written as:

$$y = x - \alpha(x). \tag{1.6}$$

1.3.1.1 Deflection Angle

The deflection of light rays occurs due to the space-time curvature induced by the mass of lensing objects. The deflection angle $\hat{\alpha}$ can be determined by solving the Einstein field equations, but finding such a solution has proven to be very difficult. Besides the trivial flat space solution, the first exact solution of these equations were found by Karl Schwarzschild and describes the gravitational field outside a spherical non-rotating mass (such as a non-rotating star or black hole). A very good approximation for the deflection angle is given by:

$$\hat{\alpha} = \frac{4\,G\,M}{r\,c^2}. \tag{1.7}$$

r ..... radial coordinate of closest approach
M ..... deflecting mass
G ..... gravitational constant
c ..... speed of light

The distance of the closest approach of a light ray relative to the deflecting mass can be approximated by the impact factor ζ. This means that the deflection angle satisfying the lens equation (Eq. 1.3) is:

$$\hat{\alpha}(\zeta) = \frac{4GM}{c^2}\,\frac{1}{\zeta} \tag{1.8}$$

which defines the deflection angle for a point mass.

1.3.2 Schwarzschild Lens and Einstein Angle

The simplest model describes a point-mass lens, commonly known as *Schwarzschild lens*, and due to the circular symmetry of the lens, exact solutions can be found for the lens equation. If we insert Eq. 1.8 in Eq. 1.3, the lens equations transforms to:

$$\beta(\Theta) = \Theta - \frac{4GM}{c^2}\frac{D_{ls}}{D_{os}}\frac{1}{\zeta}. \tag{1.9}$$

M ..... mass enclosed at some angular radius Θ

Due to the small angles involved we can apply the sine rule $\Theta \simeq \zeta/D_{ol}$ and express the impact parameter as $\zeta = \Theta \cdot D_{ol}$. Inserting this expression in Eq. 1.9 yields:

$$\beta(\Theta) = \Theta - \underbrace{\frac{4GM}{c^2}\frac{D_{ls}}{D_{os}\,D_{ol}}}_{\Theta_E^2}\frac{1}{\Theta} \tag{1.10}$$

where we have defined Θ_E as:

$$\Theta_E = \sqrt{\frac{4GM}{c^2}\frac{D_{ls}}{D_{os}\,D_{ol}}}. \tag{1.11}$$

Θ_E is also referred to as the *Einstein radius* and is used to characterize the angular scale in a lensing system. The typical image separation in multiple lens systems is of the order $2\Theta_E$. If $\beta < \Theta_E$, the quadratic equation (Eq. 1.10) has two solutions, and the source images appear at the following positions:

$$\Theta_{1,2} = \beta \pm \Theta_E. \tag{1.12}$$

In other words, in the case of a point mass lens all sources are imaged twice with the images located on either side of the optical axis (one image at $\Theta < \Theta_E$ and the other one at $\Theta > \Theta_E$). When β decreases to zero, the images appear highly magnified near $\Theta = \Theta_E$. However, if there occurs a misalignment between the source, the lens and the observer, β increases and becomes much larger than Θ_E. As a result, one of the images approaches $\Theta = 0$ and becomes very faint while the other one approaches $\Theta = \beta$ and approximates the unlensed luminosity of the source. In case of a perfect alignment between the source , the lens, and the observer (i.e. $\beta = 0$), a ring-shaped image of radius Θ_E is formed (the so-called *Einstein ring*) since the whole configuration is rotationally symmetric around the line-of-sight. It is clearly unlikely that any circularly

symmetric potential will describe galaxy potentials. In order to produce the observed image configurations, one has to consider potentials which do not have circular symmetry.

Figure 1.3 shows snapshots of three different gravitational lens situations for a circular Gaussian source. From up to down the alignment between the source and the lens gets better and in the undermost panel a perfect alignment is reached, resulting in an Einstein ring.

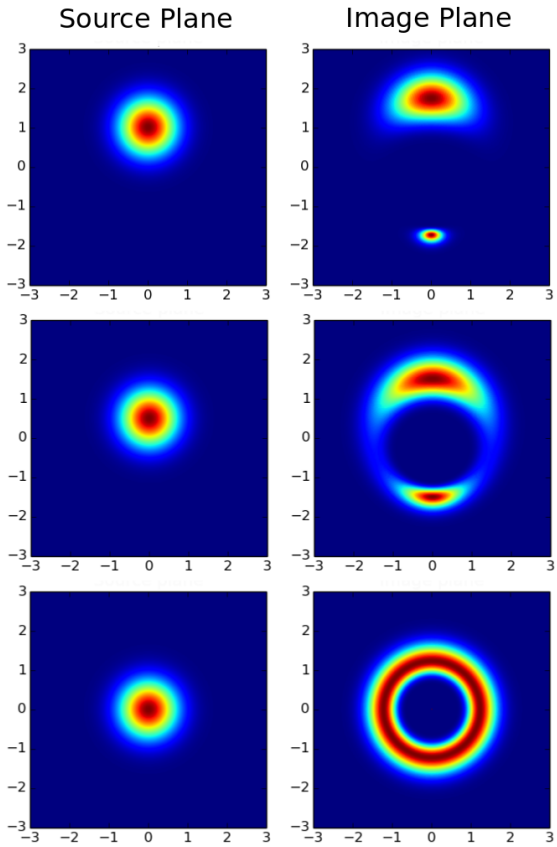

Figure 1.3: Source planes (left) and images planes (right) of three different source-lens configurations with the alignment getting better from top to bottom until a perfect alignment (Einstein ring) is reached.

1.3.3 Surface Mass Density

In the previously described *thin lens approximation* we have considered a mass sheet for the lens normal to the line-of-sight. This mass sheet has a certain surface mass density $\sum(\zeta)$. The dimensionless surface mass density (also called *convergence*) is given as:

$$\kappa(\Theta) = \frac{\sum(D_{ol}\,\Theta)}{\sum_{crit}}. \tag{1.13}$$

$\sum_{crit}$ is the critical surface mass density and is defined by:

$$\sum_{crit} = \frac{c^2}{4\pi G}\,\frac{D_{os}}{D_{ls}\,D_{ol}}. \tag{1.14}$$

The critical surface density is a characteristic value to differ between strong and weak lensing. If $\sum \geq \sum_{crit}$ (i.e. $\kappa > 1$), multiple images of the source can be formed.

1.3.4 Magnification and Image Distortion

Gravitational lensing does not only change the light path but also distorts the shape of light bundles. This leads to amplifications and distortions of the observed images of the background source.

A schematic diagram of the deformation of a gravitationally lensed background object can be seen in Fig.1.4.

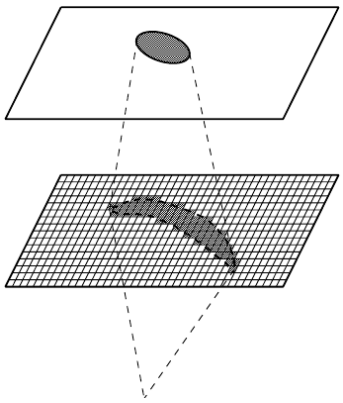

Figure 1.4: Sketch of the distortion of a lensed source (from: Oguri 2004).

The magnification of the images in a lensing scenario can either be positive or negative, and is characterized by the so-called *magnification factor* $\mu(\mathbf{x})$:

$$\mu(\mathbf{x}) = \frac{1}{det\, A(\mathbf{x})}. \tag{1.15}$$

A ..... Jacobi matrix of the lens equation
x ..... image position

The Jacobi matrix describes the distortion of the background source and is defined as:

$$A = \begin{pmatrix} 1-\kappa-\gamma_1 & -\gamma_2 \\ -\gamma_2 & 1-\kappa+\gamma_1 \end{pmatrix}. \tag{1.16}$$

κ ..... convergence
$\gamma_{1,2}$ ..... shear

The shear γ is defined as $\gamma = \sqrt{\gamma_1^2 + \gamma_2^2}$. The convergence κ causes a expansion of the light bundle while the shear γ changes its shape. In Figure 1.5 the meaning of each quantity of the Jacobi matrix is illustrated.

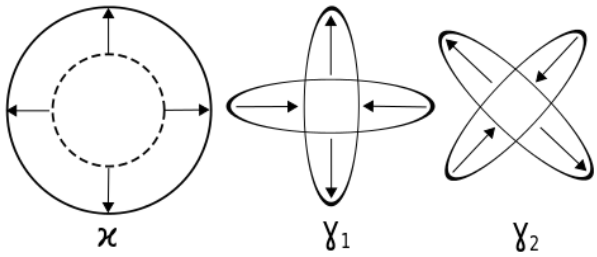

Figure 1.5: Illustration of the meaning of κ, γ_1 and γ_2 in the Jacobi matrix A defined in Eq. 1.16 (from: Oguri 2004).

From Eq. 1.16 the determinant of the Jacobi matrix can be calculated:

$$det\, A = (1-\kappa)^2 - \gamma^2. \tag{1.17}$$

And with Eq. 1.15 and Eq. 1.17 the magnification factor can be written as:

$$\mu = \frac{1}{(1-\kappa)^2 - \gamma^2}. \tag{1.18}$$

Thus, the Jacobian matrix A has two eigenvalues:

$$\lambda_{\pm} = 1 - \kappa \pm \gamma. \tag{1.19}$$

Lensed images are stretched in the two eigendirections of A and are distorted in shape and size. Shape distortions are induced only by the shear γ (due to a tidal gravitational field) whereas magnifications (i.e. the changes in size) are caused by both, the shear γ and the surface mass density κ. Since many lensing galaxies are located in galaxy groups, the additional mass distribution disturbs the gravitational potential of the lens. They contribute to the tidal gravitational field by adding shear to the lensing potential.

1.3.5 Critical Curves and Caustics

When the determinant of matrix A (Eq. 1.17) decreases to zero, the magnification factor μ diverges (*critical points*). Sets of critical points form *critical curves* which are defined by $\lambda_{\pm} = 0$. Critical curves mapped back to the source plane via the lens equation are so-called *caustic curves* (see Figure 1.6). Images get highly magnified when the source approaches a caustic curve and the number of images changes by two in case of a caustic crossing. If $\kappa(\mathbf{x}) > 1$ (or equivalently $\sum(\zeta) > \sum_{crit}$), multiple images are formed. Thus, images near critical curves are highly elongated in the radial direction and arcs are understood as the images near critical lines.

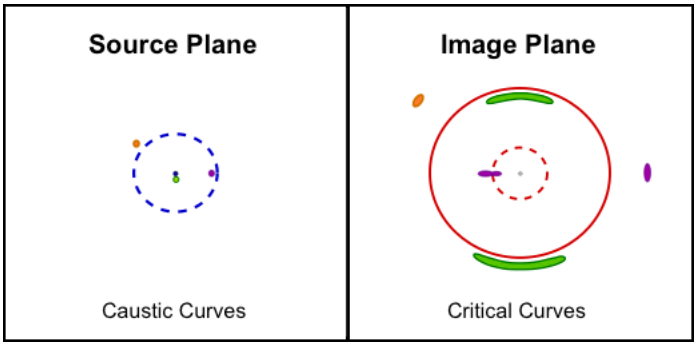

Figure 1.6: Caustics (left) and critical curves (right) of a sphere lens mass distribution. The red solid critical curve in the image plane maps into the central blue point in the source plane, whereas the dashed red line maps into the dashed blue caustics. Three sources in different positions are shown in the source plane with their respective images in the image plane (Suyu 2016; from: A. Amara).

There exist two different types of caustics: the inner and outer ones. Considering a sphere lens mass potential, a source positioned inside the inner caustic produces five images (see Figure 1.7), whereas a source located between the inner and outer caustic produces three images. If the source is positioned outside the outer caustic, it will not be multiply imaged. Note that in the case of multiple images one of the images is usually highly de-magnified and therefore cannot be observed. As a consequence, only two-image or four-image lens systems are observed (Eigenbrod, 2011; Zackrisson & Riehm, 2010).

In Figure 1.7 caustics, separating regions on the source plane that give rise to different numbers of images, are shown. The illustrated sources lie within both caustic curves, leading to the formation of five images (with one central image highly de-magnified). Depending on the position of the source relative to the caustic, three basic image configurations can occur (Eigenbrod, 2011; Amara & Kitching, 2010; Suyu, 2016):

- Einstein cross: four symmetric images
- Cusp caustic: three images close together, one on the opposite
- Fold caustic: two images close together, two with larger separation

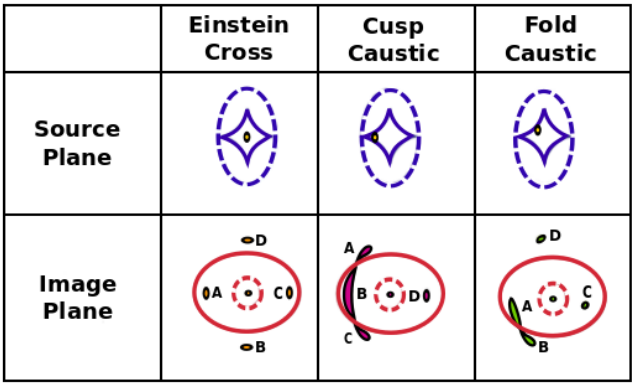

Figure 1.7: Caustics (top row) and critical curves (bottom row) of an ellipsoid lens mass distribution. Solid lines show the inner caustics, dashed lines the outer ones. The solid critical curve in the image plane maps into the astroid caustic in the source plane, whereas the small dashed critical curve maps into the large dashed caustics. Three generic image configurations (*'cross'*, *'fold'* and *'cusp'*) are shown (Zackrisson & Riehm 2010; Suyu 2016, from: A.Amara).

1.3.6 Time Delays and Fermat's Principle

Since light has a finite propagation velocity, it takes a certain amount of time before the light rays emitted by a distant source reach the Earth. The needed amount of time depends on the path taken by the light rays and, thus, will differ whether the source is gravitationally lensed or not.

When a distant quasar shows intrinsic variations, they appear at different times in its multiple observed images. This time difference between the images is called *time delay*. The total time delay consists of two contributions: the first one is due to a geometrical time delay, whereas the second one is induced by the gravitational potential of the lens. The first one occurs because bent light rays are geometrically longer than straight lines, which results in a longer traveling time. The latter one is an effect of general relativity and occurs when light rays are propagating in a gravitational field (*Shapiro effect*) - light rays passing closer to the lensing mass are slower and hence, need more time to move forward. Note that the gravitational time delay occurs at the redshift of the lens and then gets stretched due to the cosmic expansion.

Lensed images always form at points where the *Fermi* potential (i.e. the arrival time surface) is stationary. This is a consequence of Fermat's principle, which states that light rays always take the paths that extremize the arrival time τ. Stationary points can be a minimum, a maximum, or a saddle point and in the case of intrinsic source variability, flux variations will be observed first in the minimum, followed by the saddle point and in the end in the maximum. If there are several stationary points of the same type, the image farthest away from the lens is leading. Figure 1.8 shows the vector fields around the different types of stationary points (Eigenbrod, 2011; Eulaers, 2012; Oguri, 2004).

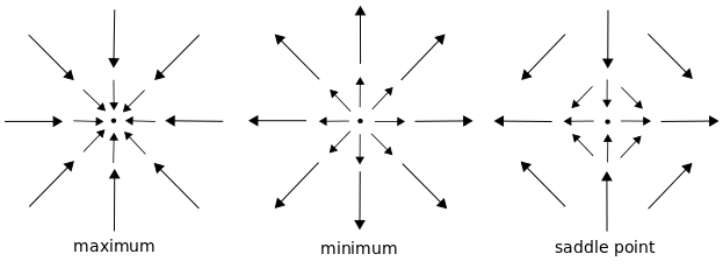

Figure 1.8: Vector fields around the three types (maximum, minimum, saddle point) of stationary points of the Fermi potential (from: Oguri 2004).

Contours of the arrival-time surface are called *isochrones*. In absence of a lens, these isochrones are concentric circles and the observed image is located at the central minimum. Small lensing masses only slightly change the shape of these lines and delocate the minimum a little. For lensing masses high enough, the contours become self-crossing and more images are produced since each crossing of the contours causes two new images. Examples of stationary points together with isochrones are shown in Figure 1.9 (Eigenbrod, 2011; Eulaers, 2012; Moore, 1996; Oguri, 2004). Lensed quasars occur typically in three- or five-image configurations with a maximum located at the center of the lensing galaxy. In general, the central maximum is highly de-magnified and almost unobservable. Therefore the number of observed quasar images seems to be even, such configurations are typically labeled double/quad-systems (Eigenbrod, 2011; Eulaers, 2012; Oguri, 2004).

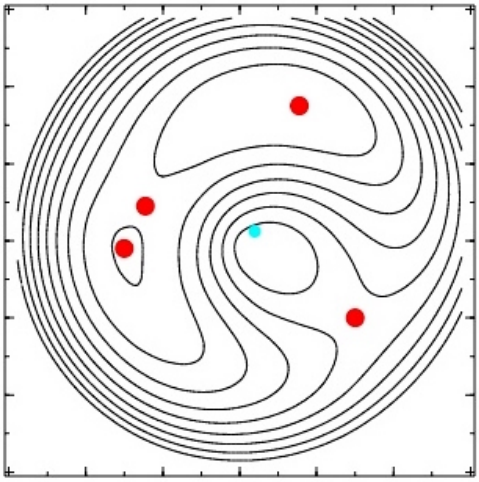

Figure 1.9: Contours (isochrones) of the Fermat potential/time-delay surface. The surface mass density of the lens galaxy is high enough to distort the surface of the Fermat potential and additional extrema/saddles appear corresponding to additional multiple images of the background source. The blue point in the center marks the position of the source, and image locations are colored in red. Two of the images are located at minima, and additional two form saddle points (Suyu 2016; from: Belokurov et al. 2009).

1.4 Fields of Gravitational Lensing

There exist four different observational flavors of gravitational lensing: strong lensing, weak lensing, flexion and microlensing. In strong lensing the background source is lensed into multiple images and in cases where the source is spatially extended, the images are distorted into rings/arcs. In weak lensing, the source is located further away from the line connecting the observer and the lens, and consequently only weak distortions of singly imaged background sources occur. Flexion is bridging the gap between strong and weak lensing, and is responsible for the weakly skewed arc-like appearance of lensed galaxies. These three regimes of gravitational lensing are shown in Figure 1.10. Last but not least, in microlensing the lenses are stars in the galaxy which lead to multiple images of the source. However, these separations between the multiple images are of the order of micro-arcseconds and cannot be resolved by telescopes. Unresolved multiple images form one single image and the observer simply sees a magnification of the background source as the lens passes between the observer and the source (Massey 2010; Suyu 2016).

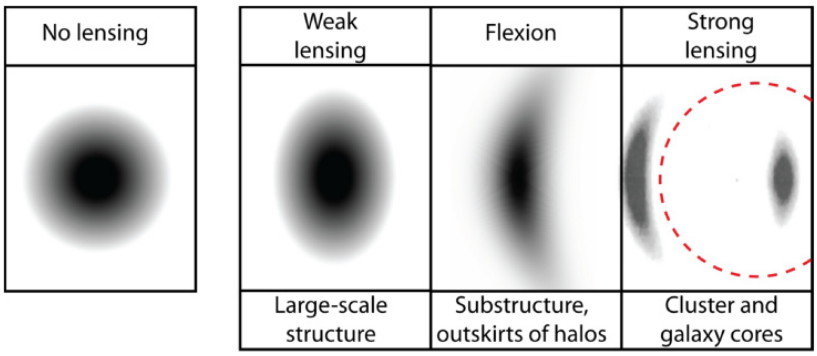

Figure 1.10: Various regimes of image distortion induced by gravitational lensing. An intrinsically circular source is distorted into en ellipse by *weak* lensing along the typical lines-of-sight through the Universe. Nearer concentrations of mass introduce a *flexion* curvature. *Strong* gravitational lensing produces multiple images/giant arcs since the light passes through the most curved space-time near massive galaxies or galaxy clusters (from: Massey et al. 2010).

1.4.1 Strong Lensing

We speak of strong lensing if the nearby space-time is so warped that light of a distant object can travel along multiple paths around the lens and still be deflected towards the observer, forming multiple images (Treu 2010). Usually, a dense concentration of mass like an elliptical galaxy or a cluster of galaxies serve as a strong lens and although strong lensing is a very rare phenomenon, we are able to observe multiple distorted images, giant arcs or nearly complete Einstein rings of lensed background objects. The effects of strong lensing can be summarized in four aspects (see, e.g., Wambsganss 2016):

- **Change of position:**
  In general, this is not observable because one needs a 'before-and-after' scenario in order to compare two angular positions.
- **Distortion:**
  Extended sources undergoing gravitational lensing get distorted; circular sources are deformed into arclets, arcs or Einstein rings.
- **(De-)Magnification:**
  Magnification is one of the most significant signatures of gravitational lensing, with magnifications up to several orders of magnitude.
- **Multiple Images:**
  Multiple imaging of the very same background source is the most dramatic effect of gravitational lensing.

Strong lensing allows us to reconstruct the total mass distribution (both baryonic and dark matter) of lenses over a wide range of cosmological distances. In addition, strong lensing provides information about the nature of galaxies (Kochanek 2006a,b) and multiple images can be used to study the lens, the source and cosmological parameters (Eulaers 2012; Amara & Kitching 2010). In Figure 1.11 a scenario with many microlenses is displayed together with all lensing effects for a particular source profile.

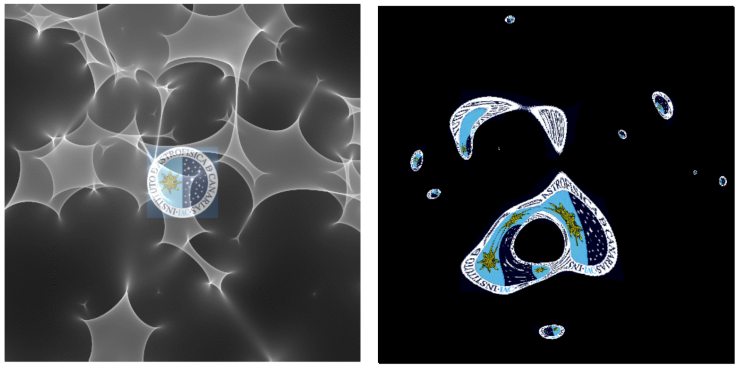

Figure 1.11: Magnification pattern (left) produced by the stars in a lensing galaxy and resulting image configuration (right) of a particular source profile (from: J. Wambsganss 2012)

.

1.4.2 Weak Lensing

Weak lensing occurs when the background sources are sufficiently distant from the lens mass distribution. Most lines-of-sight through the Universe do not pass near a strong gravitational lens. However, massive structures situated along the line-of-sight deflect the light emitted by the background sources and induce distortions in the lensed images. Since every light ray is affected by the distribution of matter along or near its path, weak lensing occurs along each line-of-sight in the Universe. Every inhomogeneous matter distribution between an observer and a distant light source affects the measurable properties of the source in two different ways: images of distant, extended sources are distorted in shape and thus, their brightness is slightly modified. While multiple images, microlensing with high magnifications and arcs are phenomena of strong lensing, in weak lensing the sources have only single lensed images whose shapes are weakly sheared and with magnifications close to unity. Either the magnification or the shear distortion can be measured, with the shear tending to have a higher signal to noise. The shear distortion introduces changes in the shape of distant galaxies, adjusting their major-to-minor axis ratio by ∼2%. In fact, the phenomena of weak lensing are so weak that they cannot be seen in an individual object but can only be detected using an ensemble of background sources. Intrinsic shapes of galaxies (elliptical, spiral arms and knots of star formation etc.) must average out as circular in the absence of lensing.

However, galaxies along adjacent lines-of-sight are sheared by a similar amount and once sheared, the average shape of adjacent galaxies is an ellipse. To infer the amount of shear produced by the foreground mass distributions, averaging over the shape of at least ∼100 galaxies is required to obtain a signal to noise of unity in shear. Weakly distorted background images can be used to map the mass distribution of the foreground lenses and thus, the dark matter distribution. Strong lensing is a rare phenomenon whereas weak lensing is much more common. Therefore, over the past few years weak lensing has rapidly become a standard cosmological tool (Eigenbrod 2011; Eulaers 2012; Massey 2010; Suyu 2016; Wambsganss 1998,2001).

1.4.3 Flexion

Flexion bends galaxy shapes into arcs. If the projected mass distribution of a lens changes the induced shear from one side of a source galaxy to the other, the galaxy begins to curve as shown in Figure 1.10. Flexion measurements can be used to fill in a gap in the reconstructed mass around galaxy clusters where the light deflection is too small for strong lensing and the number of lensed sources is too low for significant weak lensing analysis (Massey 2010).

1.4.4 Microlensing

We have seen how large mass distributions, like galaxies or cluster of galaxies, can act as gravitational lenses. There exist many examples of multiply imaged lensed quasars; however, not only large mass distributions can act as a gravitational lens but also small compact objects (i.e. stars) in the lens galaxy itself located close to the line-of-sight affect the path of the light rays and behave like small lenses. The effect of a whole galaxy acting as a lens is usually described by a smooth potential created by a continuous mass distribution, producing the observed multiple (de-)magnified macro-images of the background source. Microlensing involves many microlenses simultaneously and compact objects in the galaxies (i.e. individual stars) introduce a graininess into this potential (see Figure 1.12), giving rise to strong changes in the magnification of the macro-images. In a multiple lensed quasar, at any given time an ensemble of microlensing is affecting the quasar brightness, so that microlensing is expected to be going on all the time. Since the deflection of the light and the angular separation between the lensed images of a background source are proportional to the square-root of the mass of the lens, image separations are typically in the order of micro-arcseconds for stellar mass objects. Such small angular sepa-

rations cannot be resolved with current telescopes, and many micro-images form one single unresolved (de-)magnified image. These (de-)magnifications can reach several magnitudes and vary in time due to the relative motions between the observer, the source (quasar), and the microlenses (Wambsganss 2016; Eigenbrod 2011; see also the review by Wambsganss 2006).

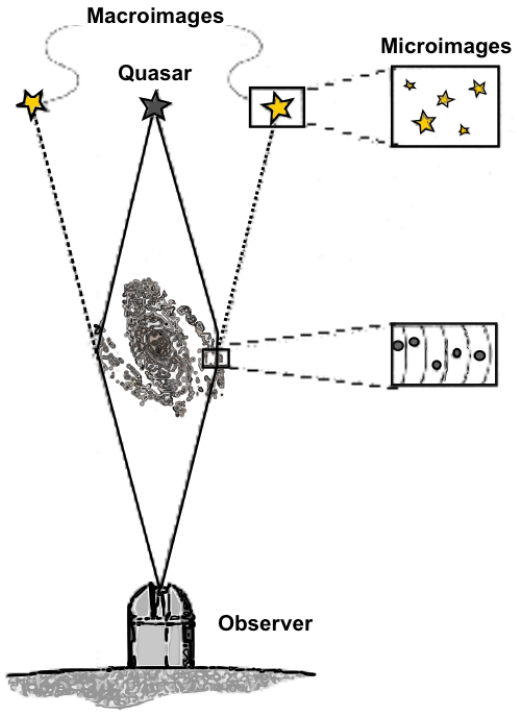

Figure 1.12: Sketch of the effect of microlensing: stars in the galaxy produce multiple micro-images and form one single unresolved (de-)magnified image (from: Refsdal & Surdej 1994).

The flux variability of the images of a gravitationally lensed quasar is a combination of the intrinsic variability of the source, correlated by a time delay between the different images, and gravitational microlensing that depends on the random distribution of stars in the lens galaxy. This last variability is uncorrelated between images (Chang & Refsdal 1979; see also review by Wambsganss 2006). Microlensing induced fluctuations take place on time-scales of a few days to several months depending on the lensed system, and are extrinsic to

the background source. Such uncorrelated variations in the observed brightness of lensed images are referred to as microlensing events (Eigenbrod 2011; Wambsganss 2016; see also the review by Wambsganss 2006).

1.4.4.1 Length and Time Scales

A source sitting at a given location at the source plane is affected by the magnification at that particular location and since the source–lens system is dynamic, the magnification will change with time. In other words, the relative motions make the source travel through the magnification map (see Section 3.2.2) and as a consequence, the observed light curves show time-dependent variations of the magnitude (Eigenbrod 2011; Jiménez-Vicente 2016). There exist two different length- and time scales for these microlensing variations:

- **Microlensing Length Scales.**
  The magnification pattern caused by stars and other compact objects in the lens galaxy has a characteristic physical scale set by the Einstein radius of the microlenses, R_E, projected onto the source plane (Mosquera & Kochanek, 2011; Poindexter & Kochanek, 2010):

$$R_E = D_{os}\left[\frac{4G\langle m\rangle}{c^2}\frac{D_{ls}}{D_{ol}D_{os}}\right]^{1/2}, \tag{1.20}$$

  where G is the gravitational constant, c the speed of light, $\langle m\rangle$ the mean mass of compact objects and D_{ol}, D_{os} and D_{ls} the distances between the observer, the lens and the source.

  The other length scale on which microlensing depends is the size of the background source, R_s. If the characteristic source size satisfies $R_s < R_E$, microlensing changes will be significant, and their amplitude will be controlled by the ratio R_s/R_E, in the sense that smaller sources lead to larger variability amplitudes. The accretion disks of lensed quasars are generally sufficiently compact to satisfy this criterion for typical microlens masses (Mosquera & Kochanek, 2011; Poindexter & Kochanek, 2010). If the emission region is much larger than R_E, little or no changes in the magnification are expected.

- **Microlensing Time Scales.**
  The timescale of microlensing variability is determined by the relative velocities of the source, the observer and the lens galaxy (including its stars). In general, the lens motions dominate (Kayser & Refsdal, 1989), leading to two different timescales. The first characteristic timescale on which microlensing fluctuations occur combines the microlensing length scale R_E with the effective velocity v_{eff} of the source. If $R_s < R_E$ is given, microlensing variability will certainly occur on the *Einstein crossing timescale* t_E, which describes the duration to cross one Einstein radius (Mosquera & Kochanek, 2011; Poindexter & Kochanek, 2010):

$$t_E = \frac{R_E}{v_{eff}}. \tag{1.21}$$

  The characteristic time to cross the Einstein radius can be determined from microlensing light curves and is sometimes discouragingly large, lasting up to several decades. However, if a compact source is traveling through active regions in the magnification pattern, magnification anomalies are expected on a considerably shorter timescale, t_s, corresponding to the time it takes the source to cross its own radius R_s (Mosquera & Kochanek, 2011):

$$t_s = \frac{R_s}{v_{eff}}. \tag{1.22}$$

  Typically, the *source crossing timescale* is ranging from weeks up to several years, although long crossing times are rare because large separation lenses are uncommon. Unfortunately, small sources with short timescales correspond to low-luminosity sources which are difficult to observe (Mosquera & Kochanek, 2011).

1.4.4.2 Microlensing Techniques

The stars in the lens galaxy produce a complicated magnification pattern in the plane of the quasar which includes caustic curves. Due to the motions of the stars in the galaxy and the relative motions between the quasar, the galaxy, and the observer, the arrangement of these caustics changes its position relative to the quasar. As a consequence, the quasar is magnified differently at different times and the number and brightness of the micro-images changes, producing a (uncorrelated) change in the total flux of the images. The exact arrangement of

the microlenses in a lens galaxy cannot be determined and microlensing simulations have to deal with this problem in a statistical way. However, simulations with different spatial distributions but with the same number of micro-lenses (the higher the number of microlenses, the higher the probability of microlensing), should lead to the same magnification histograms as the real, unknown distribution. Such tool is called magnification map (Eigenbrod 2011; Massey 2010; Wambsganss 2016). A more detailed description can be found in Section 3.2.1.

Several numerical techniques were developed in order to simulate the gravitational lens effect of many compact objects by randomly distributing microlenses in the lens plane, according to a given *surface mass density* and *shear* (Eigenbrod 2011; Massey 2010; Wambsganss 2016). These two parameters are obtained from the macro-model of the lensed system (usually an ellipsoid or an isothermal sphere with additional external shear). Kayser et al. (1986) and Schneider & Weiss (1987) developed the *inverse ray shooting* technique that produce two-dimensional magnification distributions in the source plane. More recently, Mediavilla et al. (2006) developed the *inverse polygon mapping* from the lens plane to the source plane, which is faster to compute and hence used in this work.

1.4.4.3 Applications of Quasar Microlensing

The astrophysical applications of microlensing are gaining more and more interest since the amplitude, duration, and frequency of microlensing depends on several parameters: the surface density of both, stars $\kappa_\star$ and continuously distributed dark matter κ_s, the shear γ, the mass of microlenses M, the relative transverse velocity v_T, the size of the background source r_s and the geometry of the system (Eigenbrod 2011; Wambsganss et al. 1990). The surface densities and the shear are determined by a macro-model and thus, all linear sizes scale with the square root of the mass of microlenses. With the help of microlensing we can get interesting information about the size (Wambsganss et al. 1990) and shape (Mineshige & Yonehara 1999) of the background source, as well as the mean mass of the microlenses (Kochanek 2004) and the transverse velocity of the lensing system (Gil-Merino et al. 2005). Strong microlensing variations can be either induced by a large transverse velocity or a small source size. Large sources smooth out flux anomalies in the light curves (Blackburne et al. 2011, 2014; Mosquera & Kochanek 2011) as we will see in Section 3.2.2. Microlensing can be used to probe the central emission region of lensed quasars and recent

efforts have estimated the sizes of the non-thermal (X-ray) and thermal emission regions (e.g. Chartas et al. 2009; Dai et al. 2010; Morgan et al. 2008; Pooley et al. 2007). Other studies have investigated the relationships between the accretion disk size and the black hole mass (e.g. Morgan et al. 2010), the size and the emission wavelength (e.g. Anguita et al. 2008; Bate et al. 2008; Eigenbrod et al. 2008; Poindexter et al. 2008; Floyd et al. 2009; Mosquera & Kochanek 2011), and the dark matter fraction in the lensing galaxy (e.g. Pooley et al. 2009; Mediavilla et al. 2009; Dai et al. 2010).

1.5 Lensing Phenomena

There exist various observational phenomena caused by gravitational lens effects. The observations of gravitational lensing can be divided into different categories by several criteria. For instance, a categorization due to different sources can be made: observations of point sources (stars), unresolved sources (quasars), resolved sources (optical galaxies) and extended sources (radio jets). Also the type of the lens can be used as a criterion: stellar lenses, galaxy lenses and cluster lenses. Likewise, the lens mass can serve as a criterion, for example macro-lensing versus microlensing. Yet one can also distinguish between static (detection of image configurations) and dynamic lensing (detection of changes in the configuration or magnification with time). Furthermore, the strength of lensing can be used for a classification - strong lensing induces multiple images whereas with weak lensing only statistical effects on the image shape and orientation can be detected (Joachim Wambsganss 2001).

In Figure 1.13 a sketch of three different cases of gravitational lensing is illustrated. We can see that if the lens is not spherically symmetric/perfectly aligned with the background object, multiple images of the background source are produced instead of the formation of a circular Einstein ring. If the lensing object is a cluster of galaxies, even more complex images are produced. In the following section several lensing phenomena are described, including the creation of multiple quasar images, the formation of giant luminous arcs, the occurrence of Einstein rings and the splitting into Einstein crosses.

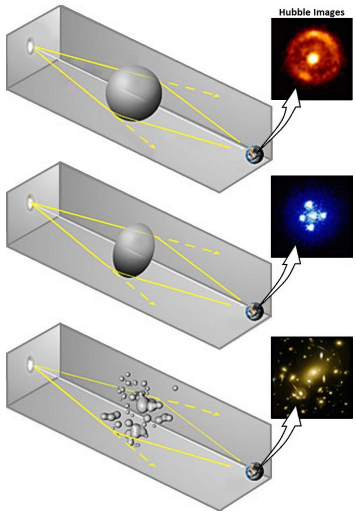

Figure 1.13: Illustration of different lensing cases: (top) an Einstein ring is produced by a spherical lens, (middle) a non-spherical lens causes a splitting into multiple images, (bottom) giant arcs and arclets are formed by a cluster of galaxies (from: ESA).

1.5.1 Multiple Images

If a background source is slightly offset, or the lens has a complex shape, the source will appear in multiple locations (Massey 2010), each of these multiple images can be brighter (magnified) or fainter (de-magnified), and the magnification will be greater close to the *critical curve* (i.e. the asymmetric equivalent of an Einstein ring, see McBreen & Metcalfe 1987). In 1912 Einstein explored gravitational lensing by a star and showed that a distant star lying close to the line-of-sight to a foreground star will be imaged twice. The first objects found to be gravitationally lensed outside our Solar System were quasars and since then, several image configurations have been found with two, three, four or even more images (see Figure 1.14). The theory predicts that the macro-images of lensed quasars should occur in odd numbers; however, in most known multiple quasar systems two (doubles) or four (quads) images can be seen. The central image (the third for a double or the fifth for a quad) is often not detectable due to high demagnifications and/or strong extinction in the central part of lensing galaxies (Wambsganss 2016). Symmetric as well as asymmetric image arrangements were discovered, allowing us to study the lens galaxy and the background source itself (Wambsganss 1998,2001).

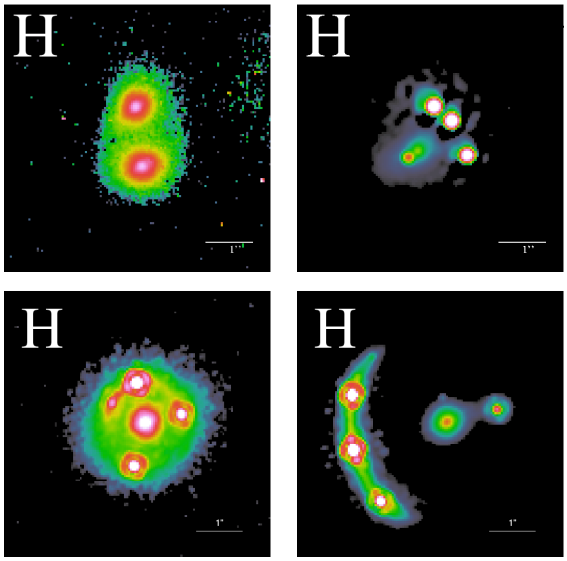

Figure 1.14: Sequence of lensed quasars, with two (top left) up to five (bottom right) images (from: CASTLES Survey).

1.5.2 Einstein Rings

If a distant background source lies directly behind a circular foreground lens, the light can travel around any side of it, and appears as a bright ring – a so-called *Einstein ring* (Einstein 1922). Einstein also concluded that the size of such a ring (proportional to the square root of the projected mass inside it) would be extremely small and that the probability of such a configuration is very low. Neither point sources nor point/circular lenses exist, nor does it ever occur that three points are perfectly aligned. Nevertheless, ring-like image configurations (see Figure 1.15) which are not perfectly circularly symmetric are possible even for not ideal conditions (finite sources, extended lenses, almost exact alignments). Kochanek et al. 2001 showed that, when compared with two-image systems, constrains from an Einstein ring yields accurate measurements of the slope of the lens galaxy's mass profile and, when combined with time delay information, provides an measurement of the Hubble constant (Suyu et al. 2010). Models of Einstein ring lenses are sensitive to perturbations of the smooth potential of the lens galaxy (Vegetti & Koopmans 2009a,b), produced by satellite galaxies and/or by dark matter sub-halos that orbit the main lens galaxy. These objects are often too faint to be detected but can be discovered indirectly through their perturbations. Therefore, Einstein ring lenses are useful to study the properties of extragalactic substructures (Suyu & Halkola 2010).

Figure 1.15: Horseshoe Einstein ring: the gravity of a bright massive foreground galaxy in the center (red) has bent the light of a distant background galaxy (blue). Due to the almost perfect alignment between the background and the foreground galaxy a nearly complete ring is formed (from: NASA/ESA/Hubble).

1.5.3 Einstein Cross

An Einstein cross is a particular form of gravitational lensing, corresponding to four images of the same background source appearing around a foreground galaxy. In fact, this configuration is formed by five images: one de-magnified image in the center and four magnified images in form of a cross (see Figure 1.16). This sort of gravitational lensing is more common than the formation of Einstein rings since a perfect alignment between a background source and foreground galaxy is rare, hence slight misalignments lead to a splitting up of the Einstein ring into four images. If the misalignment is more pronounced, a single magnified arc on one side of the lens is formed together with a de-magnified image on the other side (see Figure 1.17; Wambsganss 1998). The lack of axi-symmetry of the mass distribution also contributes to the non-formation of a ring.

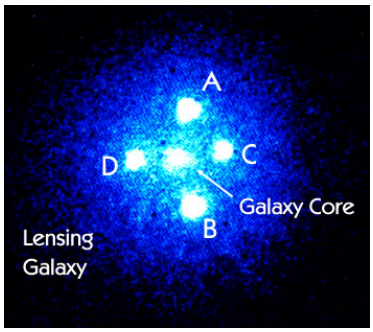

Figure 1.16: Einstein Cross QSO 2237+0305. Four images of a distant quasar appear around a foreground galaxy (from: Skyhound).

Figure 1.17: Split up Einstein Ring SDSS J120540.43+491029.3 (from: NASA/ESA/A.Bolton/SLACS Team).

1.5.4 Giant Luminous Arcs and Arclets

Giant luminous arcs are distorted and strongly elongated images (with lengths up to 20 arcseconds and length-to-width ratio ≥10) of galaxies gravitationally lensed by a foreground galaxy cluster. These elongated thin features are found in central parts of very massive galaxy clusters and most of them are clearly curved around the cluster center, having the shape of a banana. If the shape of the lensed galaxies were perfectly circular, they would be seen as ellipses. Soon after their first discovery (Lynds & Petrosian 1986; Soucail et al. 1987), spectroscopical studies showed that they are highly distorted and magnified images

of sources at much higher redshift than the cluster itself and are physically not connected to the cluster. Such arcs are pieces of Einstein rings, formed by the merging of multiple images, and their large axis ratio implies that they are located close to the critical curve of the cluster lens. Additional, less magnified images of the source are expected far away from the arc. Also slightly less distorted images with smaller axis ratio elongated in the tangential direction to the cluster center are produced, which have been termed 'arclets'. One sometimes also finds radial arcs crossing the inner critical curve, although they are generally difficult to see because they are less magnified and appear inside the Einstein radius, behind any light emitted by the lens object itself (Eigenbrod 2011; Massey 2010; Wambsganss 1998, 2016 and references therein).

The formation of giant arcs requires an almost perfect alignment between the background galaxy and the foreground cluster which is quite rare. However, several examples have been found up to now. One of the most spectacular cluster lenses (Abell 2218) producing giant luminous arcs and more than 100 smaller arclets is shown in Figure 1.18.

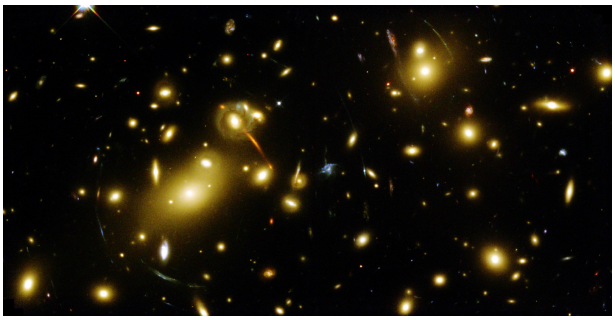

Figure 1.18: Giant luminous arcs together with many smaller arclets produced by the galaxy cluster Abell 2218 (from: NASA).

Strong lensing by clusters can be used to estimate cluster masses (by determining the arc curvature) and they also provide us with highly magnified galaxies at very high redshifts which otherwise would be too faint to be detected in their unlensed stages. Hence, they help us to investigate proto-galaxies in their early evolutionary stages. One of the most interesting results from giant arc analysis is that galaxy clusters are dominated by dark matter (Wambsganss 1998,2001 and references therein).

1.6 Applications of Gravitational Lensing

In the past decades gravitational lensing changed from a curiosity into an interesting astrophysical tool with numerous applications. These applications range from studies in the Solar System to investigations of the galactic structure up to probing cosmological objects. Through astronomical observations one can investigate all three parts in a gravitational lens scenario: the source, the lens and the geometry of the Universe.

Gravitational lensing is equally sensitive to luminous and dark matter and since the deflection of light is determined by the mass distribution of the lenses, gravitational lensing is a powerful tool to measure the total mass of celestial objects. Several important discoveries have been made, for example the detection of exoplanets far away from their host star (Bond et al. 2004), the detection of large-scale structures using weak lensing techniques (Van Waerbeke et al. 2000) and the discovery of dark matter in form of low-mass stars in our galaxy (Alcock et al. 1993; Aubourg et al. 1993). Giant luminous arcs produced by strong lensing can be used to measure the mass distribution in large galaxy clusters. A direct empirical proof of the existence of dark matter (Clowe et al. 2006) has been found and constraints on the density of dark energy in the Universe is provided from statistical studies (Turner 1990). Other applications of lensing provide estimates of cosmological parameters like the Hubble constant H_0, using the so-called time-delay method (Refsdal 1964b). This method is based on the fact that a galaxy situated on the line-of-sight of a distant background source produces multiple magnified images of the source. The light of these images follows different paths so that intrinsic variations of the source are observed at different times in each image. These time delays between the lensed images can be used to determine the value of H_0 as they are proportional to H_0^{-1} (Eigenbrod 2011). Furthermore, the motion of galaxies with respect to the smooth Hubble flow is a useful probe of cosmology, and direct measurements of peculiar velocities are possible in lensed quasar scenarios (Poindexter & Kochanek 2010; Mediavilla et al. 2015, 2016; Gil-Merino et al. 2005; Wyithe 1999).

One of the most practical properties of gravitational lenses is that they act as natural telescopes and since lenses can magnify background sources, these appear brighter and some of the most distant galaxies in the Universe have been detected (with $z_{spec} \simeq 8.7$ by Zitrin et al. 2015). Additionally, stars in the lens galaxies act as numerous microlenses and induce flux variations in the images of

the background source. Gravitational microlensing is a powerful tool for probing the physical properties of cosmologically distant lens galaxies and studying the structure of quasars (Poindexter & Kochanek 2010; Mosquera & Kochanek 2011; Wambsganss 2006). In particular, the effect of microlensing can be used to resolve and probe the inner structures of lensed quasars with resolutions far beyond the reach of presently available telescopes (Eigenbrod 2011 and references therein).

1.7 Active Galactic Nuclei

Active galactic nuclei (AGNs) are amazing power sources in the center of active galaxies, pouring out the same amount of energy as thousands of Milky-Way-like galaxies but in a volume of space comparable to the size of our Solar System (i.e. $\sim 10^{15}$ cm). AGNs are powered by supermassive black holes and accretion of the surrounding gas is the origin of their tremendous luminosity (Rees 1984). This accretion flow is also the source of X-ray, UV and optical continuum emissions which ionizes the gas in the surrounding regions. Much of the large-scale structure of AGNs has already been observationally verified; however, up to now we still do not understand the central engine itself since this region is too small to be resolved with current telescopes. Since gravitational lensing acts like a natural telescope, it can be used to resolve the most inner parts of gravitationally lensed AGNs (Eigenbrod 2011).

1.7.1 Structure of AGNs

Since their discovery, AGNs have been observed through the entire electromagnetic spectrum and several similarities in their spectra have been reported. However, also many differences have been found, like the presence or absence of broad emission lines, the strength of emission lines and other characterizing parameters, leading to a broad diversity among these objects. In fact, it appears that much of the variety in AGN classes is just the result of different orientations relative to the line-of-sight. Based on decades of investigations of active galaxies, a unified scheme has emerged in which AGNs share certain fundamental components, which are (Lawrence 1987; Eigenbrod 2011 and references therein):

- a central supermassive black hole
- an accretion disk
- a broad-line region (BLR)
- a narrow-line region (NLR)
- a torus of gas and dust (obscuring the BLR from some directions)
- relativistic jets

Figure 1.19 schematically shows the typical spatial structure of AGNs: the supermassive black hole (SMBH) in the center is surrounded by an accretion disk

producing the continuum emission. Within an expanded torus of gas and dust the broad-line region (BLR), consisting of fast circling clouds of gas, is orbiting the central SMBH, giving rise to the broad emission lines (BELs). Farther away from the center, the narrow-line region (NLR) is located, characterized by slower orbiting clouds producing the narrow emission lines (NELs). More details about each component can be found in the following subsections. Since the orientation of the observer relative to the torus axis determines the type of AGN, a unified model can be used to explain the occurrence of different AGN types. The presence or absence of jets classify whether the source is radio loud or radio quiet. Despite its success, the unification scheme does not explain all observed properties of AGNs (Antonucci 1993; Eigenbrod 2011).

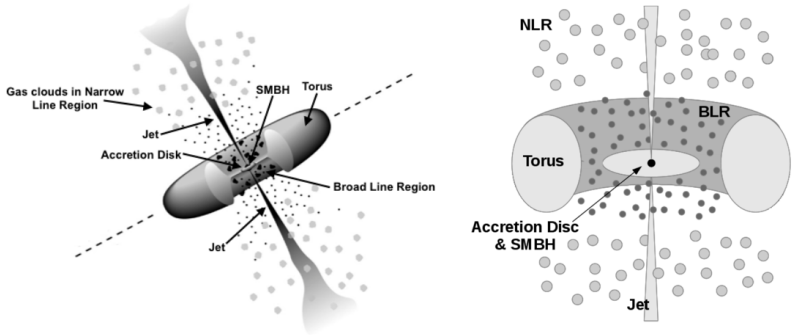

Figure 1.19: Geometry of an AGN, consisting of a supermassive black hole in the center, surrounded by an accretion disk, a broad-line region, a narrow-line region, and a dusty torus (from: Urry & Padovani 1995; Beckmann & Shrader 2012).

1.7.1.1 Supermassive Black Hole (SMBH)

Black holes are objects so massive and dense that even light cannot escape their gravity. Supermassive black holes in the center of active galaxies are among the largest type of black holes with masses ranging from 10^6 up to 10^9 $M_\odot$. They act like enormous engines, converting potential energy of infalling material from the accretion disk into kinetic and electromagnetic energy. They radiate over a trillion times more energy than our Sun and are the principal energy provider for the AGN luminosity. High energy processes occurring near the supermassive black hole generate hard X-ray emissions in the 2-20 keV range that can be observed on the Earth (Antonucci 1993; Eigenbrod 2011).

1.7.1.2 Accretion Disk

The energy production of quasars is extremely efficient and a large amount of energy is emitted in a spatially compact region of order light-days (or even light-hours). Matter is attracted towards the central supermassive black hole and since the infalling material has an angular momentum different from zero, it spins around the black hole and forms a so-called *accretion disk*. Due to the friction and magnetic interactions between the infalling material, gravitational energy is converted into magnetic fields, outflowing winds and heat. Up to 10% of the rest energy of matter is released as radiation by the conversion of gravitational energy, a mechanism far more efficient than nuclear fusion. The disk gets hotter towards the center and the innermost part of the accretion disk (i.e. at a distance of ~ 1 AU $\sim 10^{13}$ cm from the black hole) becomes extremely hot ($> 10^5$ K) and generates thermal emission. The spinning material emits over a wide range of wavelengths, reaching up to the X-ray domain (Shields 1978), although most of the emission is observed as a continuum extending from the near infrared to past 1000 Å in the ultraviolet. This is called the *big blue bump* (Shields 1978; Malkan & Sargent 1982; Elvis 1985) where the peak of the quasar emission is usually found. In order to produce such a continuum, an accretion rate of about 1-100 $M_\odot$ per year is required (Eigenbrod 2011; Goodstein 2012; Wambsganss 2016).

1.7.1.3 Broad-Line Region (BLR)

The emission of UV and X-ray light from the center/accretion disk ionizes the gas located in the broad-line region and strong, broad emission lines (see Figure 1.20) are produced over a wide range of distances from the central source (see e.g., Sulentic et al. 2000). To produce the observed broadening of these lines, the orbiting clouds of gas must have very high velocities in this region, typically reaching 5000 km/s and in some extreme cases up to 15.000 km/s. Also other spectral features are produced within the BLR, for instance iron (Fe II) gets ionized, producing a blend of emission lines predominantly in the 2000 to 3000 Å region. Along with the Balmer continuum, this blend forms a pronounced humping in the spectrum, also referred to as the *small blue bump*. Spectral features provide important information about the structure of the BLR since the BLR is too small to be resolved by telescopes. With the help of theoretical models predicting the strength of emission lines relative to the continuum, it has been found that the observed ratios are much less than expected and, as a consequence, some of the continuum radiation must be escaping directly

into space without interacting with the gas situated in the BLR. Hence, the gas in the BLR cannot be uniformly distributed but is clumpy, distributed in numerous clouds surrounding the accretion disk (Eigenbrod 2011).

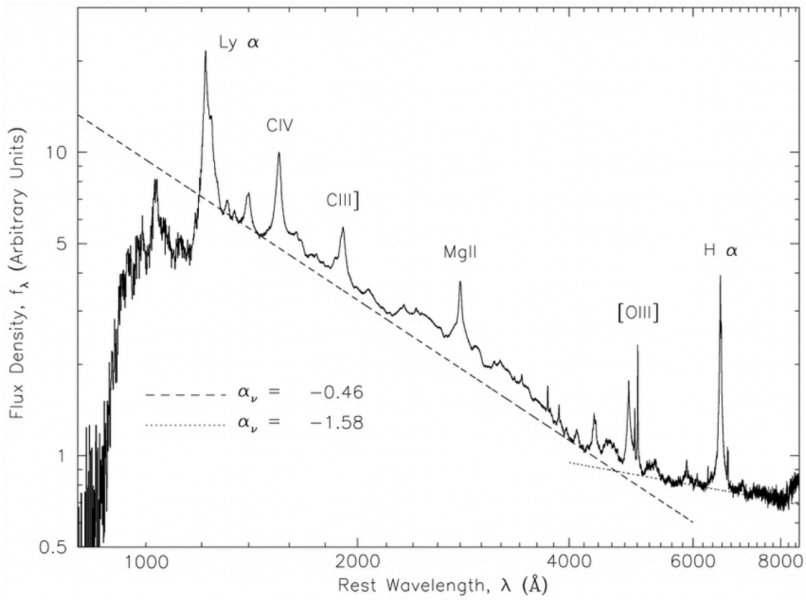

Figure 1.20: Composite quasar spectrum showing several broad emission lines on top of the big blue bump (from: Vanden Berk et al. 2001).

One way to study the structure of the BLR is *reverberation mapping* (RM), based on measuring the response of the line emission to a change in the continuum. The time delay between a given variation in the continuum and the line is directly related to the size of the emission region with smaller time lags corresponding to less extended regions. Observational evidences indicate that the BLR is stratisfied, with high ionization lines lying closer to the central engine than lower ionization lines. Our knowledge about the BLR is still sparse and it is worthwhile to use alternative methods like microlensing to study its size, structure, and kinematics (Eigenbrod 2011; see also Section 4.2).

1.7.1.4 Narrow-Line Region (NLR)

Much farther from the central source an outer layer of gas clouds form the so-called narrow-line region where emission lines show much lower line widths (typically a few hundred kilometers per second). These emission lines have significantly lower levels of ionization than in the BLR and thus, strong "forbidden" lines are produced. In contrast to the BLR, the NLR is sufficiently extended to be spatially resolved by telescopes in the nearest active galaxies. Imaging of the NLR (e.g. Evans et al. 1993) shows that it is composed of clumps and filaments forming a bi-conical structure around the central source (Mukherjee 2011).

1.7.1.5 Molecular Torus

A compact molecular torus, formed by high-density clouds, is located outside the BLR. As the torus is mainly composed of dust and molecular gas, it must lie at a sufficient distance form the central engine to prevent evaporation of the dust grains. Since the torus is located inside the NLR and at the same time, depending on its orientation, obscuring the BLR , it nicely explains why an observer might not be able to see the BLR is some AGN classes. A large amount of light emitted by the central engine is absorbed in this region and many observed differences in the types of AGNs can be explained by differences in the observing viewpoints, making the dusty torus a main element of the AGN unification model (Eigenbrod 2011; Gandhi 2003).

1.7.2 Quasars

Quasi-stellar radio sources (quasars) are giants in the AGN classes and are very luminous compact objects at cosmological distances. We can observe them until redshifts of currently z∼7, although the majority of quasars have redshifts between $1 < z < 2$ (Proft 2016). They were first discovered in the radio domain, but were identified later in the early 1960s, appearing as punctual sources on optical photographs. Therefore, they were called quasi-stellar radio sources which later became 'quasars'. Quasars emit light over the whole electromagnetic spectrum, from radio through IR, visual, UV, X-ray, and gamma-ray, with an emission peak in the ultraviolet. Hence, they present the richest and most complex spectra among all astronomical objects, with a time-variable continuum emission (Schmidt 1969) together with a superposed prominent emission line spectrum, formed by broad- and narrow components that follow the vari-

ability of the continuum after different time delays. An average quasar spectrum showing various broad emission lines on top of the *big blue bump* can be seen in Figure 1.20. Quasars are variable on essentially all time scales: the typical time scale for variability of the continuum flux is of several days, followed by correlated (but weaker) variations in the broad emission lines ranging from weeks to months. Intra-day variability can be detected in the X-ray band (see, e.g., Czerny et al. 2008) whereas narrow lines display time variations on timescales of years or decades. The time lags between different regions can be used to estimate their size, a technique commonly known as *reverberation mapping* (see, e.g., Kollatschny 2010). If the quasar is part of a gravitational lens system, microlensing can be used to reveal its structure and thus, study its kinematics. (Eigenbrod 2011; Wambsganss 2016).

1.7.2.1 Gravitational Lensed Quasars

In this thesis we will focus on applications related to gravitational lensed quasars. Discovery and identification of quasars that are multiply imaged is a difficult task since gravitational lensing is a relatively rare phenomenon. Only a small fraction (less than one percent) of quasars is lensed and observations of multiple images is challenging due to their small image separations (in range of arcseconds). There are several steps to identify and confirm quasar-lens systems (Wambsganss 2016):

(i) two (or more) point-like images of the same color

(ii) separation angle of order 1-10 arcseconds

(iii) identical redshifts

(iv) identical (or very similar) spectra

(v) lensing galaxy visible in between (with lower redshift)

(vi) identical (or very similar) change of brightness in the images (after a certain time delay)

Over the last few decades a large number of quasar surveys have been performed and up to now, a few hundred gravitationally lensed quasars have been found (Eigenbrod 2011; Wambsganss 2016 and references therein).

2

Aims of the Thesis

Over the past decades, enormous discoveries in astrophysics and cosmology have been made due to deeper theoretical understandings and continuous improvement of technical instruments. Our Universe consists of many celestial objects with tremendous physical properties like extremely high masses and densities, amazingly high temperatures and immense brightnesses - quasars being one of them. Quasars are fascinating celestial objects in the center of active galaxies and are among the most powerful objects known in the Universe, pouring out energy up to a thousand times to that emitted by the Milky Way within a very small volume of space.

Since light travels through space, it is affected by the gravitation of massive objects which induce changes in the shape and, hence, in the flux of the emitting sources. Very extraordinary phenomenons come along with gravitational lensing like multiple images, arcs, or even Einstein rings. These phenomena provide numerous applications addressing timely scientific questions of modern astrophysics. There is no chance of spatially resolving the inner parts of AGNs with current telescopes, therefore observations of gravitationally lensed quasars and galaxies provide a powerful alternative to study their inner parts and distribution of mass. In this context, the main goal of this thesis is to reveal the structure of quasars comparing measurements (obtained either from photometry or spectroscopy) between lensed images that provide evidence of the presence of microlensing. Our study is based on the idea that microlensing is sensitive to the size of the emitting region and that different spectral features (continuum, wings of high and low ionization lines, line cores, iron blends etc.) arise from different spatial regions of the quasar (accretion disk, BLR, NLR, and substructures therein). The first objective of the thesis is, then, to study the size of the accretion disks in the quadruply lensed quasars SDSS J1004+4112 and HE 0435-1223 us-

ing photometric observations. In a second step, we will use (already available) spectroscopic data from a sample of quasars to get rough constrains on the BLR size and to estimate the emitting region sizes of several UV iron (Fe II and Fe III) blends. Next, we will obtain spectroscopy – in a second epoch – for this sample in order to distinguish between intrinsic and microlensing induced variability in the profiles of the emission lines and thus, to study the geometry and kinematics of the BLR of quasars. The impact of microlensing on the emission lines can be used to estimate the size of the regions emitting the high (C IV) and low (C III] and Mg II) ionization lines separately. Finally, we measure the gravitational redshift of spectral features (e.g. the Fe III λλ2039–2113 blend) arising from very compact regions (of order a few light-days) to estimate, in a way independent of the geometry of the system, the mass of the central SMBH.

3

Methodology

This chapter provides a very short overview of the photometric and spectroscopic observations used in our publications together with the carried out data reduction. We will also introduce two methods, *inverse ray shooting* (IRS) and *inverse polygon mapping* (IPM), to compute magnification maps in order to simulate microlensing by a random distribution of stars (microlenses). Finally, we will discuss the effects of extended sources on gravitational lensing. More detailed information about the methodology is provided in each one of the sections of Chapter 4.

3.1 Data and Observations

The photometric data presented in Section 4.1.3 (Fian et al. 2016) were taken with the 82cm telescope (IAC80) at the Instituto de Astrofísica de Canarias Teide Observatory (Tenerife, Canary Islands, Spain). The quadruple wide-separation lensed quasar SDSS J1004+4112 was monitored in the Johnson-Bessell's r-band over a 7-year period.

In March 2016 we took spectra with the 4.2m William Herschel Telescope (WHT), situated at the Roque de los Muchachos in La Palma (Canary Islands, Spain). During three observing nights we obtained spectra for 11 lens systems, presented in Section A.

Figure 3.1: Optical laser ground station at the Observatorio del Teide, Tenerife (from: ESA).

Figure 3.2: William Herschel Telescope (WHT) at the Observatorio del Roque de los Muchachos (ORM).

3.1.1 Photometry[1]

The monitoring of the system SDSS J1004+4112 (Fian et al. 2016) took place between December 2003 and October 2010, with the data set consisting of 109 epochs (i.e. 109 nights of observation). The panels in Figure 3.3 show snapshots of the four brightest images A, B, C, and D at four different epochs, starting from the left: February 2004, November 2005, June 2007, and January 2010.

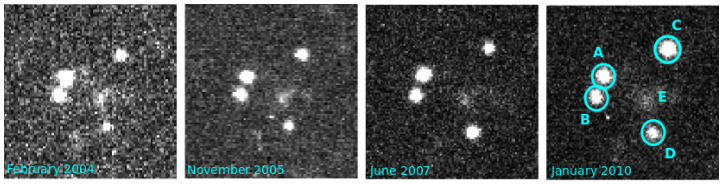

Figure 3.3: Snapshots of the four bright quasar images A, B, C, and D of SDSS J1004+4112 at four different observing epochs. The faint spot in the middle of the images is a bright galaxy belonging to the intervening lensing cluster.

The magnitudes of the four images of the quadruple lensed quasar HE 0435-1223 (Fian et al. 2018a) were monitored from August 2003 until February 2016 in the optical r-band as a part of the COSMOGRAIL program. The data set, spanning 13 years, consists of 884 epochs and fully reduced light curves are publicly available.

3.1.1.1 Data Reduction of SDSS J1004+4112

As a first step, we have to find a source with known luminosity since we cannot measure the absolute magnitude of the quasar images. The reference star has to be unsaturated and its magnitude has to be constant over time. Photometric data (magnitudes and uncertainties of the reference star(s)/quasar images) can be obtained by applying the IRAF (Image Reduction and Analysis Facility) task *qphot* to the set of fits files. To do so, the following parameters are needed:

- inner radius of the sky annulus
- width of the sky annulus (dannulus)
- aperture
- coordinate files (of quasar images and reference stars)
- instrument gain

[1] see Sections 4.1.3 and 4.1.4

We determine the annulus, the dannulus, and the aperture from the radial profile of the reference star (see Figure 3.4). We leave a buffer between the aperture and the sky annulus to keep pixels from being used for both the object and the sky. Each quasar image has to be divided by the flux of the reference star. To remove inconsistent data due to instrumental problems (or other sources of error related to the data reduction), we remove data points in which a sudden change in magnitude simultaneously appears in all the images. Thus, we compare the magnitudes between two consecutive points and if the difference in magnitude was greater than twice the standard deviation, the point is discarded.

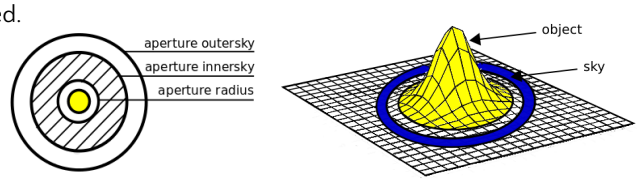

Figure 3.4: Sketch of the annulus, dannulus, and the aperture for determining the relative magnitudes of the reference star(s)/quasar images.

3.1.2 Spectroscopy[2]

We obtained ISIS long-slit spectroscopy covering the full optical range from 11 systems for which we had spectra available in previous epochs. The targets were observed with both arms of the ISIS instrument using the gratings R300B and R316B for the blue and red arm, respectively. With this setup, we were able to observe the full range between 3500 and 9000 Å with a spectral sampling of 0.9 Å/pix. This spectral range includes several typical high and low ionization lines in the rest frame of quasar spectra (e.g., C IV, CIII] and Mg II).

3.1.2.1 Data Reduction of WHT Spectroscopy

The data have been reduced using standard IRAF routines for long-slit 2D spectroscopic data. These included bias subtraction, trim images, flat field and illumination correction, cosmic ray removal, wavelength calibration, redshift correction, background subtraction, flux calibration and extraction of the 1D spectra. We used an algorithm written in Python to fit two Gaussians to the reduced data to separate them avoiding cross-contamination between the spectra of closely spaced image pairs.

[2] see Section A

In the upper panel of Figure 3.5 you can see an example (after applying the data reduction) for a system with a wide separation between lensed images. If we make a cut in the horizontal direction (see right upper panel of Figure 3.5) we obtain two nicely separated peaks. Such a case is more the exception rather than the rule as many systems consist of very close image pairs (see lower panel in Figure 3.5), and we have to apply the algorithm to separate their spectra.

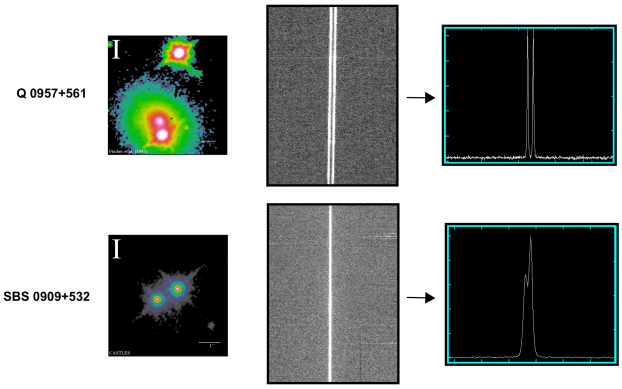

Figure 3.5: Wavelength versus spatial direction (middle) and horizontal cut (right) for systems with wide-pair (top left) and close-pair images (bottom left).

3.1.2.2 Database of Lensed Quasar Spectra

To carry out a statistical analysis of quasar spectra from different sources, we collected from the literature rest frame UV spectra of lensed quasars and added unpublished spectra taken with the William Herschel Telescope. The data from the literature were already fully reduced. For the data to be useful for our analysis, we need simultaneous spectra of at least two images for each lens system. In total we obtained a sample of 32 pairs of quasar images in 27 lens systems with up to five epochs of observation. Comparison among objects from the literature is a difficult task because of the different facilities/instruments used, the wide range of redshifts and consequently the different spectral coverage. However, all spectra used in this thesis contain at least one of the following emission lines: C IV, C III] and/or Mg II. We apply a single, homogeneous continuum subtraction and flux measuring procedure to our sample in order to obtain consistent results. The comparison of the emission line profiles for image pairs of each system is shown in Section A. Information about the systems and references are summarized in Section A.

3.2 Modeling

In the previous section we have presented the observational data and the reduction procedures. To extract information from observed light curves/spectra, a model is required representing the observational microlensing. In this section we will discuss microlensing modeling through the use of magnification maps. Such maps simulate the source plane magnification created by an ensemble of stellar-mass compact objects within a foreground galaxy.

3.2.1 Magnification Maps

A magnification map is a map that shows us the amount of magnification in a region of interest at the source plane and informs us about the way in which the lens magnifies space and, consequently, flux. Magnification maps are the basic tool to simulate microlensing induced by a random distribution of stars (microlenses). Each map in our study (appearing as network of high-magnification caustics separated by regions of lower magnifications) corresponds to a specific quasar image and shows the microlensing magnification at a given source position. The general characteristics of magnification maps are determined (for each quasar image) by the local convergence κ, and the local shear γ, which are obtained by modeling the mass distribution of the lens galaxy. Usually this is achieved by fitting an ellipsoid or a singular isothermal sphere with an additional external shear (SIS+γ_e), such as might be generated by the tide from a neighboring galaxy or cluster, to the coordinates of the images. The local convergence is proportional to the surface mass density and can be divided into $\kappa = \kappa_c + \kappa_\star$, where κ_c is the convergence due to continuously distributed matter (i.e., dark matter) and $\kappa_\star$ is the convergence corresponding to the stellar-mass point lenses (i.e., microlens stars in the galaxy). We use a surface mass fraction in stars $\kappa_\star$ of 10% (see, e.g., Mediavilla et al. 2009) and (usually) generate 2000×2000 pixel magnification maps, spanning 400×400 light-days^2 on the source plane. We get a resolution of 0.2 light-days per pixel, which is much smaller than the optical accretion disk of the quasar. We randomly distribute stars of $M = 0.3 M_\odot$ across the microlensing pattern to create the microlens convergence $\kappa_\star$. The sources can be scaled to a different stellar mass, M, using $r_s \propto \sqrt{M}$. The ratio of the magnification in a pixel to the average magnification of the map gives the microlensing magnification at the pixel and histograms of maps normalized to the mean deliver the relative frequency of microlensing magnification amplitude for a pixel-size source (see, e.g., Mediavilla et al. 2009).

Up to now, several algorithms have been developed to produce magnification maps. In this section (based on the tutorial of Jiménez-Vicente 2016), we will introduce the method of *Inverse Ray Shooting* to demonstrate the principles of calculating magnification maps. We also describe another, faster method called *Inverse Polygon Mapping* developed by Mediavilla et al. (2006).

3.2.1.1 Inverse Ray Shooting (IRS)

The Inverse Ray Shooting method has become very popular in microlensing studies and is a pretty simple algorithm with an easy implementation. It was developed by Kayser et al. (1986) and Schneider & Weiss (1987) and its basic idea is to shoot light rays from the lens plane through the star field of the lensing galaxy back to the source plane (Eigenbrod 2011; Jiménez-Vicente 2016). We have already seen in Section 1.3.1 (see Eq. 1.6) that the gravitational lens equation can be expressed in dimensionless units as:

$$y = x - \alpha(x).$$

y ..... coordinates in the source plane
x ..... coordinates in the lens plane
α ..... scaled deflection angle

To solve this equation, we have to invert it to obtain the positions of the images x_i corresponding to a given source point y. In other words, we can interpret this equation as the trajectory of a light ray going backwards from location x at the image plane to a location y on the source plane. Therefore, this equation is sometimes referred to as *ray-tracing* equation and can only be solved analytically for a few simple cases. Even multiple images of a source can be produced by this equation, so that we get several x values that are solutions for a given y. In many cases, the lens equation has to be inverted by numerical methods and an effective way to do that is to shoot rays (from a given region in the image plane) backwards, deflecting them at the lens plane and tracing them to the source plane. This method can be used to produce magnification maps simulating quasar microlensing and is called *Inverse Ray Shooting*. At source regions of very high magnification (i.e. with a huge concentration of rays) the lens transformation is no longer invertible. These locations correspond to caustics (transformed locations of the critical curves) where $det\ A(x) = 0$ (see Eq.1.15). Several images are produced if rays starting from different positions in the image plane hit the same spot on the source plane (Eigenbrod 2011; Jiménez-Vicente 2016).

Principles of the IRS Code

To obtain a magnification map, we first have to divide the source and image plane into cells/pixels. Next, one has to distribute microlenses (i.e. stars) randomly within an appropriate region and calculate the size of the shooting region. From each cell at the image plane the rays have to be traced back to the position where they hit the source plane. For each ray one has to calculate on which pixel it hits (if at all) the source plane and add 1 to the value at that pixel. The density of the collected rays at a certain position is proportional to the magnification at this point and therefore defines the magnification pattern. Finally, the map has to be normalized by the mean magnification. Note that the resolution (pixel size) of the map should be smaller than the smallest source. That means that the smallest possible source size under study is determined by the map resolution (Eigenbrod 2011; Jiménez-Vicente 2016).

Besides the size and the resolution of the map (and the number of rays shot), the following input parameters are needed to calculate microlensing magnification maps:

- **Convergence κ and Shear γ.** A macro-model of the lens galaxy provides the values for the convergence κ and shear γ at each position of the image. The total convergence κ is split into a part coming from the smooth (dark) matter distribution $\kappa_s = (1-\alpha)\,\kappa$ and a part coming from compact objects $\kappa_* = \alpha \cdot \kappa$ (Eigenbrod 2011; Jiménez-Vicente 2016).
- **Fraction of Mass in Stars α.** It is the fraction α of the surface density mass in the form of compact objects (stars).
- **Mass of Microlenses M.** For simplicity all microlens-masses in the star fields are assumed to be equal. The mass is a very important parameter as it is related to the scale of the effective Einstein radius r_E and the characteristic size of the caustics.

An example of a magnification map produced with Python can be seen in the right panel of Figure 3.6. The left panel shows the corresponding lens plane with the positions of the stars together with a box marking the shooting region. The positions of the point lenses were chosen randomly and the higher the number of microlenses, the higher the probability of microlensing. A simulation with different spatial distributions but the same number of micro-lenses should lead to the same magnification histogram as the real, unknown distribution.

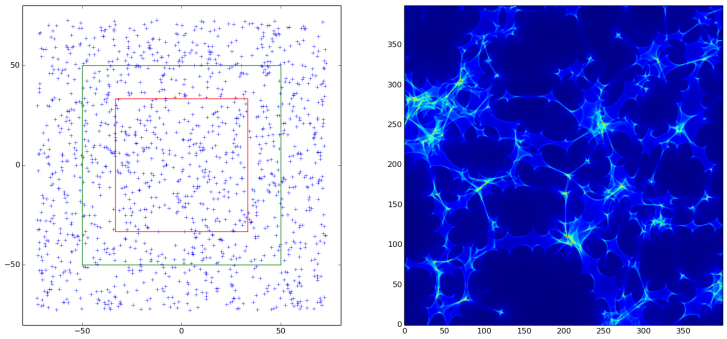

Figure 3.6: Magnification map (right) produced with Python using the IRS method. The size of the magnification map is $10r_E$ and has 400×400 pixels. The position of the stars, the ray shooting region (green-colored box) and the region mapped onto the map (red-colored box) can be seen in the left panel.

For many practical applications the IRS method it requires very long execution times. Sometimes one needs to address problems in which very compact and very large sources are involved at the same time, and ideally would like to have large magnifications maps, covered by many pixels so that small sources can be considered. In order to be able to detect small fluctuations, the pixels should contain many light rays and since it is not possible to meet all these requirements with current computing facilities, one has to find other ways to solve these problems (Eigenbrod 2011; Jiménez-Vicente 2016). The *Inverse Polygon Mapping* algorithm (Mediavilla et al. 2006, 2011) is a more complex, but significantly more efficient technique.

3.2.1.2 Inverse Polygon Mapping (IPM)

The Inverse Polygon Mapping method was developed by Mediavilla et al. (2006, 2011) and allows us to produce highly accurate maps within short computation times. The basic idea behind this algorithm is to divide the lens plane in polygonal cells (that are in principle much bigger than a single pixel), transport them backwards at the lens plane and compare them (by collecting them) with reference areas (pixels) at the source plane. Instead of shooting a high number of rays, only a small number of points defining each cell is mapped back onto the source plane. The magnification at each source pixel is computed by adding each fraction of transformed cell surface that overlays with that pixel (see Figure 3.7) instead of counting the number of rays hitting each source pixel.

The IPM allows us to shoot far fewer rays and hence, spare a lot of CPU time (Jiménez-Vicente 2016; Guerras 2014).

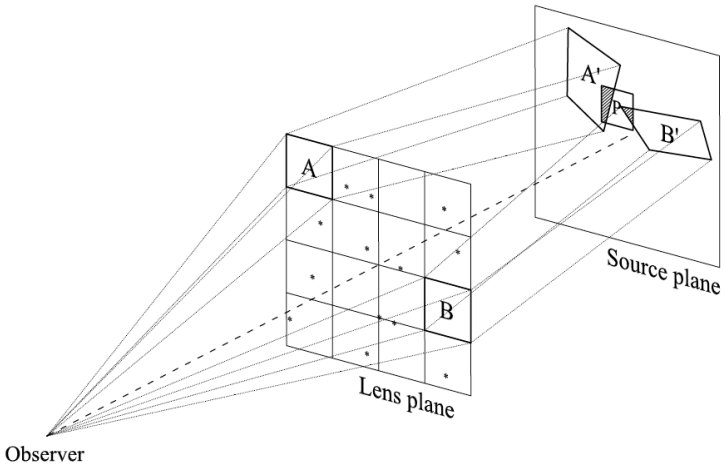

Figure 3.7: Schematic sketch of the IPM method. Two different cells *A* and *B* in the lens plane are mapped back onto the source plane (*A′* and *B′*), contributing differently (shaded area) to the magnification in pixel *P* (from: Guerras 2014).

3.2.2 Extended Sources

Up to now, we have generally assumed that the lensed background source is a point (i.e. has the size of one pixel) . A magnification pattern obtained for a distribution of point-like microlenses can be seen in the upper left panel of Figure 3.8. High magnification events occur when the source crosses a caustic. An important application of quasar microlensing is to infer the size of the emission regions in lensed quasars (e.g. Nemiroff 1988; Grieger 1990), therefore it is an interesting point to investigate the case of extended sources. If the source is larger than one pixel, the source is affected by an effective magnification, which is the convolution of the source's brightness profile $I(R)$ with the magnification map at that location (Jiménez-Vicente 2016). The effect of a finite source size is to smear out the magnification map structures and the larger the source, the larger the smearing effect. In Figure 3.8 we show the effect of extended sources with different sizes.

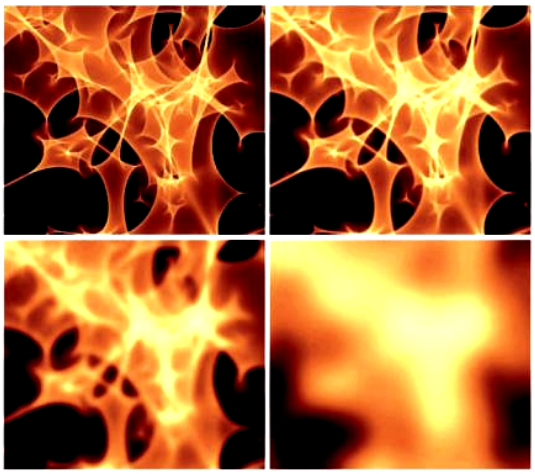

Figure 3.8: Effect of different source sizes on the magnification map structures. In the upper left panel one can see the original map with a random distribution of 1 $M_\odot$ point-like lenses. For the other maps, the total magnification of an extended source is given by the convolution of the magnification pattern with the surface brightness profile of the source (from: Eigenbrod 2011).

The effect of this blurring can also be seen clearly in the simulated light curves. A light curve for a point-source crossing several caustics can be seen in the upper panel of Figure 3.9. The movement of a large source across the magnification map is equivalent to a point source moving across a version of the map that has been smoothed by convolution with the intensity profile of the source. The light curves look smoother for larger sizes of the source and sharp changes in magnification due to caustic crossings disappear. On the contrary, small sources suffer more microlensing magnification than large sources and on this account, based on microlensing magnifications, one can estimate the size of accretion disks of quasars (Eigenbrod 2011; Jiménez-Vicente 2016). Note that strong anomalies are evidence for a relatively small source, whereas low microlensing magnifications could be due to a large source size or to a location of the source in a relatively calm region of the magnification map. Pooley et al. (2007) and Kochanek et al. (2007) found that the size of the optical and ultraviolet emission region inferred from microlensing is much larger compared to the predictions of accretion disk models based on the quasar luminosity.

Eventually, we should address to what extent the effect of the size depends on the shape of the luminosity profile of the source. Several studies (e.g. Mortonson et al. 2005; Congdon & Keeton 2007) about the effect of the source size and shape on the microlensing light curves have shown that microlensing-induced flux variations are relatively insensitive to the exact form of the source profile, and that they principally depend on the source size (Eigenbrod 2011; Jiménez-Vicente 2016). In our studies, to simulate the effect of finite sources, we model the structure of the unresolved quasar source as a circular Gaussian of size r_s, $I(R) \propto exp(-R^2/2r_s^2)$. This is quite common as the convolution with a Gaussian profile is a easy task and already implemented in most programming languages. Magnifications experienced by a source of size r_s are then found by convolving the magnification maps with the Gaussian profiles. The characteristic size r_s is related to the half-light radius; that is, the radius at which half of the light at a given wavelength is emitted, by $R_{1/2} = 1.18 r_s$.

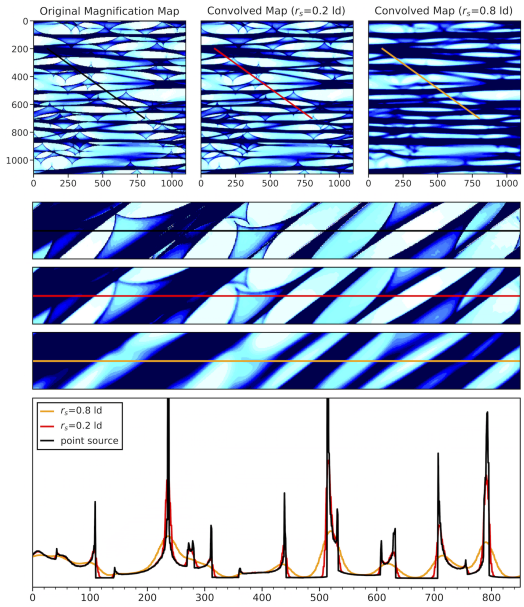

Figure 3.9: Effect of extended sources with different sizes (upper figure) and corresponding light curves (i.e. tracks on the magnification maps; lower figure). The original map of a point-source is shown together with magnification maps convolved with Gaussians of 0.2 and 0.8 light-days. For larger sources sharp changes in the magnification due to caustic crossings disappear.

4

Results

Taking into account that microlensing is sensitive to the size of the source (Morgan et al. 2010, see also the review by Wambsganss 2006), we will use our determinations of microlensing magnification amplitude in the light curves/spectra of gravitationally lensed quasars to constrain the sizes of their accretion disk, their broad-line region and the emitting regions of several iron blends. The first two out of a series of five papers have the purpose to estimate the accretion disk size in the lensed quasars SDSS J1004+4112 and HE 0435-1223 using photometric monitoring of microlensing. In the third and fourth paper we aim to measure the dimensions of the broad-line region and other emission regions (like Fe II, Fe III and the shelf-like feature at $\sim \lambda 1610$) of an average quasar through estimating the microlensing induced differences in the broad emission lines between lensed images. In the last paper, we combine the information about the emission region size of the Fe III blend (inferred from microlensing) with measurements of its gravitational redshift to estimate the mass of the central SMBH.

4.1 Accretion Disk Size[1]

Since there exists a correlation between the emission region size and microlensing magnification, photometric monitoring of microlensing is a powerful technique to measure the dimension of the accretion disk in a gravitationally lensed quasar. Our aim is to study the existence of possible microlensing events during the available seasons in optical R-band data and to use them to infer probabilistic distributions of the source sizes for the lensed quasars SDSS J1004+4112 and HE 0435-1223. Instead of the light curve fitting method (see e.g. Kochanek 2004) we follow the single epoch method combined with the flux ra-

[1] brief overview of Fian et al. 2016 and 2018a

tios of a sufficiently large source in the quasar as to be insensitive to microlensing to establish the baseline for no microlensing magnification (see, e.g., Mediavilla et al. 2009). In the present work (Sections 4.1.3 and 4.1.4) we will extend the single epoch method to all the epochs in the available light curves, increasing the statistical significance. The basic idea is to compare the histogram of microlensing magnification obtained from the observations (corresponding to the monitoring time interval) with the simulated predictions of microlensing variability for sources of different sizes (see Figure 4.1). This comparison allows us to evaluate the likelihood of the different values adopted for the size.

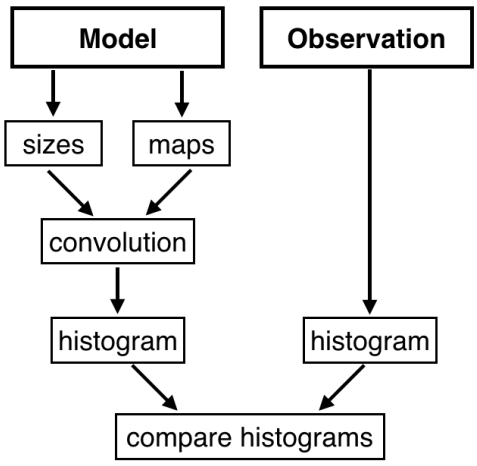

Figure 4.1: Flowchart showing the steps of estimating the source size by comparing observational microlensing histograms with histograms inferred from the model.

We use the optical light curves to infer microlensing flux variability and the mid-IR data (from the literature) to determine the baseline for no microlensing magnification. From Bayes' theorem,

$$P(r_s, p|\Delta m_{obs}) \propto P(\Delta m_{obs}|r_s, p)\, P(r_s, p) \tag{4.1}$$

we can estimate the bayesian posterior probabilities of r_s (characteristic size) and p (probability) conditioned to the measured microlensing magnification Δm_{obs} using a logarithmic/linear prior on the size.

4.1.1 Intrinsic Variability

Quasars are time variable, and fluctuations in their brightness can have two causes: they can be intrinsic to the quasar, or they can be microlens-induced. For a quasar that is not multiply imaged this difference is hard to tell. However, if the quasar is gravitationally lensed, the multiple images arrive with relative time delays of hours up to years because of the different paths taken by their light. Intrinsic variability of the source coupled with the light path time delay between the quasar images can mimic flux ratio anomalies induced by microlensing. To correct for this (and hence to distinguish the two possible causes of variability) one has to measure the time delay, and shift the light curves of the different quasar images relative to each other. After shifting the light curves in time, we can estimate the amplitude of intrinsic variability of the quasar by performing a single spline/polynomial fitting to the light curve least affected by stellar microelensing. Although we use such a fit to make a tentative estimate for the intrinsic variability of the source, some contribution from microlensing variability in the chosen image (here image B) cannot be completely discarded. In any case, this is irrelevant because in our treatment we also consider the contributions of this image to microlensing in the simulated difference light curves.

4.1.2 Microlensing

After correcting for the time delays and mean magnitude differences (using the mid-IR flux rations) between the images, we can remove the modeled intrinsic variability of the light curves in the overlapping region and finally obtain the microlensing light curves A-B, C-B, and D-B as follows:

$$\Delta m_x = m_x - m_{Bfit} - (m_x - m_B)_{midIR} \tag{4.2}$$

where $x = A, C, D$. The mid-IR emission is supposed to arise from a large enough region as to be not affected by microlensing and, hence, we use the $(m_x - m_B)_{midIR}$ offsets to set the microlensing baseline (see Mediavilla et al. 2009). From these curves that represent the differential (with respect to B, the image less prone to microlensing) microlensing of the A, C, and D images, we have obtained the microlensing variability histograms, i.e., the frequencies in which each microlensing amplitude appears in the microlensing variability light curves. Hence, we should compare the experimental histograms of the residuals with the modeled magnification histograms corresponding to the convolutions with sources of different values of r_s.

We simulate the microlensing of a finite-size source using microlensing magnification maps created with the Inverse Polygon Mapping method described by Mediavilla et al. (2006, 2011). Magnification maps are useful to us because we will extract a histogram of magnification from each map (see Figure 4.2 for an illustration of the process leading to simulated microlensing histograms).

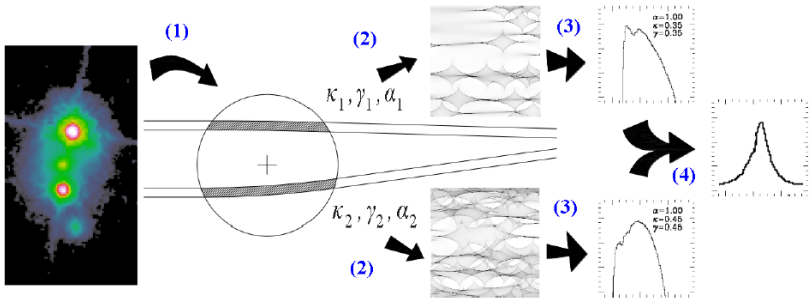

Figure 4.2: Process leading to simulated microlensing histograms. Fitting a SIS+γ_e model to the image positions yields the values for κ and γ **(1)**. Together with the value of the mass in stars α **(2)**, these are the inputs needed for generating magnification maps. From each map microlensing magnification histograms **(3)** are extracted and convolution of the histograms of an image pair **(4)** results in a microlensing difference histogram (from: Guerras 2014).

In Figure 4.3 we show the magnification maps of the four images of the lensed quasars SDSS J1004+4112 and HE 0435-1223. To model the structure of the unresolved quasar source we considered a circular Gaussian intensity profile of size r_s. We convolve the magnification maps with Gaussians of different sizes and after convolution, we normalize each magnification map by its mean value. The histograms of the normalized maps represent the histograms of the expected microlensing variability. Thus, we obtain different microlensing histograms corresponding to different source sizes for each of the images A, C, and D. Cross-correlating the histograms of A, C, and D with the histograms of B, we built the microlensing difference histograms A-B, C-B, and D-B for different values of r_s to be compared with the experimental histograms obtained from the observed light curves. Large values of r_s smear out the network of microlensing magnification caustics and reduce their dynamic range, thereby causing the histograms to become narrower. Finally, the individual probability density functions (PDF) of the quasar images have to be multiplied to get the final PDF of the accretion disk size.

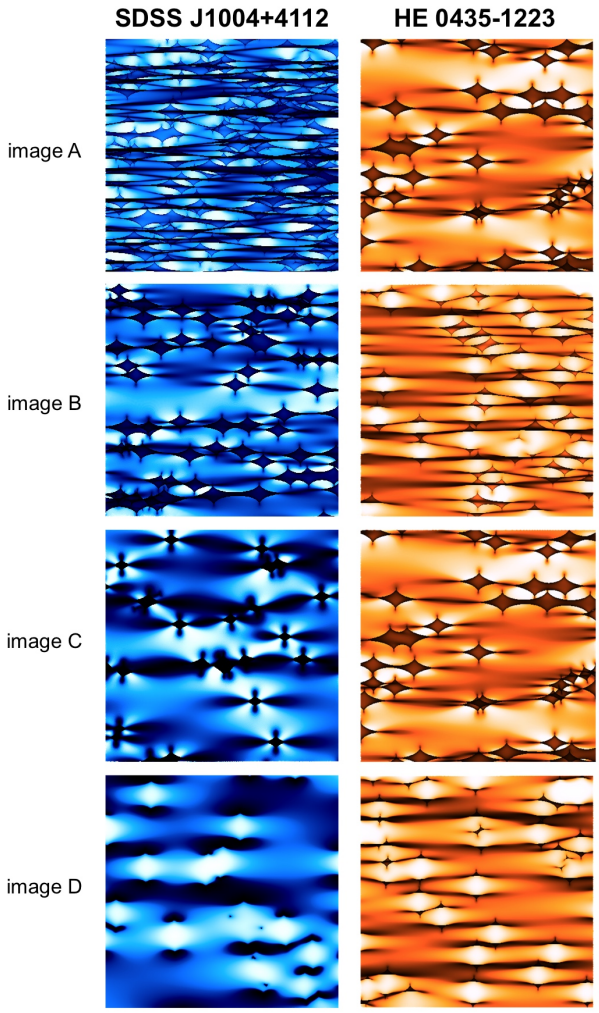

Figure 4.3: Magnification maps of the four images of the gravitationally lensed quasars SDSS J1004+4112 (left) and HE 0435-1223 (right) produced using Inverse Polygon Mapping.

4.1.3 Fian et al. 2016: Accretion Disk Size of SDSS J1004+4112

The Astrophysical Journal, 830:149 (6pp), 2016 October 20 doi:10.3847/0004-637X/830/2/149

SIZE OF THE ACCRETION DISK IN THE GRAVIATIONALLY LENSED QUASAR SDSS J1004+4112 FROM THE STATISTICS OF MICROLENSING MAGNIFICATIONS

C. Fian[1,2], E. Mediavilla[1,2], A. Hanslmeier[3], A. Oscoz[1], M. Serra-Ricart[1,2], J. A. Muñoz[4,5], and J. Jiménez-Vicente[6,7]
[1] Instituto de Astrofísica de Canarias (IAC), Vía Láctea S/N, La Laguna, E 38200, Tenerife, Spain
[2] Departamento de Astrofísica, Universidad de La Laguna, E-38200 La Laguna, Spain
[3] Institute of Physics (IGAM), University of Graz, Universitätsplatz 5, A-8010, Graz, Austria
[4] Departamento de Astronomía y Astrofísica, Universidad de Valencia, E-46100 Burjassot, Valencia, Spain
[5] Observatorio Astronómico, Universidad de Valencia, E-46980 Paterna, Valencia, Spain
[6] Departamento de Física Teórica y del Cosmos. Universidad de Granada, Av. Fuentenueva s/n, E-18071, Granada, Spain
[7] Instituto Carlos I de Física Teórica y Computacional, Universidad de Granada, Av. Fuentenueva s/n, E-18071, Granada, Spain
Received 2016 January 25; revised 2016 August 1; accepted 2016 August 2; published 2016 October 19

ABSTRACT

We present eight monitoring seasons of the four brightest images of the gravitational lens SDSS J1004+4112 observed between 2003 December and 2010 October. Using measured time delays for the images A, B, and C and the model predicted time delay for image D we have removed the intrinsic quasar variability, finding microlensing events of about 0.5 and 0.7 mag of amplitude in the images C and D. From the statistics of microlensing amplitudes in images A, C, and D, we have inferred the half-light radius (at $\lambda_{\rm rest} = 2407$ Å) for the accretion disk using two different methods, $R_{1/2} = 8.7^{+18.5}_{-5.5}\sqrt{M/0.3M_{\odot}}$ (histogram product) and $R_{1/2} = 4.2^{+3.2}_{-2.2}\sqrt{M/0.3M_{\odot}}$ lt-days (χ^2). The results are in agreement within uncertainties with the size predicted from the black hole mass in SDSS J1004 +4112 using thin disk theory.

Key words: gravitational lensing: micro – gravitational lensing: strong – quasars: individual (SDSS J1004+4112)

1. INTRODUCTION

The flux variability of the images of a gravitationally lensed quasar is a combination of the intrinsic variability of the source, correlated by a time delay between the different images, and gravitational microlensing that depends on the random distribution of stars in the lens galaxy. This last variability is uncorrelated between images (Chang & Refsdal 1979; see also the review by Wambsganss 2006). The analysis of lensed quasars' light curves has important applications in cosmology (determination of time delays to infer the Hubble constant; Refsdal 1964) and in the study of quasar structure (Chang & Refsdal 1979, 1984; see also Kochanek 2004 and Wambsganss 2006). In this paper we will focus in the last application, using microlensing statistics to determine the quasar accretion disk size (Fohlmeister et al. 2007, 2008; Pooley et al. 2007; Fohlmeister 2008; Mosquera et al. 2009, 2013; Morgan et al. 2010; Blackburne et al. 2011, 2014, 2015; Mosquera & Kochanek 2011; Sluse et al. 2011; Jiménez-Vicente et al. 2012, 2014; Motta et al. 2012; Hainline et al. 2013; Jiménez-Vicente et al. 2015a, 2015b; MacLeod et al. 2015; Mediavilla et al. 2015; Muñoz et al. 2016).

The wide-separation lensed quasar SDSS J1004+4112 is a rare example of a quasar lensed by an intervening galaxy cluster (Wambsganss 2003; Inada et al. 2006). It is lensed into five images (Inada et al. 2005), with a maximum image separation of 14″.62. The quasar has a redshift of $z_s = 1.734$ and the redshift of the galaxy cluster is $z_l = 0.68$ (Fohlmeister et al. 2008). The lag between images A, B, and C has been experimentally measured by Fohlmeister et al. (2008) who obtained a time delay of 40.6 days between components A and B and of 822 days between A and C (the largest delay measured for a gravitational lens system). It has not yet been possible to measure the time delay of image D. From a model of SDSS J1004+4112 in which the mass distribution of the system is revisited, Oguri (2010) predicts a time delay between A and D of 1218 days

After correcting for the time delays and mean magnitude differences, Fohlmeister et al. (2008) found clear indications of microlensing flux variability in the residuals of the light curves (i.e., the differences between the observed light curves and the modeled intrinsic variability of the quasar). They fitted the residual light curves of image A using a model of microlensing flux variability based on magnification maps to estimate the accretion disk size of the lensed quasar, obtaining a small size below the predictions of thin disk theory.

In this paper we present seven years, corresponding to eight observational seasons, of optical monitoring data for the four brightest images of SDSS J1004+4112 spanning 2505 days from 2003 December to 2010 October, partly coincident with the epochs studied by Fohlmeister et al. (2008), but which significantly extend the coverage by around 1200 additional days. Our aim is to use these data to study the existence of possible microlensing events and to estimate the size of the accretion disk of the lensed quasar. We have been able to carry out a microlensing analysis including image D for the first time thanks to the availability of sufficiently long observations to correct for the time delay shifting the light curves.

Instead of the light curve fitting method (see e.g., Kochanek 2004) we will follow the single epoch method combined with the flux ratios of a sufficiently large source in the quasar as to be insensitive to microlensing to establish the baseline for no microlensing magnification (see, e.g., Mediavilla et al. 2009). Based on single epoch spectroscopy Motta et al. (2012) and Jiménez-Vicente et al. (2014) obtained disk size estimates larger than the results of Fohlmeister et al. (2008). In the present work we will extend the single epoch method to all the epochs in the available light curves, increasing the statistical significance. The basic idea is to compare the histogram of microlensing magnification obtained from the observations corresponding to a time interval with the

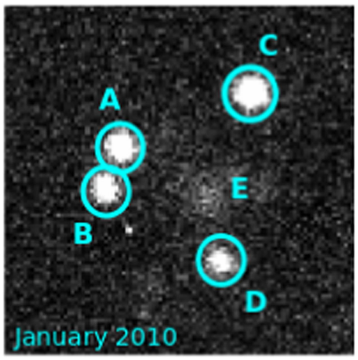

Figure 1. Image of the four brightest quasar images A, B, C, and D of SDSS J1004+4112. The faint spot in the middle of the images is a bright galaxy belonging to the intervening lensing cluster.

simulated predictions of microlensing variability for sources of different sizes. This comparison will allow us to evaluate the likelihood of the different values adopted for the size. We will use the optical light curves, with coverage extended by us, to infer microlensing flux variability and the mid-IR data from Ross et al. (2009) to determine the baseline for no microlensing variability.

The paper is organized as follows. In Section 2 we present the data and in Section 3 the light curves of each image. The estimate of the quasar accretion disk size based on the statistics of microlensing magnifications is discussed in Section 4. Finally, the main results are summarized in Section 5.

2. DATA AND OBSERVATIONS

The photometric monitoring presented in this paper took place between 2003 December and 2010 October. We monitored SDSS J1004+4112 in the Johnson-Bessell's R-band using the 82 cm telescope (IAC80) at the Instituto de Astrofísica de Canarias Teide Observatory (Tenerife, Canary Islands, Spain). Two different CCDs were used. From 2003 to 2005 a Thomson 1024 × 1024 chip was employed, giving a field of view of about 7.′5, with a pixel size of 0.″43. Since 2005 a new CCD, CAMELOT, was installed. CAMELOT hosts a E2V 2048 × 2048 chip with 0.″304 pixels, corresponding to a 10.4 × 10.4 arcmin^2 FOV. A standard R broadband filter was always used for the observations, fairly close to the Landolt R (Landolt 1992). Due to the instrumental change a constant gap of ∼0.2 mag appeared in the light curves that has been removed taking the new instrumental system as a reference. The combined data set consists of 109 epochs (i.e., 109 nights) and the average sampling rate is once every 23rd day. This large average sampling rate arises due to the relatively large seasonal gaps. There are seven seasonal gaps, the largest one stretching over 11 months from 2007 June to 2008 May, i.e., a time period of more than 300 days. The mean observational cadence of the four images is ∼9 days for the first two seasons, ∼10 days for the third and fourth season, ∼6 days for the fifth season and ∼18 days for the last two seasons.

Figure 1 shows an image taken with the IAC80 of the four brightest quasar images A, B, C, and D of SDSS J1004+4112. Photometric data were obtained by applying a completely automatic IRAF task, *pho2com*, developed by Serra-Ricart et al. (1999). This code yields accurate photometry by simultaneously fitting a stellar two-dimensional profile to each quasi-stellar object (QSO) component by means of DAOPHOT software. To remove inconsistent data due to instrumental problems or other sources of error related to the data reduction we have, in first place, removed the observations in which a sudden change in magnitude simultanously appears in all the images. In a second step, the magnitudes between two consecutive points were compared and if the difference in magnitude was greater than twice the standard deviation, the point was discarded. Only around 10 data points out of 109 had to be rejected and around 100 data points were left for analysis.

3. LIGHT CURVES AND MAGNITUDE CHANGES

In Figure 2 we show the resulting light curves of the quasar images A–D split over eight observing seasons. The dashed vertical line shown at 3700 days represents the change of the old to the new CCD and one can clearly see that the error bars of the observations with the new CCD are smaller by almost a factor of two. The images C (yellow light curve) and D (red light curve) are shifted by 0.3 mag and 1.0 mag respectively so that they do not overlap with each other.

Due to our larger uncertainties, we have not been able to improve the time delay measurements of Fohlmeister et al. (2008), therefore we use their time delay estimations (for images A, B, and C) to shift the light curves and remove intrinsic variability. For calculating the time delay between image A and B they used the polynomial fitting method and the analysis of their data yields a time delay of $\Delta t_{BA} = 40.6 \pm 1.8$ days. They also measured the time delay for the wide separated (14.″62) image C relative to the close image pair A/B. Using the dispersion spectra method they found $\Delta t_{CA} = 822 \pm 7$ days and $\Delta t_{CB} = 780 \pm 6$ days. Image D should lag the other three images but to date no features can be seen in the light curve of image D than can be matched to the first season of image A. They derived a lower limit on the time delay between images A and D of $\Delta t_{DA} > 1250$ days (3.4 years) (Fohlmeister et al. 2008; Fohlmeister 2008). We will use the model-predicted AD time delay of 1218 days of Oguri (2010), which is slightly smaller than the lower limit reported by Fohlmeister et al. (2008).

Figure 3 shows a comparison of the IAC data and the data used by Fohlmeister et al. (2008) for the quasar images A and B. The light curves show, in general, a good agreement with those of Fohlmeister et al. (2008) after applying global shifts to match both photometries in the overlapping regions. The exception is a region of image B at JD 3750 where the data of Fohlmeister et al. seem to be slightly below the expected values if one compares with the light curve for image A.

4. INTRINSIC VARIABILITY AND MICROLENSING

In Figure 2 one cannot see strong differences between the light curves A and B that could be directly related to microlensing. Thus, we can estimate the amplitude of the intrinsic variability of the quasar performing a single polynomial fitting to the B light curve. Despite the similarity between the A and B light curves, weak microlensing could be still present due to a large source size or a location of both images in regions with low microlensing magnification, even strong microlensing magnification but with different sign in A and B. Consequently, although we use the polynomial fitting to

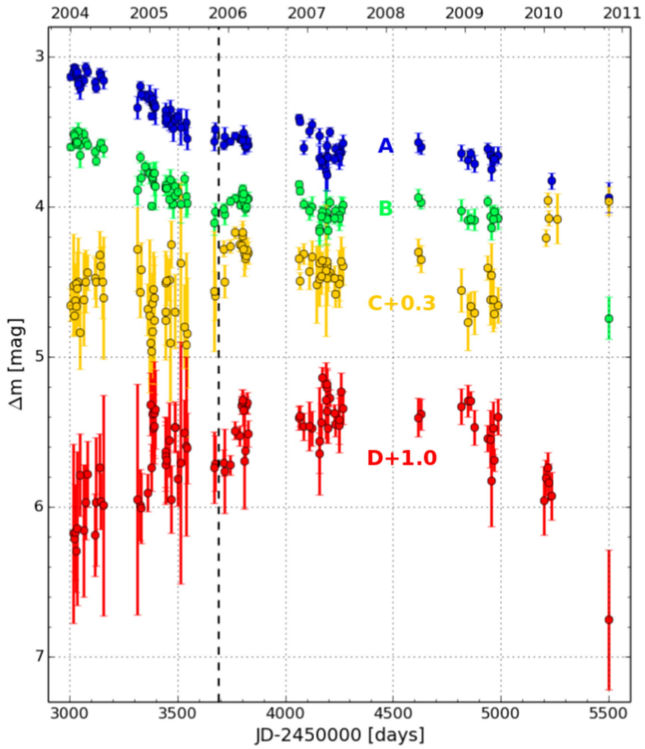

Figure 2. Light curves of the four images A, B, C, and D of the quasar SDSS J1004+4112 from 2003 December to 2010 October. Horizontal axes show the Julian (bottom) and Gregorian (upper) dates. The vertical axis is shifted to match the photometry by Fohlmeister et al. (2008). The light curves of the images C and D are shifted by 0.3 mag and 1.0 mag, respectively, so that they do not overlap with each other. We smooth the data with a square filter of ±5 days to reduce noise and emphasize trends.

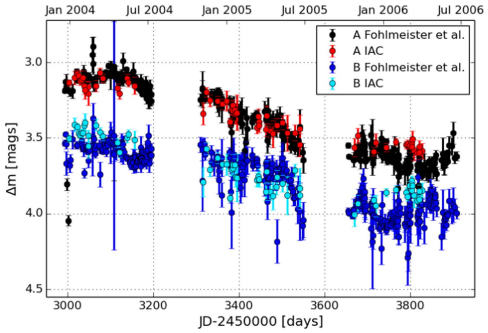

Figure 3. Light curves of images A and B of the quasar SDSS J1004+4112 from 2003 December to 2006 June. Horizontal axes show the Julian (bottom) and Gregorian (upper) dates. The IAC data are shifted to match the photometry by Fohlmeister et al. (2008) to enable a direct comparison.

make a tentative estimate for the intrinsic variability of the source, some contribution from microlensing variability cannot be completely discarded. Hence, we should compare with the A–B, C–B and D–B modeled magnification pattern/histograms for all the images. We obtain a source variability of ∼0.7 mag for all the data and of 0.5 mag for the first four seasons whereas Fohlmeister et al. (2008) found an intrinsic variability of ∼0.7 mag. Figure 4 shows the simulated quasar variability (black solid line) with the A, B, C, and D light curves overimposed. In the three panels in Figure 5 the residuals of the A, C and D light curves are shown. We have calculated the residuals from: $\Delta m_X = m_X - m_{\rm Bfit} - (m_X - m_B)_{\rm midIR}$ where X = A, C, D. The mid-IR data have been taken from Ross et al. (2009). The mid-IR emission is supposed to arise from a large enough region as to be not affected by microlensing and, hence, we use the $(m_x - m_B)_{\rm midIR}$ offsets to set the microlensing baseline (see Mediavilla et al. 2009). In Figure 5 one can see that the residuals of the A light curve are relatively constant. Only in the fourth season, variability induced by microlensing may occur with amplitudes of order 0.15 mag. As opposed to this, microlensing variability is clearly visible in the residuals of the C and D light curves with amplitudes of the order of ∼0.5 mag and ∼0.7 mag. From these curves that represent the differential (with respect to B, the image less prone to microlensing) microlensing of the A, C, and D images, we

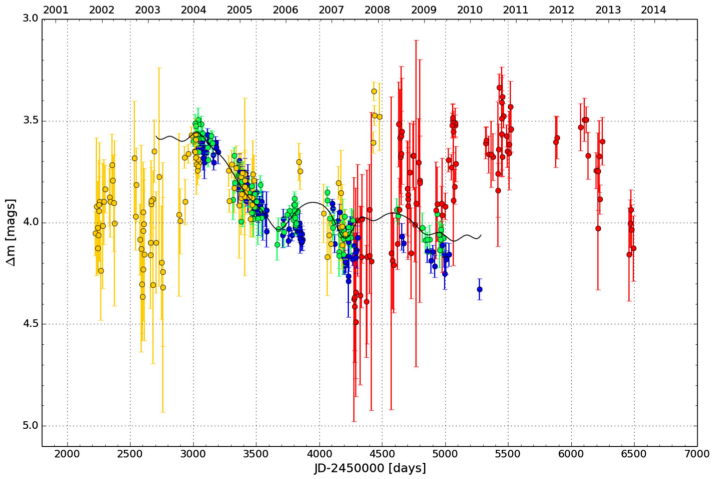

Figure 4. Image A, B, C, and D light curves of SDSS J1004+4112 in their overlap region after shifting by the respective time delays (and magnitude differences). A polynomial (black solid line) is fitted to the B light curve. We smooth the data with a square filter of ±5 days to reduce noise.

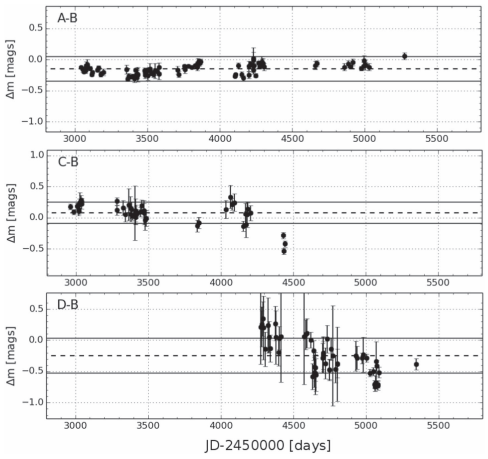

Figure 5. Differential microlensing variability of the light curves A, C, and D compared to a polynomial fit to the light curve B. The dashed horizontal lines show the mean value of the residuals. The residual magnitudes clearly show that microlensing is present in the light curves C and D.

have obtained the microlensing variability histograms (Figure 6), i.e., the frequencies in which each microlensing amplitude appears in the microlensing variability light curves. We adopt a bin size of 0.2 mag.

4.1. Microlensing Estimate of the Quasar Accretion Disk Size

Taking into account that microlensing is sensitive to the size of the source (Morgan et al. 2010; see also the review by Wambsganss 2006) we will use our determinations of microlensing magnification amplitude to estimate the size of the accretion disk in the SDSS J1004+4112 lensed quasar.

We obtained microlensing magnification maps for each image using the inverse polygon mapping method described by Mediavilla et al. (2006, 2011). We used the following parameters obtained from a singular isothermal sphere plus external shear (SIS+γ_e) model fitted to the images coordinates: convergence $\kappa = 0.48$ and shear $\gamma = 0.57$ for image A, $\kappa = 0.47$ and $\gamma = 0.39$ for B, $\kappa = 0.38$ and $\gamma = 0.33$ for C and $\kappa = 0.71$ and $\gamma = 0.83$ for image D. We used a surface mass density in stars $\kappa_* = 10\%$ (Mediavilla et al. 2009) and generated 2000×2000 pixel^2 magnification maps with a size of 24×24 Einstein radii^2. The value of the Einstein radius for this system is $2.35 \times 10^{16}\sqrt{M/0.3M_\odot}$ cm $= 9.1\sqrt{M/0.3M_\odot}$ lt-days at the lens plane. The ratio of the magnification in a pixel to the average magnification of the map gives the microlensing magnification at the pixel and histograms of normalized to the mean maps deliver the relative frequency of microlensing magnification amplitude for a pixel-size source.

To model the structure of the unresolved quasar source we considered a circular Gaussian intensity profile of size r_s, $I(R) \propto \exp(-R^2/2r_s^2)$. It is generally accepted that the specific shape of the radial profile is not important for microlensing flux variability studies because the results are essentially controlled by the half-light radius rather than by the detailed profile (Mortonson et al. 2005). The characteristic size r_s is related to the half-light radius by $R_{1/2} = 1.18r_s$. We convolve the magnification maps with Gaussians of 14 different sizes over a logarithmic grid which spans approximately from $r_s \sim 0.2$ to 55 lt-days for a mean stellar mass $\langle M \rangle = 0.3M_\odot$. The source sizes can be scaled to a different mean stellar mass, $\langle M \rangle$, using $r_s \propto \sqrt{M}$. After convolution we normalized each magnification map by its mean value. The histograms of the normalized map represent the histograms of the expected microlensing variability. Thus, we obtain 14 different microlensing histograms corresponding to different source sizes

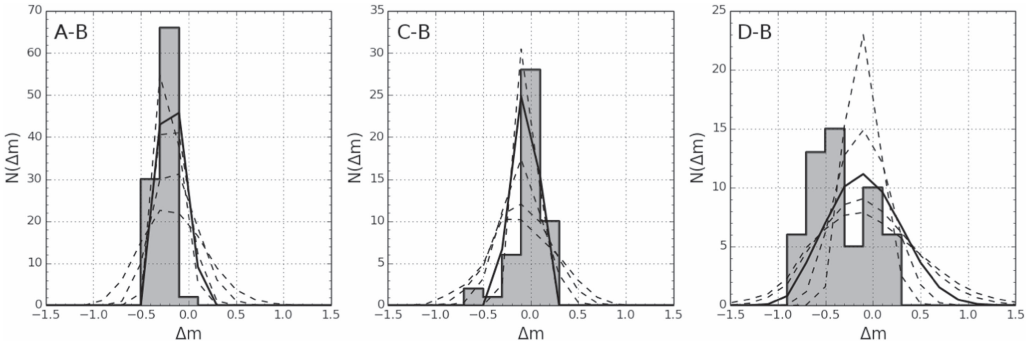

Figure 6. Microlensing frequency distributions obtained from the observed light curves (histograms) and the simulated microlensing magnification maps. The polygonal lines present model histograms for different values of r_s (6.3, 9.7, 15.0, 23.1, and 54.8 lt-days for A–B, 4.1, 6.3, 9.7, 35.6 and 54.8 lt-days for C–B, and 2.7, 4.1, 6.3, 9.7 and 15.0 lt-days for D–B). The thick lines indicate the best fit of the model to the observed data.

for each of the images A, C, and D. Finally, convolving the histograms of A, C, and D with the histogram of B we built the microlensing difference histograms A–B, C–B and D–B for different values of r_s to be compared with the experimental histograms obtained from the observed light curves (see Figure 6). The thick solid line in each panel indicates the best fit of the model to the observed frequency distributions of microlensing magnifications.

In order to study the likelihood of the different r_s we compare the microlensing histograms inferred from the model for different values of r_s with the histograms of the data using two different statistics:

i. histogram product, defined as

$$P_X(r_s) = \sum_{i=1}^{n_{\rm bin}} h^i_{X-B} \hat{h}^i_{X-B}(r_s), \quad (1)$$

where h^i_{X-B} and $\hat{h}^i_{X-B}(r_s)$ are the observed and modeled histograms and $n_{\rm bin}$ is the number of bins

ii. Pearson's χ^2 test,

$$\chi^2 = \sum_{i=1}^{n_{\rm bin}} \frac{(h^i_{X-B} - \hat{h}^i_{X-B}(r_s))^2}{h^i_{X-B}} \quad (2)$$

with

$$P_X(r_s) \propto e^{-\frac{1}{2}\chi^2}. \quad (3)$$

After multiplying the probability distributions corresponding to A, C and D we finally obtain the probability density function (PDF) of the source size,

$$P(r_s) = P_{\rm A}(r_s) \cdot P_{\rm C}(r_s) \cdot P_{\rm D}(r_s). \quad (4)$$

In the case of the histogram product method we have convolved the histograms with normal distributions with these dispersions, not finding any significant difference.

To account for the rms errors in the data in the case of the χ^2-method we applied a Monte Carlo method, producing random realizations of the histograms of the data using normal distributions of mean the value of the observed histogram and with the following dispersions: $\sigma_{\rm A} = 0.08$, $\sigma_{\rm C} = 0.14$ and $\sigma_{\rm D} = 0.22$ estimated from the data (see Figure 5). In the case of the histogram product-method we convolved the histograms with normal distributions with these dispersions, not finding any significant difference.

Figure 7 shows the resulting normalized probability distribution for both methods. For the product we obtain a disk size of $\langle r_s \rangle = 7.4^{+15.7}_{-4.7}\sqrt{M/0.3M_\odot}$. The expected value using χ^2 is $\langle r_s \rangle = 4.4^{+1.0}_{-1.0}\sqrt{M/0.3M_\odot}$ lt-days (for 68% confidence estimates). The χ^2-method seems to constrain better the size although the errors in the histograms may have been underestimated. This is supported by the rather high values of χ^2. To reach values of χ^2 close to 1 we need to multiply the typical deviation in Equation (2), $\sqrt{h^i_{X-B}}$, by a factor of 3. From the corresponding PDF (see Figure 7) we obtain a similar value $\langle r_s \rangle = 3.6^{+2.7}_{-1.9}\sqrt{M/0.3M_\odot}$ but with uncertainties more compatible with the results obtained using the product method.

Our result for each method expressed in terms of the half-light radius at $\lambda_{\rm rest} = 2407$ Å ($R_{l/2} = 8.7^{+18.5}_{-5.5}\sqrt{M/0.3M_\odot}$ and $R_{l/2} = 4.2^{+3.2}_{-2.2}\sqrt{M/0.3M_\odot}$ lt-days) is significantly greater than the value obtained by Fohlmeister et al. (2008) fitting the A and B light curves ($R_{l/2} = 2.44\ R_\lambda = 0.6^{+0.5}_{-0.3}$ lt-days), but in good agreement with the value inferred by these authors from thin disk theory using an experimental estimate of the black hole mass (Fohlmeister et al. 2008). Our estimate for the size is also in good agreement with the results of Motta et al. (2012) and Jiménez-Vicente et al. (2014) for this system, and with the average determinations obtained for a sample of lensed quasars by Jiménez-Vicente et al. (2012, 2014, 2015a, 2015b) when a fraction of mass in stars of 10% is considered.

As we have used an estimated (not measured) time delay for image D, and this image presents the largest microlensing signal in this system, it is important to check that this assumption is not biasing our results. In order to check the dependence of the results with the adopted time delay for image D, we considered ±100 days shifts of the time delays not finding any significant difference in the size calculations. On the other hand, we also repeated the computations not considering image D finding slightly larger but comparable results for the size: $\langle r_s \rangle = 9.3^{+13.8}_{-5.2}\sqrt{M/0.3M_\odot}$ for the product-method and $\langle r_s \rangle = 5.4^{+4.3}_{-2.7}\sqrt{M/0.3M_\odot}$ for χ^2.

We also checked the impact of interchanging the two images less affected by microlensing, A and B, by performing the

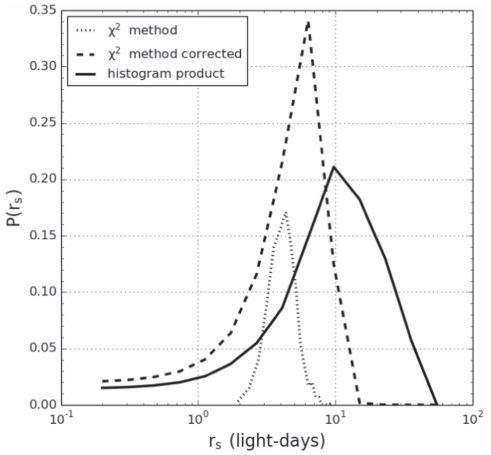

Figure 7. Probability distributions of the source size r_s for the product-method (solid line), χ^2-method (dotted line) and χ^2-method corrected with enlarged errors (dashed line).

polynomial fitting to the A light curve and considering the pairs, B–A, C–A and D–A in the calculations. The results are almost identical for the χ^2-based method, $\langle r_s \rangle = 4.6^{+5.2}_{-1.9}\sqrt{M/0.3M_\odot}$, and compatible to within errors for the product-method, $\langle r_s \rangle = 4.6^{+5.1}_{-2.9}\sqrt{M/0.3M_\odot}$.

5. SUMMARY AND CONCLUSIONS

We have presented eight seasons of monitoring data for the four brightest images of the five-image gravitational lens system SDSS J1004+4112 which significantly extend the time coverage of previous works. Taking as reference image B, which is less affected by microlensing, and using the experimental time delays inferred by Fohlmeister et al. (2008) for components A and C and the theoretical time delay modeled by Oguri (2010) for image D, we have removed the intrinsic variability from the light curves in the overlapping region. Using the mid-IR flux ratios between images determined by Ross et al. (2009) as a baseline for no microlensing magnification, we finally obtained the microlensing light curves, A–B, C–B, and D–B. We detected microlensing variability up to 0.7 mag in images C and D. The light curve of A seems to be less affected by microlensing (changes of order 0.15 mag in the fourth season of our data) in good agreement with the results of Fohlmeister et al. (2008).

We have used the statistics of microlensing magnifications along the available seasons to infer probabilistic distributions for the size using two different methods. Using the product of the observed and modeled microlensing histograms we have obtained a half-light radius of $R_{1/2} = 8.7^{+18.5}_{-5.5}\sqrt{M/0.3M_\odot}$ lt-days. A consistent but more restrictive result of $R_{1/2} = 4.2^{+3.2}_{-2.2}\sqrt{M/0.3M_\odot}$ lt-days is obtained using a χ^2 criterion to compare the observed and modeled histograms. Both results are only marginally consistent with the previous estimate by Fohlmeister et al. (2008) that obtained a smaller size, but in good agreement with the predictions of thin disk theory and with the measurements by Motta et al. (2012) and Jiménez-Vicente et al. (2014).

We thank the anonymous referee for a thorough revision and valuable suggestions. We are especially grateful to the Instituto de Astrofsica de Canarias astronomers for their observations of the data appearing in this paper. The 0.82 m IAC80 Telescope is operated on the island of Tenerife by the Instituto de Astrofsica de Canarias in the Spanish Observatorio del Teide. JJV is supported by the Spanish Ministerio de Economía y Competitividad and the Fondo Europeo de Desarrollo Regional (FEDER) through grant AYA2014-53506-P and by the Junta de Andalucía through project FQM-108. EM and JAM were supported by the Spanish MINECO with the grants AYA2013-47744-C3-1-P and AYA2013-47744-C3-3-P. JAM was also supported by the Generalitat Valenciana with the project PROMETEOII/2014/060.

REFERENCES

Blackburne, J. A., Kochanek, C. S., Chen, B., Dai, X., & Chartas, G. 2014, ApJ, 789, 125
Blackburne, J. A., Kochanek, C. S., Chen, B., Dai, X., & Chartas, G. 2015, ApJ, 798, 95
Blackburne, J. A., Pooley, D., Rappaport, S., & Schechter, P. L. 2011, ApJ, 729, 34
Chang, K., & Refsdal, S. 1979, Natur, 282, 561
Chang, K., & Refsdal, S. 1984, A&A, 132, 168
Fohlmeister, J. 2008, in Manchester Microlensing Conf.: the 12th International Conference and ANGLES Microlensing Workshop, 16 (Manchester, UK), http://pos.sissa.it/cgi-bin/reader/contribution.cgi?id=054/016
Fohlmeister, J., Kochanek, C. S., Falco, E. E., et al. 2007, ApJ, 662, 62
Fohlmeister, J., Kochanek, C. S., Falco, E. E., Morgan, C. W., & Wambsganss, J. 2008, ApJ, 676, 761
Hainline, L. J., Morgan, C. W., MacLeod, C. L., et al. 2013, ApJ, 774, 69
Inada, N., Oguri, M., Keeton, C. R., et al. 2005, PASJ, 57, L7
Inada, N., Oguri, M., Morokuma, T., et al. 2006, ApJL, 653, L97
Jiménez-Vicente, J., Mediavilla, E., Kochanek, C. S., et al. 2014, ApJ, 783, 47
Jiménez-Vicente, J., Mediavilla, E., Kochanek, C. S., & Muñoz, J. A. 2015a, ApJ, 799, 149
Jiménez-Vicente, J., Mediavilla, E., Kochanek, C. S., & Muñoz, J. A. 2015b, ApJ, 806, 251
Jiménez-Vicente, J., Mediavilla, E., Muñoz, J. A., & Kochanek, C. S. 2012, ApJ, 751, 106
Kochanek, C. S. 2004, ApJ, 605, 58
Landolt, A. U. 1992, AJ, 104, 340
MacLeod, C. L., Morgan, C. W., Mosquera, A., et al. 2015, ApJ, 806, 258
Mediavilla, E., Jiménez-vicente, J., Muñoz, J. A., & Mediavilla, T. 2015, ApJL, 814, L26
Mediavilla, E., Mediavilla, T., Muñoz, J. A., et al. 2011, ApJ, 741, 42
Mediavilla, E., Muñoz, J. A., Falco, E., et al. 2009, ApJ, 706, 1451
Mediavilla, E., Muñoz, J. A., Lopez, P., et al. 2006, ApJ, 653, 942
Morgan, C. W., Kochanek, C. S., Morgan, N. D., & Falco, E. E. 2010, ApJ, 712, 1129
Mortonson, M. J., Schechter, P. L., & Wambsganss, J. 2005, ApJ, 628, 594
Mosquera, A. M., & Kochanek, C. S. 2011, ApJ, 738, 96
Mosquera, A. M., Kochanek, C. S., Chen, B., et al. 2013, ApJ, 769, 53
Mosquera, A. M., Muñoz, J. A., & Mediavilla, E. 2009, ApJ, 691, 1292
Motta, V., Mediavilla, E., Falco, E., & Muñoz, J. A. 2012, ApJ, 755, 82
Muñoz, J. A., Vives-Arias, H., Mosquera, A. M., et al. 2016, ApJ, 817, 155
Oguri, M. 2010, PASJ, 62, 1017
Pooley, D., Blackburne, J. A., Rappaport, S., & Schechter, P. L. 2007, ApJ, 661, 19
Refsdal, S. 1964, MNRAS, 128, 307
Ross, N. R., Assef, R. J., Kochanek, C. S., Falco, E., & Poindexter, S. D. 2009, ApJ, 702, 472
Serra-Ricart, M., Oscoz, A., Sanchís, T., et al. 1999, ApJ, 526, 40
Sluse, D., Schmidt, R., Courbin, F., et al. 2011, A&A, 528, A100
Wambsganss, J. 2003, Natur, 426, 781
Wambsganss, J. 2006, arXiv:astro-ph/0604278

4.1.4 Fian et al. 2018a: Accretion Disk Size of HE 0435-1223

Draft version June 18, 2018
Typeset using LaTeX **twocolumn** style in AASTeX61

ESTIMATE OF THE ACCRETION DISK SIZE IN THE GRAVITATIONALLY LENSED QUASAR HE 0435-1223 USING MICROLENSING MAGNIFICATION STATISTICS

C. Fian,[1,2] E. Mediavilla,[1,2] J. Jiménez-Vicente,[3,4] J. A. Muñoz,[5,6] and A. Hanslmeier[7]

[1]*Instituto de Astrofísica de Canarias, Vía Láctea S/N, La Laguna 38200, Tenerife, Spain*
[2]*Departamento de Astrofísica, Universidad de la Laguna, La Laguna 38200, Tenerife, Spain*
[3]*Departamento de Física Teórica y del Cosmos, Universidad de Granada, Campus de Fuentenueva, 18071 Granada, Spain*
[4]*Instituto Carlos I de Física Teórica y Computacional, Universidad de Granada, 18071 Granada, Spain*
[5]*Departamento de Astronomía y Astrofísica, Universidad de Valencia, E-46100 Burjassot, Valencia, Spain*
[6]*Observatorio Astronómico, Universidad de Valencia, E-46980 Paterna, Valencia, Spain*
[7]*Institute of Physics (IGAM), University of Graz, Universitätsplatz 5, 8010, Graz, Austria*

ABSTRACT

We present a measurement of the accretion disk size of the quadruple lensed quasar HE 0435-1223 from well-sampled 13-yr COSMOGRAIL optical light curves. Using accurate time delays for the images A, B, C, and D, we modeled and removed the intrinsic quasar variability, and found microlensing events of amplitude up to 0.6, 0.4, and 0.5 mag in the images A, C and D respectively. From the statistics of microlensing magnifications in these images we use Bayesian methods to estimate the size of the quasar accretion disk. We have inferred the half-light radius for the accretion disk using two different methods, $R_{1/2} = 8.4^{+11.1}_{-1.9}\sqrt{M/0.3M_{\odot}}$ light-days (histogram product) and $R_{1/2} = 8.9^{+5.9}_{-1.2}\sqrt{M/0.3M_{\odot}}$ light-days (χ^2 criterion). The results are self-consistent and in good agreement with the continuum size predicted by single-epoch spectroscopy and previous studies making use of narrow-band photometry of HE 0435-1223.

Keywords: gravitational lensing: micro – quasars: individual (HE 0435-1223) – accretion, accretion disks

1. INTRODUCTION

The light curves of lensed quasar images provide a time history of the changes in brightness, and their analysis has important applications in cosmology (such as the determination of time delays to infer the Hubble constant, Refsdal 1964, the estimate of peculiar velocities, Mediavilla et al. 2016, and in the study of quasar structure, Chang & Refsdal 1979, 1984; see also Kochanek 2004 and Wambsganss 2006). In this paper we focus on the last application, using gravitational microlensing statistics to determine the quasar accretion disk size (Pooley et al. 2007; Morgan et al. 2010; Sluse et al. 2011; Blackburne et al. 2011; Motta et al. 2012; Blackburne et al. 2014, 2015; Mosquera et al. 2011; Jiménez-Vicente et al. 2012, 2014; Hainline et al. 2013; Mosquera et al. 2009, 2013; Jiménez-Vicente et al. 2015a,b; Mediavilla et al. 2015; Muñoz et al. 2016; Fian et al. 2016). The term "microlensing" describes the flux variations produced by stars in the foreground lens galaxy that result in magnification (or demagnification) of the multiple quasar images (Chang & Refsdal 1979; Kochanek 2004; Blackburne et al. 2014; see also the review by Wambsganss 2006). These flux variations between images are not correlated as would be expected from intrinsic quasar variability. The magnification produced by microlensing depends strongly upon the angular size of the source, with smaller emission regions showing larger flux anomalies and larger sources smoothing out the light curves (Mosquera & Kochanek 2011; Blackburne et al. 2011, 2014).

We study the light curves of the quadruple lensed quasar HE 0435-1233 discovered during the Hamburg/ESO Survey (HES) in the southern hemisphere (Wisotzki et al. 2002). The lens lies in a group of galaxies of at least 12 members. At a redshift of z_s = 1.689 (Wisotzki et al. 2002), HE 0435-1223 is lensed by a foreground galaxy at a redshift of z_l = 0.455 (Eigenbrod et al. 2006) into four bright point sources (plus a fuzzy object in the center) in a nearly symmetric cross-shaped configuration (Wisotzki et al. 2002; Blackburne et al. 2014). The maximum separation between images is 2.6″ (Wisotzki et al. 2002) and their time delays are relatively small owing to the symmetric distribution of the images around the lensing galaxy (Mosquera et al. 2011).

After correcting for the time delays (components A and C lead, followed by the saddlepoints B and D, see Wisotzki et al. 2002) and mean magnitude differences between the images, we find clear indications of microlensing flux variability in the residuals of the light curves (i.e., the differences between the observed light curves and the modeled intrinsic variability of the quasar).

Our aim is to estimate from the statistics of microlensing the size of the accretion disk of the lensed quasar. We use flux ratios of a large enough source in the quasar so as to be insensitive to microlensing in order to establish the baseline for no microlensing magnification (e.g., Mediavilla et al. 2009), from which the amplitude of the microlensing magnification can be measured. We then compare the histogram of microlensing magnifications obtained from the observations (corresponding to the monitoring time interval) with the simulated predictions of microlensing variability for sources of different sizes (Fian et al. 2016). This comparison allows us to evaluate the likelihood of the different values adopted for the size. In this way we extend the single epoch method to all the epochs in the available 13-yr light curves, thereby increasing the statistical significance. We use the optical light curves obtained from the COSMOGRAIL[1] project (Bonvin et al. 2017) to infer microlensing flux variability and the mid-IR data from Jackson et al. 2015 to estimate the baseline for no microlensing variability. In the present study we improve the methods for obtaining the accretion disk size discussed in Fian et al. 2016 by using more realistic estimates of the scatter of the modeled histograms.

The paper is organized as follows. In Section 2 we present the COSMOGRAIL light curves of each image of HE 0435-1223. In Section 3 we model the intrinsic variability and examine the flux ratios between the images. We outline our approaches to compute the accretion disk size in Section 4. Section 5 is devoted to analyzing our results and comparing them with past estimates. Finally, in Section 6 we briefly conclude our results and discuss future perspectives.

2. DATA

The fluxes of the four images of HE 0435-1223 were monitored from 2003 August until 2016 February in the optical *R*-band as a part of the COSMOGRAIL program. The data set consists of 884 epochs (i.e., 884 nights) and the average sampling rate is once every fifth day. Figure 1 shows the 13-yr light curves of images A–D of HE 0435-1223 as published in figure 2 of Bonvin et al. 2017. The relative shifts in magnitude between the images are chosen to ease visualization. The similarity among the four well-sampled light curves is immediately noticeable, although it can be seen that they would not overlap perfectly when shifted in time and magnitude. This mismatch between the light curves is interpreted as microlensing caused by stars in the lensing galaxy. Quasars are time variable, making it necessary to separate

[1] The data has been made publicly available by the COSMOGRAIL collaboration through https://cosmograil.epfl.ch/.

microlensing from intrinsic variability by modeling and removing the later one.

3. INTRINSIC VARIABILITY AND MICROLENSING

The images of multiple lensed quasars arrive with relative delays of hours up to years because of the different paths taken by their light. Intrinsic variability of the source coupled with the light path time delay between the quasar images can mimic flux ratio anomalies. To correct for this, we use the time delay estimates of Bonvin et al. 2017 and shift the light curves by $\Delta t_{AB} = -8.8$ days, $\Delta t_{AC} = -1.1$ days, and $\Delta t_{AD} = -13.8$ days. Owing to the symmetry of the image configuration in this system, the time delays are very short, meaning that intrinsic variations (assumed to be much slower) will show up quasi-simultaneously in all four images. Furthermore, the time delays are small compared to the typical separation between epochs and result in only small adjustments.

After shifting the light curves in time and correcting for the magnitude difference between the images, we perform a single spline fit to the B light curve in order to model the intrinsic variability of the quasar. We assume that the flux variations in image B are mainly intrinsic, as several authors claim that the B image is the least affected by stellar microlensing (Courbin et al. 2011; Motta et al. 2012), whereas A and D are affected by strong microlensing variations (Wisotzki et al. 2003; Kochanek et al. 2006; Courbin et al. 2011; Mosquera et al. 2011; Ricci et al. 2011; Motta et al. 2012). Figure 2 shows the simulated quasar variability (black solid line) with the A–D light curves superimposed. We obtain a source variability of ∼1 mag. Although we use the spline fit to make a reasonable estimate for the intrinsic variability of the source, some contribution from microlensing variability in image B is likely present.[2] We subtract the spline from the light curves and obtain the microlensing difference light curve as follows: $\Delta m_X = m_X - m_{Bfit} - (m_X - m_B)_{midIR}$ where X = A, C, D, assuming that the ratios between the midIR data from Jackson et al. 2015 (36.0±2.1 μJy for A, 26.4±2.1 μJy for B, 34.3±2.1 μJy for C, and 16.1±2.1 μJy for D) represent the true magnification ratios of the images in the absence of microlensing. The mid-IR-emitting regions of quasars should provide a good estimate of the real magnification ratios of the images as they are supposed to arise from a large enough region so as not to be affected by microlensing (see Mediavilla et al. 2009). In the three panels in Figure 3 the microlensing residuals of the A, C, and D light curves after subtraction of the spline fit are shown. Microlensing variability can be seen, particularly in the A–B residual light curve, where image A seems to have been undergoing a microlensing event between the fourth and fifth seasons, whereas C and D remained mainly constant.

[2] In any case, this is irrelevant because in our treatment we also consider the contributions of the B image to microlensing in the simulated difference light curves.

4. BAYESIAN SOURCE SIZE ESTIMATION

The effect of finite source size is to smooth out the flux variations in the light curves of lensed quasars caused by stars in the galaxy. Hence, microlensing is sensitive to the size of the source (Morgan et al. 2010, see also the review by Wambsganss 2006), and we use quantitative Bayesian methods together with our determinations of microlensing magnification amplitude to estimate the accretion disk size in the HE 0435-1223 lensed quasar.

4.1. *Simulated Microlensing Histograms*

We simulate the microlensing of a finite-size source using microlensing magnification maps created with the Inverse Polygon Mapping method described by Mediavilla et al. (2006, 2011). Each map (appearing as a network of high-magnification caustics separated by regions of lower magnifications) corresponds to a specific quasar image and shows the microlensing magnification at a given source position. The general characteristics of the magnification maps are determined (for each quasar image) by the local convergence, κ, and the local shear, γ, which were obtained by fitting a singular isothermal sphere with an external shear (SIS+γ_e), such as might be generated by the tide from a neighboring galaxy or cluster, to the coordinates of the images. The local convergence is proportional to the surface mass density and can be divided into $\kappa = \kappa_c + \kappa_\star$, where κ_c is the convergence due to continuously distributed matter (e.g., dark matter) and $\kappa_\star$ is due to the stellar-mass point lenses (e.g., microlens stars in the galaxy). The values of κ and γ (taken from Mediavilla et al. 2009) are listed in Table 1. We use a surface mass fraction in stars κ_* of 10% (Mediavilla et al. 2009) and generated 2000×2000 pixel magnification maps with a size of 19.3×19.3 Einstein radii[2]. We get a resolution of 0.2 light-days per pixel, which is much smaller than the size of the optical accretion disk of the quasar. The value of the Einstein radius for this system is $2.84 \times 10^{16}\sqrt{M/0.3M_\odot}$ cm = $11\sqrt{M/0.3M_\odot}$ light-days at the lens plane (Mosquera & Kochanek 2011). We randomly distribute stars of mass $M = 0.3\ M_\odot$ across the microlensing patterns to create the microlens convergence $\kappa_\star$. The source sizes can be scaled to a different stellar mass, M, using $r_s \propto \sqrt{M}$. The ratio of the magnification in a pixel to the average magnification of the map gives the microlensing magnification at the pixel

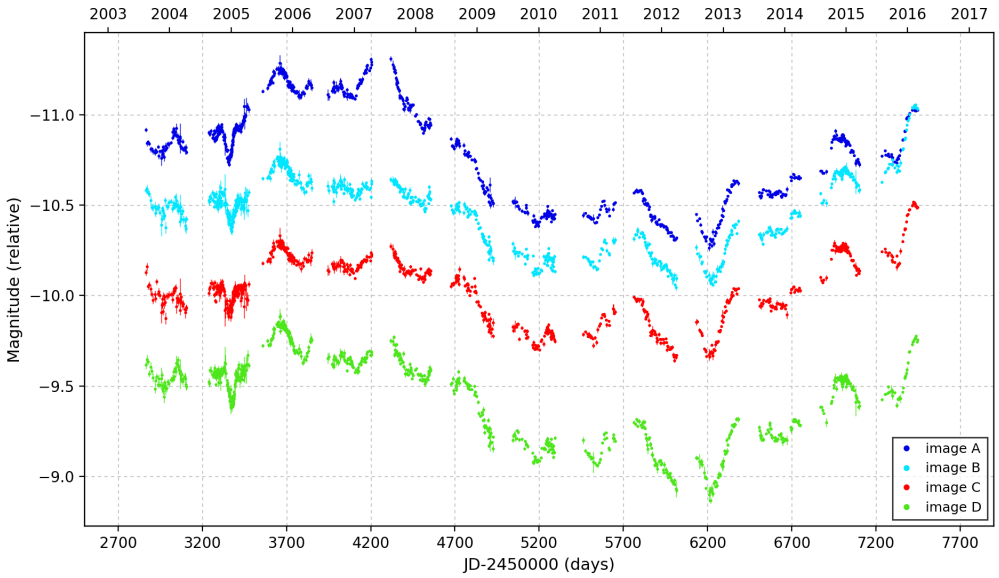

Figure 1. Light curves of the four lensed images A, B, C, and D of the quasar HE 0435-1223 from 2003 August to 2016 February as obtained by the COSMOGRAIL project (see Bonvin et al. 2017). Horizontal axes show the Julian (bottom) and Gregorian (upper) dates. The light curves of the images B, C, and D are shifted by −0.2 mag, 0.3 mag, and 0.6 mag, respectively, so that they do not overlap with each other.

Table 1. Lens Model Parameters

Image	κ	γ
A	0.46	0.39
B	0.52	0.59
C	0.46	0.39
D	0.56	0.64

and histograms of maps normalized to the mean deliver the relative frequency of microlensing magnification amplitude for a pixel-size source.

To model the structure of the unresolved quasar source we considered a circular Gaussian intensity profile of size r_s, $I(R) \propto exp(-R^2/2r_s^2)$. It is generally accepted that the specific shape of the source's radial emission profile is unimportant for microlensing flux variability studies because the results are essentially controlled by the half-light radius rather than by the detailed source profile (Mortonson et al. 2005). The characteristic size r_s is related to the half-light radius; that is, the radius at which half of the light at a given wavelength is emitted, by $R_{1/2} = 1.18\ r_s$. Finally, we convolve the magnification maps with Gaussians of 22 different sizes over a linear grid which spans from $r_s = 0.5$ to 22.5 light-days. The movement of a large source across the magnification map is equivalent to a point source moving across a version of the map that has been smoothed by convolution with the intensity profile of the source. Strong anomalies are evidence for a relatively small source, whereas low microlensing magnifications could be due to a large source size or to a location of the source in a relatively calm region of the magnification map. After convolution we normalized each magnification map by its mean value. The histograms of the normalized map represent the histograms of the expected microlensing variability. Thus, we obtain 22 different microlensing histograms corresponding to different source sizes for each of the images A, C, and D. Finally, cross-correlating the histograms of A, C, and D with the histogram of B, we built the microlensing difference histograms A-B, C-B and D-B for different values of r_s to be compared with the experimental histograms obtained from the observed light curves (see Figure 4).

4.2. *Observed Microlensing Histograms*

From the residuals that represent the differential (with respect to B, the image least prone to microlensing) microlensing of the A, C, and D images (see Figure 3), we have obtained the microlensing histograms; i.e., the frequen-

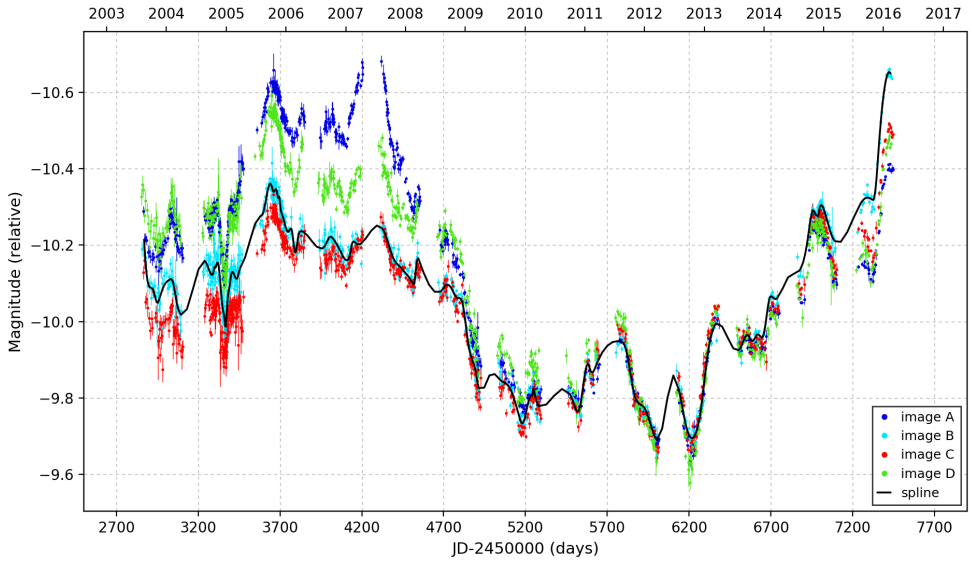

Figure 2. Image A, B, C, and D light curves of HE 0435-1223 in their overlapping region after shifting by the respective time delays (and magnitude differences). The model of the intrinsic variability of the quasar (spline-fitted to the light curve B) is shown in black.

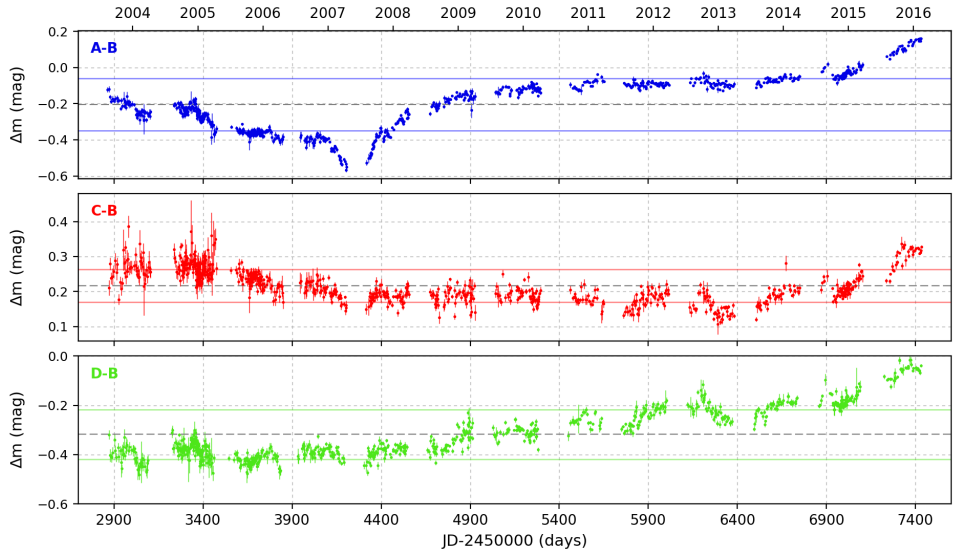

Figure 3. Differential microlensing variability of the light curves A, C, and D compared to a spline fit to the light curve B. The dashed horizontal lines show the mean value of the residuals. The residual magnitudes clearly show that microlensing is present in light curve A.

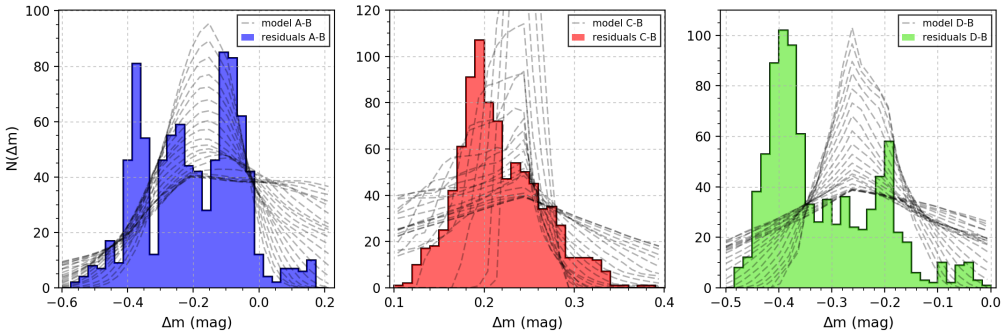

Figure 4. Microlensing frequency distributions obtained from the observed light curves (histograms) and the simulated microlensing magnification maps (dashed lines). The polygonal lines present model histograms for different values of r_s (from 0.5 to 21.5 light-days).

cies in which each microlensing amplitude appears in the microlensing light curves. We adopted a bin size of 0.05 mag. In Figure 4 we compare the A-B, C-B, and D-B modeled magnification histograms corresponding to convolutions with sources of different values of r_s (dashed lines) with the experimental microlensing histograms. Large values of r_s smear out the network of microlensing magnification caustics and reduce their dynamic range, thereby causing the histograms to become narrower.

4.3. *Methods*

To study the likelihood of the different r_s values we compare the microlensing histograms inferred from the model for different values of r_s with the histograms of the data using two different statistics:

(a) Histogram product, defined as

$$P_X(r_s) = \sum_{i=1}^{N_{bin}} h^i_{X-B}\, \hat{h}^i_{X-B}(r_s), \tag{1}$$

where h^i_{X-B} and $\hat{h}^i_{X-B}(r_s)$ are the observed and modeled histograms, and N_{bin} is the number of bins. This is a natural extension of the single-epoch method. After multiplying the probability distributions corresponding to A, C, and D we obtain the PDF of the source size,

$$P(r_s) = P_A(r_s) \cdot P_C(r_s) \cdot P_D(r_s). \tag{2}$$

(b) Pearson's χ^2-test. This is a test suited to measure the "distance" between two histograms. After normalizing all simulated histograms to the number of counts in the real data, we measure the goodness of fit between the histograms inferred from the model (for different source sizes r_s) and the histogram of the observed microlensing differences with a χ^2- statistic:

$$\chi^2 = \sum_{i=1}^{N_{bin}} \frac{(h^i_{X-B} - \hat{h}^i_{X-B}(r_s))^2}{(\sigma_{X-B})^2} \tag{3}$$

with

$$\sigma_{X-B} = \sqrt{(\sigma^{model}_{X-B})^2 + (\sigma^{obs}_{X-B})^2} \tag{4}$$

and

$$P_X(r_s) \propto e^{-\frac{\chi^2}{2}}. \tag{5}$$

Multiplying them together, we obtain the PDF of the source size,

$$P(r_s) = \prod_X P_X(r_s). \tag{6}$$

In our previous paper (Fian et al. 2016) we noticed that the application of the χ^2 method led to underestimation of the uncertainties in the size. We obtained relatively high values for χ^2, which indicates that we were probably underestimating the intrinsic scatter of the model histograms obtained from the magnification maps. It should be taken into account that the observed light curves correspond to a tiny track on the magnification map and that the scatter between the histograms corresponding to different tracks can be large. In other words, we need to know the scatter of a simple track realization with respect to the mean. In this work we propose to control this problem by estimating the uncertainties as follows: Once we have the convolved magnification maps for each image, we run 1000 tracks across them, at random starting points and in random directions (of time length corresponding to the observed light curve) in order to estimate the scatter in the magnification histogram. Scaling the COSMOGRAIL monitoring period of HE 0435-1223

(13 yr) with the Einstein crossing time computed by Mosquera & Kochanek 2011, we estimated the distance in pixels traveled by the source along the caustic pattern. For each image and each convolved map, we build histograms of the set of tracks and compute their average. From these average histograms we estimate the dispersion in each bin to get the uncertainty contributions for each image that we will use in quadrature for our χ^2 calculations. Coming from different regions of the magnifications map, the scatter among the histograms of the random trajectories is high. We calculated the χ^2 for 22 source sizes r_s, spaced linearly between 0.5 and 21.5 light-days. The minimum χ^2 using this estimate of the histogram uncertainties is $\sim$2 for A and C, and $\sim$6 for D, respectively.

In Figure 5 we show the random source trajectories from which we build these histograms superposed on the magnification map for each image (left panels). In order to make the caustics and cusps more easily visible, in this figure we did not convolve the magnification maps with the source size. In the right-hand panels of Figure 5 the histograms of the whole map are shown in gray and the average histograms of the tracks are shown in color, with different shadings standing for different convolutions of r_s.

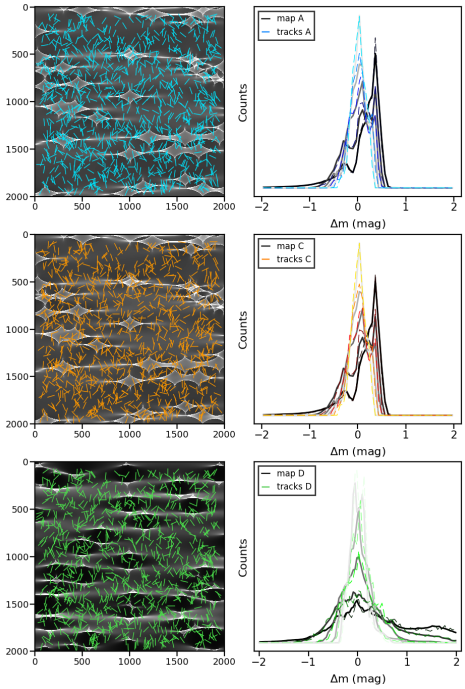

Figure 5. Random tracks superposed on magnification maps of images A (top left), C (middle left), and D (bottom left). The gray scale shows the unconvolved map with lighter colors indicating higher magnifications. The lines show the source trajectories across the pattern for the COSMOGRAIL monitoring period. Histograms derived from the magnification maps (gray) and the tracks for the images A (blue), C (red), and D (green) are shown in the right-hand panels. Different color shadings stand for different convolutions with r_s. Positive numbers of magnification denote demagnification.

5. RESULTS AND DISCUSSION

The resulting normalized probability distributions obtained using the methods discussed in Section 4.3 can be seen in Figure 6. Using a logarithmic prior, we found a size of the region emitting the R-band emission of $\langle r_s \rangle = 7.1^{+9.4}_{-1.6}\sqrt{M/0.3M_\odot}$ for 68% confidence estimates for the histogram product (solid line). Using Pearson's χ^2 statistic, we predict a source size of $\langle r_s \rangle = 7.5^{+5.0}_{-1.0}\sqrt{M/0.3M_\odot}$ light-days (dashed line). We obtained values of $\chi^2 \sim 2$ for A and C, and $\sim$6 for D.

Multiplying by a factor of 1.18, we convert r_s to half-light radii. Our result for each method expressed in terms of the half-light radius, $R_{1/2} = 8.4^{+11.1}_{-1.9}\sqrt{M/0.3M_\odot}$ light-days (histogram product) and $R_{1/2} = 8.9^{+5.9}_{-1.2}\sqrt{M/0.3M_\odot}$ light-days (Pearson's χ^2) is in good agreement with the estimates by Motta et al. 2017 ($R_{1/2} = 19^{+8}_{-6}\sqrt{M/0.3M_\odot}$ light-days), Mosquera et al. 2011 ($R_{1/2} = 5^{+4}_{-4}\sqrt{M/0.3M_\odot}$ light-days) and Blackburne et al. 2011 ($R_{1/2} = 6.7^{+3.0}_{-2.5}\sqrt{M/0.3M_\odot}$ light-days) for this system. All the estimates have been scaled to a $\lambda_0 = 2417$ Å using $R_{1/2} = (\lambda_0/\lambda)^p\, R_{1/2}(\lambda)$. Our estimates for the size are also in good agreement with the average determinations obtained for a sample of lensed quasars by Jiménez-Vicente et al. (2012, 2014, 2015b,a) when a fraction of mass in stars of 10% is considered.

6. SUMMARY AND CONCLUSIONS

The quadruple-imaged strong gravitational lens HE 0435-1223 has four nearly identical components arranged symmetrically around a luminous galaxy and is an attractive target for microlensing studies because of the relative ease of separating intrinsic from microlensing-induced variations due to the short time delay between its images. Unlike most other known quadruple lens systems, photometric monitoring of this object is also relatively easy, because of its relatively wide image separations (Wisotzki et al. 2002). We used the COSMOGRAIL light curves of the four images of HE 0435-1223 (Bonvin et al. 2017, see Figure 1) to obtain the

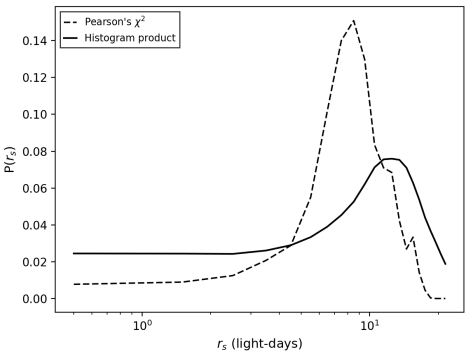

Figure 6. Probability distributions of the source size r_s for the histogram-product (solid line) and Pearson's χ^2 (dashed line).

accretion disk size. They cover a relatively long period (13 yr), which significantly extends the time coverage of previous studies and provides relatively dense coverage (one observing epoch every 5 days, 884 usable points). Taking as reference image B, which is less affected by microlensing, and using the experimental time delays inferred by Bonvin et al. 2017, we have removed the intrinsic variability from the light curves in the overlapping region. Using the mid-IR flux ratios between images determined by Jackson et al. 2015 as a baseline for no microlensing magnification, we have finally obtained the microlensing light curves, A-B, C-B, and D-B. We have clearly detected microlensing in the images A and D of HE 0435-1223 with up to 0.6 mag (0.5 mag) in A (D). The light curve of C seems to be less affected by microlensing, although some changes can be seen in the first four and last two seasons of the data.

We have used the statistics of microlensing magnifications during the available seasons in the optical R-band of HE 0435-1223 to infer probabilistic distributions for the source size using two different methods. Using the histogram product of the observed and modeled microlensing histograms we have obtained a half-light radius of $R_{1/2} = 8.4^{+11.1}_{-1.9}\sqrt{M/0.3M_\odot}$ light-days. Consistent results are obtained with Pearson's χ^2 ($R_{1/2} = 8.9^{+5.9}_{-1.2}\sqrt{M/0.3M_\odot}$ light-days). In this work we improved the uncertainty estimations for the Pearson χ^2 method to obtain self-consistent results. Our results are also in good agreement with previous estimates of other authors for this system ($R_{1/2} = 19^{+8}_{-6}\sqrt{M/0.3M_\odot}$ light-days by Motta et al. 2017, $R_{1/2} = 5^{+4}_{-4}\sqrt{M/0.3M_\odot}$ light-days by Mosquera et al. 2011 and $R_{1/2} = 6.7^{+3.0}_{-2.5}\sqrt{M/0.3M_\odot}$ light-days by Blackburne et al. 2011).

Future monitoring with the The Large Synoptic Survey Telescope (LSST) will contain a large number (∼8000, see Oguri & Marshall 2010) of light curves of gravitationally lensed quasars that will demand new techniques to compute the sizes of accretion disks in gravitationally lensed quasars. Here, we have explored new techniques based on the use of the histograms of microlensing magnifications that can be used in combination or as an alternative to the light curve fitting method (e.g., Kochanek 2004).

We thank the COSMOGRAIL collaboration for making publicly available the monitoring data of HE 0435-1223. C.F. gratefully acknowledges the financial support of a La Caixa PhD fellowship. E.M. and J.A.M are supported by the Spanish MINECO with the grants AYA2016-79014-C3-1-P and AYA2016-79014-C3-3-P. J.J.V. is supported by the Spain's Ministerio de Economía y Competitividad and the Fondo Europeo de Desarrollo Regional (FEDER) through grant AYA2014-53506-P and by the Junta de Andalucía through project FQM-108.

REFERENCES

Blackburne, J. A., Kochanek, C. S., Chen, B., Dai, X., & Chartas, G. 2014, ApJ, 789, 125
—. 2015, ApJ, 798, 95
Blackburne, J. A., Pooley, D., Rappaport, S., & Schechter, P. L. 2011, ApJ, 729, 34
Bonvin, V., Courbin, F., Suyu, S. H., et al. 2017, MNRAS, 465, 4914
Chang, K., & Refsdal, S. 1979, Nature, 282, 561
—. 1984, A&A, 132, 168
Courbin, F., Chantry, V., Revaz, Y., et al. 2011, A&A, 536, A53
Eigenbrod, A., Courbin, F., Dye, S., et al. 2006, A&A, 451, 747
Fian, C., Mediavilla, E., Hanslmeier, A., et al. 2016, ApJ, 830, 149
Hainline, L. J., Morgan, C. W., MacLeod, C. L., et al. 2013, ApJ, 774, 69
Jackson, N., Tagore, A. S., Roberts, C., et al. 2015, MNRAS, 454, 287
Jiménez-Vicente, J., Mediavilla, E., Kochanek, C. S., & Muñoz, J. A. 2015a, ApJ, 799, 149
—. 2015b, ApJ, 806, 251
Jiménez-Vicente, J., Mediavilla, E., Kochanek, C. S., et al. 2014, ApJ, 783, 47

Jiménez-Vicente, J., Mediavilla, E., Muñoz, J. A., & Kochanek, C. S. 2012, ApJ, 751, 106
Kochanek, C. S. 2004, ApJ, 605, 58
Kochanek, C. S., Morgan, N. D., Falco, E. E., et al. 2006, ApJ, 640, 47
Mediavilla, E., Jiménez-Vicente, J., Muñoz, J. A., & Battaner, E. 2016, ApJ, 832, 46
Mediavilla, E., Jimenez-Vicente, J., Muñoz, J. A., Mediavilla, T., & Ariza, O. 2015, ApJ, 798, 138
Mediavilla, E., Mediavilla, T., Muñoz, J. A., et al. 2011, ApJ, 741, 42
Mediavilla, E., Muñoz, J. A., Lopez, P., et al. 2006, ApJ, 653, 942
Mediavilla, E., Muñoz, J. A., Falco, E., et al. 2009, ApJ, 706, 1451
Morgan, C. W., Kochanek, C. S., Morgan, N. D., & Falco, E. E. 2010, ApJ, 712, 1129
Mortonson, M. J., Schechter, P. L., & Wambsganss, J. 2005, ApJ, 628, 594
Mosquera, A. M., & Kochanek, C. S. 2011, ApJ, 738, 96
Mosquera, A. M., Kochanek, C. S., Chen, B., et al. 2013, ApJ, 769, 53
Mosquera, A. M., Muñoz, J. A., & Mediavilla, E. 2009, ApJ, 691, 1292
Mosquera, A. M., Muñoz, J. A., Mediavilla, E., & Kochanek, C. S. 2011, ApJ, 728, 145
Motta, V., Mediavilla, E., Falco, E., & Muñoz, J. A. 2012, ApJ, 755, 82
Motta, V., Mediavilla, E., Rojas, K., et al. 2017, ApJ, 835, 132
Muñoz, J. A., Vives-Arias, H., Mosquera, A. M., et al. 2016, ApJ, 817, 155
Oguri, M., & Marshall, P. J. 2010, MNRAS, 405, 2579
Pooley, D., Blackburne, J. A., Rappaport, S., & Schechter, P. L. 2007, ApJ, 661, 19
Refsdal, S. 1964, MNRAS, 128, 307
Ricci, D., Poels, J., Elyiv, A., et al. 2011, A&A, 528, A42
Sluse, D., Schmidt, R., Courbin, F., et al. 2011, A&A, 528, A100
Wambsganss, J. 2006, ArXiv Astrophysics e-prints, astro-ph/0604278
Wisotzki, L., Becker, T., Christensen, L., et al. 2003, A&A, 408, 455
Wisotzki, L., Schechter, P. L., Bradt, H. V., Heinmüller, J., & Reimers, D. 2002, A&A, 395, 17

4.2 Structure of the Broad Line Region[2]

In the previous section we presented accretion disk size measurements of two gravitationally lensed quasars using their optical light curves. In this section, we continue our study with estimates of the BLR structure using spectroscopic data of a sample of lensed quasars.

To date, the primary probe of the geometry and kinematics of the BLR of AGN has been reverberation mapping (Blandford & McKee 1982, see also Peterson 2006 and references therein) based on the measurement of the lag between the intrinsic variability of the continuum and the broad emission lines. Until now, reverberation mapping (RM) studies have been largely limited to relatively nearby, lower luminosity AGNs since time delays for distant, luminous quasars are long and additionally dilated by the cosmological redshift. An alternative means of studying the structure of the BLR is to examine how it is microlensed in gravitationally lensed quasars. This method is based upon a different approach that can help overcoming the difficulties of RM. In microlensing, compact objects (i.e. stars) in the lens galaxy differentially magnify components of the quasar emission regions, leading to time- and wavelength-dependent changes in the spectra of the images (Wambsganss 2006; Abajas et al. 2002). The amplitude of the magnification is controlled by the size of the emission region, with smaller source regions showing larger magnifications. Microlensing is now a well-established tool for studying the quasar structure, for both individual objects and larger statistical samples (Sluse et al. 2012; Motta et al. 2012; Guerras et al. 2013).

Single-epoch microlensing measurements can be used to estimate (or constrain) the size of the emitting regions (e.g., Guerras et al. 2013). As a qualitative leap forward from the static single-epoch analysis, we study the variability of the emission lines by comparing spectroscopy from at least two different epochs. The response to microlensing over time of different kinematic regions (corresponding to emission lines of different origin or to different wavelength regions in a given emission line) contains a large amount of information that can improve our understanding of the BLR structure and kinematics.

[2] brief overview of Fian et al. 2018b and 2018c

4.2.1 Data Analysis Methods

A lot of information about quasars can be inferred by studying their extraordinary rich spectra since different spectral features arise from different spatial regions in the quasar. There is a time-variable continuum emission spanning several orders of magnitude in wavelength; broad emission lines follow the continuum variability after a certain time delay with smaller amplitudes, and barely/non-variable narrow emission lines have their origin in considerably larger regions (Abajas et al. 2002). In Figure 4.4 a schematic sketch is shown of different emission regions giving rise to different spectral features. As matter gradually falls into the central SMBH, it emits UV light from the accretion disk, then optical light from the BLR and finally infrared light from the large NLR (Massey 2010). From theory, we expect that spectral emission features coming from smaller regions are more affected by microlensing than features emitted in more extended regions.

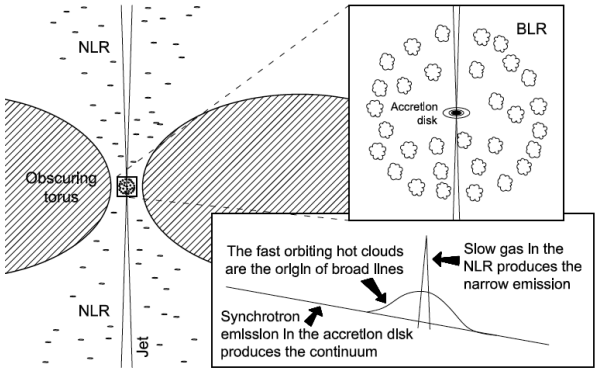

Figure 4.4: Schematic view of different spatial regions (accretion disk, BLR, NLR) giving rise to different spectral features like the continuum, the line wings, and the line core (from: Guerras 2014).

In our studies we assume that the narrow cores of the BELs arise mostly from the outer BLR and NLR and use them as a reference that is little affected by microlensing. However, microlensing could affect the high ionization lines that arise from the inner part of the BLR. To be precise, it affects the broad wings (mainly arising from Doppler broadening) of the line profiles, leaving the cores relatively unchanged (Richards et al. 2004; Lewis & Ibata 2004; Gómez-Álvarez et al. 2006). Thus, the BLR is spatially large enough so that one part can cross

a caustic while the other part remains unaffected by microlensing. Below we describe our data analysis methods:

(a) **Estimate Microlensing in the BELs.**
We will focus on the low ionization lines C III] λ1909 and Mg II λ2798, and the high ionization line C IV λ1549. For each emission line we use DIPSO in STARLINK to fit a straight line $y = a\lambda + b$ to the continuum on either side of the emission line and subtract it from the spectrum. In oder to quantify the effects of microlensing on the BLR, we want to untangle microlensing from the macro-magnification produced by the lens galaxy and extinction. We attempt this by normalizing the continuum-subtracted spectra for all images and all epochs to match the core of the emission line defined by the flux within a narrow interval (± 6Å) centered on the peak of the line. In principle, the cores of the emission lines can be used as a reference that is little affected by microlensing and intrinsic variability (see Guerras et al. 2013) as they arise from a significantly larger region than the wings. Under this assumption, the ratio of the line wing fluxes of two images, F_{1wings}/F_{2wings}, yields a measurement of the size of the high velocity wing emission regions. To prevent an underestimation of the microlensing in the wings we separate the line core form the wings by a buffer of ±9Å. We then can estimate the average wing emission in different wavelength intervals (see Figure 4.5). In those cases in which the emission line is affected by absorption lines an integration window avoiding absorption features was chosen.

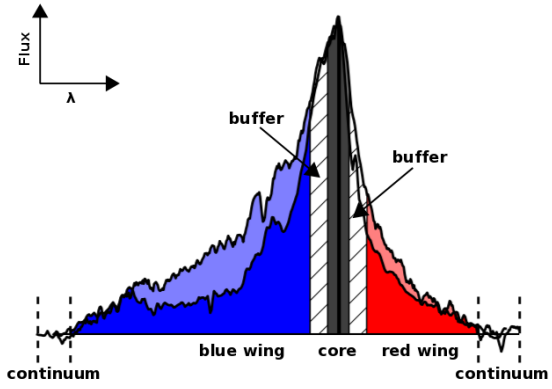

Figure 4.5: Sketch of measuring the magnitude differences in the wings of a BEL.

We use the following statistics to calculate the magnitude difference in the wings between two different images/epochs (x,y):

$$\Delta m_i = w_i * (y_i - x_i) \tag{4.3}$$

with weights $w_i = \sqrt{(y_i + x_i)}/(y_i + x_i)$, selected to equalize the deviations of the differences. From the mean value in a given wavelength interval, $\langle \Delta m_i \rangle$, we compute the magnitude difference between images/epochs, $\Delta m = \langle \Delta m_i \rangle$, and its standard deviation σ.

Given the estimates of the differential microlensing in the wings between pairs of images in each system for different emission lines, we can estimate the size of their emission region by comparing them with a set of computer-generated histograms. We treat each microlensing measurements as a single epoch event and from the microlensing magnification corresponding to all the image pairs, in all available epochs of observation, we compute the joint microlensing probability, $P(r_s)$, by combining the likelihoods for the individual lines. Using this method, we obtain an average estimate of the emitting region size for each emission line that reveals the structure of the BLR in lensed quasars.

(b) **Extinction Correction.**
We have also analyzed the wavelength regions between C IV, C III], and Mg II to measure the changes in the UV Fe II and Fe III emission line blends, the complex formed by the He line, the O III]/Al II blend and the subjacent pseudo-continuum, and the red shelf of C IV. We follow the definition of the wavelength regions of Guerras et al. (2013); Vestergaard & Wilkes (2001) and Vanden Berk et al. (2001) and again use the cores of the C IV, C III], and Mg II emission lines as a baseline for no microlensing. We fit various straight lines to the continuum regions bracketing the emission line windows and subtract them from the spectra. Then, for each image pair and each epoch, we normalize the continuum-subtracted spectra to match the core of the Mg II (C III]) emission line. In many cases, the Mg II (C III]) based normalization does not match the C III] (C IV) emission line. We assume that this mismatch of the line cores arise from differential extinction in the lens galaxy. This is corrected by applying a linear extinction correction to match both emission lines simultaneously. Finally, for each pair of images (and each epoch) we compare the flux ratios in the defined emission line windows of the continuum-subtracted and extinction-

corrected spectra using the same statistics as described before.

We have studied, in most cases, up to 11 different spectral features (emission lines of blends) between the C III] and Mg II lines (see Section 4.2.3). We find that some of the objects, once subtracted the continuum emission, show remarkable differences in the intensity of the iron blends (especially Fe III), while the rest of the spectra match nicely. The strong microlensing of some of these emission blends suggests that they may arise from a very small region. While lighter elements produce a relatively small number of well known emission lines, the iron emission consists of a complex set of electronic levels giving rise to many superposed lines, resulting in several blended bands across the quasar spectra (Guerras et al. 2013). Both the mechanism generating the iron emission and the spatial scale of the emitting regions are poorly understood. In Section 4.2.3 we use microlensing magnification measurements in a sample of 26 quasars to investigate the origin of several UV Fe II and Fe III blends.

(c) **Intrinsic Variability vs. Microlensing.**
Although it is limited, the temporal sampling available allows us to identify intrinsic variability and to classify the differences between pairs of spectra as candidates for intrinsic variability or microlensing. In principle, at a given epoch, intrinsic variability should affect all the images of a lensed quasar in the same way, whereas microlensing may induce differences between the spectra of different images. However, the time delay in the arrival of the light from two lensed images can complicate this simple scheme by inducing differences between images which may arise from intrinsic variability. Spectroscopic monitoring of at least two epochs is useful to untangle the causes of variability. If the different images change in the same way, the origin of the variability must be intrinsic but if one of the images exhibits differences with respect to the other we may expect that it is affected by microlensing.

4.2.2 Modeling the BLR Size

Our simulations are based on 2000 × 2000 (3000 × 3000 in Fian et al. 2018b) pixel microlensing maps, spanning 400 × 400 light-days^2 (600 × 600) on the source plane, generated using the Inverse Polygon Mapping method described in Mediavilla et al. (2006, 2011). The general characteristics of the magnification maps are determined (for each quasar image) by the local convergence

κ and the local shear γ, which were obtained by fitting a singular isothermal sphere with an external shear (SIS+γ_e) that reproduce the coordinates of the images (Mediavilla et al. 2006). We used $\alpha = 0.1$ for the fraction of mass in compact objects (i.e. stars) and consider 0.3 $M_\odot$ microlenses. To simulate the effect of finite sources we model the luminosity profile of the region emitting the BEL wings/iron blends as a Gaussian and the magnifications experienced by a source of size r_s are then found by convolving the magnification maps with the Gaussian profiles of sigma r_s. Following a Bayesian approach, we estimated the probability of r_s and p conditioned to the measured microlensing magnifications.

4.2.3 Fian et al. 2018b: BLR Structure, Size and Kinematics I

The Astrophysical Journal, 859:50 (26pp), 2018 May 20 https://doi.org/10.3847/1538-4357/aabc0d

Microlensing and Intrinsic Variability of the Broad Emission Lines of Lensed Quasars

C. Fian[1,2], Eduardo Guerras[3], E. Mediavilla[1,2], J. Jiménez-Vicente[4,5], J. A. Muñoz[6,7], E. E. Falco[8], V. Motta[9], and A. Hanslmeier[10]
[1] Instituto de Astrofísica de Canarias, Vía Láctea S/N, La Laguna E-38200, Tenerife, Spain
[2] Departamento de Astrofísica, Universidad de la Laguna, La Laguna E-38200, Tenerife, Spain
[3] Homer L. Dodge Department of Physics and Astronomy, University of Oklahoma, Norman, OK 73019, USA
[4] Departamento de Física Teórica y del Cosmos, Universidad de Granada, Campus de Fuentenueva, E-18071 Granada, Spain
[5] Instituto Carlos I de Física Teórica y Computacional, Universidad de Granada, E-18071 Granada, Spain
[6] Departamento de Astronomía y Astrofísica, Universidad de Valencia, E-46100 Burjassot, Valencia, Spain
[7] Observatorio Astronómico, Universidad de Valencia, E-46980 Paterna, Valencia, Spain
[8] Harvard-Smithsonian Center for Astrophysics, 60 Garden St., Cambridge, MA 02138, USA
[9] Instituto de Física y Astronomía, Universidad de Valparaíso, Avda. Gran Bretaña 1111, Playa Ancha, Valparaíso 2360102, Chile
[10] Institute of Physics (IGAM), University of Graz, Universitätsplatz 5, A-8010, Graz, Austria
Received 2018 January 9; revised 2018 March 27; accepted 2018 March 28; published 2018 May 23

Abstract

We study the broad emission lines in a sample of 11 gravitationally lensed quasars with at least two epochs of observation to identify intrinsic variability and to disentangle it from microlensing. To improve our statistical significance and emphasize trends, we also include 15 lens systems with single-epoch spectra. Mg II and C III] emission lines are only weakly affected by microlensing, but C IV shows strong microlensing in some cases, even for regions of the line core, presumably associated with small projected velocities. However, excluding the strongly microlensed cases, there is a strikingly good match, on average, between the red wings of the C IV and C III] profiles. Analysis of these results supports the existence of two regions in the broad-line region (BLR), one that is insensitive to microlensing (of size $\gtrsim$50 lt-day and kinematics not confined to a plane) and another that shows up only when it is magnified by microlensing (of size of a few light-days, comparable to the accretion disk). Both regions can contribute in different proportions to the emission lines of different species and, within each line profile, to different velocity bins, all of which complicates detailed studies of the BLR based on microlensing size estimates. The strength of the microlensing indicates that some spectral features that make up the pseudo-continuum, such as the shelf-like feature at λ1610 or several Fe III blends, may in part arise from an inner region of the accretion disk. In the case of Fe II, microlensing is strong in some blends but not in others. This opens up interesting possibilities to study quasar accretion disk kinematics. Intrinsic variability seems to affect the same features prone to microlensing, with similar frequency and amplitude, but does not induce outstanding profile asymmetries. We measure intrinsic variability ($\lesssim$20%) of the wings with respect to the cores in the C IV, C III], and Mg II lines consistent with reverberation mapping studies.

Key words: gravitational lensing: micro – quasars: emission lines – quasars: general

1. Introduction

To date, the primary probe of the geometry and kinematics of the broad-line regions (BLRs) of active galactic nuclei (AGNs) has been reverberation mapping (RM; Blandford & McKee 1982; see also Peterson 2006, and references therein) based on the measurement of the lag between the intrinsic variability of the continuum and that of the broad emission lines (BELs). This technique has shown that the global structure of the BLR is consistent with photoionization models (Bentz et al. 2009). RM results also suggest that there is no common kinematic structure, with differing sources showing signs of inward, outward, and rotating disk-like velocity structures (e.g., Bentz et al. 2010; Grier et al. 2017a, and references therein). Until now, RM studies have been largely limited to relatively nearby, lower-luminosity AGNs. Very recently, new results for individual (Shen et al. 2016; Grier et al. 2017b) or composite (Li et al. 2017) sources ($z \lesssim 1.1$) of intermediate luminosity based on the first year of the Sloan Digital Sky Survey (SDSS) RM project have been presented, mainly for Hα, Hβ, and Mg II. However, there are few RM measurements for C IV (Kaspi et al. 2007), which is the most easily studied line in quasars with $1.5 \lesssim z \lesssim 2.5$.

An alternative means of studying the structure of the BLR is to examine how it is microlensed in gravitationally lensed quasars. In microlensing, the stars in the lens galaxy differentially magnify components of the quasar emission regions, leading to time- and wavelength-dependent changes in the spectra of the images (Abajas et al. 2002; Wambsganss 2006). The amplitude of the magnification is controlled by the size of the emission region, with smaller source regions showing larger magnifications. Microlensing is now a well-established tool for studying quasar structure, for both individual objects and larger statistical samples (Motta et al. 2012; Sluse et al. 2012; Guerras et al. 2013a, 2013b).

In Guerras et al. (2013a; see also Motta et al. 2012) we compared the emission-line profiles of pairs of images from a sample of 13 lensed quasars for which archival single-epoch spectroscopy is available. For single-epoch data some method is needed to separate the effects of microlensing from those of extinction and uncertainties in the magnification produced by the lens galaxy (macro-magnification). In principle, the cores of the emission lines can be used as a reference that is little affected by microlensing. Specifically, the ratio of the line core fluxes of two images to their line wing fluxes gives an estimate of the size of the wing emission

Table 1
Database of Lensed Quasar Spectra

Object	Image	Epoch	Date	C IV	C III]	Mg II	Region 1[a]	Region 2[b]	Facilities	References
HE 0047−1756	A, B	I	2002 Sep 04	x	x	⋯	x	⋯	Magellan	Wisotzki et al. (2004)
		II	2005 Jul 18	⋯	x	x	⋯	x	VLT	Sluse et al. (2012)
		III	2008 Jan 13	⋯	x	x	⋯	x	Magellan	Rojas et al. (2014)
Q0142−100	A, B	I	2006 Aug 15	x	x	⋯	x	⋯	VLT	Sluse et al. (2012)
		II	2008 Jan 12	x	⋯	⋯	x	x	MMT	V. Motta (2018, private communication)
SDSS J0246−0825	A, B	I	2006 Aug 22	⋯	⋯	⋯	⋯	x	VLT	Sluse et al. (2012)
HE 0435−1223	A, B	I	2002 Sep 05	x	x	x	x	⋯	CAO	Wisotzki et al. (2003)
	B,D	II	2004 Oct–Nov	⋯	x	x	x	x	VLT	Eigenbrod et al. (2007)
	A, B, C, D	III	2008 Jan 12	x	x	x	x	x	MMT	Motta et al. (2017)
	A, C, D	IV	2007 Dec 10	x	x	⋯	x	x	Magellan	V. Motta (2018, private communication)
HE 0512−3329	A, B	I	2001 Aug 13	⋯	⋯	⋯	x	⋯	HST	Wucknitz et al. (2003)
SDSS J0806+2006	A, B	I	2005 Apr 12	⋯	x	x	⋯	x	APO	Inada et al. (2006)
		II	2006 Apr 22	⋯	x	x	⋯	x	VLT	Sluse et al. (2012)
HS 0818−1227	A, B	I	2008 Jan 12	⋯	⋯	⋯	x	⋯	MMT	Motta et al. (2012)
SBS 0909+532	A, B	I	2003 Mar 07	⋯	⋯	⋯	x	x	HST	Mediavilla et al. (2005)
SDSS J0924+0219	A, B	I	2005 Jan 14	⋯	⋯	⋯	⋯	x	VLT	Eigenbrod et al. (2006)
FBQ 0951+2635	A, B	I	1997 Feb 14	⋯	⋯	x	⋯	x	Keck	Schechter et al. (1998)
		II	2006 Mar 31	⋯	⋯	x	⋯	⋯	VLT	Sluse et al. (2012)
Q0957+561	A	I	1999 Apr 15	x	x	x	x	x	HST	Goicoechea et al. (2005)
	B	I	2000 Jun 2	x	x	x	x	x	HST	Goicoechea et al. (2005)
	A, B	II	2008 Jan 12	x	x	x	x	⋯	MMT	Motta et al. (2012)
SDSS J1001+5027	A, B	I	2003 Nov 20	⋯	⋯	⋯	x	x	APO	Oguri et al. (2005)
SDSS 1004+4112	A, B, C, D	I	2003 May 31	x	x	x	x	x	APO	Richards et al. (2004)
	A, B	II	2004 Jan 19	x	x	⋯	x	⋯	WHT	Gómez-Álvarez et al. (2006)
		III	2008 Jan 12	x	x	⋯	x	x	MMT	Motta et al. (2012)
Q1017−207	A, B	I	1996 Oct 28	⋯	⋯	⋯	x	⋯	HST	Surdej et al. (1997)
SDSS J1029+2623	A, B	I	2008 Jan 12	⋯	⋯	⋯	x	⋯	MMT	Motta et al. (2012)
HE 1104−1805	A, B	I	2008 Jan 11	x	⋯	⋯	x	⋯	MMT	Motta et al. (2012)
		II	2008 Apr 07	x	x	x	x	x	VLT	Motta et al. (2012)
		III	1993 May 11	x	x	⋯	x	⋯	NTT	Wisotzki et al. (1993)
		IV	1994 Nov 29	x	⋯	⋯	x	⋯	ESO 3.6 m	Wisotzki et al. (1995)
SDSS J1138+0314	B, C	I	2005 May 10	⋯	⋯	⋯	x	⋯	VLT	Sluse et al. (2012)

Table 1
(Continued)

Object	Image	Epoch	Date	C IV	C III]	Mg II	Region 1[a]	Region 2[b]	Facilities	References
SDSS J1155+6346	A, B	I	2010 Sept 20	⋯	⋯	⋯	x	⋯	HST	Rojas et al. (2014)
SDSS J1206+4332	A, B	I	2004 Jun 21	⋯	⋯	⋯	x	x	APO	Oguri et al. (2005)
SDSS J1335+0118	A, B	I	2005 Feb 17	⋯	⋯	⋯	⋯	x	VLT	Sluse et al. (2012)
SDSS J1339+1310	A, B	I	2013 Apr 13	⋯	x	x	x	x	GTC	Shalyapin & Goicoechea (2014)
		II	2014 Mar 27	⋯	x	x	x	x	GTC	Goicoechea & Shalyapin (2016)
		III	2014 May 20	x	x	⋯	⋯	⋯	GTC	Goicoechea & Shalyapin (2016)
SDSS J1353+1138	A, B	I	2005 Apr 12	⋯	⋯	⋯	⋯	x	Keck	Inada et al. (2006)
Q1355−2257	A, B	I	2005 Mar 13	⋯	⋯	⋯	⋯	x	VLT	Sluse et al. (2012)
SBS 1520+530	A, B	I	1996 Jun 12	⋯	⋯	⋯	x	⋯	SAO	Chavushyan et al. (1997)
WFI 2033−4723	A1, A2, B, C	I	2003 Sep 15	x	x	x	x	⋯	Magellan	Morgan et al. (2004)
	B, C	II	2005 May 13	⋯	x	x	⋯	x	VLT	Sluse et al. (2012)
		III	2008 Apr 14	⋯	x	x	⋯	x	VLT	Motta et al. (2017)
HE 2149−2745	A, B	I	2000 Nov 19	x	x	x	x	x	VLT	Burud et al. (2002)
		II	2006 Aug 04	x	x	⋯	x	x	VLT	Sluse et al. (2012)
		III	2008 May 07	x	x	x	x	x	VLT	Motta et al. (2017)

Notes.
[a] Region between C IV and C III].
[b] Region between C III] and Mg II.

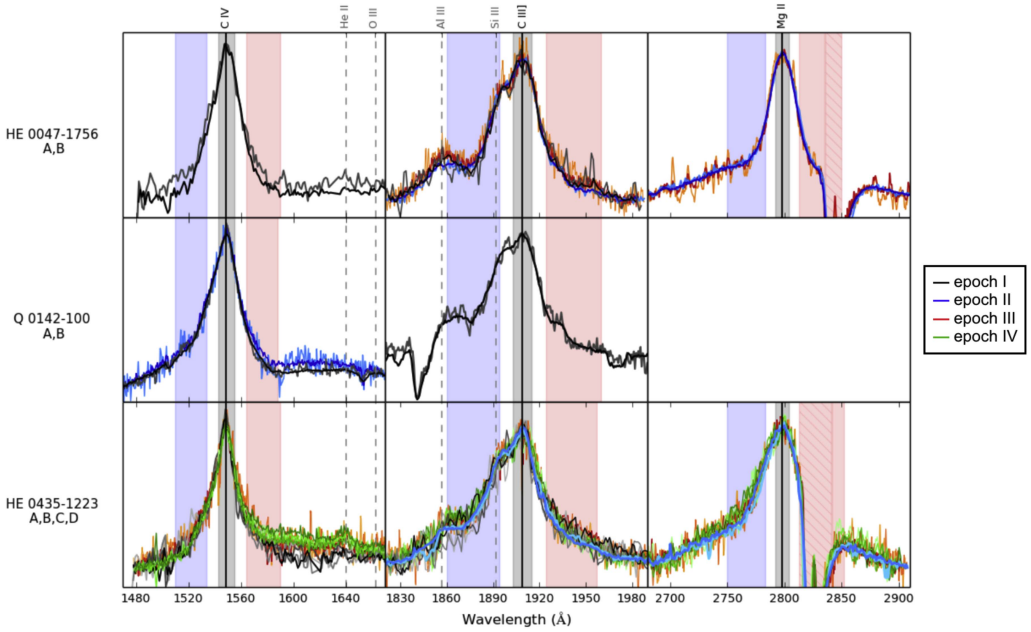

Figure 1. C IV, C III], and Mg II emission line profiles from different epochs superimposed after subtracting the continuum and matching the line core. Different colors correspond to different epochs, and different color shadings stand for different images in the corresponding epoch. Blue/red shaded regions show the integration windows used for the magnitude difference calculations. The ordinate is in arbitrary units of flux. Note: due to the lack of wavelength coverage toward the blue, the definition of the continuum window on this side slightly overlaps with the blue wing in the case of SDSS J1339+1310 (epochs I and II).

regions. Guerras et al. (2013a) were able to measure wing microlensing magnifications of ∼0.1 mag, which, under the above hypothesis, led to estimates for the BLR size of $r_s = 24^{+22}_{-15}$ and $r_s = 55^{+150}_{-35}$ lt-day (90% confidence) for the high- and low-ionization lines, respectively. As expected from ionization stratification, high-ionization lines come from a smaller region than low-ionization lines, and higher-luminosity quasars have larger emission regions. The sizes were somewhat smaller than those found for existing (full-line) reverberation studies, as expected from measuring the size of the line wings. Using similar techniques, Guerras et al. (2013b) have found a strong microlensing signal (up to ∼0.6 mag) in the UV pseudo-continuum emission from Fe II and Fe III, indicating that the region emitting this pseudo-continuum is quite small, with a size comparable to that of the accretion disk determined from microlensing of the continuum.

As a qualitative leap forward from the static single-epoch analysis, here we study the variability of the emission lines by comparing spectroscopy from at least two different epochs. The response to microlensing over time of different kinematic regions (corresponding to emission lines of different origin or to different wavelength regions in a given emission line) contains a large amount of information that can improve our understanding of the BLR structure and kinematics. The analysis may be complex, for in a microlensing event the source structure and the pattern of microlensing magnification are convolved, but the expectations are promising.

On the other hand, the comparison of two epochs of spectroscopic observations is necessary to study intrinsic quasar variability that may be of great interest by itself and in comparison with microlensing. In particular, we would like to compare the frequency and amplitude of both sources of variability and determine whether they affect the same kinematic regions or not. This last question may be very interesting when cross-checking the results obtained from reverberation mapping and microlensing.

Spectroscopic monitoring of at least two epochs is also useful to separate intrinsic variability and microlensing. In principle, at a given epoch, intrinsic variability should affect all the images of a lensed quasar in the same way, whereas microlensing may induce differences between the spectra of different images. However, the time delay in the arrival of the light from two lensed images can complicate this simple scheme by inducing differences between images that may arise from intrinsic variability. Although there are reasons to suppose that the contamination by intrinsic variability modulated by the time delay is weak (Guerras et al. 2013b), a second epoch of spectroscopic observations can allow us to untangle the causes of variability. If the different images change in the same way, the origin of the variability must be intrinsic, but if one of the images exhibits differences with respect to the others, we may expect that it is affected by microlensing.

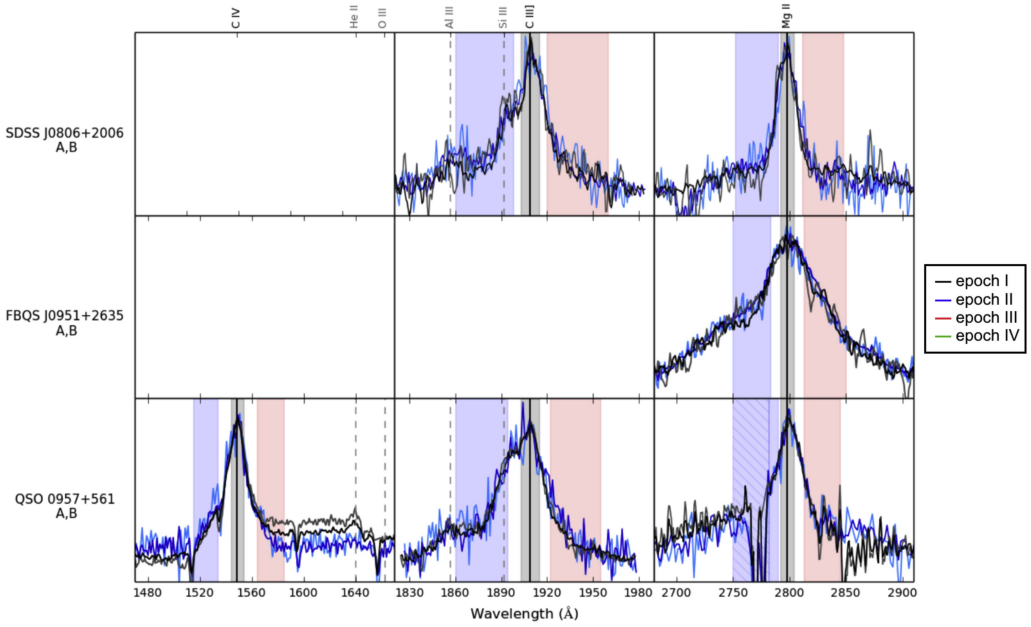

Figure 1. (Continued.)

Finally, the changes in the spectra of an image between two epochs are completely unaffected by extinction and uncertainties in the lens model and hence potentially provide independent estimates of the microlensing of the core and wings. This enables us to make independent estimates of the sizes of the two regions rather than (to be precise) of the differences in the sizes of the two regions measured when only a single epoch is available.

Obviously, all these positive prospects for the study of BEL variability are affected by the quality of the data, which, in our case, include several old spectra available in the literature, as described in Section 2. Section 2 also includes the data analysis. Section 3 is devoted to the discussion of the results in the context of BLR structure and kinematics. Finally, the main conclusions are summarized in Section 4.

2. Data Analysis and Results

2.1. Data

We collected from the literature rest-frame UV spectra of lensed quasars obtaining a sample of 26 lensed quasars, of which 11 are observed in (at least) two different epochs. Information about the observations and references is summarized in Table 1.

As mentioned in Section 1, one of the motivations to consider a second-epoch spectroscopy is the possibility of comparing the intensity of a given spectral feature (the wing of the C III] line, for instance) of the same image (A) in two epochs (I and II), to study differences of the type $(A^{I}–A^{II})_{wing(C\ III])}$. This difference is free from extinction or inaccurate macro-modeling effects. However, it is not free from instrumental problems such as slit misalignment or errors in the calibration of the instrumental response with wavelength, which, unfortunately, are likely present in the available data. Thus, we need a nonchanging reference spectral feature to scale the spectra. As a first step (Section 2.2) we consider the usual assumption of single-epoch-based studies that the cores of C IV, C III], and Mg II (defined by the flux within a narrow interval of ±6 Å centered on the peak of the line) arise from a substantially larger area than the wings (∼30 Å wavelength intervals on either side of the emission-line peak) and are consequently little affected by microlensing (see Guerras et al. 2013a, and references therein). Specifically, we start using the cores of the C IV, C III], and Mg II lines as references to study the wings of these lines and other weaker emission lines and blends in the C IV-to-Mg II wavelength range. Next (Section 2.3), we discuss the hypothesis of unchanging cores by studying the variability of the cores of C IV and C III], taking Mg II as reference.

2.2. Variability Taking as Reference the Cores of the C IV, C III], and Mg II Emission Lines

Figure 1 shows, for 11 lens systems with at least two epochs of observation (Table 1), the core-matched spectra in the wavelength regions around the C IV, C III], and Mg II lines (see Appendix A for details about the core-matching analysis). The spectra of 26 lens systems (11 with at least two epochs of observation and 15 with single-epoch spectra), split into two wavelength regions from C IV to C III] and from C III] to Mg II,

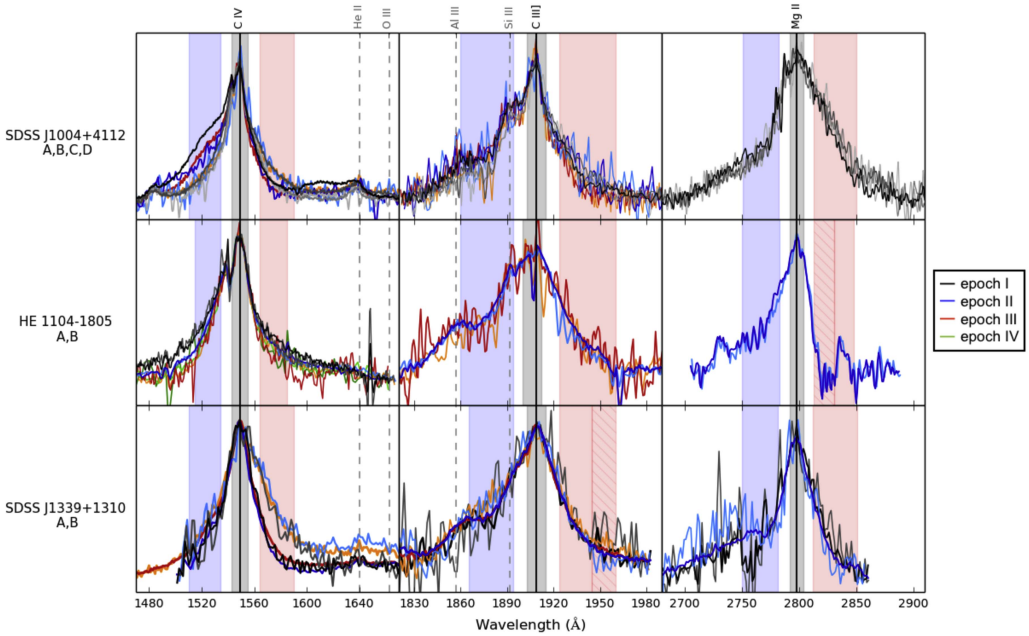

Figure 1. (Continued.)

are shown in Figure 2. Under the assumption that the line core arises from a significantly larger region than the wings, the $(F_{1\mathrm{core}}/F_{2\mathrm{core}})/(F_{1\mathrm{wings}}/F_{2\mathrm{wings}})$ ratio of the line core fluxes of two images, $F_{1\mathrm{core}}/F_{2\mathrm{core}}$, to the line wing fluxes of these two images, $F_{1\mathrm{wings}}/F_{2\mathrm{wings}}$, yields a measurement of the size of the high-velocity wing emission regions. The computed magnitude differences between images with signal-to-noise ratio (S/N) greater than 1.5 (see Appendix A for the details of the computation) are given for each epoch in Tables 2 (C IV, C III], and Mg II) and 4 (other considered emission-line features). Similarly, the magnitude differences between epochs for each image are presented in Tables 3 (C IV, C III], and Mg II) and 5 (other emission-line features). To qualify the magnitude differences between epochs or/and images as candidates for intrinsic variability or microlensing, we have used the following criteria: (i) the S/N should be greater than 2, (ii) any difference between images is considered a candidate for microlensing, (iii) we consider as a candidate for intrinsic variability a difference between two epochs when it is present in at least two images, and (iv) when neither criterion (ii) nor criterion (iii) applies, we consider that we have insufficient information to qualify the difference, although intrinsic variability may be more likely (partial evidence of intrinsic variability). The resulting classification of the differences between spectra corresponding to several emission-line features in the C IV-to-Mg II wavelength range is included in Tables 2, 3, 4, and 5.

The first result that can be inferred from Figures 1–3 as shown in Tables 2–5 is that the Mg II line is weakly affected by either microlensing or intrinsic variability with no significant changes ($S/N \gtrsim 2$) in the selected windows.[11] A similar result can be derived for the C III] line.[12]

In the case of C IV the presence of microlensing or intrinsic variability is more the rule than the exception, particularly in the extreme red wing. In Figure 3 we show the mean+σ spectra of the C IV emission line for each system to emphasize the variability in the wings. There is evidence, at the 2σ level, of intrinsic variability within the defined integration windows in one image of Q0142–100 and in HE 1104–1805. There is also evidence of intrinsic variability in the extreme red wing of C IV, specifically in the shelf-like feature blueward of He II, around λ1610.[13] Microlensing is detected in C IV, at the 2σ level, in the integration windows[14] as defined in Figure 1 and in the shelf-like feature at $\sim\lambda$1610.[15] The origin of this feature is uncertain (e.g., Fine et al. 2010, and references therein). It has been interpreted as an (extreme) C IV red wing or another species. In most of our objects[16] microlensing or intrinsic variability seems to affect, in a more or less smooth way, the whole red wing. However,

[11] Except for a difference between images D and B in the blue wing of HE 0435–1223 at epoch II.
[12] With only two exceptions: B–A at epoch I in HE 0435–1223 and C–B at epoch I in WFI J2033–4723.
[13] In Q0142−100, QSO 0957+561, HE 1104–1805, and HE 2149–2745.
[14] In SDSS J1004+4112, HE 0435−1223, and SDSS J1339+1310.
[15] It may be strongly microlensed ($\gtrsim 2\sigma$) in HE 0435−1223, SDSS J1004+4112, and SDSS J1339+1310.
[16] Q0142−100, HE 0435−1223, QSO 0957+561, HE 1104−1805, and SDSS J1339+1310.

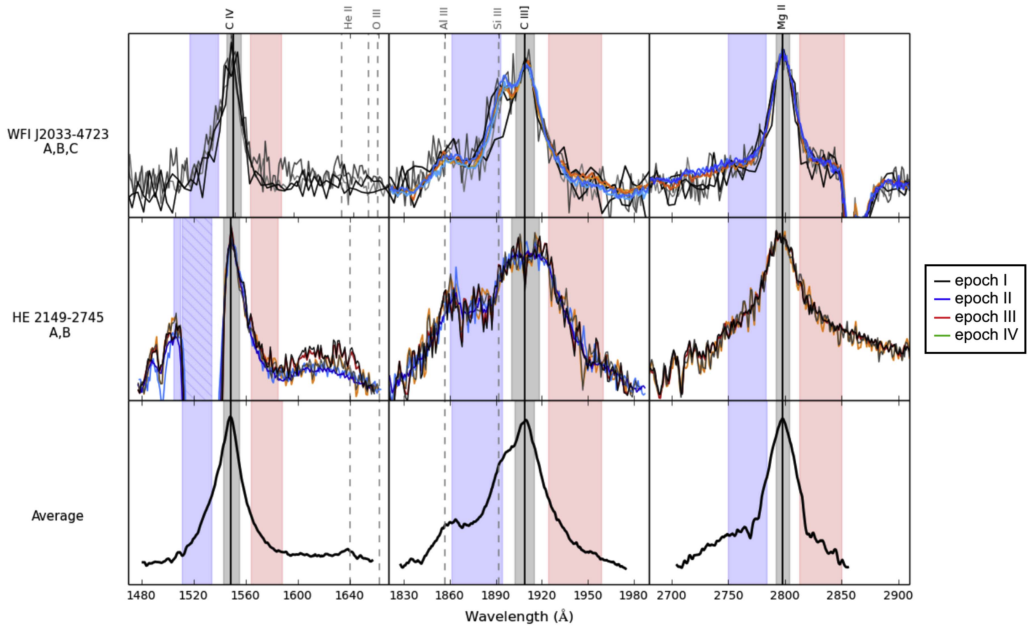

Figure 1. (Continued.)

the absence of a blue counterpart of this feature would need further explanation. On the other hand, in SDSS J1004+4112 (and perhaps HE 2149–2745), a feature at $\sim\lambda1610$ shows up very distinctly, which supports the hypothesis of an unidentified species. Apart from this feature, in the pseudo-continua between C IV and C III] and between C III] and Mg II, there are several lines and blends showing evidence of intrinsic variability and microlensing at the 2σ level (see Appendix B), which very noticeably affect the complex formed by the He II emission line, the O III]/Al II blend, and the underlying pseudo-continuum in the C IV–C III] wavelength range[17] and the Fe II and Fe III blends in the C III]–Mg II range.

According to the criteria explained in Appendix A (see Tables 2–5), we can consistently separate most of the observed systems in terms of intrinsic variability or microlensing. There are four objects clearly dominated by microlensing (SDSS J0806+2006, FBQS J0951+2635, SDSS J1004+4112, and SDSS J1339+1310) and five objects in which intrinsic variability prevails (Q0142–100, HE 1104–1805, WFI J2033–4723, HE 2149–2745, and HE 0047–1756; in the last object there is evidence of microlensing in epoch I). The differences observed in QSO 0957+561 may be explained by intrinsic variability combined with the large time delay between the images of this double, plus a possible contribution from microlensing. Finally, HE 0435–1223 shows both intrinsic variability[18] and microlensing of relatively lower amplitude.[19]

In Figures 4 and 5 we present, for the different species, histograms of microlensing magnification and intrinsic variability. We have overlaid the corresponding Gaussian kernel density estimates of the probability density functions (pdf's) to show the impact of errors in the individual measurements. According to these figures, within the limitations of the size of the sample of lens systems and of the data quality, intrinsic variability and microlensing seem to affect the same spectral features with similar strength. The impact of microlensing (and of intrinsic variability) looks similar for the shelf-like feature at $\sim\lambda1610$, Fe II and III, and significantly smaller for C IV. Comparing with microlensing data of the continuum, we can say that the former features exhibit microlensing values similar to those typical of the optical continuum ($|\Delta m_{\rm opt}| \sim 0.3$ mag; see Jiménez-Vicente et al. 2015) and that, in extreme cases, some spectral features (Fe III $\lambda\lambda2039$–2113, for instance) can undergo microlensing magnifications close to those typical of the X-ray continuum ($|\Delta m_{\rm Xray}| \sim 1$ mag; see Jiménez-Vicente et al. 2015).

Moreover, we obtain rms intrinsic variabilities of the wings with respect to the cores of 18%, 12%, and 15% for the C IV, C III], and Mg II lines, respectively. This implies that the intrinsic variability affects the wings and core with different intensity, and/or that there is a delay between both. This difference is

[17] Other lines in this wavelength range, such as Al III and Si III], are also affected by microlensing, but their study is hampered because they are strongly blended with C III].

[18] Strong in the shelf-like feature at $\sim\lambda1610$, He II, Fe II, and Fe III, and weaker in C IV.

[19] Mainly in B–A (epoch IV in C IV, shelf-like feature at $\lambda1610$ and Fe III).

Table 2
Differences between Images—C IV, C III], and Mg II Lines

Emission Line	Wing	Object	Image Pair	Epoch	$d^a \pm \sigma^b$	d/σ	Classification
C IV	Blue wing	SDSS 1004+4112	B–A	I	0.56 ± 0.16	3.4	Microlensing
				III	0.39 ± 0.07	5.8	Microlensing
			C–A	I	0.69 ± 0.14	4.8	Microlensing
			D–A	I	0.90 ± 0.36	2.5	Microlensing
			C–B	I	0.13 ± 0.06	2.2	Microlensing
	Red wing	HE 0435–1223	B–A	IV	0.20 ± 0.07	2.8	Microlensing
			D–B	IV	−0.12 ± 0.08	1.5	
			D–C	I	−0.39 ± 0.27	1.5	
		SDSS 1004+4112	B–A	I	0.30 ± 0.06	5.1	Microlensing
				II	−0.53 ± 0.31	1.7	
				III	−0.52 ± 0.15	3.6	Microlensing
			C–B	I	0.35 ± 0.10	3.5	Microlensing
			D–B	I	0.40 ± 0.26	1.6	
		SDSS J1339+1310	B–A	III	−0.62 ± 0.15	4.2	Microlensing
C III]	Blue wing	SDSS 1004+4112	C–A	I	0.33 ± 0.18	1.9	
		WFI 2033–4723	C–B	II	0.12 ± 0.06	2.1	Microlensing
	Red wing	HE 0435–1223	B–A	I	0.29 ± 0.14	2.0	Microlensing
			C–A	I	0.29 ± 0.15	1.9	
		HE 1104–1805	B–A	II	0.21 ± 0.14	1.5	
Mg II	Blue wing	HE 0435–1223	D–B	II	0.11 ± 0.04	3.0	Microlensing
	Red wing	HE 0435–1223	D–B	II	−0.27 ± 0.16	1.7	

Notes.
[a] Magnitude difference.
[b] Standard deviation of magnitude difference.

observed in RM studies with resolution in velocity and is the basis for studying the kinematic structure of the BLR (e.g., Bentz et al. 2010; Grier et al. 2017a, and references therein). Typical rms variabilities for C IV and C III] of about 13% ± 9% have been found by Kaspi et al. (2007). For the Mg II line, an rms variability of about 19% ± 3% can be inferred from the reduced sample of sources of Shen et al. (2016). In spite of the reasonable agreement between these quantities and our results, the extent of the comparison is limited by the heterogeneity of the samples (in luminosity, redshift, and timescales) and by the fact that Kaspi et al. (2007) and Shen et al. (2016) are measuring the variability of the whole line.

2.3. Variability of the Cores of the C IV and C III] Emission Lines Taking Mg II as Reference

One important consequence of the previous section is that there is little differential microlensing between the core and wings of Mg II (the same result also applies to the red wing of C III]). This result looks, in principle, consistent with the relatively small range of velocities corresponding to the wings of Mg II (as compared with C IV). However, this conclusion should be regarded with caution for, as we shall see later, the correspondence between velocity channel and microlensing impact is not simple. On the other hand, there are several systems (SDSS J1004+4112 and SDSS J1339+1310, in particular) in which microlensing is strongly affecting the wings of C IV (with respect to the core) without traces of this microlensing in the wings of Mg II. Consequently, it seems very unlikely that microlensing is present in Mg II but does affect the core and the wings with the same strength. Thus, it is reasonable to assume that the entire Mg II line is weakly sensitive to microlensing and to use this line as a reference to match the spectra of an image at different epochs. Therefore, we circumvent the problems originating from inaccuracies in the alignment of the slit and in the calibration of the spectra, and thus we obtain a measurement of intrinsic variability unaffected by extinction or macro-magnification modeling.

2.3.1. Core Microlensing

Let us start the core microlensing study (taking Mg II as reference) by computing, for each available epoch, differences of the type $(B–A)_{core(C\ III])} - (B–A)_{core(Mg\ II)}$, which we expect to be less affected by instrumental and calibration problems. In principle, this difference is sensitive to the differential microlensing between the cores of both emission lines, to differential extinction, and to differences in intrinsic variability between both lines during the time delay between A and B. If we assume that the Mg II line is fairly insensitive to

Table 3
Differences between Epochs—C IV, C III], and Mg II Lines

Emission Line	Wing	Object	Image	Epoch	$d^a \pm \sigma^b$	d/σ	Classification
C IV	Blue wing	Q0142–100	A	II–I	−0.07 ± 0.05	1.5	
		SDSS 1004+4112	A	II–I	0.28 ± 0.07	4.1	Microlensing Variability
				III–I	0.18 ± 0.04	4.2	Microlensing Variability
				III–II	−0.10 ± 0.06	1.5	
		HE 1104–1805	A	II–I	0.14 ± 0.08	1.7	
				III–I	0.26 ± 0.14	1.9	
				IV–I	0.28 ± 0.15	1.9	
				IV–II	0.19 ± 0.10	1.9	
			B	II–I	0.18 ± 0.11	1.6	
				III–I	0.36 ± 0.21	1.8	
				IV–I	0.22 ± 0.15	1.5	
				III–II	0.19 ± 0.11	1.7	
	Red wing	Q0142–100	A	II–I	−0.20 ± 0.08	2.5	Intrinsic Variability?
		HE 0435–1223	C	III–I	−0.49 ± 0.34	1.5	
		SDSS 1004+4112	A	III–I	0.26 ± 0.08	3.1	Microlensing Variability
		HE 1104–1805	A	II–I	0.14 ± 0.06	2.1	Intrinsic Variability
				IV–II	0.11 ± 0.04	2.7	Intrinsic Variability?
			B	IV–I	0.43 ± 0.20	2.2	Intrinsic Variability
				IV–II	0.35 ± 0.19	1.8	
				IV–III	0.26 ± 0.16	1.7	
C III]	Red wing	HE 0047–1756	A	III–II	−0.30 ± 0.20	1.5	
Mg II	Blue wing	HE 0435–1223	A	IV–III	−0.12 ± 0.08	1.5	
			D	III–II	−0.21 ± 0.11	1.9	
				IV–III	−0.20 ± 0.12	1.6	
		FBQ 0951+2635	A	II–I	−0.11 ± 0.07	1.5	
		WFI 2033–4723	C	III–II	0.12 ± 0.07	1.6	
	Red wing	HE 0435–1223	D	IV–III	−0.37 ± 0.23	1.6	

Notes.
[a] Magnitude difference.
[b] Standard deviation of magnitude difference.

microlensing, this difference basically measures extinction and the impact of microlensing in the C III] core. The average of the absolute value of these differences is 0.09 ± 0.08 mag (68% confidence interval), indicating that there is little differential microlensing between C III] and Mg II (as shown in Table 6).

We repeat the same calculation for the C IV core but now using the core of C III] as reference, $(B–A)_{\mathrm{core(C\ IV)}} - (B–A)_{\mathrm{core(C\ III])}}$, in order to prevent the larger extinction impact of a direct comparison with Mg II, obtaining a mean value for the absolute differences of 0.12 ± 0.11 mag (68% confidence interval; see Table 6). Taking into account that the typical rms uncertainty in the determination of a single B–A difference is around 0.05 mag and other possible sources of uncertainty of the matching process, we can conclude that microlensing should have, on average, little impact in the cores of Mg II, C III], and C IV lines.[20] However, it is important to notice that in the two strongest cases of microlensing in the C IV line, if we match the C III] lines, the core of C IV is affected by microlensing with maximum amplitudes of 0.23 ± 0.07 mag (SDSS J1004+4112) and 0.16 ± 0.03 mag (SDSS J1339+1310).

[20] For the same reason, differential extinction may have on average only a marginal impact between Mg II and C III] and between C III] and C IV, although it is clear that extinction can play an important role in some of the outliers in the histograms of core microlensing (not shown here).

2.3.2. Core Intrinsic Variability

We can now try to compare a given image in two different epochs by computing the differences $(A^I–A^{II})_{\mathrm{core(C\ III])}} - (A^I–A^{II})_{\mathrm{core(Mg\ II)}}$ or $(A^I–A^{II})_{\mathrm{core(C\ IV])}} - (A^I–A^{II})_{\mathrm{core(Mg\ II)}}$. These types of quantities are supposed to be free from extinction and are affected by intrinsic variability and microlensing. After our previous conclusion about the low impact of microlensing in the cores of C IV, C III], and Mg II, we can reasonably think that they will mainly measure intrinsic variability. These quantities can nevertheless be strongly affected by uncertainties in the calibration of the spectral response at two different epochs. We have computed the absolute values of the differences between the cores of C III] (with respect to Mg II) and C IV (with respect to C III]) to obtain averages of 0.24 ± 0.21 mag and 0.29 ± 0.25 mag for the C III] and C IV cores, respectively (see Table 7). The scatter is

Table 4
Differences between Images—Other Emission-line Features

Emission Line	Object	Image Pair	Epoch	$d^a \pm \sigma^b$	d/σ	Classification
Red shelf λλ1580–1620	HE 0435–1223	B–A	IV	0.25 ± 0.08	3.3	Microlensing
		C–A	IV	0.14 ± 0.08	1.7	
		D–B	IV	−0.17 ± 0.06	2.9	Microlensing
	QSO 0957+561	B–A	I	−0.37 ± 0.24	1.6	
	SDSS J1004+4112	C–A	I	0.68 ± 0.34	2.0	Microlensing
		D–A	I	0.58 ± 0.23	2.5	Microlensing
		C–B	I	0.51 ± 0.11	4.6	Microlensing
	HE 1104–1805	B–A	I	0.15 ± 0.10	1.5	
	SDSS 1339+1310	B–A	I	−0.89 ± 0.48	1.9	
			II	1.53 ± 0.29	5.2	Microlensing
			III	−0.77 ± 0.09	8.8	Microlensing
Fe III λλ1978–2018	FBQS J0951+2635	B–A	I	−1.11 ± 0.43	2.6	Microlensing
	QSO 0957+561	B–A	II	−0.43 ± 0.11	3.9	Microlensing or intrinsic variability + $\Delta\tau$
	SDSS 1339+1310	B–A	I	−1.05 ± 0.71	1.5	
			II	−0.97 ± 0.56	1.7	
Fe III λλ2039–2113	QSO 0957+561	B–A	II	0.40 ± 0.10	3.2	Microlensing or intrinsic variability + $\Delta\tau$
	SDSS J1004+4112	C–A	I	1.29 ± 0.85	1.5	
	SDSS 1339+1310	B–A	I	−0.96 ± 0.29	3.3	Microlensing
			II	−0.74 ± 0.37	2.0	Microlensing
Fe III λλ2386–2449	HE 0047–1756	B–A	II	−0.11 ± 0.07	1.6	
	HE 0435–1223	B–A	IV	−0.27 ± 0.13	2.1	Microlensing
		C–A	III	−0.25 ± 0.16	1.6	
		D–A	III	0.19 ± 0.12	1.5	
		C–B	IV	0.29 ± 0.16	1.8	
		D–B	IV	0.28 ± 0.14	1.9	
		D–C	III	0.43 ± 0.23	1.9	
	SDSS J0806+2006	B–A	I	−0.68 ± 0.24	2.8	Microlensing
	FBQS J0951+2635	B–A	II	−0.19 ± 0.12	1.6	
	SDSS 1339+1310	B–A	I	−0.42 ± 0.24	1.7	
			II	−0.30 ± 0.12	2.5	Microlensing
Fe II λλ2158–2197	FBQS J0951+2635	B–A	II	−0.70 ± 0.27	2.6	Microlensing
	QSO 0957+561	B–A	II	0.37 ± 0.18	2.0	Microlensing or intrinsic variability + $\Delta\tau$
	SDSS 1339+1310	B–A	I	−1.24 ± 0.27	4.6	Microlensing
			II	−1.13 ± 0.72	1.6	
Fe II λλ2209–2239	SDSS 1339+1310	B–A	I	−1.62 ± 0.81	2.0	Microlensing
Fe II λλ2261–2364	HE 0435–1223	D–C	III	−0.23 ± 0.15	1.5	
	FBQS J0951+2635	B–A	I	−0.66 ± 0.37	1.8	
	SDSS 1339+1310	B–A	I	−0.86 ± 0.30	2.9	Microlensing
			II	−0.46 ± 0.20	2.3	Microlensing
Fe II λλ2460–2564	HE 0047–1756	B–A	I	−0.12 ± 0.08	1.6	
	HE 0435–1223	B–A	IV	−0.33 ± 0.29	1.6	
		C–A	III	−0.29 ± 0.12	2.5	Microlensing

Table 4
(Continued)

Emission Line	Object	Image Pair	Epoch	$d^a \pm \sigma^b$	d/σ	Classification
		D–A	III	0.17 ± 0.11	1.5	
		C–B	IV	0.33 ± 0.22	1.5	
		D–C	III	0.47 ± 0.13	3.6	Microlensing
	SDSS J0806+2006	B–A	I	−0.72 ± 0.21	3.4	Microlensing
	FBQS J0951+2635	B–A	II	−0.20 ± 0.09	2.2	Microlensing
	SDSS 1339+1310	B–A	I	−0.16 ± 0.10	1.6	
Fe II λλ2596–2645	HE 0435–1223	B–A	I	1.28 ± 0.80	1.6	
		C–B	I	−1.04 ± 0.68	1.5	
	FBQS J0951+2635	B–A	II	−0.27 ± 0.17	1.6	
	SDSS J1004+4112	B–A	I	−0.70 ± 0.38	1.9	

Notes.
[a] Magnitude difference.
[b] Standard deviation of magnitude difference.

too high to establish any reasonable comparison with other measurements. Nevertheless, we should take into account that, owing to the heterogeneity of the instrumentation used to obtain the data, errors of 20% in the spectral response in the observed wavelength range cannot be discarded. Therefore, we cannot be sure about the real impact of intrinsic variability on the cores, and the above values should be interpreted as upper bounds.

As a consequence of the analysis of this section, the microlensing results of Section 2.2 based on the hypothesis of core matching in a given epoch are reliable, whereas it cannot be excluded that the results concerning intrinsic variability of the wings might be somewhat affected by core intrinsic variability.

2.4. Microlensing Variability

We have identified differences in a given image between two epochs that can be consistently attributed to microlensing variability in the four systems dominated by microlensing (SDSS J0806+2006, FBQS J0951+2635, SDSS J1004+4112, SDSS J1339+1310) and, at a lower amplitude, in HE 0435–1223. In all these systems, microlensing variability is clearly noticeable in several Fe III and Fe II blends. The well-studied case of SDSS J1004+4112 (Richards et al. 2004; Gómez-Álvarez et al. 2006; Motta et al. 2012; Fian et al. 2016, and references therein) presents outstanding examples of variability induced by microlensing in all the high-ionization lines. Note the high asymmetry of the effect, dominant in the blue part of the lines (see Figure 2). In contrast, in SDSS J1339+1310 the enhancement of C IV is clearly asymmetrical toward the red. From Mosquera & Kochanek (2011), we derived the effective transverse velocity for SDSS J1004+4112 and SDSS J1339+1310 and made two rough estimates of the distance moved by the accretion disk relative to the magnification pattern during the time elapsed between epochs of observation (∼1 yr in SDSS J1339+1310 and ∼5 yr in SDSS J1004+4112). For SDSS J1339+1310 the distance traveled in the source plane is too small (less than 0.6 lt-day) to see variability in both wings. In SDSS J1004+4112 we have obtained more interesting results, owing to a larger displacement of the source (∼4 lt-day), leading to variations in both wings. If we compare epochs I and II, we can see that the magnified blue wing fades while the red wing enhances. This supports that the separation between the approaching and receding parts of the microlensed region of the BLR is of about a few light-days.

In several cases, mainly affecting the shelf-like feature at ∼λ1610 and several blends of Fe II and Fe III, the impact of microlensing and microlensing variability (see Tables 2–5) is $|\Delta m| \gtrsim 1$ mag, comparable to the typical microlensing magnification amplitudes observed in the X-ray continuum.

It is important to notice that the spectral features mainly affected by intrinsic variability are also the C IV wings, some blends of Fe II and Fe III, and the shelf-like feature at ∼λ1610. In contrast with microlensing, we have not observed marked asymmetries induced by intrinsic variability in the line profiles. This result supports (within the statistical significance of our relatively limited sample) the hypothesis that the small region sensitive to microlensing is not systematically affected by extinction, beaming, or any other mechanism that may selectively enhance one part of it. Consequently, the asymmetric enhancements observed, in either the blue or red parts of microlensed line profiles, likely originate from an anisotropic distribution of microlensing magnification in the source plane.

3. Discussion

3.1. Microlensing and Kinematics

The main result of the previous sections is that the cores of C IV, C III], and Mg II and the wings of the last two lines are only weakly affected by microlensing. However, the wings of C IV can be strongly affected. In other high-ionization emission-line features, such as the Fe III λλ2039–2113 blend and the shelf-like feature at ∼λ1610, the whole feature may be globally affected by high-magnification microlensing.

To discuss these results with more detailed kinematic information than the separation between core and wings, in Figure 6 we have overlapped the averaged line profiles corresponding to C IV, C III], Mg II, and Fe III λλ2039–2113.

Table 5
Differences between Epochs—Other Emission-line Features

Emission Line	Object	Image	Epoch	$d^a \pm \sigma^b$	d/σ	Classification
Red shelf λλ1580–1620	Q0142–100	A	II–I	−0.36 ± 0.08	4.5	Intrinsic variability?
	HE 0435–1223	A	III–I	−0.99 ± 0.52	1.9	
			IV–III	−0.32 ± 0.12	2.6	Microlensing variability
		B	IV–I	−0.48 ± 0.32	1.5	
		C	IV–I	−0.90 ± 0.60	1.5	
		D	IV–I	−0.50 ± 0.30	1.6	
	QSO 0957+561	A	II–I	0.50 ± 0.21	2.4	Intrinsic variability?
		B	II–I	0.93 ± 0.55	1.7	
	SDSS J1004+4112	A	II–I	0.33 ± 0.18	1.9	
			III–I	0.44 ± 0.08	5.4	Microlensing variability
	HE 1104–1805	A	III–I	1.19 ± 0.67	1.8	
			IV–I	0.33 ± 0.08	4.3	Intrinsic variability?
			III–II	1.24 ± 0.81	1.5	
			IV–II	0.24 ± 0.08	2.9	Intrinsic variability?
	SDSS 1339+1310	A	III–II	0.68 ± 0.24	2.8	Microlensing variability
	HE 2149–2745	A	II–I	0.52 ± 0.18	2.9	Intrinsic variability?
			III–II	−0.51 ± 0.16	3.2	Intrinsic variability?
		B	II–I	0.28 ± 0.19	1.5	
Fe II λλ1705–1730	HE 1104–1805	B	IV–III	−0.70 ± 0.53	1.5	
	SDSS 1339+1310	A	III–I	1.24 ± 0.85	1.5	
		B	III–I	1.28 ± 0.74	1.7	
Fe II λλ1760–1800	Q0142–100	A	II–I	−1.17 ± 0.62	1.9	
Fe III λλ1978–2018	QSO 0957+561	A	II–I	0.97 ± 0.55	1.8	
	HE 1104–1805	A	III–II	−0.73 ± 0.40	1.8	
	SDSS 1339+1310	B	II–I	1.02 ± 0.67	1.5	
Fe III λλ2039–2113	QSO 0957+561	A	II–I	1.30 ± 0.67	1.9	
		B	II–I	1.70 ± 0.89	1.9	
Fe III λλ2386–2449	HE 0047–1756	A	II–I	−0.82 ± 0.08	10.4	Intrinsic variability
		B	II–I	−0.97 ± 0.12	8.4	Intrinsic variability
	HE 0435–1223	A	IV–III	0.43 ± 0.17	2.6	Intrinsic variability
		B	IV–I	−0.39 ± 0.17	2.4	Microlensing variability
		C	III–I	−0.58 ± 0.28	2.1	Intrinsic variability?
			IV–III	0.70 ± 0.16	4.4	Intrinsic variability
	SDSS J0806+2006	B	II–I	0.78 ± 0.40	2.0	Microlensing variability
	SDSS J1004+4112	A	III–I	−0.43 ± 0.20	2.2	Microlensing variability?
	WFI J2033–4723	B	II–I	−0.25 ± 0.13	2.0	Intrinsic variability
		C	II–I	−0.31 ± 0.11	2.7	Intrinsic variability
	HE 2149–2745	B	II–I	0.26 ± 0.13	2.0	Intrinsic variability?
			III–II	−0.28 ± 0.12	2.4	Intrinsic variability?
Fe II λλ2158–2197	QSO 0957+561	B	II–I	1.13 ± 0.73	1.6	
Fe II λλ2209–2239	HE 0435–1223	C	IV–I	0.69 ± 0.42	1.7	
			IV–III	1.34 ± 0.86	1.6	
		D	III–II	−1.14 ± 0.53	2.1	Intrinsic variability?

Table 5
(Continued)

Emission Line	Object	Image	Epoch	$d^a \pm \sigma^b$	d/σ	Classification
Fe II λλ2261–2364	HE 0047–1756	A	II–I	−0.46 ± 0.13	3.5	Intrinsic variability?
		B	II–I	−0.71 ± 0.46	1.5	
	HE 0435–1223	A	IV–I	0.75 ± 0.46	1.6	
			IV–III	0.88 ± 0.41	2.1	Intrinsic variability
		C	IV–III	0.84 ± 0.34	2.5	Intrinsic variability
		D	III–II	−0.60 ± 0.22	2.8	Intrinsic variability?
			IV–III	1.09 ± 0.54	2.0	Intrinsic variability
	FBQS J0951+2635	B	II–I	0.52 ± 0.24	2.2	Microlensing variability
Fe II λλ2460–2564	HE 0047–1756	A	II–I	−0.74 ± 0.07	11.3	Intrinsic variability
		B	II–I	−0.87 ± 0.08	10.5	Intrinsic variability
	HE 0435–1223	A	IV–I	0.49 ± 0.32	1.5	
			IV–III	0.65 ± 0.21	3.1	Intrinsic variability
		C	III–I	−0.57 ± 0.24	2.4	Microlensing variability
			IV–III	0.95 ± 0.20	4.7	Intrinsic variability
		D	IV–II	0.44 ± 0.28	1.6	
	SDSS J0806+2006	A	II–I	0.61 ± 0.31	1.9	
	FBQS J0951+2635	A	II–I	−0.19 ± 0.12	1.5	
		B	II–I	−0.27 ± 0.18	1.5	
	SDSS 1339+1310	A	II–I	−0.30 ± 0.19	1.6	
	WFI J2033–4723	C	II–I	−0.24 ± 0.10	2.5	Intrinsic variability?
	HE 2149–2745	A	II–I	0.28 ± 0.09	3.0	Intrinsic variability
			III–II	−0.29 ± 0.09	3.3	Intrinsic variability
		B	II–I	0.37 ± 0.15	2.5	Intrinsic variability
			III–II	−0.38 ± 0.16	2.4	Intrinsic variability
Fe II λλ2596–2645	HE 0047–1756	A	II–I	−0.68 ± 0.17	4.0	Intrinsic variability
		B	II–I	−0.82 ± 0.22	3.7	Intrinsic variability
	HE 0435–1223	A	IV–I	1.40 ± 0.77	1.8	
			IV–III	1.34 ± 0.78	1.7	
		B	IV–II	0.98 ± 0.47	2.1	Intrinsic variability
		C	IV–III	1.28 ± 0.71	1.8	
		D	IV–II	1.16 ± 0.43	2.7	Intrinsic variability
			IV–III	0.97 ± 0.57	1.7	

Notes.
[a] Magnitude difference.
[b] Standard deviation of magnitude difference.

The wings of Mg II correspond to relatively low velocities as compared with other lines. This is consistent with the weak impact of microlensing on this line. Regarding C III] and C IV, the red parts of these lines match very well, except at the lowest intensity level, where the shelf-like feature at ∼λ1610 is present in C IV (the blue side of C III] is blended with Al III, Si III, and Fe II, and no reasonable comparison can be made). In spite of this remarkable kinematic coincidence, the C IV line can be strongly affected by microlensing, whereas C III] seems to be rather insensitive to this effect (see, e.g., the cases of SDSS J1004+4112 and SDSS J1339+1310). In addition, they have a different degree of ionization (C IV is of high ionization and C III] of low ionization). These results suggest that both lines are mostly generated in the same region, but that there is also a contribution, exclusive to the C IV line, from emitters located in a region small enough to be strongly affected by microlensing. As far as a zero-velocity contribution from the emitters in this region can be expected, the core of the C IV line may also undergo some microlensing at a lower level of amplitude, compatible with our results in Section 2.3.2 (about 20% of microlensing magnification in the cores of SDSS J1004+4112 and SDSS J1339+1310).

Table 6
Core Differences between Images

Object	Image Pair	Epoch	C IV		C III	
			$d^a \pm \sigma^b$	d/σ	$d^a \pm \sigma^b$	d/σ
HE 0047–1756	B–A	I	−0.08 ± 0.03	1.1	...	...
		II	...	...	−0.01 ± 0.01	1.2
		III	...	...	0.01 ± 0.04	0.4
Q0142–100	B–A	I	0.03 ± 0.03	1.1	...	...
		II	0.05 ± 0.02	2.2	...	...
HE 0435–1223	B–A	I	−0.07 ± 0.04	1.7	...	...
		IV	−0.34 ± 0.03	12.3	0.09 ± 0.02	4.1
	C–A	I	0.02 ± 0.07	0.3	...	...
		III	−0.08 ± 0.04	2.0	0.08 ± 0.04	2.1
		IV	0.05 ± 0.04	1.2	0.14 ± 0.02	7.2
	D–A	I	−0.09 ± 0.03	2.7	...	...
		III	0.08 ± 0.07	1.2	−0.19 ± 0.07	2.9
		IV	−0.39 ± 0.03	13.2	0.07 ± 0.05	1.4
	C–B	I	0.08 ± 0.08	1.0	...	...
		IV	0.38 ± 0.04	10.8	0.06 ± 0.02	3.3
	D–B	I	−0.03 ± 0.05	0.6	...	...
		II	...	...	0.03 ± 0.03	1.2
		IV	−0.05 ± 0.03	1.5	−0.01 ± 0.03	0.3
	D–C	I	−0.11 ± 0.03	3.2	...	...
		III	0.16 ± 0.09	1.8	−0.26 ± 0.08	3.5
		IV	−0.44 ± 0.02	19.6	−0.07 ± 0.04	1.8
SDSS J0806+2006	B–A	I	...	...	−0.23 ± 0.03	7.5
		II	...	...	−0.02 ± 0.05	0.3
FBQS J0951+2635	B–A	I	...	...	0.25 ± 0.08	3.3
QSO 0957+561	B–A	I	−0.09 ± 0.05	2.0	0.10 ± 0.02	5.3
		II	0.08 ± 0.07	1.1	0.14 ± 0.04	3.3
SDSS J1004+4112	B–A	I	0.06 ± 0.02	2.5	0.11 ± 0.03	3.4
		II	0.17 ± 0.06	2.6	...	...
		III	0.10 ± 0.04	2.3	0.00 ± 0.03	0.1
	C–A	I	0.05 ± 0.04	1.1	0.18 ± 0.13	1.4
	D–A	I	0.13 ± 0.03	4.8	0.19 ± 0.04	4.6
	C–B	I	−0.01 ± 0.05	0.3	0.07 ± 0.13	0.5
	D–B	I	0.08 ± 0.03	2.5	0.07 ± 0.05	1.4
	D–C	I	0.10 ± 0.03	3.5	0.00 ± 0.12	0.0
HE 1104–1805	B–A	I	0.06 ± 0.02	3.0	...	...
		II	0.01 ± 0.02	0.07	−0.13 ± 0.14	1.0
		III	−0.08 ± 0.03	2.6	...	...
		IV	−0.14 ± 0.02	7.7	...	...
SDSS 1339+1310	B–A	I	−0.35 ± 0.04	9.9	−0.06 ± 0.07	0.9
		II	−0.33 ± 0.06	5.2	−0.13 ± 0.02	5.5
		III	−0.20 ± 0.03	8.1	...	...
WFI J2033–4723	A2–A1	I	−0.10 ± 0.16	0.6	...	...
	B–A1	I	−0.26 ± 0.10	2.5	...	...
	B–A2	I	−0.21 ± 0.11	1.9	...	...
	C–A1	I	−0.16 ± 0.10	1.7	...	...
	C–A2	I	−0.11 ± 0.12	1.0	...	...
	C–B	I	0.08 ± 0.14	0.5	...	...
		II	...	...	0.03 ± 0.02	1.1
		III	...	...	0.03 ± 0.02	1.4
HE 2149–2745	B–A	I	0.04 ± 0.04	0.9	−0.01 ± 0.03	0.3
		II	−0.03 ± 0.04	0.8	0.03 ± 0.03	0.9
		III	0.03 ± 0.05	0.6	0.00 ± 0.04	0.0

Notes.
[a] Magnitude difference.
[b] Standard deviation of magnitude difference.

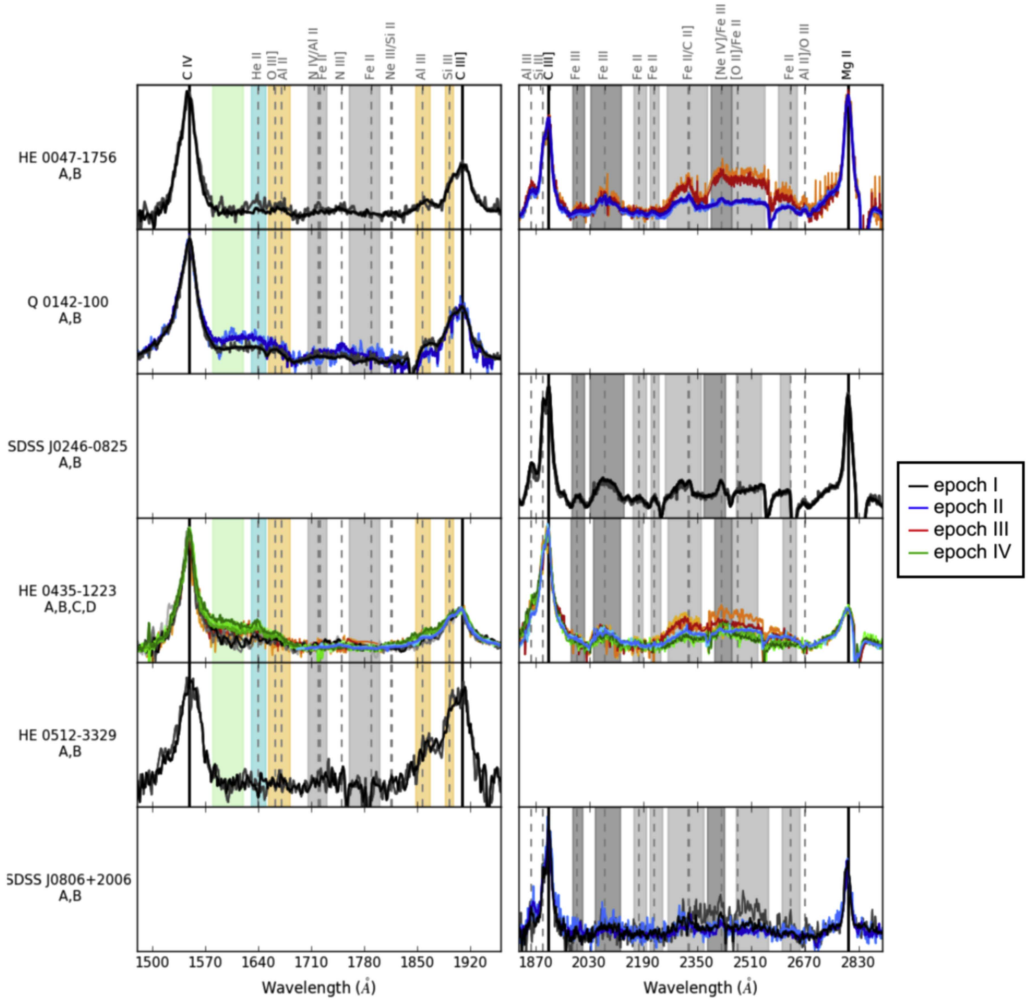

Figure 2. Wavelength regions between C IV, C III], and Mg II from different epochs superimposed after continuum subtraction, matching the line cores and extinction correction. Different colors correspond to different epochs, and different color shadings stand for different images in the corresponding epoch. Shaded regions of different color show the integration windows used for the magnitude difference calculation of different emission-line features. The ordinate is in arbitrary units of flux.

Even if Fe III $\lambda\lambda$2039–2113 is the iron spectral feature least contaminated by other species, it is still a blend of many Fe III single emission lines (Vestergaard & Wilkes 2001), and its kinematic interpretation is not straightforward. A simple fit to the blend of the average spectrum based on the sum of Gaussians of the same FWHM (considering the nominal wavelengths and strengths of the single Fe III lines of this blend; Vestergaard & Wilkes 2001) results in a kinematic FWHM of about 9400 km s^{-1}, significantly greater than that corresponding to C IV. In addition, the strength of microlensing in the Fe III $\lambda\lambda$2039–2113 blend can, in some cases, be greater than in the optical continuum, comparable even to that of the X-ray regions.

In Figure 7 we represent the average amplitude of microlensing with respect to the line broadening for Fe III, C IV, C III], and Mg II. There is a global trend relating high microlensing with line broadening. Notice the high differential microlensing of C IV with respect to C III], even when both lines have close FWHMs, revealing the existence of the small region prone to microlensing not contributing to C III].

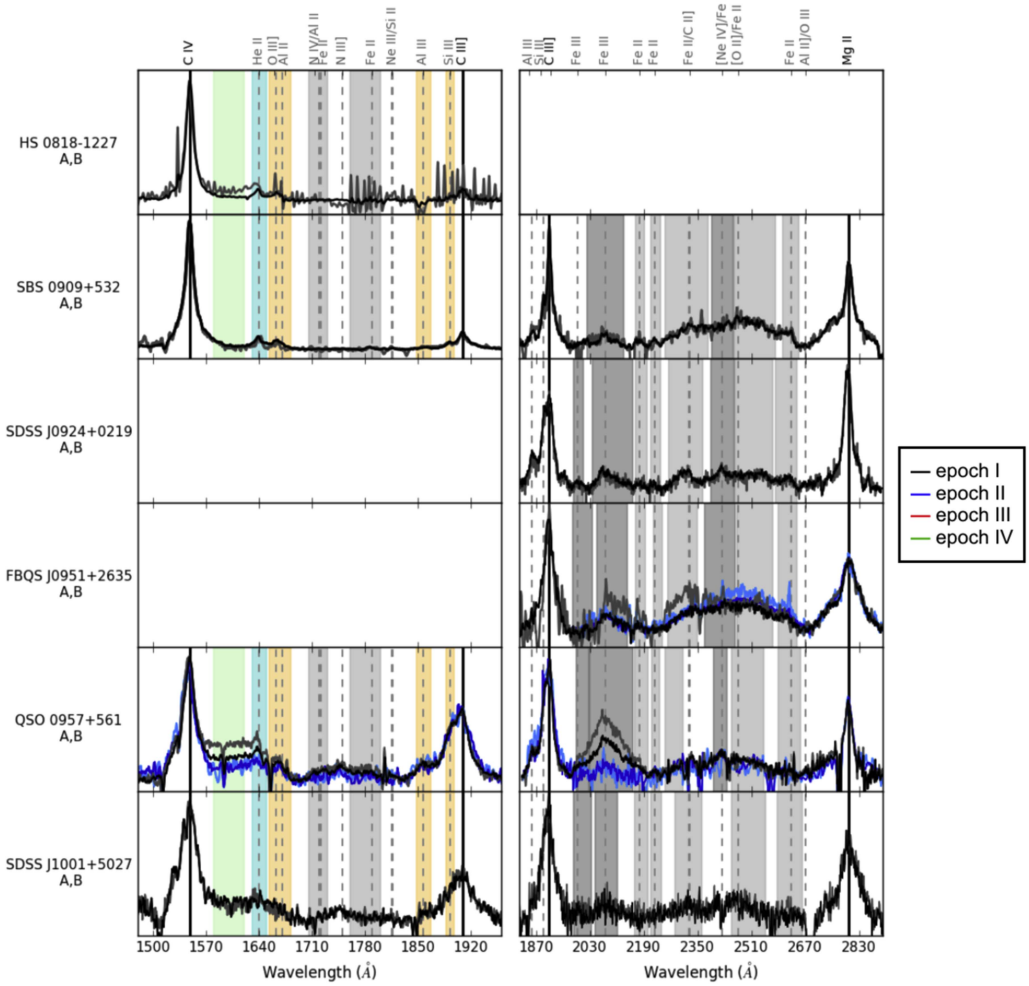

Figure 2. (Continued.)

3.2. Microlensing and Size

Single-epoch microlensing measurements can be used to estimate (or constrain) the size of the emitting regions (e.g., Guerras et al. 2013a). For the size calculations we will treat each event as a single-epoch event. From the microlensing magnification corresponding to all the lens image pairs with more than one epoch of observation we compute the joint microlensing probability, $P(r_s)$, of obtaining an average estimate of the size, following the steps described in Guerras et al. (2013a),

$$P(r_s) = \prod_i P_i(r_s), \quad (1)$$

$$P_i(r_s) \propto e^{-\frac{\chi_i^2(r_s)}{2}}, \quad (2)$$

$$\chi_i^2(r_s) = \sum_{\alpha_i} \sum_{\beta_i < \alpha_i} \left(\frac{\Delta m^{\rm obs}_{\beta_i \alpha_i} - \Delta m_{\beta_i \alpha_i}(r_s)}{\sigma_{\beta_i \alpha_i}} \right)^2, \quad (3)$$

where $\Delta m^{\rm obs}_{\beta_i \alpha_i}$ is the observed differential microlensing magnification between images α and β of system i and $\Delta m_{\beta_i \alpha_i}(r_s)$ is the differential microlensing magnification predicted by the simulations for a given value of r_s. The simulations are based on 3000×3000 pixel magnification maps, spanning 600×600 lt-day^2 on the source plane, obtained using the Inverse

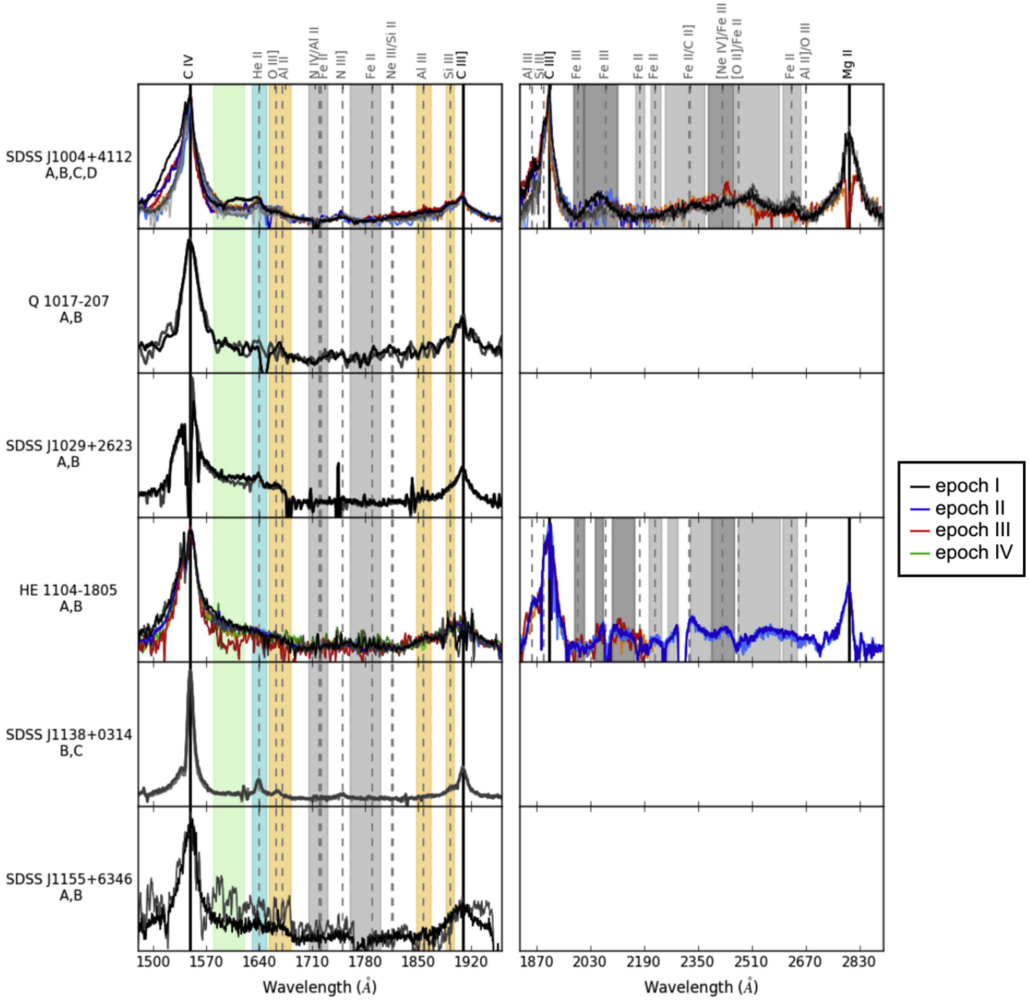

Figure 2. (Continued.)

Polygon Mapping method (Mediavilla et al. 2006, 2011). The general characteristics of the magnification maps are determined (for each quasar image) by the local convergence κ and the local shear γ, which were obtained by fitting a singular isothermal sphere with an external shear (SIS+γ_e) that reproduce the coordinates of the images (Mediavilla et al. 2006). We have assumed a mean stellar mass of $0.3\,M_{\odot}$. To simulate the effect of the finite source, we have convolved the magnification maps with 2D Gaussian profiles of sigma r_s, logarithmically spanning an interval between 0.2 and 120 lt-day. Sizes are converted to half-light radius multiplying by 1.18, $R_{1/2} = 1.18\,r_s$.

The resulting joint likelihood function can be seen in Figure 8. From Figure 8 we can estimate a size for the region emitting the low-ionization emission of $50.3^{+30.4}_{-14.0}$ $\sqrt{M/0.3\,M_{\odot}}$ lt-day. This result is in good agreement with the estimates by Guerras et al. (2013a). It is also in agreement, within the uncertainties, with the RM size estimates for Mg II of the two SDSS-RM sources of highest luminosity in the comparatively low luminosity sample of Shen et al. (2016) (object 101, $\tau = 36.7^{+10.4}_{-4.8}$ days; object 589, $\tau = 34.0^{+6.0}_{-12.7}$ days). Finally, our measurement matches very well the Bentz et al. (2013) size–luminosity relation based on Hβ RM.

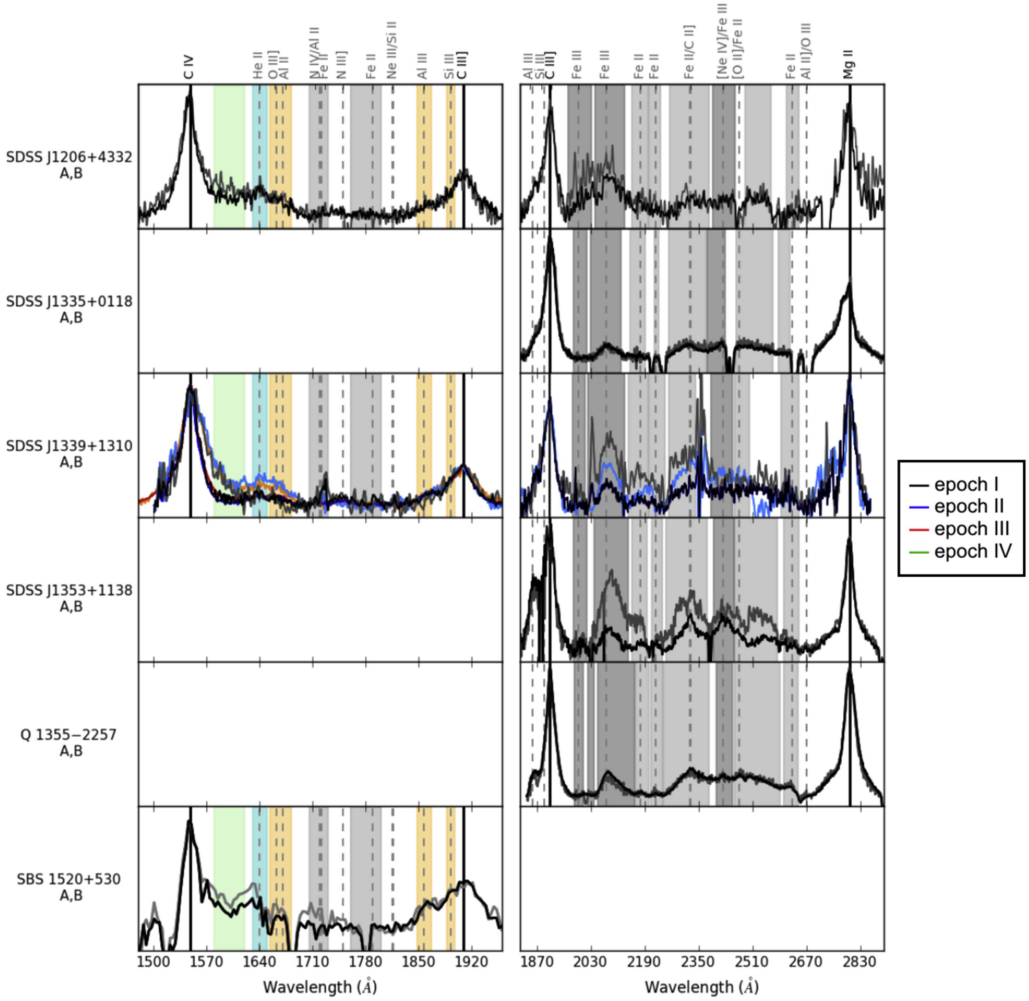

Figure 2. (Continued.)

In principle, we could now repeat the same procedure with the high-ionization lines, starting with C IV. However, from our previous kinematic analysis, we know that the C IV microlensed line profile is likely a combination of emission coming from the large region weakly sensitive to microlensing, where C III] and Mg II originate, and from another small region that shows up in the line profile only when microlensing is present. Moreover, we can suspect that the proportion of the contributions from the two regions to the line profile changes with wavelength. Thus, we should refine the previous approach taken in Guerras et al. (2013a, 2013b), in which the core and wings were supposed to come exclusively from one of the regions. Instead of this approach, which is complex and needs some modeling (we defer it to future work), we are going to suppose that the spectral features with the highest microlensing magnification arise exclusively from the small region susceptible of microlensing. From the likelihood function corresponding to the observed microlensing (see Figure 9) we infer (using a logarithmic prior for the size) a size of $4.1^{+0.8}_{-0.8}\sqrt{M/0.3\,M_{\odot}}$ lt-day for the $\sim\lambda1610$ feature at the red shelf of C IV, comparable to the optical continuum. In Figure 10 we show the pdf's corresponding to three different blends of Fe III ($\lambda\lambda1978$–2018, $\lambda\lambda2039$–2113, and $\lambda\lambda2386$–2449). The

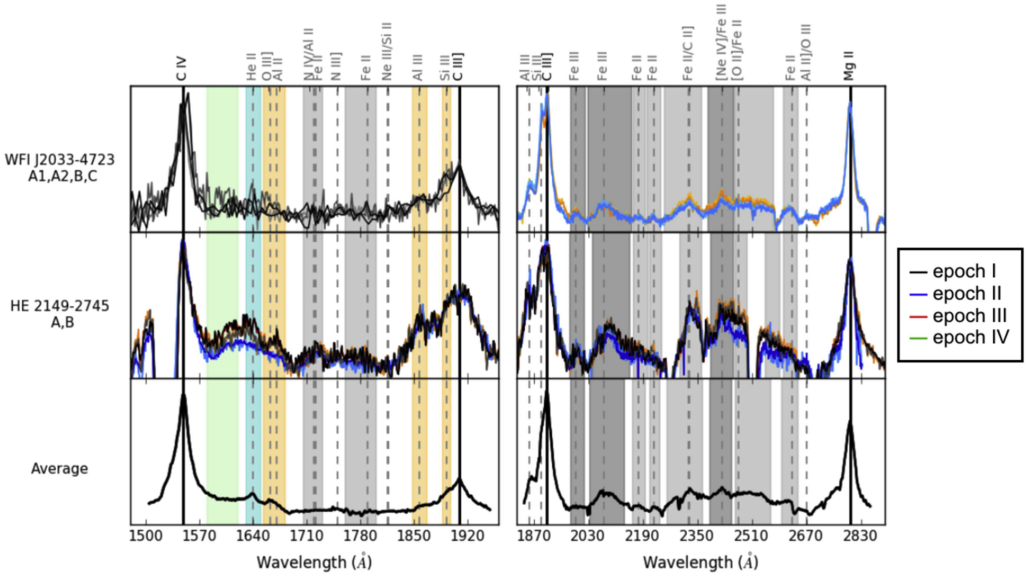

Figure 2. (Continued.)

estimated average size, $11.3^{+5.0}_{-4.0}\sqrt{M/0.3\,M_{\odot}}$ lt-day, is consistent within the errors with the sizes measured for the red shelf feature at $\sim\lambda1610$. Actually, the highest microlensing values are measured in Fe III, but the presence of several systems with low microlensing amplitudes in the subsample of systems with more than one epoch of observation (used to compute the pdf's) has made slightly larger the size of Fe III. We obtain slightly larger sizes for the emission regions if we take into account the rescaling of the radii by the luminosity of the systems ($r_i = r_0\sqrt{L_i/L_0}$).

In Figure 11 we finally present the pdf's corresponding to several blends of Fe II ($\lambda\lambda$1705–1730, $\lambda\lambda$1760–1800, $\lambda\lambda$2158–2197, $\lambda\lambda$2209–2239, $\lambda\lambda$2261–2364, $\lambda\lambda$2460–2564, and $\lambda\lambda$2596–2645). The main result that can be inferred from this figure is the different sensitivity to microlensing, which implies different sizes. The microlensing-based size of the $\lambda\lambda$2158–2197 blend is $5.2^{+1.8}_{-2.2}\sqrt{M/0.3\,M_{\odot}}$ lt-day, comparable to the sizes of the Fe III emitting regions. In contrast, the other blends seem to arise from regions of significantly larger size.

3.3. Structure and Kinematics of the BLR

From the impact of microlensing, which we have separately studied in the core and wings of the C IV, C III], and Mg II emission lines, we can attempt to broadly outline a basic relationship between kinematics and structure in the BLR. In the first place, both kinematic regions, core and wings, seem to be little affected by microlensing in C III] and Mg II, indicating that these low-ionization lines (as has been usually assumed) arise from a large region, with a lower limit in size of about 50 lt-day according to microlensing estimates. The absence of a central dip in any of the cores of the line profiles (as in most quasars and AGNs; see Popović et al. 2004) very likely indicates that the motion of the emitters contributing to the core is not confined to a plane (Mathews 1982). The average line profiles of C III] and C IV match very well (at least in the unblended red part), thereby indicating that both arise mainly from the same region. However, the resemblance between the line profiles is broken by the changes induced by microlensing that reveal the existence of a second region that only shows up in the presence of microlensing. This region contributes to the C IV line (with high strength to the wings and a lower amplitude to the core) but not to C III] or Mg II. According to the high impact of microlensing in other high-ionization lines and blends studied, these features also arise from this region, whose size, according to microlensing estimates, would be a few light-days. This and the high velocities involved make it natural to identify the relatively small region with (part of) the accretion disk. In some cases (Fe III $\lambda\lambda$2039–2113, for instance) the large microlensing magnifications and the high velocities involved support the hypothesis that the emitters may arise from an inner region of the accretion disk.

Microlensing provides estimates of the emitting region sizes, which, combined with the Doppler broadening of the emission lines, should help us to study the kinematics of the BLR and the mass of the central black hole, $M_{\rm BH}$, in a similar way as with RM. It is common in RM studies to suppose that the broadening of the lines (FWHM or σ) is related to the mass of the central BH through the virial theorem according to

$$M_{\rm BH} \simeq 9.8 \times 10^7\, M_{\odot} f \left(\frac{R_{\rm BLR}}{5\ \text{lt-days}}\right)\left(\frac{\Delta v_{\rm FWHM}}{10{,}000\ \ \text{km s}^{-1}}\right)^2. \quad (4)$$

Table 7
Core Differences between Epochs

Object	Image Pair	Epoch	C IV		C III	
			$d^a \pm \sigma^b$	d/σ	$d^a \pm \sigma^b$	d/σ
HE 0047–1756	A	III–II	...	...	−0.01 ± 0.05	0.2
	B	III–II	...	...	0.02 ± 0.04	0.5
Q0142–100	A	II–I	−0.55 ± 0.03	18.1	...	...
	B	II–I	−0.53 ± 0.03	16.2	...	...
HE 0435–1223	A	III–I	0.85 ± 0.05	16.0	...	...
		IV–I	0.64 ± 0.03	21.4	...	...
		IV–III	−0.21 ± 0.06	3.4	−0.73 ± 0.06	11.6
	B	IV–I	0.35 ± 0.05	7.7	...	...
		IV–II	...	...	−0.39 ± 0.02	24.6
	C	III–I	0.74 ± 0.04	20.9	...	...
		IV–I	0.67 ± 0.08	8.3	...	...
		IV–III	−0.09 ± 0.08	1.1	−0.67 ± 0.05	13.7
	D	III–I	1.02 ± 0.08	13.5	...	...
		IV–I	0.33 ± 0.08	4.1	...	...
		III–II	...	...	0.03 ± 0.06	0.5
		IV–II	...	...	−0.44 ± 0.06	7.1
		IV–III	−0.69 ± 0.12	5.9	−0.47 ± 0.08	6.1
SDSS J0806+2006	A	II–I	...	...	0.24 ± 0.07	3.5
	B	II–I	...	...	0.46 ± 0.09	4.9
QSO 0957+561	A	II–I	−0.49 ± 0.09	5.2	0.12 ± 0.03	3.8
	B	II–I	−0.33 ± 0.04	8.8	0.17 ± 0.07	2.4
SDSS J1004+4112	A	II–I	−0.08 ± 0.02	3.5	...	...
		III–I	0.14 ± 0.05	3.1	−0.04 ± 0.04	1.2
		III–II	0.24 ± 0.07	3.3	...	...
	B	II–I	0.02 ± 0.05	0.3	...	...
		III–I	0.20 ± 0.04	4.6	−0.15 ± 0.02	7.8
		III–II	0.18 ± 0.07	2.4	...	...
HE 1104–1805	A	II–I	0.37 ± 0.01	27.2	...	...
		III–I	0.44 ± 0.05	9.2	...	...
		IV–I	0.51 ± 0.03	15.5	...	...
		III–II	0.06 ± 0.03	1.9	...	...
		IV–II	0.27 ± 0.01	21.4	...	...
		IV–III	0.21 ± 0.04	5.2	...	...
	B	II–I	0.33 ± 0.02	18.0	...	...
		III–I	−0.04 ± 0.03	1.3	...	...
		IV–I	0.45 ± 0.04	10.6	...	...
		III–II	−0.04 ± 0.03	1.3	...	...
		IV–II	0.12 ± 0.05	2.7	...	...
		IV–III	0.17 ± 0.04	4.7	...	...
SDSS 1339+1310	A	II–I	0.11 ± 0.04	2.9	−0.32 ± 0.07	22.5
		III–I	0.03 ± 0.04	0.7	...	...
		III–II	−0.09 ± 0.02	4.0	...	...
	B	II–I	0.13 ± 0.06	2.0	−0.38 ± 0.05	7.3
		III–I	0.16 ± 0.03	5.2	...	...
		III–II	0.03 ± 0.06	0.5	...	...
WFI J2033–4723	B	III–II	...	...	−0.03 ± 0.06	0.6
	C	III–II	...	...	−0.03 ± 0.04	0.9
HE 2149–2745	A	II–I	−0.17 ± 0.03	5.1	−0.31 ± 0.03	10.2
		III–I	−0.02 ± 0.01	1.4	−0.04 ± 0.01	4.3

Table 7
(Continued)

Object	Image Pair	Epoch	C IV		C III	
		III–II	0.13 ± 0.05	2.5	0.26 ± 0.03	9.6
	B	II–I	−0.23 ± 0.04	6.0	−0.28 ± 0.05	5.3
		III–I	−0.02 ± 0.02	1.2	−0.04 ± 0.03	1.1
		III–II	0.21 ± 0.05	4.5	0.24 ± 0.06	4.2

Notes.
[a] Magnitude difference.
[b] Standard deviation of magnitude difference.

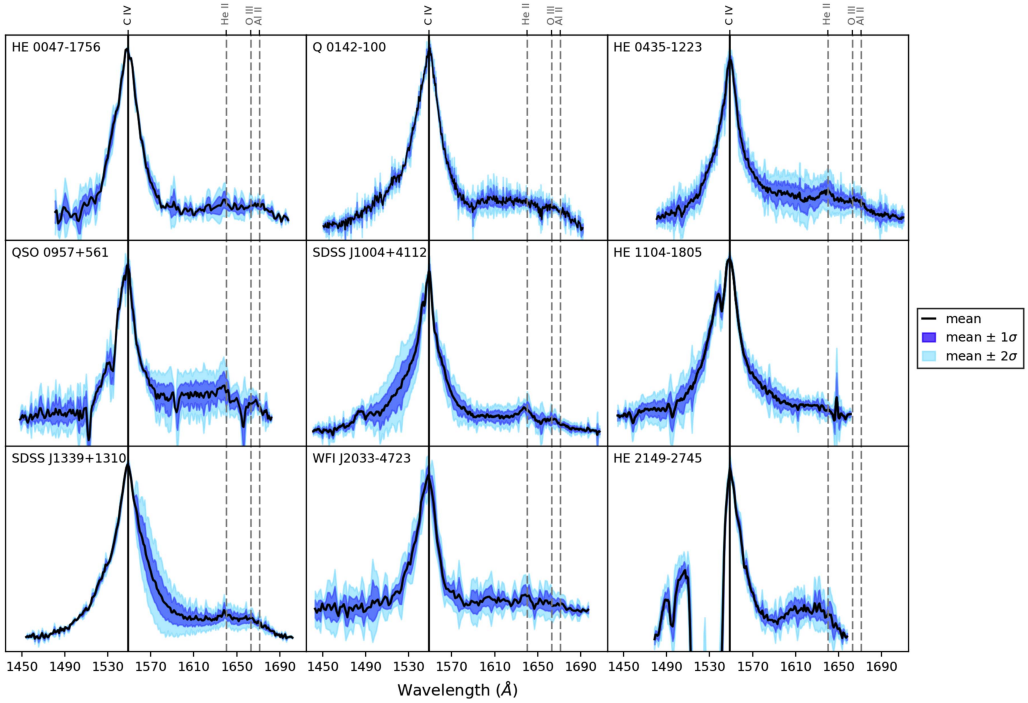

Figure 3. Average (black) spectra for the C IV emission line with 1σ (dark blue) and 2σ (light blue) intervals.

When we apply this relationship to C IV emission lines with $\Delta v_{\rm FWHM} \sim 4700\,{\rm km\,s^{-1}}$ (corresponding to the average C IV line obtained from our sample) and $R_{\rm BLR} \sim 50.3^{+30.4}_{-14.0}$ lt-day (corresponding to the large BLR region little affected by microlensing), we obtain $M_{\rm BH} \sim 4^{+2.4}_{-1.2} \times 10^8\,M_\odot$, for $f = 2$, which is a reasonable result for the bright quasars of our sample (Mosquera et al. 2013). A consistent result, $M_{\rm BH} \sim 3.9^{+1.8}_{-1.4} \times 10^8\,M_\odot$ ($f = 2$), is obtained by considering the Fe III $\lambda\lambda$2039–2113 blend of size $R_{\rm BLR} \sim 11.3^{+5}_{-4}$ lt-day and velocity $\Delta v_{\rm FWHM} \sim 9400\,{\rm km\,s^{-1}}$. The coincidence between both estimates indicates that microlensing-based sizes are in agreement with the hypothesis of virialized kinematics.

Microlensing may, in addition, give more precise information relating velocity and size by considering not the mean properties of the line as a whole but discrete velocity bins in the emission line. However, Equation (4) cannot be directly applied to a velocity bin. Its direct application, considering Gaussian sources, to velocity bins in the range 1000–10,000 km s^{-1} (in the cases of SDSS J1339+1310 and SDSS J1004+4112) leads to microlensing sizes so small, as compared with those inferred from RM, that the obtained central black hole masses would be unexpectedly low. Consequently, a kinematic model that describes the geometry of the region contributing to each velocity interval is needed, to simulate the impact of microlensing in this region. On the other hand, as discussed above, we should

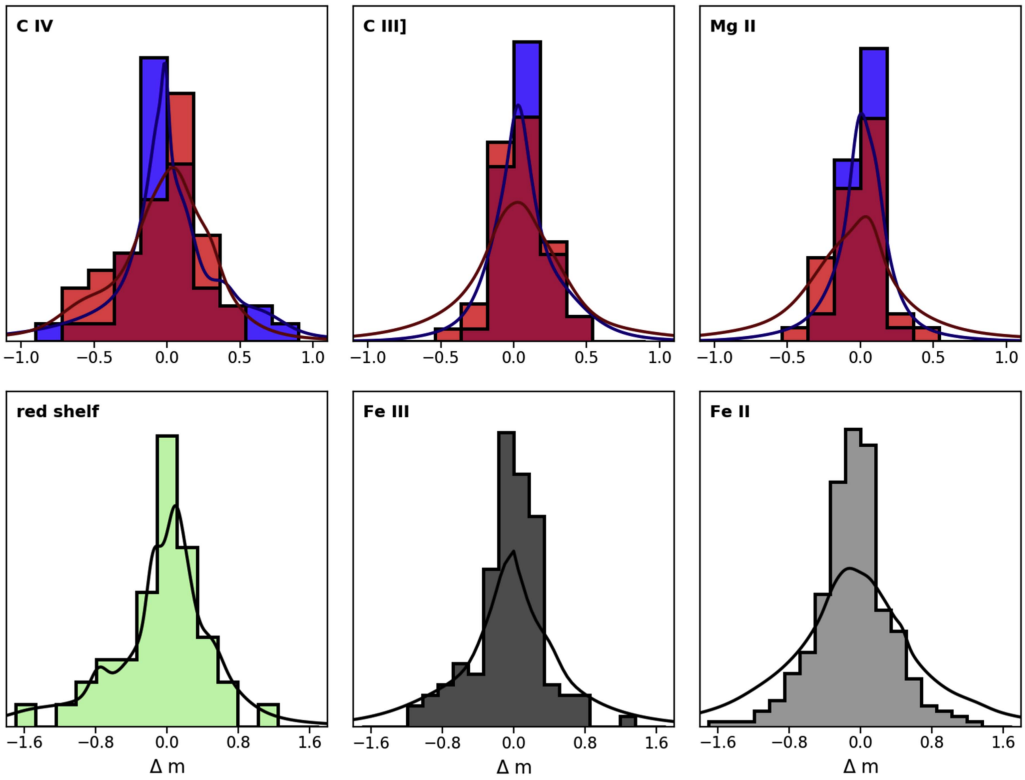

Figure 4. Histograms of microlensing magnification difference between images for different emission-line features. Black curves show the corresponding Gaussian kernel density estimates of the pdf's. For the BELs, C IV, C III], and Mg II (top row) histograms of the blue and red wings are shown. The blue (red) curve illustrates the Gaussian density estimate for the blue (red) wing.

also take into account that the C IV line profile has contributions from two different regions, but that one of them is much more sensible to microlensing than the other.

There are other high-ionization lines that seem to arise exclusively from the small region sensitive to microlensing that, owing to the high microlensing magnifications observed, we have identified with the accretion disk, even with its inner regions. A study based on these lines is not straightforward, as they usually form blends and the S/N of the available observations is not sufficient. In any case, an interesting conclusion is that the BEL of these species may be used to study the kinematics of quasar accretion disks.

4. Conclusions

We have analyzed the BEL of a sample of 11 gravitationally lensed quasars with at least two epochs of observation. We have studied, in most cases, up to 11 different spectral features (emission lines or blends) between the C IV and Mg II lines. Although it is limited, the temporal sampling available has allowed us to identify intrinsic variability and to classify the differences between pairs of spectra as candidates for intrinsic variability or microlensing. The main conclusions are the following:

1. We can consistently separate a group of four systems dominated by microlensing (SDSS J0806+2006, FBQS J0951+2635, SDSS J1004+4112, and SDSS J1339 +1310) and another group of five objects in which intrinsic variability prevails (Q0142−100, HE 1104−1805, WFI J2033−4723, HE 2149−2745, and HE 0047−1756). The case of QSO 0957+561 may be explained by intrinsic variability combined with the time delay between the images plus a possible contribution from microlensing. Finally, HE 0435−1223 seems to be a hybrid case with both microlensing and intrinsic variability present.
2. We study the effects of microlensing and intrinsic variability in the core of the lines (which have been considered unchanging in single-epoch-based studies). On average, we measure a weak microlensing effect in the cores of C III] ($\lesssim 0.09 \pm 0.08$ mag with respect to Mg II) and C IV ($\lesssim 0.12 \pm 0.11$ mag with respect to C III]), although in the two strongest cases of microlensing, the core of C IV is significantly affected (0.23 ± 0.07 mag in

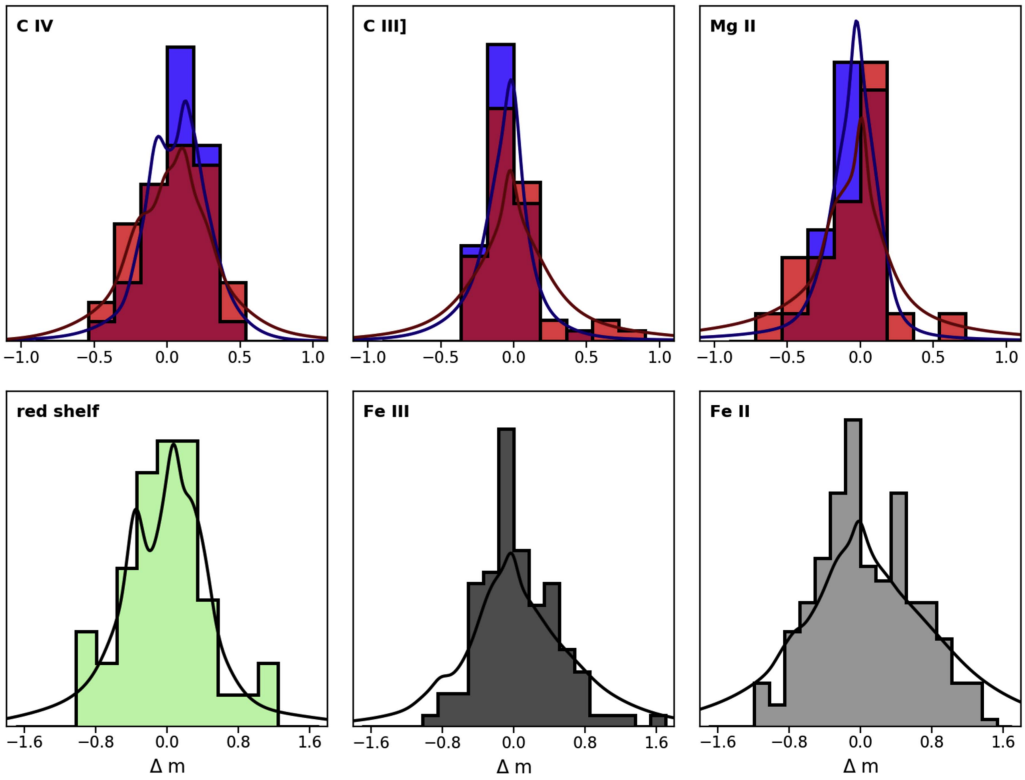

Figure 5. Histograms of the difference between epochs for different emission-line features. Black curves show the corresponding Gaussian kernel density estimates of the pdf's. For the BELs, C IV, C III], and Mg II (top row) histograms of the blue and red wings are shown. The blue (red) curve illustrates the Gaussian density estimate for the blue (red) wing.

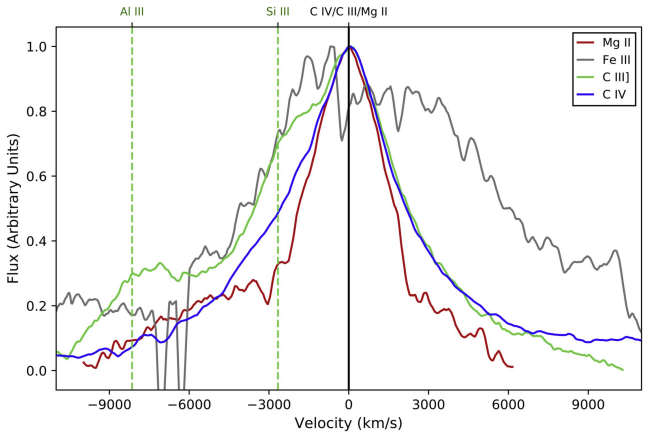

Figure 6. Average line profiles of C IV, C III], Mg II, and Fe II λλ2040–2100 as a function of velocity.

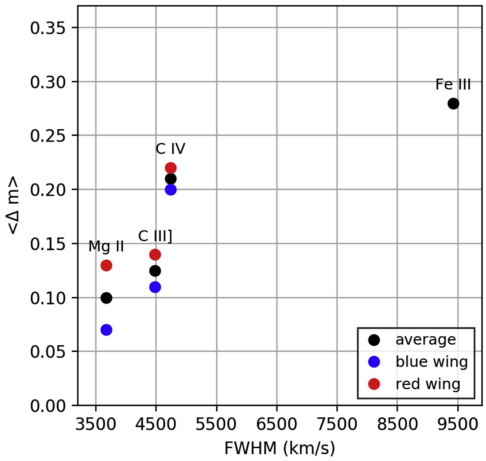

Figure 7. Average amplitude of microlensing between images as a function of the line broadening for C IV, C III], Mg II, and Fe III.

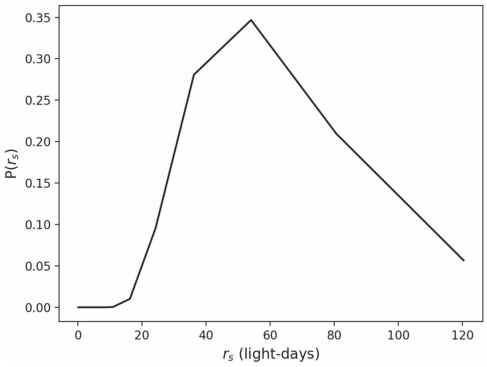

Figure 8. Joint likelihood for the low-ionization lines C III] and Mg II.

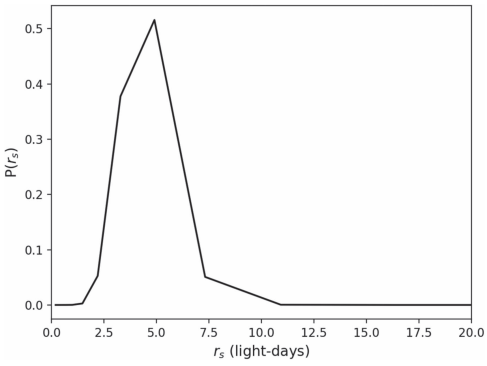

Figure 9. Joint likelihood for the red shelf.

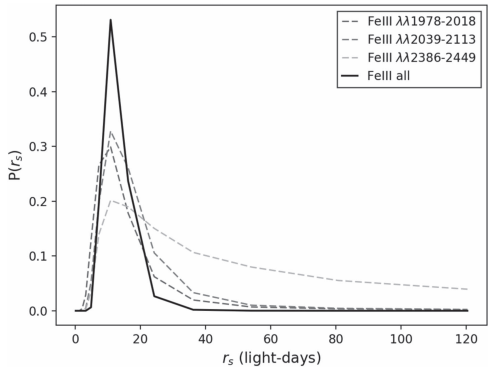

Figure 10. Joint likelihood for Fe III (solid black line). Dashed lines show the joint likelihood functions for different Fe III emitting regions (see Figures 3).

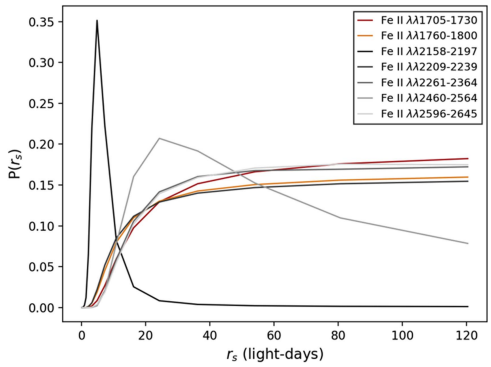

Figure 11. Joint likelihood functions for different Fe II emitting regions (see Figures 3).

SDSS J1004+4112 and 0.16 ± 0.03 mag in SDSS J1339 +1310). Taking the cores as reference, we find that the wings of Mg II and C III] are not significantly affected (at the 2σlevel) by either intrinsic variability or microlensing. On the other hand, the wings of C IV and the other spectral features analyzed (λ1610 shelf-like feature, He II, the O III]/Al II blend, Al III, Si III, Fe II, and Fe III) show strong changes. These results basically confirm the existence of two distinct regions suggested in single-epoch-based studies,[21] one large and insensitive to microlensing and another small and prone to microlensing, but with a significant nuance: the small region also contributes to the core of the high-ionization lines, although it shows up only in the presence of strong microlensing. We have also analyzed core intrinsic variability and obtained estimates of $\lesssim 0.24 \pm 0.21$ mag for C III] (with respect to Mg II) and $\lesssim 0.29 \pm 0.25$ mag for C IV (with respect to C III]). Owing to the presence of systematic instrumental effects, these

[21] Which could neither remove intrinsic variability nor be used to study the impact of microlensing on the cores.

values should be regarded as upper limits on the intrinsic variability of the cores.

3. There is evidence of microlensing variability in the four systems dominated by microlensing and in the hybrid case, HE 0435−1223. Owing to the changes in some spectral features (C IV wings mainly), strong microlensing variability can induce very noticeable asymmetries in the line profile shape. Intrinsic variability affects the same spectral features with similar strength, although no outstanding evidence of asymmetry associated with intrinsic variability has been detected. These results support the hypothesis that the small region susceptible to both intrinsic variability and microlensing is intrinsically symmetrical (i.e., not differentially obscured by dust or magnified by relativistic beaming) and that the asymmetry induced by microlensing in the line profile is related to the anisotropic spatial distribution of microlensing magnification at the source plane.
4. The relative impact of microlensing indicates that the Mg II and C III] emission lines arise from a region ∼50 lt-day in size, in good agreement with RM studies. The kinematic coincidence, in the absence of microlensing, between C III] and C IV supports the hypothesis that a large part of the C IV line also arises from this large region. As the cores of the lines show no central dip, the hypothesis of motion not confined to a plane is supported. The small regions (a few light-days in size) inferred for several high-ionization lines suggest that these lines arise from the accretion disk. In the Fe III λλ2039–2113 blend, a spectral feature relatively uncontaminated by other species, we measure very large microlensing variability (comparable in some extreme cases to that typical of X-ray) and the largest kinematic broadening. These results suggest that Fe III (and likely other high-ionization species present in strongly microlensed complexes) may arise in part from an inner region of the accretion disk. RM studies of the strongly microlensed iron spectral features could be of great interest in probing the accretion disk of quasars.

We thank Burud, Chavushyan, Eigenbrod, Goicoechea, Gómez-Álvarez, Inada, Morgan, Oguri, Richards, Rojas, Schechter, Shalyapin, Sluse, Surdej, Wisotzki, and Wucknitz for kindly making the spectroscopic data listed in Table 1 available. We thank the anonymous referee for valuable suggestions. C.F. gratefully acknowledges the financial support of a La Caixa PhD fellowship. E.M. is supported by the Spanish MINECO with grants AYA2013-47744-C3-3-P and AYA2013-47744-C3-1-P. J.A.M. is supported by the Generalitat Valenciana with grant PROMETEO/2014/60. J.J.-V. is supported by the Spanish Ministerio de Economía y Competitividad and the Fondo Europeo de Desarrollo Regional (FEDER) through grant AYA2014-53506-P and by the Junta de Andalucía through project FQM-108.

Appendix A
Data Analysis Methods

For each of the brightest emission lines (C IV, C III], and Mg II) we fit a straight line $y = a\lambda + b$ to the continuum on either side of the emission line and subtract it from the spectrum. For all images and all epochs we normalize the continuum-subtracted spectra to match the core of the emission line defined by the flux within a narrow interval (±6 Å) centered on the peak of the line. The magnitude differences of the wings are then constructed from the fluxes found after subtracting the linear model for the continuum emission underneath the line profile. We estimate the average wing emission in different wavelength intervals (∼25 Å for C IV, ∼35 Å for C III] and Mg II) on either side of the emission-line peak, corresponding to velocity intervals of ∼4500 km s^{-1} for C IV, ∼5300 km s^{-1} for C III], and ∼3600 km s^{-1} for Mg II. We have separated the line core from the wings by a buffer of ±9 Å to prevent underestimation of the microlensing in the wings. In those cases in which the emission line is affected by absorption lines an integration window avoiding absorption features was chosen. See the core-matched spectra corresponding to C IV, C III], and Mg II in Figure 1. We use the following statistics to calculate the magnitude difference between two different images/epochs (x, y):

$$d_i = w_i * (y_i - x_i), \quad (5)$$

with weights $w_i = \sqrt{\langle y_i + x_i \rangle / (y_i + x_i)}$, selected to equalize the typical deviations of the differences. From the mean value in a given wavelength interval, $\langle d_i \rangle$, we compute the magnitude difference between images/epochs, $d = \langle d_i \rangle$, and its standard deviation σ (see Tables 2–5).

We have also analyzed the wavelength regions between C IV, C III], and Mg II to measure the changes in the UV Fe II and Fe III emission line blends, the complex formed by the He II line, the O III]/Al II blend and the subjacent pseudo-continuum, and the red shelf of C IV. We follow the definition of the wavelength regions of Guerras et al. (2013a, 2013b), Vestergaard & Wilkes (2001), and Vanden Berk et al. (2001) and use the cores of the C IV, C III], and Mg II emission lines as a baseline for no microlensing. We fit various straight lines to the continuum regions bracketing the emission-line windows and subtract them from the spectra. Then, for each image pair and each epoch, we normalize the continuum-subtracted spectra to match the core of the Mg II (C III]) emission line. In many cases, the Mg II (C III]) based normalization does not match the C III] (C IV) emission line. We assume that this mismatch of the line cores arises from differential extinction in the lens galaxy. This is corrected by applying a linear extinction correction to match both emission lines simultaneously (obviously, this correction is applied to the data in Section 2.2 but not in Section 2.3). Finally, for each pair of images (and each epoch) we compare the flux ratios in the defined emission-line windows of the continuum-subtracted and extinction-corrected spectra using the same statistics as described before. See the resulting core-matched spectra and chosen integration windows in Figure 2.

Appendix B
Intrinsic Variability and Microlensing in the C IV-to-Mg II Wavelength Region

In the wavelength region between C IV and C III], there is evidence of variability at the 2σ level that very noticeably affects the complex formed by the He II line, the O III]/Al II blend, and the subjacent pseudo-continuum. We find microlensing in HE 0047−1756, HE 0435−1223, SDSS J1004+4112, and SDSS J1339+1310 and intrinsic variability in Q0142−100, HE 0435−1223, and HE 2149−2745 (with partial evidence in QSO 0957+561 and HE 1104−1805). In the Al III lines there is microlensing in SDSS J1004+4112 and partial evidence of

intrinsic variability in HE 0435−1223. In the Si III lines there is evidence of microlensing in HE 0435−1223, SDSS J1004+4112, HE 1104–1805, and WFI J2033−4723 and partial evidence of intrinsic variability in HE 0435−1223. Finally, the Fe II blends included in this spectral range show no evidence of intrinsic variability or microlensing.

In the wavelength region between C III] and Mg II there is also evidence of intrinsic variability and microlensing affecting several lines and complexes, particularly the Fe II and Fe III iron lines. In Fe II we detect (2σ level) microlensing in HE 0435−1223, SDSS J0806+2006, FBQS J0951+2635, QSO 0957+561 (this can be also interpreted as intrinsic variability plus a time delay), and SDSS J1339+1310 and intrinsic variability in HE 0047−1756, HE 0435−1223, WFI J2033−4723 (partial evidence), and HE 2149−2745. In the Fe III $\lambda\lambda$2040–2100 blend, we obtain basically the same results, microlensing in HE 0435−1223, SDSS J0806+2006, FBQS J0951+2635, QSO 0957+561 (this can be also interpreted as intrinsic variability plus a time delay), and SDSS J1339+1310 and intrinsic variability in HE 0047−1756, HE 0435−1223, SDSS J1339+1310, WFI J2033−4723, and HE 2149−2745 (partial evidence).

ORCID iDs

E. E. Falco https://orcid.org/0000-0002-7061-6519
V. Motta https://orcid.org/0000-0003-4446-7465

References

Abajas, C., Mediavilla, E., Muñoz, J. A., Popović, L. Č, & Oscoz, A. 2002, ApJ, 576, 640
Bentz, M. C., Denney, K. D., Grier, C. J., et al. 2013, ApJ, 767, 149
Bentz, M. C., Peterson, B. M., Netzer, H., Pogge, R. W., & Vestergaard, M. 2009, ApJ, 697, 160
Bentz, M. C., Walsh, J. L., Barth, A. J., et al. 2010, ApJ, 716, 993
Blandford, R. D., & McKee, C. F. 1982, ApJ, 255, 419
Burud, I., Courbin, F., Magain, P., et al. 2002, A&A, 383, 71
Chavushyan, V. H., Vlasyuk, V. V., Stepanian, J. A., & Erastova, L. K. 1997, A&A, 318, L67
Eigenbrod, A., Courbin, F., Dye, S., et al. 2006, A&A, 451, 747
Eigenbrod, A., Courbin, F., & Meylan, G. 2007, A&A, 465, 51
Fian, C., Mediavilla, E., Hanslmeier, A., et al. 2016, ApJ, 830, 149
Fine, S., Croom, S. M., Bland-Hawthorn, J., et al. 2010, MNRAS, 409, 591
Goicoechea, L. J., Gil-Merino, R., & Ullán, A. 2005, MNRAS, 360, L60
Goicoechea, L. J., & Shalyapin, V. N. 2016, A&A, 596, A77
Gómez-Álvarez, P., Mediavilla, E., Muñoz, J. A., et al. 2006, ApJL, 645, L5
Grier, C. J., Pancoast, A., Barth, A. J., et al. 2017a, ApJ, 849, 146
Grier, C. J., Trump, J. R., Shen, Y., et al. 2017b, ApJ, 851, 21
Guerras, E., Mediavilla, E., Jimenez-Vicente, J., et al. 2013a, ApJ, 764, 160
Guerras, E., Mediavilla, E., Jimenez-Vicente, J., et al. 2013b, ApJ, 764, 160
Inada, N., Oguri, M., Becker, R. H., et al. 2006, AJ, 131, 1934
Jiménez-Vicente, J., Mediavilla, E., Kochanek, C. S., & Muñoz, J. A. 2015, ApJ, 806, 251
Kaspi, S., Brandt, W. N., Maoz, D., et al. 2007, ApJ, 659, 997
Li, J., Shen, Y., Horne, K., et al. 2017, ApJ, 846, 79
Mathews, W. G. 1982, ApJ, 258, 425
Mediavilla, E., Mediavilla, T., Muñoz, J. A., et al. 2011, ApJ, 741, 42
Mediavilla, E., Muñoz, J. A., Kochanek, C. S., et al. 2005, ApJ, 619, 749
Mediavilla, E., Muñoz, J. A., Lopez, P., et al. 2006, ApJ, 653, 942
Morgan, N. D., Caldwell, J. A. R., Schechter, P. L., et al. 2004, AJ, 127, 2617
Mosquera, A. M., & Kochanek, C. S. 2011, ApJ, 738, 96
Mosquera, A. M., Kochanek, C. S., Chen, B., et al. 2013, ApJ, 769, 53
Motta, V., Mediavilla, E., Falco, E., & Muñoz, J. A. 2012, ApJ, 755, 82
Motta, V., Mediavilla, E., Rojas, K., et al. 2017, ApJ, 835, 132
Oguri, M., Inada, N., Hennawi, J. F., et al. 2005, ApJ, 622, 106
Peterson, B. M. 2006, in ASP Conf. Ser. 360, AGN Variability from X-Rays to Radio Waves, ed. C. M. Gaskell et al. (San Francisco, CA: ASP), 191
Popović, L. Č., Mediavilla, E., Bon, E., & Ilić, D. 2004, A&A, 423, 909
Richards, G. T., Keeton, C. R., Pindor, B., et al. 2004, ApJ, 610, 679
Rojas, K., Motta, V., Mediavilla, E., et al. 2014, ApJ, 797, 61
Schechter, P. L., Gregg, M. D., Becker, R. H., Helfand, D. J., & White, R. L. 1998, AJ, 115, 1371
Shalyapin, V. N., & Goicoechea, L. J. 2014, A&A, 568, A116
Shen, Y., Horne, K., Grier, C. J., et al. 2016, ApJ, 818, 30
Sluse, D., Hutsemékers, D., Courbin, F., Meylan, G., & Wambsganss, J. 2012, A&A, 544, A62
Surdej, J., Claeskens, J.-F., Remy, M., et al. 1997, A&A, 327, L1
Vanden Berk, D. E., Richards, G. T., Bauer, A., et al. 2001, AJ, 122, 549
Vestergaard, M., & Wilkes, B. J. 2001, ApJS, 134, 1
Wambsganss, J. 2006, in Saas-Fee Advanced Course 33, Gravitational Lensing: Strong, Weak and Micro, ed. G. Meylan et al. (Berlin: Springer), 453
Wisotzki, L., Becker, T., Christensen, L., et al. 2003, A&A, 408, 455
Wisotzki, L., Koehler, T., Ikonomou, M., & Reimers, D. 1995, A&A, 297, L59
Wisotzki, L., Koehler, T., Kayser, R., & Reimers, D. 1993, A&A, 278, L15
Wisotzki, L., Schechter, P. L., Chen, H.-W., et al. 2004, A&A, 419, L31
Wucknitz, O., Wisotzki, L., Lopez, S., & Gregg, M. D. 2003, A&A, 405, 445

4.3 SMBH Masses of Quasars from Fe III Gravitational Redshift[3]

Analyzing the BELs (Section 4.2.3), we found very high microlensing magnifications in the Fe III$\lambda\lambda$2039–2113 blend (a relatively isolated feature according to Guerras et al. 2013, originating in a small region of a few light-days across), comparable or even greater than the typical microlensing magnification measured in the optical (see Figure 4.6). In some cases these magnifications reach values similar to those observed in the X-ray continuum ($\sim$ 1 mag). In addition, and to our surprise, the Fe III $\lambda\lambda$2039–2113 blend in the spectrum stacked from the objects in our sample seemed to be redshifted. The objective of the following paper was to measure the shifts of the Fe III lines of this blend, to explore their consistence with the gravitational redshift hypothesis, and to discuss their possible use in the determination of SMBH masses.

We performed a fit to model the Fe III feature using a Gaussian for each one of the blended single lines according to Vestergaard & Wilkes (2001). When applying the fit, we allowed a shift in wavelength, a multiplicative factor for the flux and a free value for the broadening σ. These three, independent parameters are identical for all (in total 18) Gaussian lines in the blend and their sum matched very well with the shape of the blend, but indeed appeared to be redshifted by $\sim$10 Å. We repeated the fit for each one of the objects separately and, almost for all of them, the fit was very good but only when a redshift was allowed. The same result was obtained after fitting the Fe III feature in the SDSS composite quasar spectrum from Vanden Berk et al. (2001).

[3] brief overview of Mediavilla et al. 2018

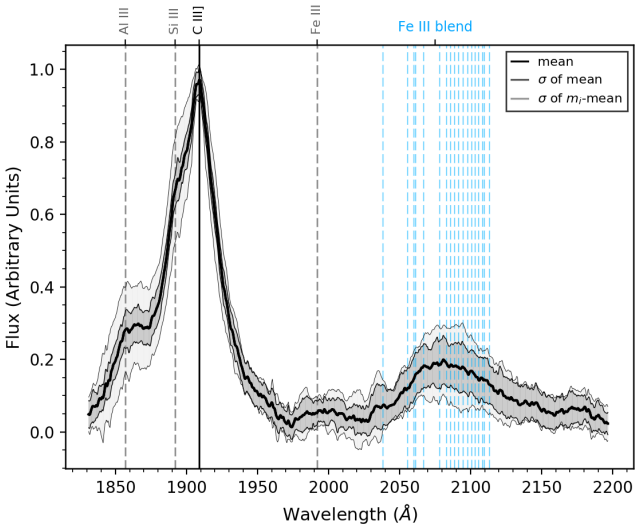

Figure 4.6: Average (black) spectra of the C III] emission line together with the redshifted Fe III λλ2039-2113 blend. One (two) sigma intervals are shown in dark (light) gray.

In order to search for some systematic trend of the redshift, we repeated the fit in 27 composites of the BOSS quasar spectra sampled in redshift, luminosities and spectral index. The first result was the correlation of the measured redshift $(\Delta\lambda/\lambda)$ with σ^2/λ^2. The correlation between $(\Delta\lambda/\lambda)$ and $(\sigma/\lambda)^2$ through the 27 composite spectra of BOSS is an important support to our supposition that $\Delta\lambda/\lambda$ is a gravitational redshift. Such redshift measurements of the Fe III λλ2039-2113 blend may be an excellent proxy for estimating the black hole mass to size ratio even for a single object as it depends only on gravitational and transverse Doppler redshifts not related to the projected velocity of the emitters:

$$\lambda = \lambda_0 \frac{\sqrt{\frac{r-2}{r-3}}}{\sqrt{1-\frac{2}{r}}} \left[1 + \sqrt{\frac{1}{r-2}}\, cos(\phi) sin(i)\right] \tag{4.4}$$

λ_0 ..... rest wavelength
i ..... inclination
r ..... size of the emission region
ϕ ..... periapsis

It does not seem to exist a noticeable correlation with luminosity in the range covered by BOSS composites but surprisingly there is a rather clear correlation with the spectral index, corresponding the largest redshifts to the steeper power-laws. If these results are true, an estimate of the redshift of the Fe III blend in combination with a reverberation mapping based estimate of the emitting region size can measure the mass of the black hole in a single object without the uncertainty in the virial factor *f*.

4.3.1 Mediavilla et al. 2018: Measuring SMBH Masses

Systematic Redshift of the Fe III UV Lines in Quasars. Measuring Supermassive Black Hole Masses under the Gravitational Redshift Hypothesis.

E. MEDIAVILLA[1,2], J. JIMÉNEZ-VICENTE[3,4], C. FIAN[1,2], J. A. MUÑOZ[5,6], E. FALCO[7], V. MOTTA[8] & E. GUERRAS[9]

ABSTRACT

We find that the Fe III$\lambda\lambda$2039-2113 spectral feature in quasars appears systematically redshifted by amounts **accountable** under the hypothesis of gravitational redshift induced by the central supermassive black hole. **Our** analysis of 27 composite spectra from the BOSS survey indicates that the redshift and the broadening of the lines in the Fe III$\lambda\lambda$2039-2113 blend roughly follow the expected correlation in the weak limit of Schwarzschild geometry for virialized kinematics. Assuming that the Fe III UV redshift provides a measure of $\frac{M_{BH}}{R}$ ($\frac{\Delta\lambda}{\lambda} \simeq \frac{3}{2}\frac{G}{c^2}\frac{M_{BH}}{R}$) and using different estimates of the emitting region size, R (either from gravitational microlensing, reverberation mapping or from the scaling of size with intrinsic quasar luminosity), we obtain masses for 10 objects which are in agreement within uncertainties with previous mass estimates based on the virial theorem. Reverberation mapping estimates of the size of the Fe III$\lambda\lambda$2039-2113 emitting region in a sample of objects would be needed to confirm the gravitational origin of the measured redshifts. Meanwhile, we present a tentative black

[1]Instituto de Astrofísica de Canarias, Vía Láctea S/N, La Laguna 38200, Tenerife, Spain

[2]Departamento de Astrofísica, Universidad de la Laguna, La Laguna 38200, Tenerife, Spain

[3]Departamento de Física Teórica y del Cosmos, Universidad de Granada, Campus de Fuentenueva, 18071 Granada, Spain

[4]Instituto Carlos I de Física Teórica y Computacional, Universidad de Granada, 18071 Granada, Spain

[5]Departamento de Astronomía y Astrofísica, Universidad de Valencia, 46100 Burjassot, Valencia, Spain.

[6]Observatorio Astronómico, Universidad de Valencia, E-46980 Paterna, Valencia, Spain

[7]Harvard-Smithsonian Center for Astrophysics, 60 Garden St., Cambridge, MA 02138, USA

[8]Instituto de Física y Astronomía, Facultad de Ciencias, Universidad de Valparaíso, Avda. Gran Bretaña 1111, 2360102 Valparaíso, Chile

[9]Homer L. Dodge Department of Physics and Astronomy, The University of Oklahoma, Norman, OK, 73019, USA

hole mass scaling relationship based on the Fe III$\lambda\lambda$2039-2113 redshift useful to measure the black hole mass of one individual object from a single spectrum.

Subject headings: (black hole physics — gravitational lensing: micro)

1. Introduction

In the classical picture of quasars, a central supermassive black hole (BH) is surrounded by an inspiraling disk that transports matter into the depth of the gravitational well of the BH, releasing huge quantities of energy (Zeldovich 1964, Salpeter 1964). This central engine illuminates gas clouds located in a larger region (Broad Line Region, BLR) giving rise to very broad emission lines (BEL) whose width and shape are determined by the kinematics of the gas clouds, ultimately ruled by the central BH. Thus, the kinematics of the BLR potentially provides a means of measuring the central masses of supermassive BH and of studying the structure of the accretion disk.

Specifically, the methods for estimating BH masses in distant quasars[1] are mainly based on the measure of the broadening of the BEL in combination with the virial theorem (see, e.g., Peterson 2014). According to this theorem, the square of the line-broadening, $(\Delta v)^2$, is a proxy for M/R that, in combination with a determination of the size, R, can provide an estimate of the mass,

$$M = f\frac{(\Delta v)^2 R}{G}. \quad (1)$$

The dimensionless factor, f, includes the effects of the unknown BLR geometry, kinematics and inclination. **Without** more information, it is a common practice to use an average value for f obtained **by** calibrating with other methods[2], even when f is different for each object. This virial factor, by itself, limits the accuracy of individual estimates of mass to $\sim$0.4 dex (Peterson 2014). The size can be determined from reverberation mapping (see, e.g., the reviews by Peterson 1993, 2006), which is an observationally expensive technique, or alternatively using the size-luminosity, R-L, relationship for AGN, a shortcut inferred from reverberation mapping results (Kaspi et al. 2000, 2005, Bentz et al. 2009, Zu et al.

[1]In the nearby universe, masses of supermassive black holes have been determined in around 70 galaxies by direct modeling of the stellar or gas dynamics (see, e.g., McConnell & Ma 2013).

[2]The $M_{BH} - \sigma_*^2$ relationship, for instance (Ferrarese & Merritt 2000, Gebhardt et al. 2000, Tremaine et al. 2002).

2011). Both techniques are relatively accurate and the main experimental problem to apply Eq. 1 (in addition to the unknown factor f), arises from the determination of the line widths (Peterson 2014), due to both, the ambiguity in the definition of Δv (FWHM, σ, use of the variable or constant part of the spectra, etc.), and the presence of contaminating features (extra components, blended lines, pseudo-continuum, etc.).

An alternative path to BH masses is the gravitational redshift of the BEL. If we consider the width of the BEL as caused by motion in the gravitational field of a central mass, a simple calculation shows that we should expect measurable gravitational and transverse Doppler redshifts (see, e.g., Netzer 1977, Anderson 1981, Mediavilla & Insertis 1989). Indeed, in the weak limit of the Schwarzschild metric, the velocity of the emitters is proportional to $\sqrt{GM/R}$, and the gravitational plus transverse Doppler redshift[3] will tend to $\frac{3}{2}\frac{G}{c^2}\frac{M}{R}$. Thus, line broadenings typical of the BEL, $\Delta v \gtrsim 10^3\,\mathrm{km\,s^{-1}}$, will result in redshifts $z_{grav} = \frac{\Delta\lambda}{\lambda} \gtrsim 0.003$, which for UV lines corresponds to displacements $\Delta\lambda \gtrsim 6$Å, which should be very easy to measure.

However, experimental results do not satisfy these theoretical expectations. According to massive analysis of quasar spectra like SDSS (Vanden Berk et al. 2001) and BOSS (Harris et al. 2016), the peaks of the brightest permitted and semi forbidden lines can appear shifted either towards the red or the blue, but with blue shifts being more frequent and strong, the opposite to what is expected. This indicates that the shifts of the BEL peaks are probably of kinematic origin. Nevertheless, the profiles of some BEL (Hβ in many cases) can show redward asymmetries (Peterson et al. 1985, Sulentic 1989, Zheng & Sulentic 1989, Popović et al. 1995, Corbin et al. 1997), that have been sometimes interpreted as the result of gravitational redshift (Jonić et al. 2016), although the presence of an extra component redshifted due to inflow is, perhaps, a more accepted explanation for the line asymmetry. In a few cases in which spectroscopic monitoring is available, the redshift between the mean and rms profiles of Balmer lines has been associated **with** gravitational redshift (Kollatschny 2003, Liu et al. 2017)[4]. There has also been continued controversy about the existence of redshifts in Fe II emission. **Hu et al. (2008) interpreted the redshift measured in the Fe II optical lines of a sample of SDSS spectra in terms of kinematics dominated by infall. In this scenario, to prevent the gas from being accelerated away from the central source by the radiation force, Ferland et al. (2009) propose that we only observe the shielded face of near-side infalling clouds. However, Kovačević**

[3]Hereafter we refer to the combined gravitational and transverse Doppler effects as gravitational redshift.

[4]In any case, the presence of gas cold enough as to generate the Balmer lines so close to the BH as to justify the redshift needs to be explained (Bon et al. 2015).

et al. (2010) report only a slight redshift of the Fe II optical lines. The same result is reached by Sulentic et al. (2012) who find that the Fe II optical lines follow the same kinematics as the Balmer lines. Finally, Kovačević-Dojčinović & Popović (2015) find a significant average redshift in the UV lines that, however, is not present in the optical lines. In any case, **the Fe II redshifts** were interpreted as inflow of gas clouds located at the outer parts of the BLR, leaving aside the gravitational redshift scenario.

The main cause of the scarcity of unquestionable identifications of gravitational redshift is likely the complex morphology of the lines, with several kinematic components arising from different regions, and often blended with lines from other species that may significantly distort the shape and change the width of the line profile. To achieve a robust detection of gravitational redshift we need a feature associated **with** one single ion, not blended with emission lines of other species, and that presumably originates from an inner region of the BLR.

The size of the region giving rise to an emission line in the quasar spectrum can be estimated from the changes in magnification of the emission line induced by gravitational microlensing[5], so that the larger the changes the smaller the size. According to previous studies (Guerras et al. 2013a,b, Fian et al. 2018), the Fe III$\lambda\lambda$2039-2113 blend is a relatively isolated feature strongly affected by microlensing and hence must originate in a small region (a few light-days across) where gravitational redshift is significant. The objective of this work is, then, to measure the shifts of the Fe III lines of this blend, to explore their consistence with the gravitational redshift hypothesis, and to discuss their possible use in the determination of SMBH masses and in the study of the physics of accretion disks.

The paper is organized as follows: In §2 we fit the Fe III$\lambda\lambda$2039-2113 blend in a sample of high S/N spectra collected from several data sources. §3 is devoted to deriving a scaling relationship of mass with redshift and luminosity. Finally, in §4 we summarize the main conclusions.

[5]When a distant quasar is lensed by the gravitational potential of an intervening (lens) galaxy, the relative movement between the quasar and the distribution of stars in the lens galaxy can change the brightnesses of the images, an effect called quasar gravitational microlensing (Chang & Redfsdal 1979, 1984, see also the review by Wambsganss 2006).

2. Results: Fe III$\lambda\lambda$2039-2113 Redshift Measurements

2.1. Data

The data analyzed in this work have different origins. The 14 lensed quasar spectra fitted in §2.2 have been compiled from many sources in the literature (see details in Fian et al. 2018). In §2.2 we also analyze the publicly available SDSS composite spectrum (Van den Berk et al. 2001) and the 27 BOSS quasar composite spectra (Jensen et al. 2016). Finally, in §3.1 the monitoring series of spectra of NGC 5548 (Korista et al. 1995) and the spectrum from NGC 7469 (Kriss et al. 2000) are used to determine the BH masses. All the spectra are corrected from cosmological redshift.

2.2. Analysis and results

We model the Fe III$\lambda\lambda$2039-2113 spectral feature in 14 lensed quasars (Fian et al., 2018). First, we fit the continuum to a straight line defined in two windows at the blue (2013.3 Å, 2017.9 Å) and red (2195.3 Å, 2205.0 Å) sides of the blend. Then we subtract the continuum and fit the feature using a template of 19 single Fe III lines between 2038.5 and 2113.2Å of fixed relative amplitudes as provided by Vestergaard & Wilkes (2001). The (Gaussian) lines are broadened, shifted and scaled with the same width, σ (= FWHM/2.35), wavelength shift, $\Delta\lambda$, and scale factor. In Figure 1 we can see that this template is able to reproduce very well the shape of the Fe III$\lambda\lambda$2039-2113 feature in the spectra of the objects in our sample[6], but the fitted features are redshifted in all the objects except one (SDSS 1004+4112, which is strongly affected by microlensing). Leaving aside this object, we find that the average of this systematic redshift is $\langle\Delta\lambda\rangle = 10.3$ Å with a scatter between objects of ± 5.9 Å. If we take the microlensing based size inferred by Fian et al. (2018) for the Fe III UV lines[7], $R = 1.18 \times 11.3^{+5}_{-4}$ light-days, we can estimate the average mass of the supermassive black holes of the lensed quasars under the hypothesis of a gravitational origin for the redshift. **If we assume that gravitational and transverse Doppler are the physical phenomena giving rise to the redshift, we have (see, e.g., Mediavilla & Insertis, 1989),** $\nu = (\nu_0/\gamma)\sqrt{1 - 2GM_{BH}/Rc^2}$ **with** $\gamma = (1 - (v/c)^2)^{-1/2}$. In the weak limit of the Schwarzschild metric, $v \simeq GM_{BH}/R$, and we have,

[6]See also other fits in the upper panel of Figure 2, and Figures 3 and 4.

[7]**Fiann et al. (2018) consider a disk with a Gaussian radial profile, for which the half-light radius, R, is obtained from the reported Gaussian sigma, r_s, through $R = 1.18 r_s$.**

$$z_{grav} = \frac{\Delta\lambda}{\lambda} \simeq \frac{3}{2}\frac{G}{c^2}\frac{M_{BH}}{R}, \quad (2)$$

and,

$$M_{BH} \simeq \frac{2c^2}{3G}\frac{\Delta\lambda}{\lambda}R = \left(\frac{z_{grav}}{0.005}\right)\left(\frac{R}{10\,\mathrm{light\,days}}\right)\left(0.58\times10^9 M_\odot\right). \quad (3)$$

Susbtituting in Equation 3 the mean redshift of the iron lines and the microlensing based size, we obtain for the average mass of the supermassive black holes, $\langle M_{BH}\rangle \simeq (0.83 \pm 0.47)\times10^9 M_\odot$, where the uncertainty arises partly from the method and partly from the intrinsic scatter between objects. This value is in good agreement, in mean and scatter, with virial based estimates for lensed quasars (see, e.g., Figure 8 of Mosquera et al. 2013). In fact, if we consider the 8 lensed quasars in our sample (HE 0047-1756, SDSS 0246-0285, SDSS 0924+0219, FBQ 0951+2635, Q 0957+561, HE 1104-1805, SDSS 1335+0118 and HE 2149-2745) that have virial mass estimates by Peng et al. (2006) and Assef et al. (2011), we obtain from Eq. 3, $\langle M_{BH}^{micro}\rangle \simeq (0.9\pm0.5)\times10^9 M_\odot$, in very good agreement with the average of their virial masses, $\langle M_{BH}^{virial}\rangle \simeq 0.93\times10^9 M_\odot$.

Because of the interesting implications of these results, and to exclude any systematic issue in our sample of lensed quasars, we fit the Fe III$\lambda\lambda$2039-2113 feature in the high S/N composite SDSS spectrum (Vanden Berk et al. 2001), in which we also measure a strong global redshift of the feature of ~ 7 Å (Figure 2). Looking for further confirmation, we fit another two UV features of Fe III that, in spite of their lower intensity, can be modeled in this high S/N composite spectrum: the Fe IIIλ2419 line and the Fe III$\lambda\lambda$1970-2039 blend. The Fe IIIλ2419 line (Figure 2) appears blended with a narrow line identified as Ne IVλ2424 (Vanden Berk et al. 2001). Figure 2 shows that, while the Ne IV narrow line can be well fitted at its nominal wavelength (Vanden Berk et al. 2001), the Fe III line has a clear redshift with respect to it. Finally, the redshift is also observed in the (noisier) Fe III$\lambda\lambda$1970-2039 blend. The best fit estimates of the redshift, $z = \Delta\lambda/\lambda$, of these features are: 0.0034 ± 0.0002 (Fe III$\lambda\lambda$2039-2113), 0.0037 ± 0.0001 (Fe IIIλ2419) and 0.0034 ± 0.0007 (Fe III$\lambda\lambda$1970-2039). For the widths, σ/λ, we obtain: 0.0057 ± 0.0003 (Fe III$\lambda\lambda$2039-2113), 0.0059 ± 0.0002 (Fe IIIλ2419) and 0.0055 ± 0.0006 (Fe III$\lambda\lambda$1970-2039). The good agreement between the fitted parameters of the three Fe III features confirms that the redshift is intrinsic to the Fe III emitters.

Going a step further, to study the incidence and meaning of the observed redshift using high S/N spectra, we fit (see Figures 3 and 4) the Fe III$\lambda\lambda$2039-2113 feature in the 27 composite spectra of the BOSS survey (Jensen et al. 2016). The fits are very good with $\chi^2_{red} \leq 2$, although some of the spectra have a low S/N ratio. **We can use BOSS composites to discuss virialization. If the kinematics is virialized (Eq. 1), we should have,**

$$G\frac{M_{BH}}{R} = f(\Delta v)^2 = f\left(\frac{\sigma}{\lambda}\right)^2 c^2, \quad (4)$$

where we have taken $\sigma c/\lambda$ as representative of the line broadening[8], Δv. Combining Eq. 4 with the expression for the mass in terms of the redshift (Eq. 2), we obtain,

$$\frac{\Delta\lambda}{\lambda} = \frac{3}{2} f \left(\frac{\sigma}{\lambda}\right)^2. \quad (5)$$

Taking logarithms, we can write this condition of virialized kinematics in a linear shape convenient for quantitative fitting,

$$\log\left(\frac{\sigma}{\lambda}\right)^2 = -\log\frac{3f}{2} + \log\left(\frac{\Delta\lambda}{\lambda}\right). \quad (6)$$

The measured redshifts, $z = \Delta\lambda/\lambda$, and widths of the Fe III lines, $\left(\frac{\sigma}{\lambda}\right)^2$, obtained from the BOSS composite spectra (excluding the cases with S/N < 3.0) follow this correlation though with a relatively high scatter (Figure 5). Fitting Eq. 6 to the data we obtain (R-squared ~ 0.75),

$$\log\left(\frac{\sigma}{\lambda}\right)^2 = -2.09 \pm 0.64 + (0.99 \pm 0.26)\log\left(\frac{\Delta\lambda}{\lambda}\right). \quad (7)$$

The large uncertainties in the fit parameters (Eq. 7) can have an intrinsic origin, for the virial factors, f, can be significantly different from system to system depending on physical unknowns like the flatness of the emitter's distribution, its orientation, or the presence of non gravitational forces (e.g., radiation pressure). It is likely that the criteria to form the BOSS composites may be biased with respect to any of these unknowns giving rise to an intrinsic scatter in f. On the other hand, radial motions may also contribute to the redshift in a variable way from object to object, increasing the scatter. In any case, alternative explanations (inflow, for instance, may be another mechanism giving rise to the redshifts) would need additional physics to explain the observed trend between broadening and redshift. Thus, while a tight correlation between $\Delta\lambda/\lambda$ and $\left(\frac{\sigma}{\lambda}\right)^2$ is not generally expected, the trend found between these two quantities among the composite spectra of BOSS supports

[8]**For our Gaussian based fits, $\sigma = FWHM/2.35$ but in many applications of the virial theorem based on emission-line profiles, σ is the second moment of the experimental line profile, and $FWHM/\sigma$ depends on the profile shape (Collin et al. 2006).**

the gravitational interpretation of the Fe III$\lambda\lambda$2039-2113 redshifts and indicates that the kinematics is not far from virialized.

Although the fits of the Vestergaard & Wilkes (2001) template to the Fe III$\lambda\lambda$2039-2113 feature of BOSS composites are very good, it is true that this template is based on one particular object. To eliminate any possible bias related to the use of the template, we have performed an alternative study based on the centroid of the blend, $\lambda_c = \langle\lambda\rangle$, in each composite spectrum. The standard deviation between the redshift measurements based on either the fit of the template or the centroid of the blend is ~ 0.5 Å. This result confirms the redshift estimates irrespective of the choice of template. Another possible source of uncertainty in the measurement of the redshifts is the difficulty to determine the systemic velocity of the quasars, which may depend on the choice of the spectral features. However, this indetermination can account for shifts of roughly a few hundred $\mathrm{km\,s^{-1}}$, randomly distributed between blue- and red-shifts while we are measuring exclusively redshifts of about one thousand $\mathrm{km\,s^{-1}}$. In addition, this problem should be mitigated in the case of BOSS composites resulting from the average of many spectra.

3. Discussion: Black Hole Mass Estimates Based on Fe III$\lambda\lambda$2039-2113 Redshift

Under the hypothesis that the redshift of the Fe III$\lambda\lambda$2039-2113 is of gravitational origin, we can invert Equation 2 to derive the central BH mass corresponding to any object for which an estimate of R_{FeIII} can be obtained (see Eq. 3). We are going to consider three different methods for computing sizes: reverberation mapping, scaling of the size of the BLR with luminosity and gravitational microlensing.

3.1. Mass Estimates of the Central Black Holes in NGC 5548 and NGC 7469 based on Fe III$\lambda\lambda$2039-2113 Redshift and Reverberation Mapping

NGC 5548 is a widely studied AGN[9] for which reverberation mapping has yielded estimates of the size for the continuum and several strong emission lines (see, e.g., Clavel et al. 1991, Korista et al. 1995, Peterson et al. 2002; see also Pei et al. 2017 and references

[9]**Notice, however, that some common conceptions about this AGN could change if the suspected existence of a supermassive BH binary in the center of this galaxy (Li et al. 2016) is confirmed.**

therein).

We fit the Fe III$\lambda\lambda$2039-2113 blend in each of the spectra of the monitoring series (Korista et al. 1995), deriving the light curve of the Fe III amplitude (Figure 6). We infer a lag of the Fe III relative to the UVλ1970 continuum of 3.3 ± 0.8 (2.8 ± 1.4) days when the centroid (peak) of the cross correlation centroid (peak) distribution CCCD (CCPD) is taken as reference. The errors have been estimated applying flux randomization Monte Carlo methods. Adopting these lags as estimates of R_{FeIII} and using the measurement of the redshift from the fit to the average spectra, $z_{grav}(FeIII) = (\Delta\lambda/\lambda)_{FeIII} = 0.0056 \pm 0.0010$, we obtain, $M_{BH} = 2.2^{+0.6}_{-0.4} \times 10^8 M_\odot$ ($M_{BH} = 1.8^{+1.0}_{-0.9} \times 10^8 M_\odot$) for the centroid (peak). These values are relatively large but in agreement within uncertainties with recent estimates of the black hole mass derived from the virial **theorem** ($M = 1.2^{+0.4}_{-0.3} \times 10^8 M_\odot$, Ho & Kim, 2015; $M = 6.7^{+2.7}_{-2.7} \times 10^7 M_\odot$, Pei et al 2017), taking into account a 30% uncertainty in the average virial factor f (Woo et al. 2015), and the intrinsic scatter between objects (0.35 dex according to Ho & Kim 2015).

We also fit the Fe III$\lambda\lambda$2039-2113 feature in another well studied galaxy, NGC 7469 (Kriss et al. 2000). We measure $z_{grav}(FeIII) = 0.0026 \pm 0.0005$. In this case there is no UV spectroscopic monitoring to obtain the light curve of the Fe III blend, but we can set an upper limit to the size of ~ 0.7 light-days. This value corresponds to the reverberation lag of He II. This is a high ionization line, known from the impact of microlensing (Fian et al. 2018) to arise from a region of size comparable or somewhat greater than that corresponding to Fe III. Taking this upper limit, we infer $M_{BH} \leq 2.1^{+0.4}_{-0.4} \times 10^7 M_\odot$, compatible with **previous** virial estimates ($M = 1.5^{+0.6}_{-0.4} \times 10^7 M_\odot$, Ho & Kim, 2015, $1 - 6 \times 10^7 M_\odot$, **Shapovalova et al. 2016**).

Finally, it is also important to stress that, once the size is known via reverberation mapping, the mass of the object is directly obtained from the redshift without using any previous calibration, i.e., in combination with reverberation mapping, the gravitational redshfit of the Fe III$\lambda\lambda$2039-2113 feature is a *primary* method to determine masses. In fact, because gravitational redshift does not depend on geometrical considerations, it may become the primary calibrator of all the other methods used to measure the mass of the BH.

3.2. Black Hole Mass Estimates Based on Fe III$\lambda\lambda$2039-2113 Redshift and Quasar Luminosity.

Reverberation mapping is an observationally expensive technique to estimate sizes. An alternative is to use the scaling of the size of the BLR with luminosity, $R \propto (\lambda L_\lambda)^\alpha$ (Kaspi

et al. 2000, 2005)**. In combination with the line width of the BLR lines as an estimator of the virial velocity,** empirical BH mass calibrations, $M_{BH} \propto FWHM^2\,(\lambda L_\lambda)^\alpha$**, can be obtained. The most reliable** $R - L_\lambda$ **relationship is based on H**β **and** L_{5100}**. Other determinations, related to H**α**, Mg II or CIV, are re-calibrated from the** $R(H\beta) - L_{5100}$ **relationship. In spite of some problems associated with it (see, e.g., Mejía-Restrepo et al. 2016), the calibration using the CIV line is important because it is the only prominent broad emission line that lies within the optical window at high-z as is the case in many of the objects we studied.**

Specifically, for high redshift quasars, BH masses can be estimated from the CIVλ1549 broadening using[10] **(Mejía-Restrepo et al. 2016)**,

$$M_{BH}(CIV) = 10^{6.353\pm0.013}\left(\frac{FWHM_{CIV}}{10^3\,\mathrm{km\,s^{-1}}}\right)^2\left(\frac{\lambda L_\lambda(1450\,\text{Å})}{10^{44}\,\mathrm{erg\,s^{-1}}}\right)^{0.599\pm0.001} M_\odot. \quad (8)$$

Thus, we can use the $FWHM_{CIV}$ measurements available for the BOSS composites (Jensen et al. 2016) to re-calibrate Eq. 8 in terms of the Fe III gravitational redshift[11]. On average, we find for the BOSS composite spectra: $< FWHM_{CIV} >= (0.27 \pm 0.02) < \sqrt{z_{grav}(FeIII)} > c$, where the uncertainty is the standard error in the mean. Substituting this in Eq. 8 we obtain a mass scaling relationship based on the gravitational redshift of Fe III,

$$M_{BH}^{BOSS}(FeIII) = 10^{7.69^{+0.06}_{-0.07}}\left(\frac{z_{grav}(FeIII)c}{10^3\,\mathrm{km\,s^{-1}}}\right)\left(\frac{\lambda L_\lambda(1350\,\text{Å})}{10^{44}\,\mathrm{erg\,s^{-1}}}\right)^{0.599\pm0.001} M_\odot. \quad (9)$$

To check the validity of this relationship, we compare in Figure 7 the mass estimates obtained applying Eq. 9 to the measured Fe III gravitational redshifts of the lensed quasars in our sample (Fian et al. 2018) with the virial based masses obtained by Peng et al. (2006) and Assef et al. (2011). We have 8 objects in common: HE 0047-1756, SDSS 0246-0285, SDSS 0924+0219, FBQ 0951+2635, Q 0957+561, HE 1104-1805, SDSS 1335+0118 and HE 2149-2745. We have also included NGC 5548 and NGC 7469 in the plot (gravitational redshift masses obtained from Eq. 9 and virial masses from Vestergaard & Peterson 2006). The global agreement over two orders of magnitude in mass is very noticeable, showing that the Fe III$\lambda\lambda$2039-2113 gravitational redshift can be used to measure the BH mass.

[10]**The use of other standard calibrations (e.g. Vestergaard & Peterson 2006, Assef et al. 2011) do not substantially affect the results.**

[11]This is supported by Eq.5 which relates broadenings and redshifts.

The intercept of the best fit with slope unity (dashed line in Figure 7) corresponds to the shift in the calibration that we would obtain following the usual steps to derive the mass scaling relationships (see, e.g., Peterson et al., 2004; Vestergaard & Peterson, 2006): (i) adopt a R-L relationship, $R \propto L^{0.599}$, and (ii) use the available virial based mass estimates to calibrate our unscaled masses, $\mu = (z_{grav}(FeIII)c/10^3\,\mathrm{km\,s^{-1}})\left(\lambda L_\lambda(1350\,\text{Å})/10^{44}\,\mathrm{erg\,s^{-1}}\right)^{0.599} M_\odot$. The relatively small value of the shift in the calibration, **0.04** dex, as compared with the $1\,\sigma$ scatter of the masses with respect to the best fit, **0.26** dex, indicates that there is a good agreement between the BOSS composite spectra based calibration and the independent calibration that would be obtained fitting the virial masses. The **0.26** dex scatter of the masses **relative** to the fit, also indicates that Eq. 9 is reliable taking into account that virial masses are themselves uncertain typically by ~ 0.3 dex (Vestergaard & Peterson 2006).

Notice that the R-L relationship is very tight (with errors comparable to the lags inferred from reverberation mapping, Peterson 2014). Thanks to this and because the Fe III gravitational redshift is easy to measure from a single spectrum, Equation 9 provides a robust estimate of the mass of a quasar or AGN. An attempt to fit the Fe III$\lambda\lambda$2039-2113 blend in a sample of ∼200 SDSS individual quasars (S/N $\gtrsim$ 20) shows that the redshift can be measured with a reasonable accuracy in 25% of them. This implies a number of potential BH mass determinations of more than one thousand from available and future quasar surveys.

3.3. Black Hole Mass Estimates Based on Fe III$\lambda\lambda$2039-2113 Redshift and Microlensing Size Scaling.

Using microlensing based sizes, we can also estimate the BH masses directly from the equation of the redshift in the weak limit of the Schwarzschild metric (Eq. 3). We do not have individual estimates of size for each object, but we can use the average microlensing size estimated by Fian et al. (2018) re-scaling it by applying the $R \propto \sqrt{\lambda L_\lambda}$ relationship:

$$M_{BH} \simeq \frac{2c^2}{3G}\frac{\Delta\lambda}{\lambda}\langle R\rangle\frac{\sqrt{\lambda L_\lambda}}{\langle\sqrt{\lambda L_\lambda}\rangle}. \quad (10)$$

This equation is, indeed, very similar to Equation 9 but has been derived on different grounds. Inserting the value of $\langle R\rangle$ from Fian et al. (2018) and the average of the square root of the luminosities of the quasars, $\langle\sqrt{\lambda L_\lambda}\rangle$, used by these authors to infer $\langle R\rangle$, we can write,

$$M_{BH} \simeq \frac{\Delta\lambda}{10.3\,\text{Å}}\sqrt{\frac{\lambda L_\lambda}{10^{45.79}\,\mathrm{erg\,s^{-1}}}} \times (0.83 \pm 0.47) \times 10^9 M_\odot. \quad (11)$$

It is convenient to rewrite this equation to compare it with the equivalent expression (Eq. 9) based on the BOSS composite spectra calibration,

$$M_{BH}^{micro}(FeIII) = 10^{7.85^{+0.20}_{-0.36}} \left(\frac{z_{grav}(FeIII)c}{10^3\,\mathrm{km\,s^{-1}}}\right) \left(\frac{\lambda L_\lambda(1350\,\text{Å})}{10^{44}\,\mathrm{erg\,s^{-1}}}\right)^{0.5} M_\odot. \quad (12)$$

Thus, Eqs. 9 and 12 agree within uncertainties. This agreement is noteworthy taking into account that the calibration of Eq. 11 (and hence Eq. 12) resides on gravitational microlensing while Eq. 9 has been calibrated from the widths of the CIV lines of BOSS composites. Figure 8 shows the good agreement, 0.27 dex of scatter ($1\,\sigma$), between the mass estimates obtained using Eq. 11 and the virial masses.

3.4. Best Fit of the Mass Scaling Relationship to the Virial Masses Leaving Free the $R \propto L^b$ Law.

Finally, it is also interesting to perform a fit of Equation 10 to the virial masses of our 10 objects but now leaving free the exponent of the R-L relationship, $R \propto \lambda L_\lambda^b$. A change of scale, a, is also allowed. Specifically we fit a and b parameters in,

$$\log\left(\frac{M_{vir}}{0.83\times10^9 M_\odot}\right) = \log\left(a\frac{\Delta\lambda}{10.3\,\text{Å}}\right) + b\log\left(\frac{L_\lambda}{\langle\lambda L_\lambda^b\rangle^{1/b}}\right), \quad (13)$$

where $\langle\lambda L_\lambda^b\rangle$ is computed taking into account all the objects used by Fian et al. (2018) to estimate the average microlensing size. We obtain $a = 1.1\pm0.3$ and $b = 0.57\pm0.08$. That is, Eq. (10) agrees within uncertainties with the best fit to virial masses. To show this explicitly we can, once more, write Eq. 13 as,

$$M_{BH}^{best\,fit}(FeIII) = 10^{7.89^{+0.11}_{-0.13}} \left(\frac{z_{grav}(FeIII)c}{10^3\,\mathrm{km\,s^{-1}}}\right) \left(\frac{\lambda L_\lambda(1350\,\text{Å})}{10^{44}\,\mathrm{erg\,s^{-1}}}\right)^{0.57\pm0.08} M_\odot, \quad (14)$$

in agreement within uncertainties with both, M_{BH}^{micro} (Eq. 12) and M_{BH}^{BOSS} (Eq 9). In Figure 9 we compare the results of $M_{BH}^{best\,fit}$ with the virial masses ($1\,\sigma = 0.26$ dex).

Thus, according to the results discussed in sections 3.2, 3.3 and 3.4, from three different methods (Eqs. 9, 12 and 14), we have obtained consistent (within uncertainties) coefficients of the relationship that scales the masses of the BH with redshift and luminosity.

4. Conclusions

We have studied the Fe III$\lambda\lambda$2039-2113 emission line blend in 14 spectra of lensed quasars, in two well known AGN (NGC 5548 and NGC 7469), in the SDSS quasar composite spectrum and in 27 BOSS quasar spectra composites. This feature is relatively free of contamination from lines of other species and, according to the impact of microlensing magnification on it, arises from an inner region of the BLR. The main results are:

1 - The Fe III$\lambda\lambda$2039-2113 feature appears systematically redshifted. In the high S/N ratio SDSS composite spectrum, this redshift is also consistently measured in the Fe IIIλ2419 line and the Fe III$\lambda\lambda$1970-2039 blend.

2 - There is a correlation, though with a large scatter, between the observed redshift and the broadening of the Fe III$\lambda\lambda$2039-2113 lines. This dependence is expected in the case of virialized kinematics if the redshift is gravitational. The scatter may reflect the differences in geometry, kinematics and impact of non gravitational forces, among the quasars.

3 - In combination with microlensing based estimates of the Fe III UV emitting region size, the measured redshifts for gravitational lenses lead, under the gravitational redshift hypothesis, to values for the central BH mass, $\langle M_{BH} \rangle \simeq (0.9 \pm 0.5) \times 10^9 M_\odot$, in good agreement with previous virial based estimates.

4 - We present a scaling relationship of mass with redshift and luminosity useful to measure the BH mass of one individual object from a single spectrum. This relationship can be formally derived from the Schwarzschild metric and is consistently calibrated using three different methods: the broadening of the CIV lines of the BOSS composite spectra, the strength of gravitational microlensing in the Fe III UV lines, and the best fit to the available virial masses. The two first methods are completely independent and the estimated masses using any of them are in statistical agreement with virial masses over two orders of magnitude ($1\,\sigma$ scatter of 0.27 dex comparable to the intrinsic scatter of the virial masses).

5 - If the gravitational redshift hypothesis is correct, the application of the scaling relationship to spectra of available quasar surveys will provide thousands of estimates of supermassive BH masses. Future mass estimates based on the Fe III redshift and reverberation mapping may become the primary calibrator for all BH mass measurement methods.

Although the good matching between the masses derived from the measured redshifts of the Fe III$\lambda\lambda$2039-2113 feature and the virial masses makes gravitational redshift a compelling explanation, the potential importance of the confirmation of this hypothesis is worthy of additional study. However this is not straightforward. Because of the large intrinsic uncertainties of the virial method applied to individual objects, a direct confirmation based

on the comparison with virial masses, can be firmly established only from a large enough sample. In addition, as virial masses are not exempt of biases arising from the geometry of the emitters distribution or by the presence of non gravitational forces, this comparison will actually be two-way, testing both, the conditions of applicability of the virial theorem and the gravitational redshift hypothesis. For these reasons, the most convincing support likely will be based on high S/N reverberation mapping studies of the Fe III$\lambda\lambda$2039-2113 blend in several objects, which can confirm the small size of the region emitting this spectral feature and provide an accurate R-L relationship for it.

We are grateful to the anonymous referee for a thorough revision and valuable suggestions. We thank the SDSS and BOSS surveys for kindly providing the data. This research was supported by the Spanish MINECO with the grants AYA2013-47744-C3-3-P and AYA2013-47744-C3-1-P. J.A.M. is also supported by the Generalitat Valenciana with the grant PROMETEO/2014/60. J.J.V. is supported by the project AYA2014-53506-P financed by the Spanish Ministerio de Economía y Competividad and by the Fondo Europeo de Desarrollo Regional (FEDER), and by project FQM-108 financed by Junta de Andalucía. V.M. gratefully acknowledges support from FONDECYT through grant 1120741 and Centro de Astrofísica de Valparaíso.

REFERENCES

Anderson, K. S. 1981, ApJ, 246, 13

Assef, R. J., Denney, K. D., Kochanek, C. S., et al. 2011, ApJ, 742, 93

Bentz, M. C., Peterson, B. M., Netzer, H., Pogge, R. W., & Vestergaard, M. 2009, ApJ, 697, 160

Bon, N., Bon, E., Marziani, P., & Jovanović, P. 2015, Ap&SS, 360, 7

Chang, K., & Refsdal, S. 1979, Nature, 282, 561

Chang, K., & Refsdal, S. 1984, A&A, 132, 168

Clavel, J., Reichert, G. A., Alloin, D., et al. 1991, ApJ, 366, 64

Collin, S., Kawaguchi, T., Peterson, B. M., & Vestergaard, M. 2006, A&A, 456, 75

Corbin, M. R. 1997, ApJ, 485, 517

Ferland, G. J., Hu, C., Wang, J.-M., et al. 2009, ApJ, 707, L82

Ferrarese, L., & Merritt, D. 2000, ApJ, 539, L9

Fian, C., Guerras, E., Mediavilla, E., et al. 2018, arXiv:1805.09619

Gebhardt, K., Bender, R., Bower, G., et al. 2000, ApJ, 539, L13

Guerras, E., Mediavilla, E., Jimenez-Vicente, J., et al. 2013a, ApJ, 764, 160

Guerras, E., Mediavilla, E., Jimenez-Vicente, J., et al. 2013b, ApJ, 778, 123

Harris, D. W., Jensen, T. W., Suzuki, N., et al. 2016, AJ, 151, 155

Ho, L. C., & Kim, M. 2014, ApJ, 789, 17

Ho, L. C., & Kim, M. 2015, ApJ, 809, 123

Hu, C., Wang, J.-M., Ho, L. C., et al. 2008, ApJ, 687, 78-96

Jensen, T. W., Vivek, M., Dawson, K. S., et al. 2016, ApJ, 833, 199

Jonić, S., Kovačević-Dojčinović, J., Ilić, D., & Popović, L. Č. 2016, Ap&SS, 361, 101

Kaspi, S., Smith, P. S., Netzer, H., et al. 2000, ApJ, 533, 631

Kaspi, S., Maoz, D., Netzer, H., et al. 2005, ApJ, 629, 61

Kollatschny, W. 2003, A&A, 412, L61

Korista, K. T., Alloin, D., Barr, P., et al. 1995, ApJS, 97, 285

Kovačević, J., Popović, L. Č., & Dimitrijević, M. S. 2010, ApJS, 189, 15

Kovačević-Dojčinović, J., & Popović, L. Č. 2015, ApJS, 221, 35

Kriss, G. A., Peterson, B. M., Crenshaw, D. M., & Zheng, W. 2000, ApJ, 535, 58

Li, Y.-R., Wang, J.-M., Ho, L. C., et al. 2016, ApJ, 822, 4

Liu, H. T., Feng, H. C., & Bai, J. M. 2017, MNRAS, 466, 3323

McConnell, N. J., & Ma, C.-P. 2013, ApJ, 764, 184

Mediavilla, E., & Insertis, F. M. 1989, A&A, 214, 79

Mejía-Restrepo, J. E., Trakhtenbrot, B., Lira, P., Netzer, H., & Capellupo, D. M. 2016, MNRAS, 460, 187

Mosquera, A. M., Kochanek, C. S., Chen, B., et al. 2013, ApJ, 769, 53

Netzer, H. 1977, MNRAS, 181, 89P

Pei, L., Fausnaugh, M. M., Barth, A. J., et al. 2017, ApJ, 837, 131

Peng, C. Y., Impey, C. D., Rix, H.-W., et al. 2006, ApJ, 649, 616

Peterson, B. M., Meyers, K. A., Carpriotti, E. R., et al. 1985, ApJ, 292, 164

Peterson, B. M. 1993, PASP, 105, 247

Peterson, B. M., Berlind, P., Bertram, R., et al. 2002, ApJ, 581, 197

Peterson, B. M., Ferrarese, L., Gilbert, K. M., et al. 2004, ApJ, 613, 682

Peterson, B. M. 2006, Astronomical Society of the Pacific Conference Series, 360, 191

Peterson, B. M. 2014, Space Sci. Rev., 183, 253

Popovic, L. C., Vince, I., Atanackovic-Vukmanovic, O., & Kubicela, A. 1995, A&A, 293, 309

Salpeter, E. E. 1964, ApJ, 140, 796

Shapovalova, A. I., Popović, L. Č., Chavushyan, V. H., et al. 2017, MNRAS, 466, 4759

Sulentic, J. W. 1989, ApJ, 343, 54

Sulentic, J. W., Marziani, P., Zamfir, S., & Meadows, Z. A. 2012, ApJ, 752, L7

Tremaine, S., Gebhardt, K., Bender, R., et al. 2002, ApJ, 574, 740

Vanden Berk, D. E., Richards, G. T., Bauer, A., et al. 2001, AJ, 122, 549

Vestergaard, M., & Wilkes, B. J. 2001, ApJS, 134, 1

Vestergaard, M., & Peterson, B. M. 2006, ApJ, 641, 689

Wambsganss, J. 2006, Saas-Fee Advanced Course 33: Gravitational Lensing: Strong, Weak and Micro, 453

Woo, J.-H., Yoon, Y., Park, S., Park, D., & Kim, S. C. 2015, ApJ, 801, 38

Zel'dovich, Y. B. 1964, Soviet Physics Doklady, 9, 195

Zheng, W., & Sulentic, J. W. 1990, ApJ, 350, 512

Zu, Y., Kochanek, C. S., & Peterson, B. M. 2011, ApJ, 735, 80

This preprint was prepared with the AAS LaTeX macros v5.2.

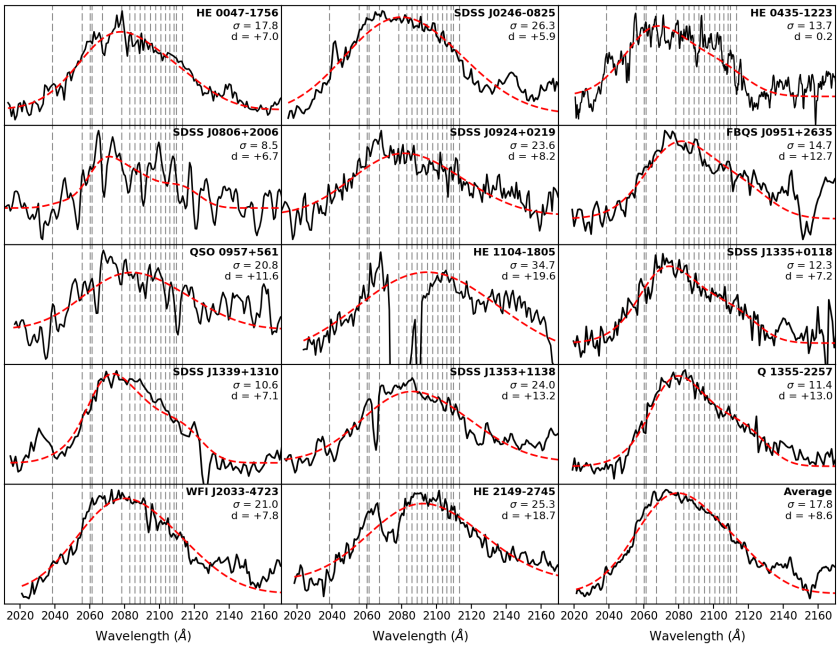

Fig. 1.— Fits to the Fe III$\lambda\lambda$2039-2113 blend in 14 lensed quasars. The broadening, σ, and shift, $d = \Delta\lambda$, of the iron lines are indicated for each spectrum (in Å). The continuous (dashed) curve corresponds to the data (fit). Vertical dashed lines are located at the wavelengths corresponding to the Fe III lines of **the** Vestergaard & Wilkes (2001) template at rest. The spectra have been shifted by an amount $-d$ to match the template rest frame.

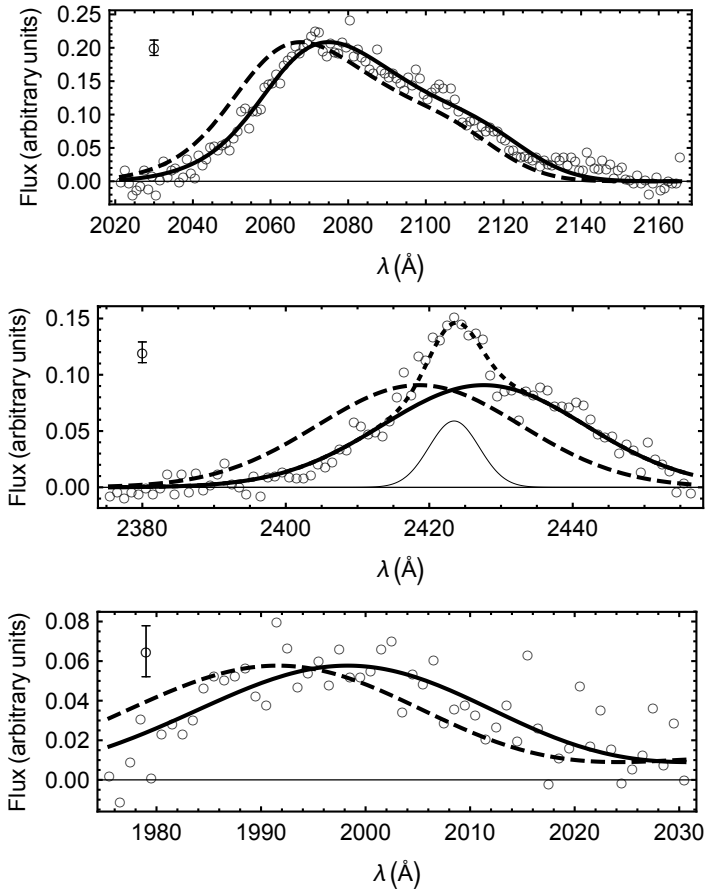

Fig. 2.— Fits of three UV iron features, Fe III$\lambda\lambda$2039-2113 (upper panel), Fe III$\lambda\lambda$2419 (middle panel) and Fe III$\lambda\lambda$1970-2039 (lower panel), in the SDSS composite spectrum (Van den Berk et al. 2001). Notice the redshifts between the rest frame features (dashed curves) and the best fits (solid curves). In the case of Fe IIIλ2419 (middle panel) the thin curve represents the unshifted, narrow Ne IVλ2424 line, and the dotted curve the total fit. Average error bars are included in each panel.

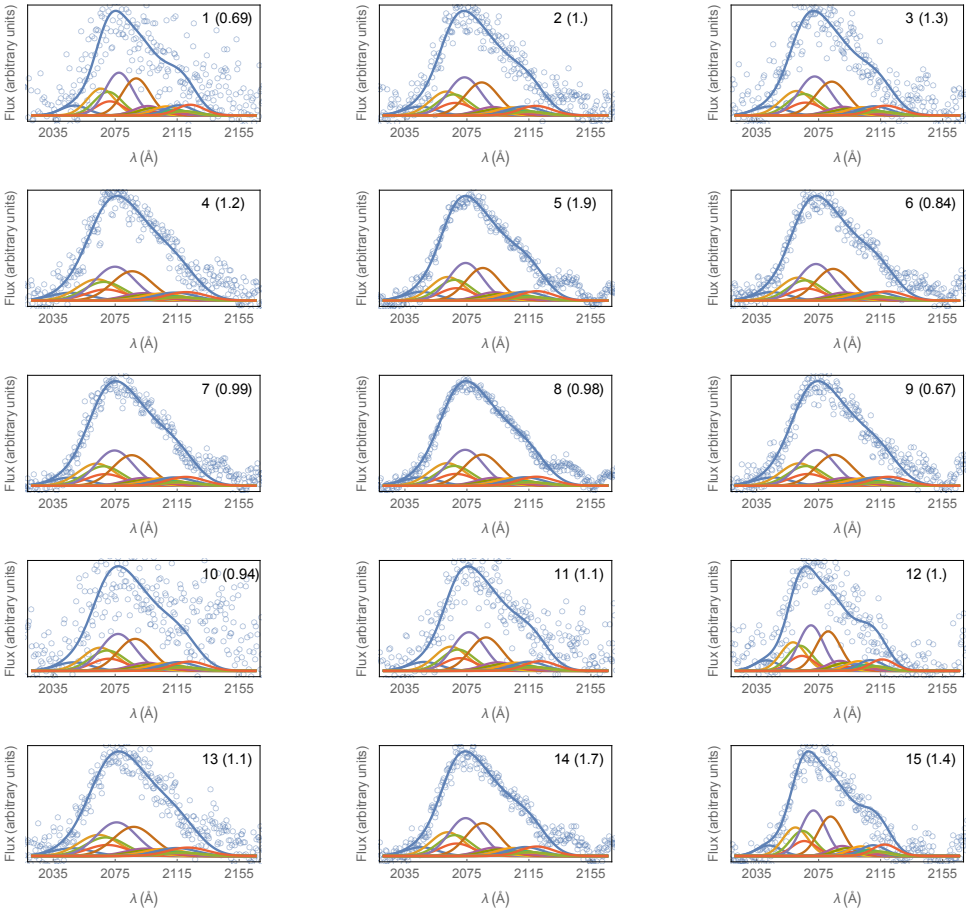

Fig. 3.— Fits of **the** Vestergaard & Wilkes (2001) template to the 27 composite spectra of the BOSS survey. Open circles correspond to the data, the blue line to the template and the other lines to the Gaussians representing each of the Fe III lines. The number of each composite is indicated and, in parentheses, the reduced chi-squared value, χ^2_{red} (see text).

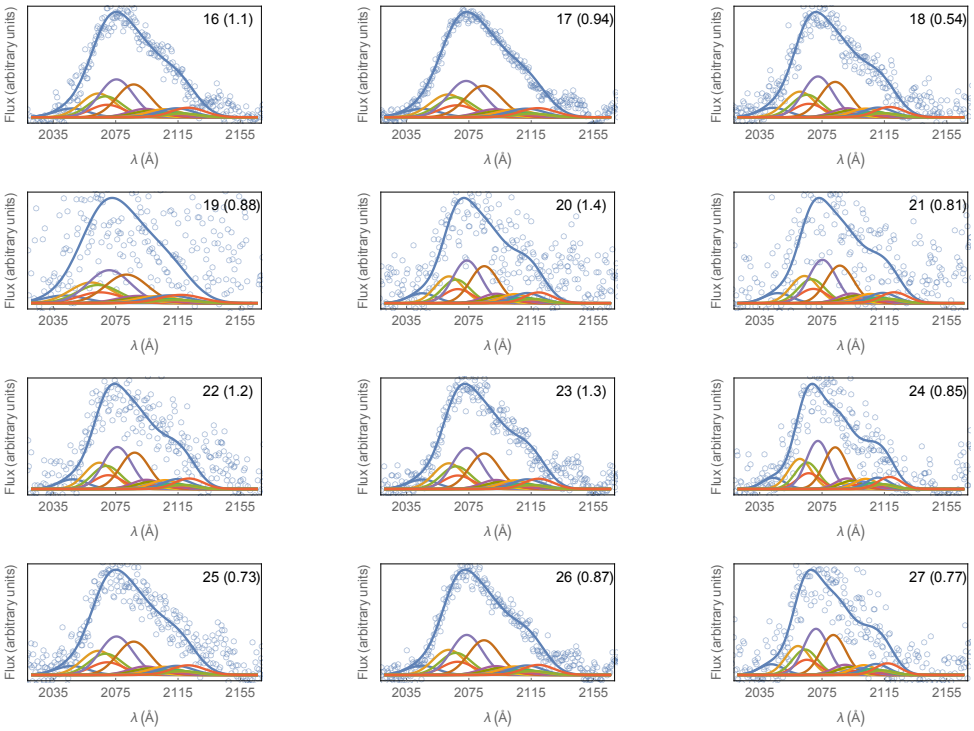

Fig. 4.— Continuation of Figure 3.

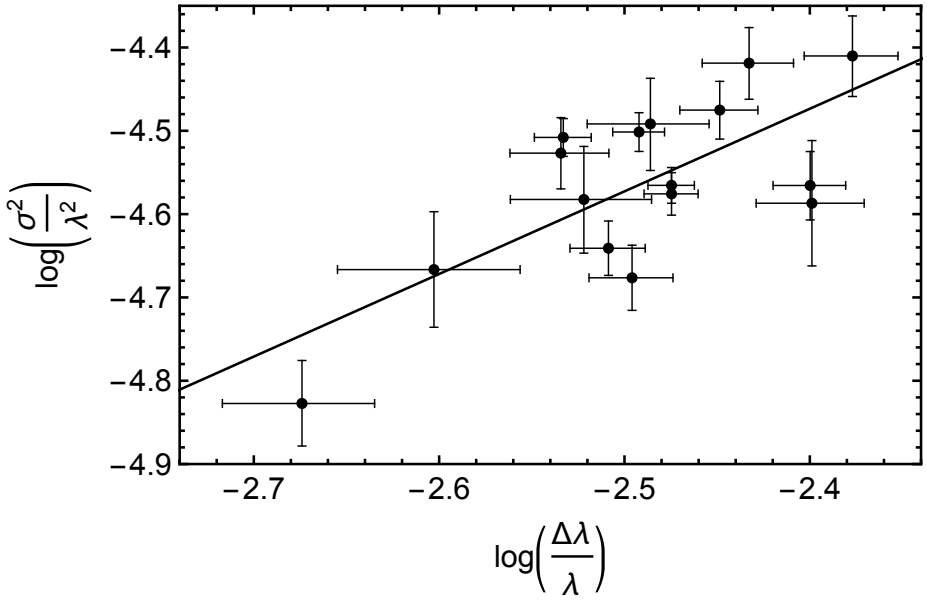

Fig. 5.— Fe III$\lambda\lambda$2039-2113 width squared, $\left(\frac{\sigma}{\lambda}\right)^2$, versus redshift, $\frac{\Delta\lambda}{\lambda}$, obtained from the composite spectra of the BOSS survey with S/N > 3. The straight line is the best fit to the data points (see text).

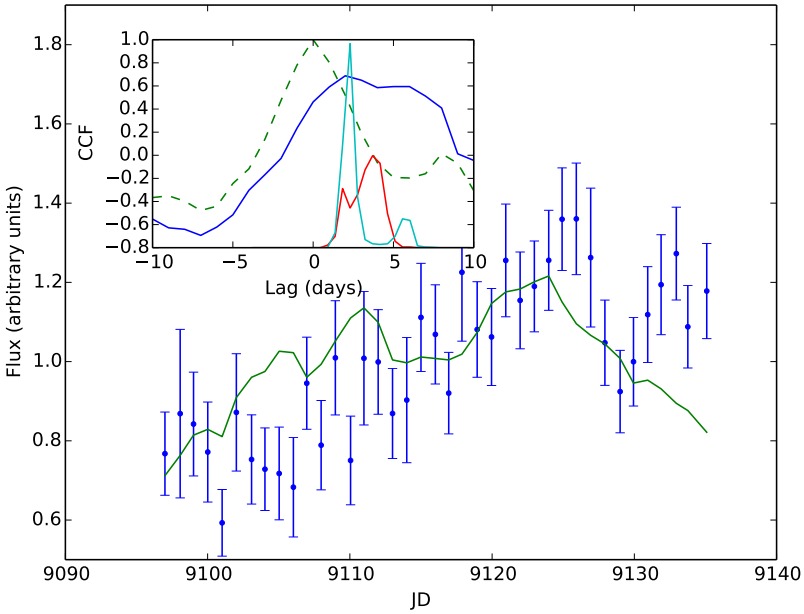

Fig. 6.— Reverberation lag of Fe III$\lambda\lambda$2039-2113 for NGC 5548. Main plot: Fe III$\lambda\lambda$2039-2113 (blue dots) and UV continuum at 1790Å (green line). Inset: CCF (Cross Correlation Function) in blue, Continuum ACF (Auto Correlation Function) in dashed green. CCCD (Cross Correlation Centroid Distribution) in red, CCPD (Cross Correlation Peak Distribution) in cyan.

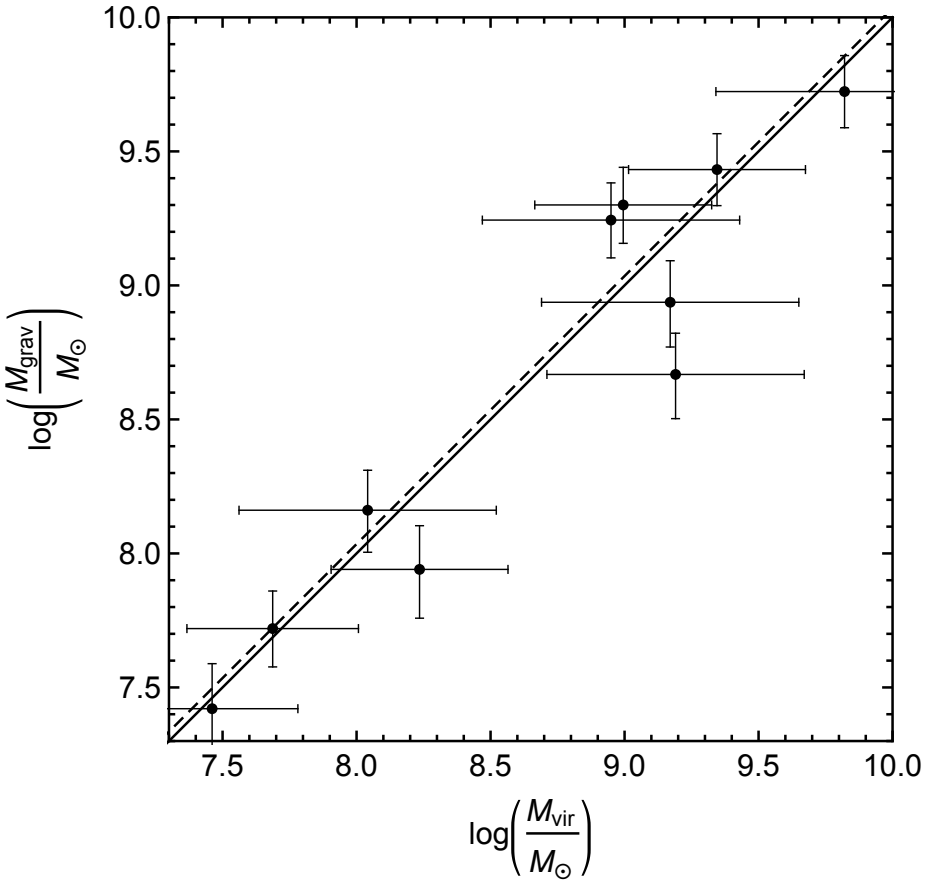

Fig. 7.— Comparison between the virial and gravitational redshift based masses (calibration based on the widths of the CIV lines in the BOSS composite spectra). The solid line corresponds to $M_{grav}^{BOSS} = M_{vir}$. The dashed line corresponds to the best linear fit to the data with slope unity. The small separation between both lines indicates the good agreement between the BOSS based calibration and the calibration that would be obtained using the virial based mass estimates (see text). Errors in M_{vir} are from Assef et al. (2011) or correspond to the dispersions of the virial relationships (Peng et al. 2006, Vestergaard & Peterson 2006). Errors in M_{grav}^{BOSS} include a (conservative) error of ± 1.5 Å in the gravitational redshift estimate, and 0.13 dex of intrinsic scatter in the R-L relationship (Peterson 2014).

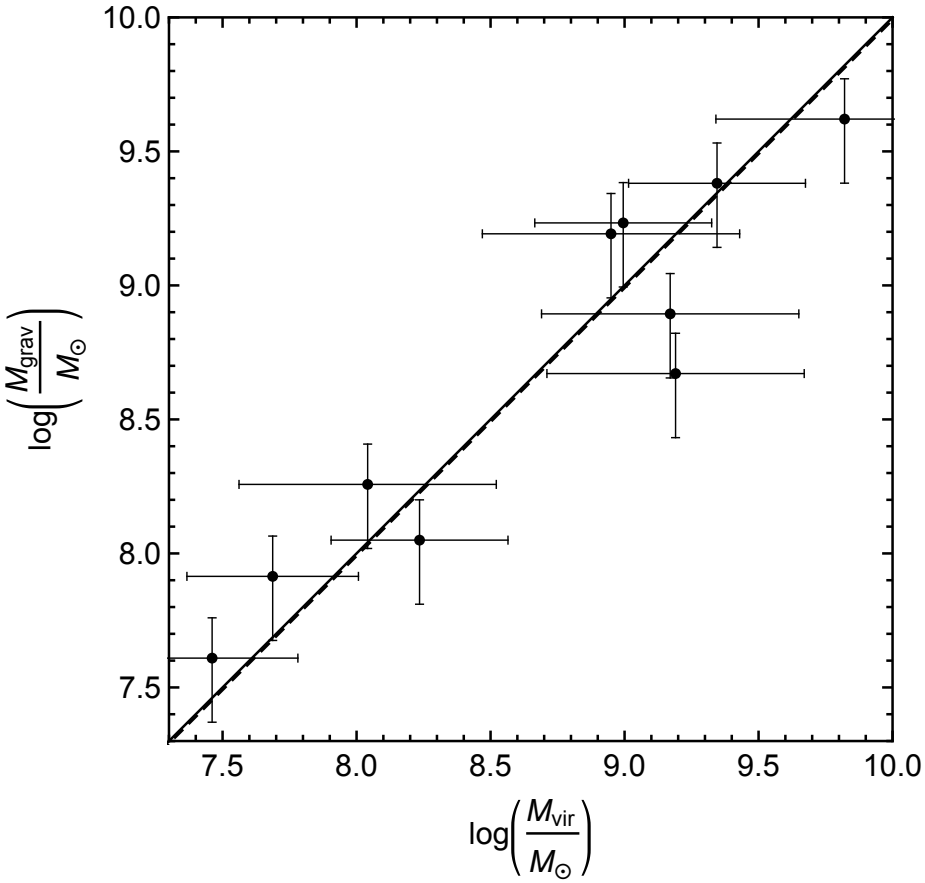

Fig. 8.— Comparison between the virial and gravitational redshift based masses (calibrated using microlensing to determine a **reference size**). The continuous line corresponds to $M_{grav}^{micro} = M_{vir}$. The dashed line corresponds to the best linear fit to the data with slope unity. The very small **separation** between both lines indicates the excellent agreement between the microlensing based calibration and the calibration that would be obtained using the virial based mass estimates. Errors in M_{vir} are from Assef et al. (2011) or correspond to the dispersions of the virial relationships (Peng et al. 2006, Vestergaard & Peterson 2006). Errors in M_{grav}^{micro} include the scatter in the estimate of the average gravitational redshift, the error in the microlensing estimate of the size, and 0.13 dex of intrinsic scatter in the R-L relationship (Peterson 2014).

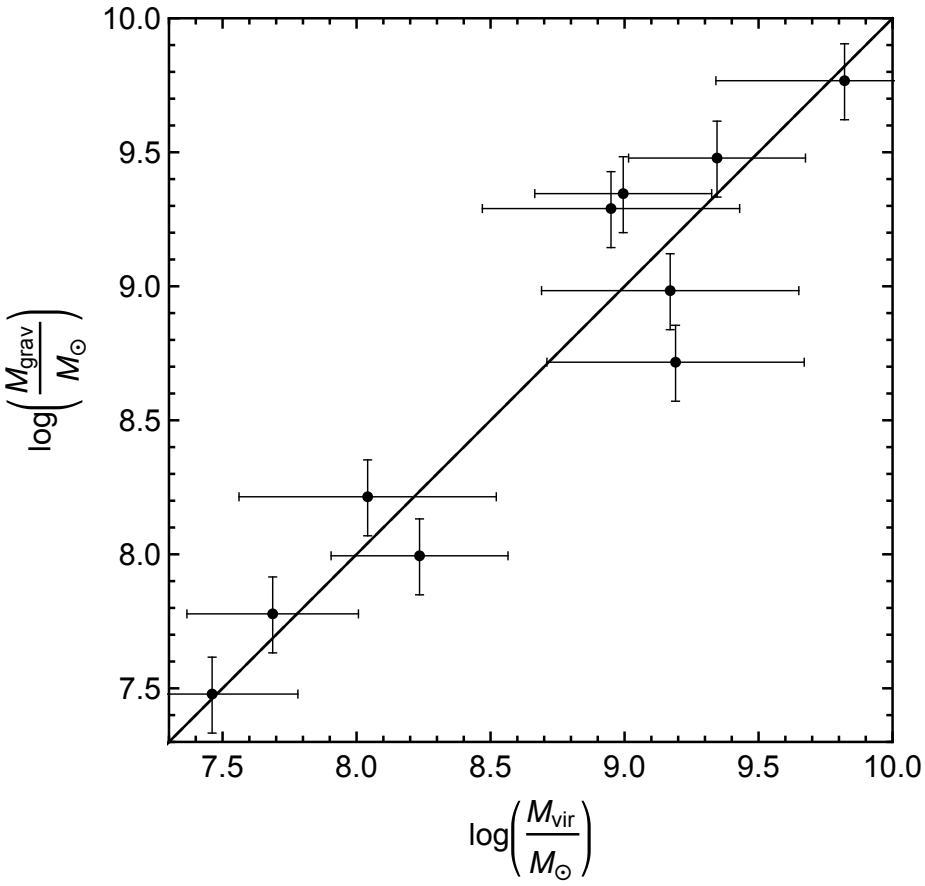

Fig. 9.— Best fit of the mass scaling relationship based on the redshift to the virial masses leaving free the $R \propto L^b$ law. The continuous line corresponds to $M_{grav}^{best\,fit} = M_{vir}$. The best linear fit to the data with slope unity is indistinguishable from this line. Errors in $M_{vir}^{best\,fit}$ are from Assef et al. (2011) or correspond to the dispersions of the virial relationships (Peng et al. 2006, Vestergaard & Peterson 2006). Errors in $M_{grav}^{best\,fit}$ include the error in the parameters of the fit and 0.13 dex of intrinsic scatter in the R-L relationship (Peterson 2014).

5

Conclusions

We have demonstrated that photometric and spectroscopic monitoring of microlensing in gravitationally lensed quasars is a powerful tool to probe the innermost regions of quasars which is far beyond the possibilities of current telescopes. A review of the most important results, like estimating the size of accretion disks, measuring the size/inferring the structure of the BLR, and calculating the mass of supermassive black holes at the center of the quasar engine is listed below.

1 – **Size of the Accretion Disk in the Gravitationally Lensed Quasar SDSS J1004 +4112 from the Statistics of Microlensing Magnifications (Fian et al. 2016)**
We have presented monitoring data for the four brightest images of the five-image gravitational lens system SDSS J1004+4112 which significantly extend the time coverage of previous works. We have used the statistics of microlensing magnifications along the available seasons to infer probabilistic distributions for the source size using two different methods. Using the product of the observed and modeled microlensing histograms we have obtained a half-light radius of $R_{1/2} = 8.7^{+18.5}_{-5.5}\sqrt{M/0.3M_{\odot}}$ light-days. A consistent but more restrictive result of $R_{1/2} = 4.2^{+3.2}_{-2.2}\sqrt{M/0.3M_{\odot}}$ light-days has been obtained using a χ^2 criterion to compare the observed and modeled histograms. Both results are in good agreement with measurements by Motta et al. (2012) and Jiménez-Vicente et al. (2014).

2 – **Estimate of the Accretion Disk Size in the Gravitationally Lensed Quasar HE 0435-1223 using Microlensing Magnification Statistics (Fian et al. 2018a)**
We have used the COSMOGRAIL light curves of the four images of HE 0435-1223 (Bonvin et al. 2017) to obtain the accretion disk size. We have also used two different statistical methods, but in this work we have im-

proved the uncertainty estimations for the Pearson χ^2 method. Using the histogram product of the observed and modeled microlensing histograms we have obtained a half-light radius of $R_{1/2} = 8.4^{+11.1}_{-1.9}\sqrt{M/0.3M_\odot}$ light-days. Consistent results are obtained with Pearson's χ^2 ($R_{1/2} = 8.9^{+5.9}_{-1.2}$ $\sqrt{M/0.3M_\odot}$ light-days). Our results are also in good agreement with previous estimates of other authors for this system ($R_{1/2} = 5^{+4}_{-4}\sqrt{M/0.3M_\odot}$ light-days by Mosquera et al. 2011 and $R_{1/2} = 6.7^{+3.0}_{-2.5}\sqrt{M/0.3M_\odot}$ light-days by Blackburne et al. 2011).

3 – Microlensing and Intrinsic Variability of the Broad Emission Lines of Lensed Quasars (Fian et al. 2018b)

We have analyzed the BELs of a sample of 11 gravitationally lensed quasars with at least two epochs of observation. We have studied, in most cases, up to 11 different spectral features (emission lines or blends) between the C IV and Mg II lines. Although it is limited, the temporal sampling available has allowed us to identify intrinsic variability and to classify the differences between pairs of spectra as candidates for intrinsic variability or microlensing. Taking the cores as reference, we found that the wings of the low ionization lines are not significantly affected (at the 2σ level) by either intrinsic variability or microlensing. On the other hand, the wings of C IV and the other spectral features analyzed (the λ1610 shelf-like feature, He II, the O III]/Al III blend, Al III, Si III, Fe II, and Fe III) show strong changes. These results basically confirm the existence of two spatially distinct regions, one large and insensitive to microlensing and another small and prone to microlensing, giving rise to the broadest components of the lines. The relative impact of microlensing indicates that the low ionization lines arise from a region of ∼50 light-days in size, in good agreement with RM studies. The small regions (a few light-days in size) inferred for several high ionization lines suggest that these lines arise from the accretion disk. In the Fe III$\lambda\lambda$2039-2113 blend, a spectral feature relatively uncontaminated by other species, we measure very high microlensing variability (comparable in some extreme cases to that typical of X-ray) and the largest kinematic broadening. These results suggest that the Fe III (and likely other high ionization species present in strongly microlensed complexes) may arise in part from an inner region of the accretion disk. RM studies of the strongly microlensed iron spectral features could be of great interest in probing the accretion disks of quasars.

4 – Microlensing of the Broad Emission Lines in 27 Gravitationally Lensed Quasars: Broad Line Region Structure and Kinematics (Fian et al., to be submitted)

In our previous work we studied microlensing in the wings of the BELs among 11 strongly lensed quasars, in this work we extend the study by 16 systems and analyze their spectra in up to five epochs of observation. From a statistical analysis using measured microlensing magnifications between image pairs of 27 lensed quasars we estimate the average sizes for the BELs from the product of individual likelihood functions for each image pair, epoch and system. Consistent with other recent studies (see Guerras et al. 2013 and references therein) we found that microlensing depends on the degree of ionization, with higher magnifications observed in the higher ionization lines. This indicates that the emission regions associated with high ionization lines are more compact, as would be expected from photoionization models (Motta & Falco 2016). We obtain size estimates of ∼30 and ∼65 light-days for the C III] and Mg II emission regions. The high impact of microlensing in the C IV emission line indicates that this line arises from a significantly smaller region.

5 – Systematic Redshift of the Fe III UV Lines in Quasars. Measuring Supermassive Black Hole Masses under the Gravitational Redshift Hypothesis (Mediavilla et al. 2018).

We have studied the Fe III λλ2039–2113 emission line blend in 14 spectra of lensed quasars, in two well known AGN (NGC 5548 and NGC 7469), in the SDSS quasar composite spectrum and in 27 BOSS quasar spectra composites. This feature is relatively free of contamination from lines of other species and, according to the impact of microlensing magnification on it, arises from an inner region of the BLR. We find that the Fe III λλ2039–2113 feature appears systematically redshifted by ∼10 Å on average. In combination with microlensing based estimates of the Fe III UV emitting region size from our previous paper (Fian et al. 2018b), the measured redshift for gravitational lenses lead, under the gravitational redshift hypothesis, to values for the central black hole mass, $\langle M_{BH} \rangle \simeq (0.9 \pm 0.5) \times 10^9 M_\odot$, in good agreement with previous virial based estimates.

5.1 Work in Progress and Future Prospects

As seen throughout this thesis, the spectra and light curves of gravitationally lensed quasars are extremely useful to address numerous astrophysical and cosmological questions. In this section we list current work in progress and several prospects for the future.

1 – Unveiling the structure of Q 0957+561.
The quasar QSO 0957+561 was discovered in 1979 by Walsh et al. (1979) and was the first identified gravitationally lensed object. The gravitational field of a foreground galaxy cluster produces two images (A and B) of the same background source, with intrinsic flux variations in B lagging those in A by around 14 months (e.g. Kundić et al. 1997; Gil-Merino et al. 2012). QSO 0957+561 has been monitored over the past 21 years in the R- and V-band, allowing us to estimate its accretion disk size applying the methods described in Section 4.1. In addition, we will apply *PyCS* (a tool provided by COSMOGRAIL) to estimate the time delay between the images. Thus, we are planning to study the structure function of the UV variability. We also posses spectra in ∼20 different epochs (from 1999 to 2016, most of them obtained and kindly provided by Shalyapin and Goicoechea), making it possible to study the structure of the BLR in greater detail.

2 – Estimate the accretion disk size of RX J1131–1231.
COSMOGRAIL provides nine years of optical monitoring in the R-band of the four images of the gravitationally lensed quasar RX J1131–1231. The time delays between the three close images A, B and C are compatible with being zero, while a time delay of 91 days has been measured for image D (Tewes et al. 2013). Our idea is to develop a more rigorous method to estimate the accretion disk size, considering all the permutations of microlensing and hence avoiding to favor any image. A second way to improve our treatment will be to take into account systematic errors and allow for a shift (± 1 and 2σ) of the observed microlensing histograms with respect to the simulated ones. After estimating the probability of r_s for each position of the observed histogram, we can add their probabilities to obtain the final PDF of the source size, $p(r_s)$.

3 – Estimate the accretion disk size of QSO 2237+0305.
Since 1997 OGLE is monitoring the quadruple lensed quasar Q2237+0305 (Huchra's lens) and rapid intrinsic variability as well as several high magnification microlensing events have been detected, making this system an interesting target for studying the size of the continuum emitting region. The photometry of this objects has just been released until 2009 and we are still waiting for the new data of OGLE-IV to be published.

4 – Build database of light curves and study the average accretion disk size.
We will bring together as many light curves of lensed quasars as possible from the Liverpool Quasar Lens Monitoring (LQLM), VizieR, COSMOGRAIL, OGLE and IAC80, with the goal of performing a joint study of all the light curves with our new statistical methods. Our plan is to compute the accretion disk size of an average quasar and estimate the mass fraction in compact objects in the lens galaxies. If light curves are available in several photometric bands, we can also study the average temperature profile of the accretion disk.

5 – Reverberation mapping of the Fe III λλ2039–2113 blend.
Additional studies are required to confirm the gravitational redshift hypothesis to measure supermassive black hole masses using the Fe III UV lines in quasars. The most convincing support likely will be based on high S/N reverberation mapping studies of the Fe III λλ2039–2113 blend in several objects, which can confirm the small size of the emitting region for this spectral feature and provide an accurate R-L relationship for it. We will gather a sample of quasars with strong Fe III emission suitable for RM and ask for observing time at the GTC and VLT.

6 – Study of the kinematic response to microlensing.
The next step in microlensing-based developments will be high resolution studies of the BLR structure, revealed by chromatic asymmetries in the BEL wings of gravitationally lensed quasars. For a few objects (SDSS J1004+4112, SDSS J1339+1310 and SDSS J1206+4332) we can study the microlensing response of different kinematic bins in the wings of the high ionization line C IV. If we have a kinematic model, we can compute the theoretical microlensing response using the spatial distribution predicted by this model for each bin and compare it with the measured microlensing response to analyze the likelihood of the kinematic model (i.e. to probe and constrain the kinematics of the emitters). In particular, in the case of Keplerian rotation around a central supermassive black hole, the sizes of

the emitting regions scale with the mass of the BH and, hence, so does inversely the microlensing amplitude, greater for smaller sizes. Consequently, microlensing can be potentially used as a primary indicator of the central BH mass. We can obtain an estimate of the BH mass for each one of the different kinematic bins which can be used to test the consistence of the hypothesis of Keplerian rotation. From our spectroscopic data we can also derive velocity-microlensing response curves useful to discuss the structure and kinematics of the BLR. Thus, we could use the observed microlensing response for the different bins to study the dependence of the amplitude of the velocity field with distance.

Until now, we have studied the microlensing magnifications vs. velocity responses in two objects (SDSS 1339+1310 and SDSS J1004+4112, see Figure 5.1), obtaining spatially resolved velocity curves ranging from the outer BLR down to the inner parts of the accretion disk (110 to 3 light-days). In both cases, the kinematics can be well fit by Keplerian rotation, but the inferred supermassive black hole mass is too small. This may be explained by a high inclination (as microlensing, in principle, is sensitive to the projected surface of the source) or by departures from circular rotation.

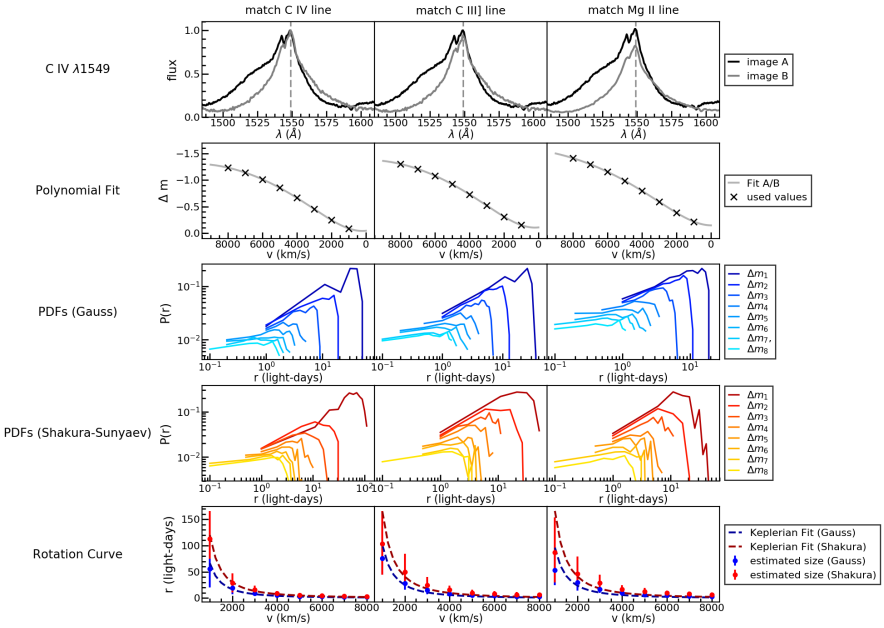

Figure 5.1: C IV emission line (first row) of the images A and B of SDSS J1004+4112. Magnitude differences between the images together with a polynomial fit are shown in the second row. In the third and fourth row PDFs corresponding to different microlensing values are shown for a Gaussian profile (blue) and a Sunyaev-Shakura disk (red). In the last row the size of the emitting region is plotted against the velocity. We performed a Keplerian fit to calculate the mass of the central SMBH.

Bibliography

Abajas, C., Mediavilla, E., Muñoz, J. A., Popović, L. Č., & Oscoz, A. 2002, ApJ, 576, 640

Abdo, A. A. 2013, Gravitational Lensing @ONLINE, http://www.pa.msu.edu/~abdo/GravitationalLensing.pdf, ,

Alcock, C., Akerlof, C. W., Allsman, R. A., et al. 1993, Natur, 365, 621

Amara, A., & Kitching, T. 2010, Strong Lensing @ONLINE, http://gravitationallensing.pbworks.com/w/page/15553257/Strong%20Lensing, ,

Anguita, T., Faure, C., Yonehara, A., et al. 2008, A&A, 481, 615

Antonucci, R. 1993, ARA&A, 31, 473

Aubourg, E., Bareyre, P., Bréhin, S., et al. 1993, Natur, 365, 623

Bate, N. F., Floyd, D. J. E., Webster, R. L., & Wyithe, J. S. B. 2008, MNRAS, 391, 1955

Beckmann, V., & Shrader, C. R. 2012, Active Galactic Nuclei

Belokurov, V., Evans, N., Hewett, P., et al. 2009, Mon.Not.Roy.Astron.Soc., 392, 104

Berkeley, J. C. 2011, Gravitational Lensing @ONLINE, http://www.minorplanetobserver.com/MPOSoftware/CanopusPhotometry.htm, ,

Blackburne, J. A., Kochanek, C. S., Chen, B., Dai, X., & Chartas, G. 2014, ApJ, 789, 125

Blackburne, J. A., Pooley, D., Rappaport, S., & Schechter, P. L. 2011, ApJ, 729, 34

Blandford, R. D., & McKee, C. F. 1982, ApJ, 255, 419

Bond, I. A., Udalski, A., Jaroszyński, M., et al. 2004, ApJL, 606, L155

Bonvin, V., Courbin, F., Suyu, S. H., et al. 2017, MNRAS, 465, 4914

Chang, K., & Refsdal, S. 1979, Natur, 282, 561

Chartas, G., Kochanek, C. S., Dai, X., Poindexter, S., & Garmire, G. 2009, ApJ, 693, 174

Clowe, D., Bradač, M., Gonzalez, A. H., et al. 2006, ApJL, 648, L109

Congdon, A. B., & Keeton, C. R. 2007, in Astronomical Society of the Pacific Conference Series, Vol. 371, Statistical Challenges in Modern Astronomy IV, ed. G. J. Babu & E. D. Feigelson, 411

Czerny, B., Siemiginowska, A., Janiuk, A., & Gupta, A. C. 2008, MNRAS, 386, 1557

Dai, X., Bregman, J. N., Kochanek, C. S., & Rasia, E. 2010, ApJ, 719, 119

Eigenbrod, A. 2011, Gravitational Lensing of Quasars, Fundamental sciences: Physics (EFPL Press)

Eigenbrod, A., Courbin, F., Meylan, G., et al. 2008, A&A, 490, 933

Einstein, A. 1922, Annalen der Physik, 14, 582

—. 1936, Science, 84, 506

Elvis, M. 1985, in Galactic and Extra-Galactic Compact X-ray Sources, ed. Y. Tabaka & W. H. G. Lewin, 291

Eulaers, E. 2012, PhD thesis, Universitè de Liége

Evans, I. N., Tsvetanov, Z., Kriss, G. A., et al. 1993, ApJ, 417, 82

Fian, C., Mediavilla, E., Hanslmeier, A., et al. 2016, ApJ, 830, 149

Floyd, D. J. E., Bate, N. F., & Webster, R. L. 2009, MNRAS, 398, 233

Gandhi, P. 2003, Super Massive Black Holes @ONLINE, `http://www.astro.isas.jaxa.jp/~pgandhi/nakshatra/nakshatra.html`, ,

Gil-Merino, R., Goicoechea, L. J., Shalyapin, V. N., & Braga, V. F. 2012, ApJ, 744, 47

Gil-Merino, R., Wambsganss, J., Goicoechea, L. J., & Lewis, G. F. 2005, A&A, 432, 83

Gómez-Álvarez, P., Mediavilla, E., Muñoz, J. A., et al. 2006, ApJL, 645, L5

Goodstein, D. 2012, Adventures in cosmology (New Jersey, NJ: World Scientific)

Grieger, B. 1990, in Lecture Notes in Physics, Berlin Springer Verlag, Vol. 360, Gravitational Lensing, ed. Y. Mellier, B. Fort, & G. Soucail, 198–202

Grocutt, E. 2014, What is Gravitational Lensing? @ONLINE, `http://www.cfhtlens.org/public/what-gravitational-lensing`, ,

Guerras, E. 2014, PhD thesis, Universidad de La Laguna

Guerras, E., Mediavilla, E., Jimenez-Vicente, J., et al. 2013, ApJ, 778, 123

Guerras, E., Mediavilla, E., Jimenez-Vicente, J., et al. 2013, The Astrophysical Journal, 764, 160

Jiménez-Vicente, J. 2016, Tutorial on inverse ray shooting, ed. E. Mediavilla, J. A. Muñoz, F. Garzon, & T. J. Mahoney, Canary Islands Winter School of Astrophysics (Cambridge University Press), 251–290

Jiménez-Vicente, J., Mediavilla, E., Kochanek, C. S., et al. 2014, ApJ, 783, 47

Joachim Wambsganss, Arlie O. Petters, H. L. 2001, Singularity Theory and Gravitational Lensing (Birkhäuser Boston)

Kayser, R., & Refsdal, S. 1989, Natur, 338, 745

Kayser, R., Refsdal, S., & Stabell, R. 1986, A&A, 166, 36

Kochanek, C. 2006a, in KITP Conference: Applications of Gravitational Lensing: Unique Insights into Galaxy Formation and Evolution, 19

Kochanek, C. S. 2004, Astrophysical Journal, 605, 58

Kochanek, C. S. 2006b, in Saas-Fee Advanced Course 33: Gravitational Lensing: Strong, Weak and Micro, ed. G. Meylan, P. Jetzer, P. North, P. Schneider, C. S. Kochanek, & J. Wambsganss, 91–268

Kochanek, C. S., Dai, X., Morgan, C., Morgan, N., & Poindexter, G., S. C. 2007, in Astronomical Society of the Pacific Conference Series, Vol. 371, Statistical Challenges in Modern Astronomy IV, ed. G. J. Babu & E. D. Feigelson, 43

Kochanek, C. S., Keeton, C. R., & McLeod, B. A. 2001, ApJ, 547, 50

Kollatschny, W. 2010, Memorie della Societa Astronomica Italiana Supplementi, 15, 94

Kundić, T., Turner, E. L., Colley, W. N., et al. 1997, ApJ, 482, 75

Lawrence, A. 1987, PASP, 99, 309

Lemon, C. A., Auger, M. W., McMahon, R. G., & Ostrovski, F. 2018, MNRAS, arXiv:1803.07601

Lewis, G. F., & Ibata, R. A. 2004, MNRAS, 348, 24

Lynds, R., & Petrosian, V. 1986, in BAAS, Vol. 18, Bulletin of the American Astronomical Society, 1014

Malkan, M. A., & Sargent, W. L. W. 1982, ApJ, 254, 22

Massey, R. 2010, in Astronomical Society of the Pacific Conference Series, Vol. 426, 2009 Snowbird Particle Astrophysics and Cosmology Workshop (SNOWPAC 2009), ed. D. B. Kieda & P. Gondolo, 115

Massey, R., Kitching, T., & Richard, J. 2010, Reports on Progress in Physics, 73, 086901

McBreen, B., & Metcalfe, L. 1987, Natur, 330, 348

Mediavilla, E., Jiménez-Vicente, J., Muñoz, J. A., & Battaner, E. 2016, ApJ, 832, 46

Mediavilla, E., Jimenez-Vicente, J., Muñoz, J. A., Mediavilla, T., & Ariza, O. 2015, ApJ, 798, 138

Mediavilla, E., Mediavilla, T., Muñoz, J. A., et al. 2011, ApJ, 741, 42

Mediavilla, E., Muñoz, J. A., Lopez, P., et al. 2006, Astrophysical Journal, 653, 942

Mediavilla, E., Muñoz, J. A., Falco, E., et al. 2009, ApJ, 706, 1451

Mineshige, S., & Yonehara, A. 1999, PASJ, 51, 497

Moore, C. B. 1996, PhD thesis, Massachusetts Institute of Technology

More, A., Oguri, M., Kayo, I., et al. 2016, MNRAS, 456, 1595

Morgan, C. W., Kochanek, C. S., Dai, X., Morgan, N. D., & Falco, E. E. 2008, ApJ, 689, 755

Morgan, C. W., Kochanek, C. S., Morgan, N. D., & Falco, E. E. 2010, ApJ, 712, 1129

Mortonson, M. J., Schechter, P. L., & Wambsganss, J. 2005, ApJ, 628, 594

Mosquera, A. M., & Kochanek, C. S. 2011, ApJ, 738, 96

Mosquera, A. M., Muñoz, J. A., Mediavilla, E., & Kochanek, C. S. 2011, ApJ, 728, 145

Motta, V., & Falco, E. 2016, Four case studies of microlensing, ed. E. Mediavilla, J. A. Muñoz, F. Garzon, & T. J. Mahoney, Canary Islands Winter School of Astrophysics (Cambridge University Press), 51–120

Motta, V., Mediavilla, E., Falco, E., & Muñoz, J. A. 2012, ApJ, 755, 82

Mukherjee, E. 2011, Clarifications on AGN @ONLINE, http://ay20-eric.blogspot.com.es/2011/10/clarifications-on-agn.html, ,

Nemiroff, R. J. 1988, ApJ, 335, 593

Oguri, M. 2004, PhD thesis, University of Tokyo

Peterson, B. M. 2006, in Lecture Notes in Physics, Berlin Springer Verlag, Vol. 693, Physics of Active Galactic Nuclei at all Scales, ed. D. Alloin, 77

Poindexter, S., & Kochanek, C. S. 2010, ApJ, 712, 658

Poindexter, S., Morgan, N., & Kochanek, C. S. 2008, ApJ, 673, 34

Pooley, D., Blackburne, J. A., Rappaport, S., & Schechter, P. L. 2007, Astrophysical Journal, 661, 19

Pooley, D., Rappaport, S., Blackburne, J., et al. 2009, ApJ, 697, 1892

Proft, S. 2016, PhD thesis, Fakultät für Physik und Astronomie Heidelberg

Rees, M. J. 1984, ARA&A, 22, 471

Refsdal, S. 1964a, MNRAS, 128, 307

—. 1964b, MNRAS, 128, 307

—. 1964c, MNRAS, 128, 295

Renn, J., Sauer, T., & Stachel, J. 1997, Science, 275, 184

Richards, G. T., Keeton, C. R., Pindor, B., et al. 2004, ApJ, 610, 679

Schmidt, M. 1969, ARA&A, 7, 527

Schneider, P., & Weiss, A. 1987, Max Planck Institut fur Astrophysik Report, 311

Shields, G. A. 1978, Natur, 272, 706

Sluse, D., Hutsemékers, D., Courbin, F., Meylan, G., & Wambsganss, J. 2012, A&A, 544, A62

Soucail, G., Mellier, Y., Fort, B., Mathez, G., & Cailloux, M. 1987, The Messenger, 50, 5

Sulentic, J. W., Marziani, P., & Dultzin-Hacyan, D. 2000, ARA&A, 38, 521

Suyu, S. H. 2016, Lensing basics, ed. E. Mediavilla, J. A. Muñoz, F. Garzon, & T. J. Mahoney, Canary Islands Winter School of Astrophysics (Cambridge University Press), 1–30

Suyu, S. H., & Halkola, A. 2010, A&A, 524, A94

Suyu, S. H., Marshall, P. J., Auger, M. W., et al. 2010, ApJ, 711, 201

Tewes, M., Courbin, F., Meylan, G., et al. 2013, A&A, 556, A22

Treu, T. 2010, ARA&A, 48, 87

Turner, E. L. 1990, ApJL, 365, L43

Urry, C. M., & Padovani, P. 1995, PASP, 107, 803

Van Waerbeke, L., Mellier, Y., Erben, T., et al. 2000, A&A, 358, 30

Vanden Berk, D. E., Richards, G. T., Bauer, A., et al. 2001, AJ, 122, 549

Vegetti, S., & Koopmans, L. V. E. 2009a, MNRAS, 392, 945

—. 2009b, MNRAS, 400, 1583

Vestergaard, M., & Wilkes, B. J. 2001, ApJS, 134, 1

Walsh, D., Carswell, R. F., & Weymann, R. J. 1979, Natur, 279, 381

Wambsganss, J. 1998, Living Reviews in Relativity, 1, 12

—. 2006, ArXiv Astrophysics e-prints, astro-ph/0604278

Wambsganss, J. 2016, Gravitational (micro)lensing of quasars and AGN, ed. E. Mediavilla, J. A. Muñoz, F. Garzon, & T. J. Mahoney, Canary Islands Winter School of Astrophysics (Cambridge University Press), 121–140

Wambsganss, J., Paczynski, B., & Schneider, P. 1990, ApJL, 358, L33

Wyithe, J. S. B. 1999, ArXiv Astrophysics e-prints, astro-ph/9909358

Zackrisson, E., & Riehm, T. 2010, Adv.Astron., 2010, 478910

Zitrin, A., Labbé, I., Belli, S., et al. 2015, ApJL, 810, L12

Zwicky, F. 1937, ApJ, 86, 217

A

Fian et al. 2018c: BLR Structure, Size and Kinematics II

Draft version June 18, 2018
Typeset using LaTeX **twocolumn** style in AASTeX61

MICROLENSING OF THE BROAD EMISSION LINES IN 27 GRAVITATIONALLY LENSED QUASARS: BROAD LINE REGION STRUCTURE AND KINEMATICS

C. Fian,[1,2] E. Mediavilla et al.,[1,2] and V. Motta[3]

[1] *Instituto de Astrofísica de Canarias, Vía Láctea S/N, La Laguna 38200, Tenerife, Spain*
[2] *Departamento de Astrofísica, Universidad de la Laguna, La Laguna 38200, Tenerife, Spain*
[3] *Instituto de Física y Astronomía, Universidad de Valparaíso, Avda. Gran Bretaña 1111, Playa Ancha, Valparaíso 2360102, Chile*

ABSTRACT

We study the structure and kinematics of the Broad Line Region (BLR) of a sample of 27 gravitationally lensed quasars with up to five different epochs of observation. This sample is composed of ∼100 spectra from the literature plus 22 unpublished spectra of 11 systems. The broad emission lines (BELs) in lensed quasars are expected to be magnified differentially owing to the different sizes of the regions from which they originate. Focusing on the most common broad emission lines in our spectra (C IV, C III] and Mg II), we find that the low ionization line Mg II is only weakly affected by microlensing. In contrast, the high ionization line C IV shows strong microlensing in some cases, indicating that its emission region is more compact. Thus, the BEL profiles are deformed differentially depending on the geometry and kinematics of the corresponding emitting region. We detect microlensing in either the blue or the red wing (or in both wings with different amplitudes) of C IV in more than 50% of the systems and find outstanding asymmetries in the wings of QSO 0957+561, SDSS J1004+4112, SDSS J1206+4332 and SDSS J1339+1310. This observation implies that the BLR is, in general, not spherically symmetric and supports the existence of two regions in the BLR, one insensitive to microlensing and another that only shows up when it is magnified by microlensing. We statistically model the distribution of microlensing magnifications and determine a maximum likelihood estimate for the sizes of the C IV, C III] and Mg II emitting regions. Our estimate for Mg II, $R_{1/2} = 67.3^{+3.8}_{-15.7}\sqrt{M/M_\odot}$, is in good agreement with previous results from smaller samples, while we obtain smaller sizes for the C III] and CIV lines, $R_{1/2} = 31.0^{+1.9}_{-4.0}\sqrt{M/M_\odot}$ and $R_{1/2} = 15.5^{+0.8}_{-3.9}\sqrt{M/M_\odot}$, respectively.

Keywords: quasars: emission lines — gravitational lensing: micro — quasars: general

1. INTRODUCTION

Gravitational lensing is a powerful tool to study the structure of lensed quasars (Pooley et al. 2007; Mosquera et al. 2009; Blackburne et al. 2011; Mosquera & Kochanek 2011). Since the discovery of multiply lensed quasars, anomalies in the flux ratios between the images were found, which were thought to be associated with different phenomena: a complex mass distribution of the lens galaxy, dust extinction, dark matter substructure and microlensing. Quasar microlensing, produced by compact objects (i.e. stars) in the lens galaxy is one of the most likely explanations (Chang & Refsdal 1979; Congdon & Keeton 2005; Wambsganss 2006). They differentially magnify components of the quasar emission regions, leading to time and wavelength-dependent changes in the flux ratios of the images (Wambsganss 2006; Abajas et al. 2002). Microlensing is size sensitive, with smaller source regions showing larger magnifications. Regions with sizes comparable to the angular Einstein radius R_E or smaller are expected to be significantly magnified (Wambsganss 1998, 2006; Schmidt & Wambsganss 2010).

Strong, broad emission lines are characteristic of many galactic nuclei (AGNs) and are produced over a wide range of distances from the central source (see e.g., Sulentic et al. 2000). The narrow line region (NLR) is typically large enough to be insensitive to microlensing by solar mass objects. Also the BELs in gravitationally lensed quasars are expected to be much less affected by microlensing than the continuum. However, the effect of microlensing on the BLR has been first addressed by Nemiroff 1987 and soon after by Schneider & Wambsganss 1990. To be precise, microlensing affects the broad wings of the emission lines that correspond to regions of high velocities, whereas the line cores are supposed to be insensitive to microlensing as they arise from regions spatially much more extended than the region contributing to the wings (Abajas et al. 2002; Richards et al. 2004; Lewis & Ibata 2004; Gómez-Álvarez et al. 2006; Guerras et al. 2013). For this reason, we will use the line cores as reference to set the baseline for no microlensing. The wings of low ionization lines are only weakly affected by microlensing, indicating that they arise from a considerably larger region than the high ionization lines (Guerras et al. 2013). The study of changes induced in the line profiles by microlensing impose significant constraints on the geometry and kinematics of the BLR and on its dependence with ionization degree.

In our previous work (Fian et al. 2018) we compared the emission line profiles of pairs of images from a sample of 11 lensed quasars for which archival spectroscopy was available in more than one epoch. We were able to measure microlensing of $\sim$0.11 mag on average for the low ionization lines, which allowed us to produce estimates for the BLR size of $r_s = 50.3^{+30.4}_{-14.0}$ light-days. Here, we will improve these result by extending the study to a sample of 27 lensed quasars with up to 5 different epochs of observation and by estimating the size of the emission region for each emission line. Our data consist of microlensing measurements based on the comparison between the flux ratios of the wings between pairs of images of around 100 high ionization lines (C IV) and nearly 200 low ionization lines (C III] and Mg II). Prior to that, we match the cores of the emission lines to provide an unmicrolensed baseline that also removes the effects of dust extinction. In this way, constraints on the size of the BLR and on its kinematics can be obtained. We were able to make new, statistically more significant estimates of the BLR size for the high and low ionization lines. To our knowledge, no similar long time baseline spectroscopic study of gravitational lenses has ever been carried out before, so these results are a new and unique probe of the BLR structure.

The paper is organized as follows. In Section 2 we describe the spectra collected from the literature and the extraction and calibration of the new, unpublished spectra. Section 2 also includes the analysis of the microlensing signal observed in the BELs. In Section 3 the main results are shown. In Section 4 we use these microlensing estimates to derive constraints on the typical size of the BEL emitting regions of an average quasar. Section 5 is devoted to the kinematics of the BLR. In Section 6, we estimate the mass of the SMBH using the previously obtained sizes and kinematic information. We discuss and summarize our results in Section 7.

2. DATA AND ANALYSIS

2.1. *Data*

In Fian et al. (2018) we collected from the literature rest frame UV spectra of lensed quasars. In this work we add unpublished spectra taken with the 4.2m William Herschel Telescope (WHT), located at the Roque de los Muchachos in La Palma (Canary Islands, Spain). We obtained ISIS long-slit spectroscopy covering the full optical range for 11 systems for which we had spectra available in previous epochs. The targets were observed with both arms of the ISIS instrument using the gratings R300B and R316B for the blue and red arm, respectively. With this setup, we were able to observe the full range between 3500 and 9000 Å with a spectral sampling of 0.9 Å/pix. This spectral range includes several typical high and low ionization lines of quasars (C IV, C III] and Mg II). The data have been reduced using standard IRAF routines for long-slit 2-D spectroscopic data. These included bias subtraction, flat field and illumination correction, cosmic ray removal, wavelength calibration, background subtraction, flux calibration and extraction of the 1-D spectra. The

data from the literature were already fully reduced. To avoid cross-contamination between the spectra of closely spaced image pairs, we fit two Gaussians to the reduced data in order to separate them. To provide a bigger statistical sample and emphasize trends we also include nine lens systems with single-epoch spectra. In total we gathered a sample of 32 pairs of quasar images in 27 lens systems with up to five epochs of observation. The superpositions of the emission lines corresponding to different images and epochs for each system are shown in Figures 1-4. Information about the systems and references are summarized in Table 1. The following data is provided: name of the object, number of images, number of epochs, observing date, facility and reference.

2.2. *Data Analysis Methods*

We will focus on the low ionization lines C III] λ1909 and Mg II λ2798 and the high ionization line C IV λ1549. For each emission line we used DIPSO in STARLINK to fit a straight line $y = a\lambda + b$ to the continuum on either side of the emission line and subtract it from the spectrum. In order to quantify the effects of microlensing on the BLR, we want to untangle microlensing from the macro-magnification produced by the lens galaxy and extinction. We attempt this by normalizing the continuum-subtracted spectra for all images and all epochs to match the core of the emission line defined by the flux within a narrow interval ($\pm$6Å) centered on the peak of the line. The continuum-subtracted and core matched spectra in the wavelength regions around the C IV, C III], and Mg II emission lines can be seen in Figures 1 to 4. In principle, the cores of the emission lines can be used as a reference that is little affected by microlensing and intrinsic variability (see Guerras et al. 2013; Fian et al. 2018) as they arise from a significantly larger region than the wings. Under this assumption, the ratio of the line wing fluxes between pairs of images at the same epoch or between different epochs for the same image, F_{1wings}/F_{2wings}, yields a measurement of the size of the emitting region. To prevent an underestimation of the microlensing in the wings we separate the line core from the wings by a buffer of $\pm$9Å. We then can estimate the average wing emission in different wavelength intervals ($\sim$25Å for C IV, $\sim$35Å for CIII] and Mg II) on either side of the emission line peak, corresponding to velocity intervals of $\sim$4500 km/s for C IV, $\sim$5300 km/s for CIII], and $\sim$3600 km/s for Mg II. In those cases in which the emission line is affected by absorption lines an integration window avoiding absorption features was chosen (see Figures 1 to 4). We use the following statistics to calculate the magnitude difference in the wings at each wavelength x between two different images/epochs (α,β):

$$\Delta m_x = w_x * (\beta_x - \alpha_x), \quad (1)$$

with weights $w_x = \sqrt{<\beta_x + \alpha_x>/(\beta_x + \alpha_x)}$, selected to equalize the typical deviations of the differences. From the mean value in a given wavelength interval, $\langle \Delta m_x \rangle$, we compute the magnitude difference between images/epochs, $\Delta m = \langle \Delta m_x \rangle$, and its standard deviation σ. We will not use values with uncertainties above a given threshold ($\sigma = 0.5$mag). The estimated magnitude differences between images with S/N ratio greater than 1.5 are given for each epoch in Table 2 and similarly, the magnitude differences between epochs for each image are presented in Table 3. To qualify the magnitude differences between images and/or epochs as candidates for microlensing or intrinsic variability we have used the same criteria as in Fian et al. 2018: (i) the S/N ratio should be greater than 2, (ii) any difference between images is considered a candidate for microlensing, (iii) we consider as a candidate for intrinsic variability a difference between two epochs when it is present in at least two images, (iv) when neither (ii) nor (iii) apply we consider that we have insufficient information to qualify the difference, although intrinsic variability may be more likely (partial evidence of intrinsic variability). The resulting classification is also shown in Tables 2 and 3.

3. RESULTS

In general, there is a good match between the emission line profiles of different images at different epochs, as seen in Figures 1 to 4. The Mg II line is only weakly affected by either microlensing or intrinsic variability (consistent with the results presented in our previous work). Only one system (HE 0435-1223) shows a small change (0.11 mag) with S/N > 2 in the selected integration window for the blue wing as defined in Figure 1. Visually inspecting the data, we find changes in the extreme red wings of SBS 0909+532 and SDSS J1206+0118. These changes could have their origin in the UV Fe II blend $\lambda\lambda$2861-2917 located redward of Mg II, showing up with different intensities for different quasar spectra (see Kovačević-Dojčinović & Popović 2015).

Contrary to the results obtained from the limited sample presented in our previous work we find, on the basis of more available epochs, that the CIII] line seems to be significantly more affected by microlensing than the Mg II line, indicating that it arises from a more compact region inside the BLR. We detect microlensing at the 2σ level within the defined integration windows in four systems (SDSS J0246-0825, HE 0435-1223, SDSS J1155+6346, WFI 2033-4723), whereas evidence of intrinsic variability (at the 2σ level) can only be found in one system (Q0957+561). Also the systems SDSS 1004-4112, SDSS J1155+6346 and HE 1104-1805 show microlensing differences at a smaller S/N ratio ($\sigma \geq 1.5$).

In the case of C IV there are obvious differences in the selected windows of the line profiles with nearly half of the

sample showing changes due to microlensing and/or intrinsic variability. After consistently separating microlensing from intrinsic variability according to the criteria explained in Section 2.2 (see also Tables 2 and 3), we find that nine objects are clearly affected by microlensing at the 2σ level (HE 0435-1223, HS 0818-1227, FBQS J0951+2635, QSO 0957+561, SDSS J1004+4112, SDSS J1138+0314, SDSS J1206+4332, SDSS J1339+1310, HE 2149-2745) and two systems show evidences of intrinsic variability at the 2σ level (HE 1104-1805, HE 2149-2745). The fact that for some systems C IV does not show microlensing anomalies may be because its emission region is either too big or it lies in a region without significant microlensing fluctuations. However, the non-detection of microlensing also puts constrains on the size of the emission region and should be taken into account. Additional three systems (SBS 0909+532, Q1017-207, SBS 1520+530) are showing evidences of microlensing at the 1.5σ level and Q 0142-100 seems to be dominated by intrinsic variability. The differences observed in QSO 0957+561 may be explained by intrinsic variability combined with the large time-delay between the images of this double plus a possible contribution from microlensing. It is important to notice that intrinsic variability mainly affects the wings of C IV but in contrast with microlensing it does not induce marked asymmetries in the line profile.

In Figure 5 and 6 we show, for systems with at least two epochs of observation, the average spectra with one/two sigma intervals to emphasize the variability in the wings. There are several systems (Q 0142-100, HE 0435-1223, FBQS J0951+2635, QSO 0957+561, SDSS J1004+4112, HE 1104-1805, SDSS J1206+4332, SDSS J1339+1310, HE 2149-2745) in which microlensing and/or intrinsic variability is strongly affecting the wings of C IV (mainly the red wing) with little or no traces of variability in the wings of C III] and Mg II (except the blue wing of C III] in SDSS J1004+4112 and the extreme red wing of Mg II in SDSS J1206+4332).

In Figures 7 and 8 we present histograms of the differences between images/epochs for the C IV, C III] and Mg II lines. We have overlaid the corresponding Gaussian kernel density estimates of the probability density functions (PDFs) to show the impact of errors in the individual measurements. The first thing to note is that microlensing/intrinsic variability effects diminish according to the sequence: C IV > C III] > Mg II. The second thing to note is that the differences between the images are more or less of the same order of magnitude as differences between the epochs.

4. STRUCTURE OF THE BROAD LINE REGION

Given the estimates of the differential microlensing in the wings between pairs of images in each system for different emission lines, we can estimate the size of their emission region and thus reveal the structure of the BLR in lensed quasars. We treat each microlensing measurement as a single epoch event and from the microlensing magnification corresponding to all the image pairs, in all available epochs of observation, we compute the joint microlensing probability, $P(r_s)$, to obtain an average estimate of the size. We follow the steps described in Guerras et al. (2013),

$$P(r_s) = \prod_i P_i(r_s), \tag{2}$$

$$P_i(r_s) \propto e^{-\frac{\chi^2_i(r_s)}{2}}, \tag{3}$$

$$\chi^2_i(r_s) = \sum_{\alpha_i} \sum_{\beta_i<\alpha_i} \left(\frac{\Delta m^{obs}_{\beta_i\alpha_i} - \Delta m_{\beta_i\alpha_i}(r_s)}{\sigma_{\beta_i\alpha_i}} \right)^2, \tag{4}$$

where $\Delta m^{obs}_{\beta_i\alpha_i}$ is the observed differential microlensing magnification between images α and β of system i and $\Delta m_{\beta_i\alpha_i}(r_s)$ is the differential microlensing magnification predicted by the simulations for a given value of r_s.

Our simulations are based in 2000×2000 pixel microlensing magnification maps, generated at the positions of the images using the Inverse Polygon Mapping method described in Mediavilla et al. (2006, 2011). To compute the magnification maps we used the local convergence κ and the local shear γ, obtained by fitting a singular isothermal sphere with an external shear (SIS+γ_e) that reproduce the coordinates of the images (Mediavilla et al. 2006). The produced maps span 400×400 light-days^2 on the source plane, with a pixel size of 0.2 light-days. We assume a mean stellar mass of $M = 0.3 M_\odot$ and for the fraction of mass in stars we use $\alpha = 0.1$. All linear sizes can be rescaled with the square root of the microlens mass $\sqrt{M/M_\odot}$. To simulate the effect of finite sources we model the luminosity profile of the region emitting the wings as a Gaussian ($I \propto exp(-R^2/2rs^2)$) and the magnifications experienced by a source of size r_s are then found by convolving the magnification maps with the Gaussian profiles of sigma r_s. We used a logarithmic grid for the source sizes, spanning an interval between $\sim$1 to 100 light-days. These sizes can be converted to half-light radii multiplying by 1.18, $R_{1/2} = 1.18 r_s$.

The resulting joint likelihood functions, scaled to a mean microlens mass of $\langle M \rangle = 1 M_\odot$, for the C IV, C III] and Mg II emission lines can be seen in Figure 9. From the right panel in Figure 9 we can infer (using a logarithmic prior for the size) a size of $r_s = 57.0^{+3.2}_{-13.3} \sqrt{M/M_\odot}$ light-days (68% confidence) for the region emitting the Mg II line. This result is in good agreement with the size of the LIL obtained by Guerras et al. (2013) ($r_s = 55^{+150}_{-35} \sqrt{M/M_\odot}$ light-days).

From the likelihood function (middle panel of Figure 9) corresponding to the observed microlensing we estimate a size of $r_s = 26.3^{+1.6}_{-3.4}\sqrt{M/M_\odot}$ light-days for the region emitting C III]. Note that this line is blended with Al III and Si III in the wavelength range used to define the red wing, therefore we are likely underestimating the size of its emitting region. For C IV, we obtain a size of $r_s = 13.1^{+0.7}_{-3.3}\sqrt{M/M_\odot}$ light-days, indicating that this line is formed in the inner part of the BLR close to the accretion disk.

5. KINEMATICS OF THE BROAD LINE REGION

We present inferences on the kinematics of the BLR by studying the line profiles corresponding to C IV, C III] and Mg II as a function of velocity. In Figure 10 a superposition of the average line profiles for each system can be seen as well as the global average for all systems. The wings of Mg II correspond to relatively low velocities as compared with C III] and C IV, which is consistent with the weak impact of microlensing on this line. From Figure 10 we see that, in general[1], the core ($|\Delta v| \leq 700$ km/s) and the emission line component defined by $|\Delta v| < 3000$ km/s is narrower for Mg II when compared with those of C III] and C IV. The high-velocity wings of Mg II ($|\Delta v| > 4000$ km/s) are blended by several Fe II lines (Vestergaard & Wilkes 2001; Vestergaard et al. 2011) and no reasonable comparison can be made.

Regarding C III], to ease visualization in the case of symmetric line profiles, we mirror the red part of the emission line profile in order to remove the blending by Al III and Si III in the blue wing. In most cases[2], the red part of C III] and C IV match very well, except at the lowest intensity level where the shelf-like feature $\sim \lambda 1610$ (see, e.g. Fian et al. (2018)) is present in C IV. This striking kinematic coincidence propounds that both lines are mostly generated in the same region. However, the C IV line can be strongly affected by microlensing (see, for instance, the cases of QSO 0957+561, SDSS J1004+4112, SDSS J1206+4332 and SDSS J1339+1310), whereas C III] seems to be rather insensitive to this effect (except the blue wing of SDSS J1004+4112). This fact reveals the existence of an emitter located in a region small enough to be prone to microlensing, exclusively contributing to the C IV line but not to C III].

We made four rough estimates of the distance moved by the accretion disk relative to the magnification pattern during the time elapsed between epochs of observation (∼1 year in SDSS J1339+1310, ∼12 years in SDSS J1206+4332, ∼13 years in SDSS J1004+4112, and ∼17 years in QSO 0957+561) for these systems. As discussed in our previous work, the distance traveled in the source plane is too small (∼0.6 light-days) for SDSS J1339+1310 to see variability in both wings. However, for SDSS J1206+4332 and SDSS J1004+4112 we obtained more interesting results, owing to larger displacements of the source (∼8 light-days for SDSS J1206+4332 and ∼12 light-days for SDSS J1004+4112). If we compare the four epochs in SDSS J1004+4112, we can see that the strongly magnified blue wing fades while the red wing enhances. In SDSS J1206+4332 we detect, when comparing epoch I and II, a slight demagnification of image B in the blue wing while the red wing enlarges. These observations confirm that the separation between the approaching and recending parts of the microlensed region of the BLR is about a few light-days in size. The case of QS0 0957 is more complex as the changes induced in the red wing may be due to intrinsic variability combined with the large time-delay between the images plus a possible contribution from microlensing. Although the distance moved on the source plane by this system is rather large (∼17 light-days), we do not detect an enhancement in the blue wing. This result can be explained by an unusually large accretion disk (paper in preparation).

In the left panel of Figure 11 we show the average amplitude of microlensing between images of all systems as a function of the Mg II, C III], and C IV line broadenings. By using the average line profile of as many lines as possible we hope to even out the deviations in the line profile introduced by the individual lines. We do not take into account noisy spectra and spectra with absorption features. There are a couple of important issues to keep in mind when estimating the FWHM of the BELs: (i) it plays an important role where to fit and subsequently subtract the continuum underneath the line; for all systems and images we fit the continuum in the same wavelength regions (we allow some margin for a better adjustment of the fit to the corresponding continuum); (ii) blending by other emission lines may lead to an overestimation of the FWHM; (iii) an added complication in measuring the FWHM is the setting of the zero point in the emission line. To estimate the uncertainties in the measured FWHM, we vary the zero point of the line by ± 10% (see Figure 12), leading to variations of ∼25% in the FWHM. Note that one of the main sources of error in the measurement of the FWHM of C IV is the fraction of the shelf-like feature at $\sim \lambda 1610$ under the emission line. The C III] is blended with Al III and Si III in the blue wing and therefore this wing cannot be used to compute the FWHM. It is important to remove these effects when measuring the line width

[1] HE 0047-1756, SDSS J0246-0825, SDSS J0806+2006, SDSS J0924+0219, QSO 0957+561, HE 1104-1805, SDSS J1339+1310, SDSS J1353+1138, WFI J2033-4723, HE 2149-2745

[2] HE 0047-1756, Q 0142-100, HE 0435-1223, SBS 0909+532, QSO 0957+561, SDSS J1001+5027, SDSS J1004+4112, HE 1104-1805, SDSS J1138+0314, SDSS J1206+5332

to prevent an overestimation of the FWHM. We attempt this by using twice the distance of the half maximum of the line center to the red wing. In the case of Mg II, the line is located in the middle of the small blue bump of thousands of Fe II lines and is seriously contaminated by the blended iron lines and by the Balmer continuum (Vestergaard & Wilkes 2001; Vestergaard et al. 2011; Kovačević-Dojčinović et al. 2017). Hence, we are likely overestimating the FWHM of the Mg II line since half of the Mg II profile is submerged in the Fe II emission.

6. ESTIMATE OF THE SMBH MASS

It has become common practice to estimate central black hole masses based on the information that can be obtained from single-epoch spectra of multiple lensed quasars in a similar way as with reverberation mapping (RM). The Doppler broadening of the emission lines (FWHM) can be used as a proxy for the virial velocity (Shen & Kelly 2012; Marziani & Sulentic 2012; Coatman et al. 2016) and combined with the size estimates of the emitting regions provided by microlensing we can estimate the virial mass, M_{BH}, according to

$$M_{BH} \simeq 9.8 \times 10^7 M_\odot \, f \left(\frac{R_{BLR}}{5\,\mathrm{light\,days}} \right) \left(\frac{\Delta v_{FWHM}}{10000\,\mathrm{km\,s^{-1}}} \right)^2 \quad (5)$$

with f, the fudge-factor, containing the unknown characteristics of structure, geometry, and details of the velocity field and its inclination along the line-of-sight (see Peterson 2011). This approach assumes that the BLR is virialized and provides a powerful tool for obtaining black hole masses of distant quasars by using the emission line widths of Mg II and C IV to probe the BLR velocities when the Balmer lines are redshifted out of the optical observing window (Vestergaard & Wilkes 2001).

We apply this relationship to the C IV, C III] and Mg II emission lines with Δv_{FWHM} corresponding to the FWHM of the average line profiles obtained from our sample and R_{BLR} corresponding to the sizes estimated using microlensing. We use a χ^2 criterion to test for goodness of fit to those three points and we obtain a black hole mass of $M_{BH} \sim 2.4^{+1.5}_{-0.4} 10^8 M_\odot$ for $f = 2$, which is a reasonable result for the bright quasars of our sample (Mosquera & Kochanek 2011). From Figure 12 we can conclude that on average the microlensing-based sizes are in agreement with the hypothesis of virialized kinematics. Our result is also consistent within the uncertainties with the black hole mass obtained in our previous work ($M_{BH} \sim 3.9^{+1.8}_{-1.4} 10^8 M_\odot$) by considering the Fe III $\lambda\lambda$2039-2113 blend of size $R_{BLR} \sim 11.3^{+5}_{-4}$ light-days and of velocity Δv_{FWHM} ∼9400 km/s.

7. CONCLUSION

In our previous work we studied microlensing in the wings of the BELs among 11 strongly lensed quasars, in this work we extend the study by 16 systems and analyze their spectra in up to five epochs. In total, taking into account all images and all epochs, we studied ∼100 C IV lines, more than 110 C III] lines and around 80 Mg II lines. We have identified various signatures of microlensing in the wings of the BELs and, subsequently, measuring its strength allowed us to constrain the sizes of their emitting region and hence study their kinematics. We finally discuss the consequences of our results and draw following conclusions:

1 – *Microlensing.* The main results of the previous sections are that the Mg II line is formed (as usually assumed) in an outer part of the BLR as it is only weakly affected by microlensing, whereas the wings of C IV suffer strong microlensing, indicating that this line forms very close to the accretion disk. We find in our sample that around 50% of the systems show microlensing in the C IV line. Despite the large occurrence of microlensing in the wings of C IV, also C III] is significantly microlensed in about 25% of the systems. Significant variations caused by microlensing are rare in the wings of Mg II, with only two systems showing changes associated to microlensing. We do not detect microlensing simultaneously in all three emission lines, indicating a different origin/size of their emitting region.

2 – *Intrinsic Variability.* The temporal sampling (up to five epochs of observation) allowed us to identify intrinsic variability and to classify the differences between pairs of spectra as candidates for intrinsic variability or microlensing. We derive robust estimates of both, intrinsic variability and amplitude of microlensing between the lensed images, and consistently separated a group of five objects dominated by microlensing (SBS 0909+532, FBQS J0951+2635, SDSS J1004+4112, SDSS J1206+4332, and SDSS J1339+1310) and another group of three systems in which intrinsic variability prevails (Q 0142-100, HE 1104-1805, and WFI 2033-4723). Two systems (HE 0435-1223 and HE 2149-2745) seem to be hybrid cases with both microlensing and intrinsic variability present. Finally, the case of QSO 0957+561 may be explained by intrinsic variability combined with the large time-delay between the images plus a possible contribution from

microlensing.

3 – *Size, Structure and Geometry.* The fact that the wings of Mg II are generally not affected by microlensing whereas the wings of C IV (C III]) show strong (moderate) changes favors the hypothesis of two distinct regions, one large and insensitive to microlensing and the other one small and prone to microlensing. We frequently detect microlensing in either the blue or the red wing of C III] and/or C IV instead of a signal affecting symmetrically both components. This result implies that the BLR does not have a spherically symmetric geometry.

Strong microlensing can induce very noticeable asymmetries in the line profile shape of C IV. Intrinsic variability seems to affect the wings with similar strength, although no outstanding evidence of asymmetry associated with intrinsic variability has been detected. These simple observations support the hypothesis that the small region prone to both microlensing and intrinsic variability is intrinsically symmetrical, and that the asymmetry induced by microlensing in the line profile is related to the anisotropic spatial distribution of microlensing magnification at the source plane.

From a statistical analysis using measured microlensing magnifications between image pairs of 27 lensed quasars we estimate the average sizes for the BELs from the product of individual likelihood functions for each image pair, epoch and system. This method includes the cases with little or no microlensing that by themselves contribute to the size estimates. Consistent with other recent studies (see Guerras et al. 2013 and references therein) we found that microlensing depends on the degree of ionization, with magnifications more pronounced in the high ionization lines. Taking as reference the cores (which have been considered unchanging in single epoch based studies), we find that the wings of Mg II are not significantly affected by either microlensing or intrinsic variability. The relative impact of microlensing is larger in C III] when compared with Mg II, indicating that the emission region associated with this line is more compact. We obtain size estimates of ∼30 and ∼65 light-days for the C III] and Mg II emission lines, in good agreement with RM studies (?). The high impact of microlensing in the C IV emission line indicates that this line arises from a region of ∼15 light-days in size.

4 – *Kinematics.* From the impact if microlensing and intrinsic variability in the wings of C IV, C III] and Mg II, we attempt to broadly outline a basic relationship between kinematics and structure in the BLR. The unblended red part of the average line profiles of C IV and C III] match very well in the absence of microlensing. This kinematic coincidence indicates that both lines arise mainly from the same region. However, this alikeness in the line profiles is broken by the changes induced my microlensing, resulting in strong deformations in the C IV line profile while leaving unchanged the line profile of C III]. The high impact of microlensing in C IV reveals the existence of a second region (a few light-days in size), only contributing to the C IV line but not to C III] or Mg II.

5 – *Line Deformations.* Depending on the structure of the BLR, microlensing could modify the broad line profiles. The frequent observation of asymmetric deformations of the emission lines and detection of microlensing in only one of the wings (i.e. either of the red or blue component) demonstrates that the BLR does not have, in general, a spherically symmetric geometry. Microlensing of a spherically symmetric BLR would lead to symmetric variations of the emission lines, while microlensing of a Keplerian disk leads to asymmetric variations (see e.g. Sluse et al. 2012 and references therein). We have been able to unveil outstanding microlensing-induced deformations in the wings of C IV in four systems (QSO 0957+561, SDSS J1004+4112, SDSS J1206+4332, and SDSS J1339+1310). For SDSS J1206+4332 and SDSS J1339+1310 we detect clearly asymmetrical enhancements toward the red. In the well studied case of SDSS J1004+4112 (Richards et al. 2004; Gómez-Álvarez et al. 2006; Motta et al. 2012; Fian et al. 2016 and references therein) we detect variable enhancements in both wings, again highly asymmetric but this time the blue part is dominant.

C.F. gratefully acknowledges the financial support of a La Caixa PhD fellowship. E.M. and J.A.M are supported by the Spanish MINECO with the grants AYA2016-79014-C3-1-P and AYA2016-79014-C3-3-P. J.J.V. is supported by the Spain's Ministerio de Economía y Competitividad and the Fondo Europeo de Desarrollo Regional (FEDER) through grant AYA2014-53506-P and by the Junta de Andalucía through project FQM-108.

REFERENCES

Abajas, C., Mediavilla, E., Muñoz, J. A., Popović, L. Č., & Oscoz, A. 2002, ApJ, 576, 640
Blackburne, J. A., Pooley, D., Rappaport, S., & Schechter, P. L. 2011, ApJ, 729, 34
Burud, I., Courbin, F., Magain, P., et al. 2002, A&A, 383, 71
Chang, K., & Refsdal, S. 1979, Nature, 282, 561
Chavushyan, V. H., Vlasyuk, V. V., Stepanian, J. A., & Erastova, L. K. 1997, A&A, 318, L67
Coatman, L., Hewett, P. C., Banerji, M., & Richards, G. T. 2016, MNRAS, 461, 647
Congdon, A. B., & Keeton, C. R. 2005, MNRAS, 364, 1459
Eigenbrod, A., Courbin, F., Dye, S., et al. 2006, A&A, 451, 747
Eigenbrod, A., Courbin, F., & Meylan, G. 2007, A&A, 465, 51
Fian, C., Guerras, E., Mediavilla, E., et al. 2018, ApJ, 859, 50
Fian, C., Mediavilla, E., Hanslmeier, A., et al. 2016, ApJ, 830, 149
Goicoechea, L. J., Gil-Merino, R., & Ullán, A. 2005, MNRAS, 360, L60
Goicoechea, L. J., & Shalyapin, V. N. 2016, A&A, 596, A77
Gómez-Álvarez, P., Mediavilla, E., Muñoz, J. A., et al. 2006, ApJL, 645, L5
Guerras, E., Mediavilla, E., Jimenez-Vicente, J., et al. 2013, The Astrophysical Journal, 764, 160. http://stacks.iop.org/0004-637X/764/i=2/a=160
Inada, N., Oguri, M., Becker, R. H., et al. 2006, AJ, 131, 1934
Kovačević-Dojčinović, J., Marčeta-Mandić, S., & Popović, L. Č. 2017, Frontiers in Astronomy and Space Sciences, 4, 7
Kovačević-Dojčinović, J., & Popović, L. Č. 2015, ApJS, 221, 35
Lewis, G. F., & Ibata, R. A. 2004, MNRAS, 348, 24
Marziani, P., & Sulentic, J. W. 2012, NewAR, 56, 49
Mediavilla, E., Mediavilla, T., Muñoz, J. A., et al. 2011, ApJ, 741, 42
Mediavilla, E., Muñoz, J. A., Kochanek, C. S., et al. 2005, ApJ, 619, 749
Mediavilla, E., Muñoz, J. A., Lopez, P., et al. 2006, ApJ, 653, 942
Morgan, N. D., Caldwell, J. A. R., Schechter, P. L., et al. 2004, AJ, 127, 2617
Mosquera, A. M., & Kochanek, C. S. 2011, ApJ, 738, 96
Mosquera, A. M., Muñoz, J. A., & Mediavilla, E. 2009, ApJ, 691, 1292
Motta, V., Mediavilla, E., Falco, E., & Muñoz, J. A. 2012, ApJ, 755, 82
Motta, V., Mediavilla, E., Rojas, K., et al. 2017, ApJ, 835, 132
Nemiroff, R. J. 1987, PhD thesis, Pennsylvania Univ., Philadelphia., doi:10.5281/zenodo.33974
Oguri, M., Inada, N., Hennawi, J. F., et al. 2005, ApJ, 622, 106
Peterson, B. M. 2011, ArXiv e-prints, arXiv:1109.4181
Pooley, D., Blackburne, J. A., Rappaport, S., & Schechter, P. L. 2007, ApJ, 661, 19
Richards, G. T., Keeton, C. R., Pindor, B., et al. 2004, ApJ, 610, 679
Rojas, K., Motta, V., Mediavilla, E., et al. 2014, ApJ, 797, 61
Schechter, P. L., Gregg, M. D., Becker, R. H., Helfand, D. J., & White, R. L. 1998, AJ, 115, 1371
Schmidt, R. W., & Wambsganss, J. 2010, General Relativity and Gravitation, 42, 2127. https://doi.org/10.1007/s10714-010-0956-x
Schneider, P., & Wambsganss, J. 1990, A&A, 237, 42
Shalyapin, V. N., & Goicoechea, L. J. 2014, A&A, 568, A116
Shen, Y., & Kelly, B. C. 2012, ApJ, 746, 169
Sluse, D., Hutsemékers, D., Courbin, F., Meylan, G., & Wambsganss, J. 2012, A&A, 544, A62
Sulentic, J. W., Marziani, P., & Dultzin-Hacyan, D. 2000, ARA&A, 38, 521
Surdej, J., Claeskens, J.-F., Remy, M., et al. 1997, A&A, 327, L1
Vestergaard, M., Denney, K., Fan, X., et al. 2011, in Narrow-Line Seyfert 1 Galaxies and their Place in the Universe, 38
Vestergaard, M., & Wilkes, B. J. 2001, ApJS, 134, 1
Wambsganss, J. 1998, Living Reviews in Relativity, 1, 12
Wambsganss, J. 2006, in Saas-Fee Advanced Course 33: Gravitational Lensing: Strong, Weak and Micro, ed. G. Meylan, P. Jetzer, P. North, P. Schneider, C. S. Kochanek, & J. Wambsganss, 453–540
Wisotzki, L., Becker, T., Christensen, L., et al. 2003, A&A, 408, 455
Wisotzki, L., Koehler, T., Ikonomou, M., & Reimers, D. 1995, A&A, 297, L59
Wisotzki, L., Koehler, T., Kayser, R., & Reimers, D. 1993, A&A, 278, L15
Wisotzki, L., Schechter, P. L., Chen, H.-W., et al. 2004, A&A, 419, L31
Wucknitz, O., Wisotzki, L., Lopez, S., & Gregg, M. D. 2003, A&A, 405, 445

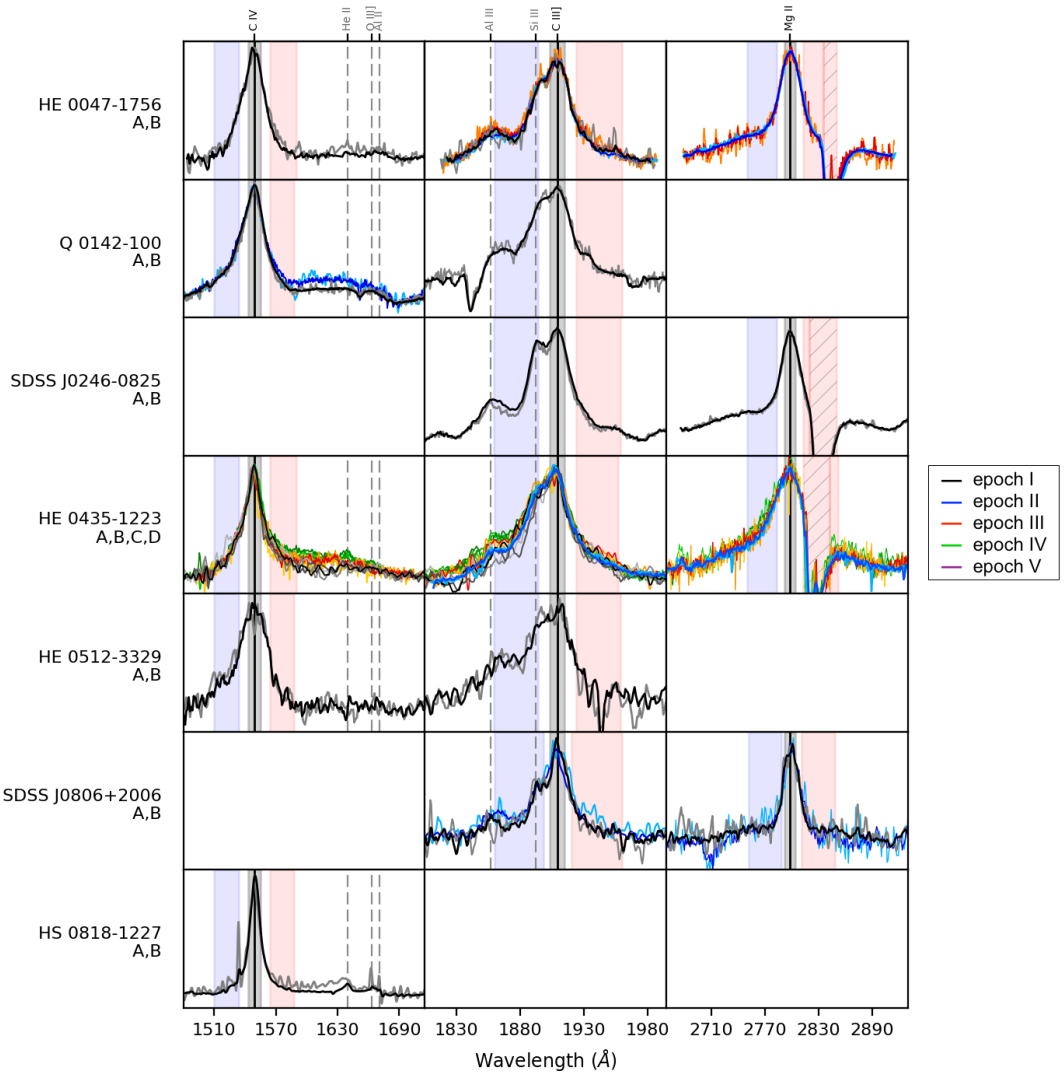

Figure 1. C IV, C III] and Mg II emission line profiles from different epochs and images overimposed after subtracting the continuum and matching the line core. Different color shadings stand for different images in the corresponding epoch. Blue/red shaded regions show the integration windows used for the magnitude difference calculations. The flux is in arbitrary units.

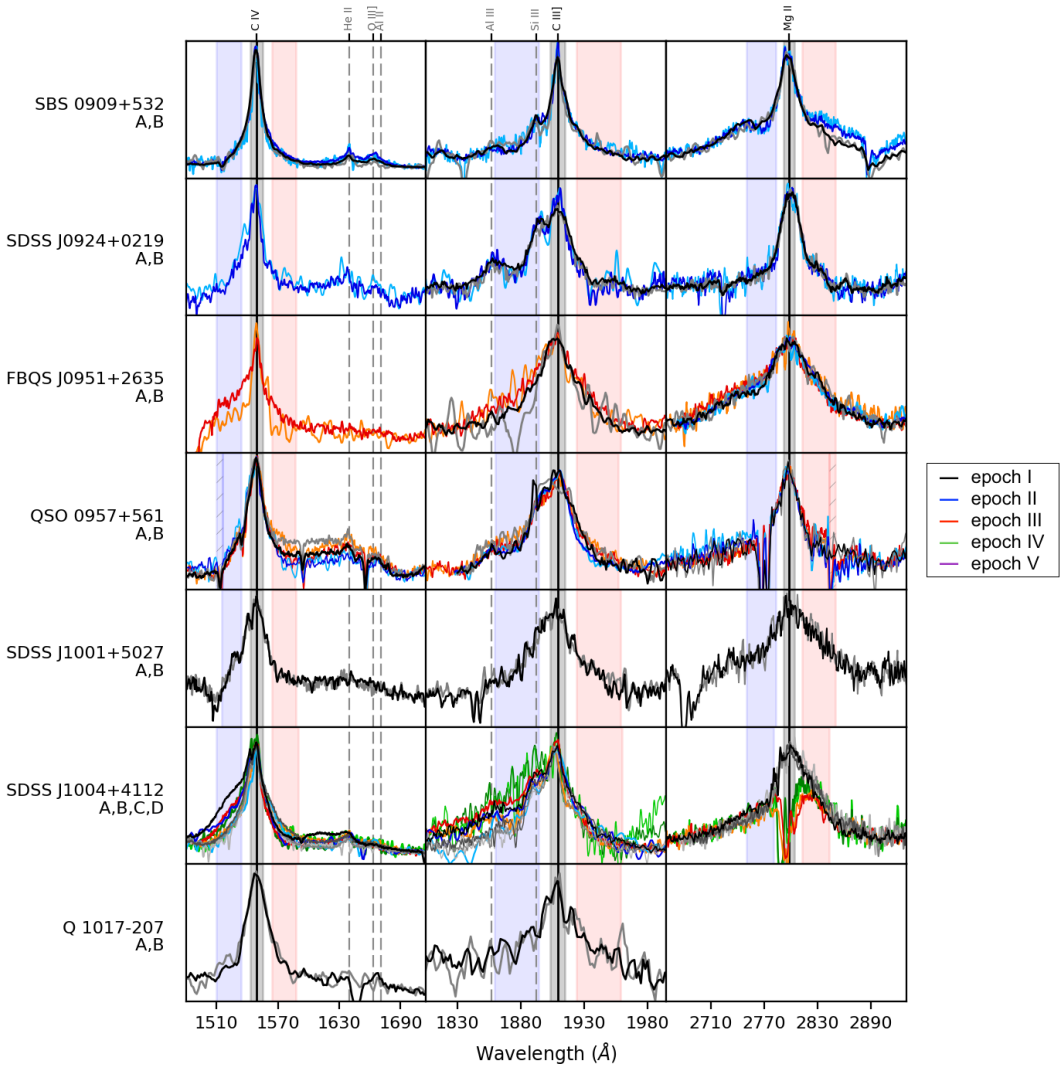

Figure 2. Continuation of Figure 1.

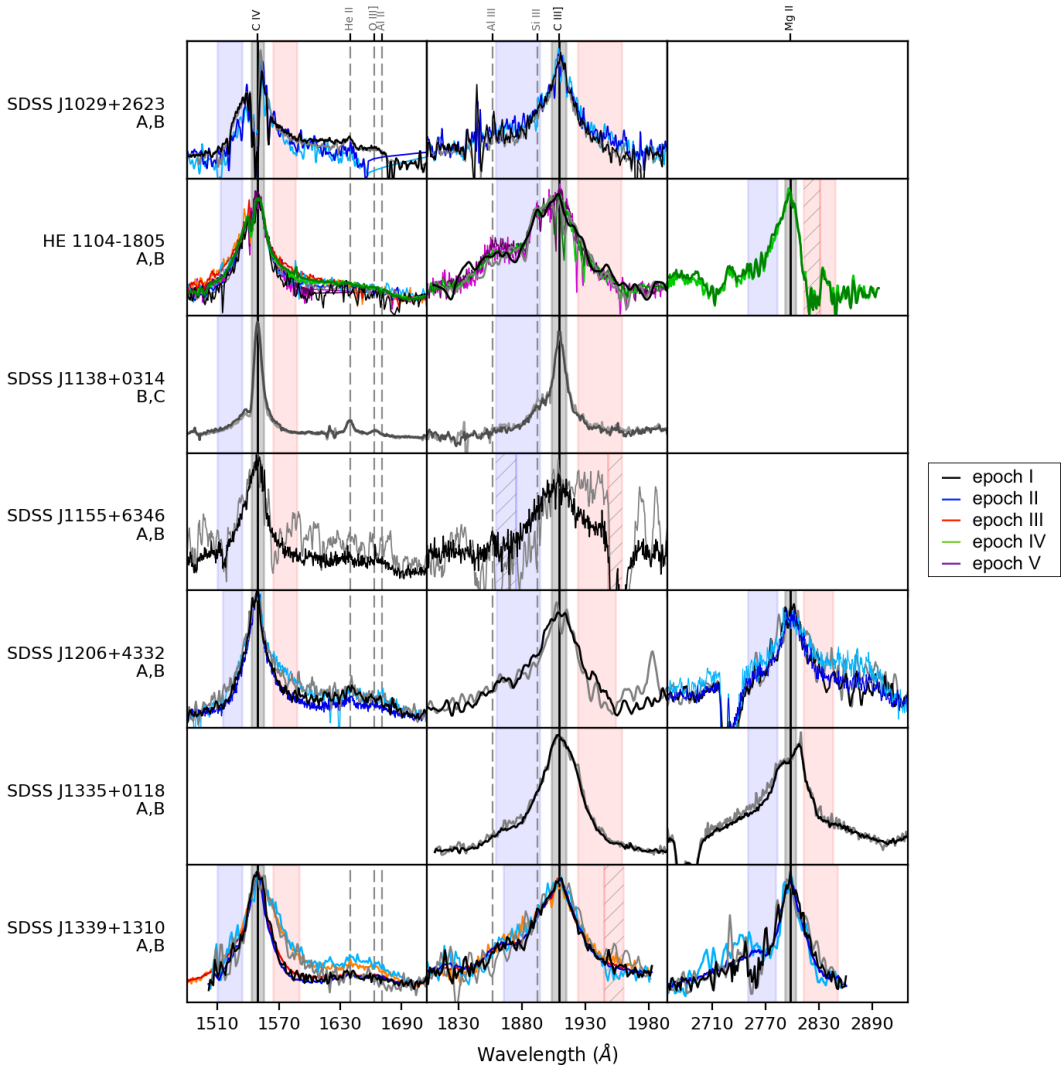

Figure 3. Continuation of Figure 1.

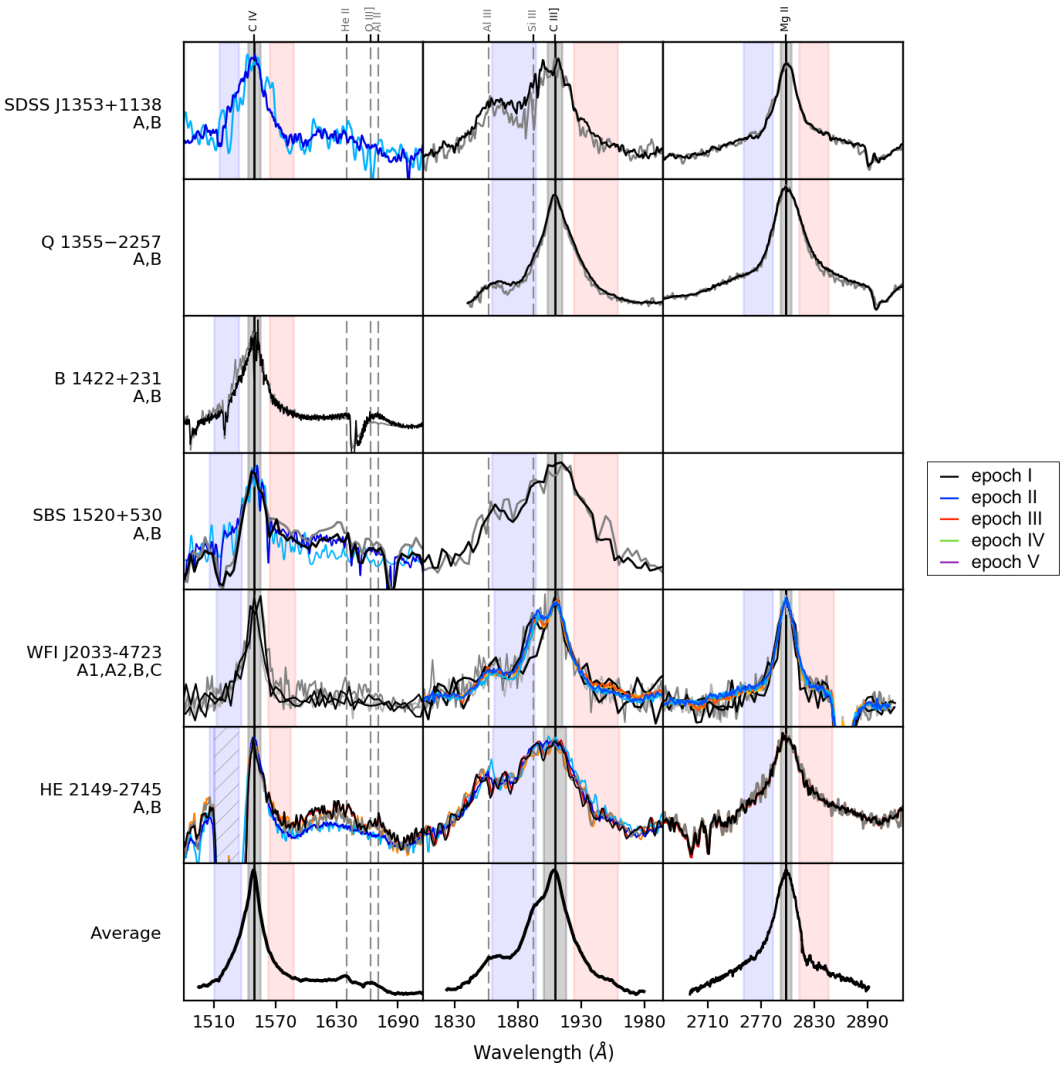

Figure 4. Continuation of Figure 1.

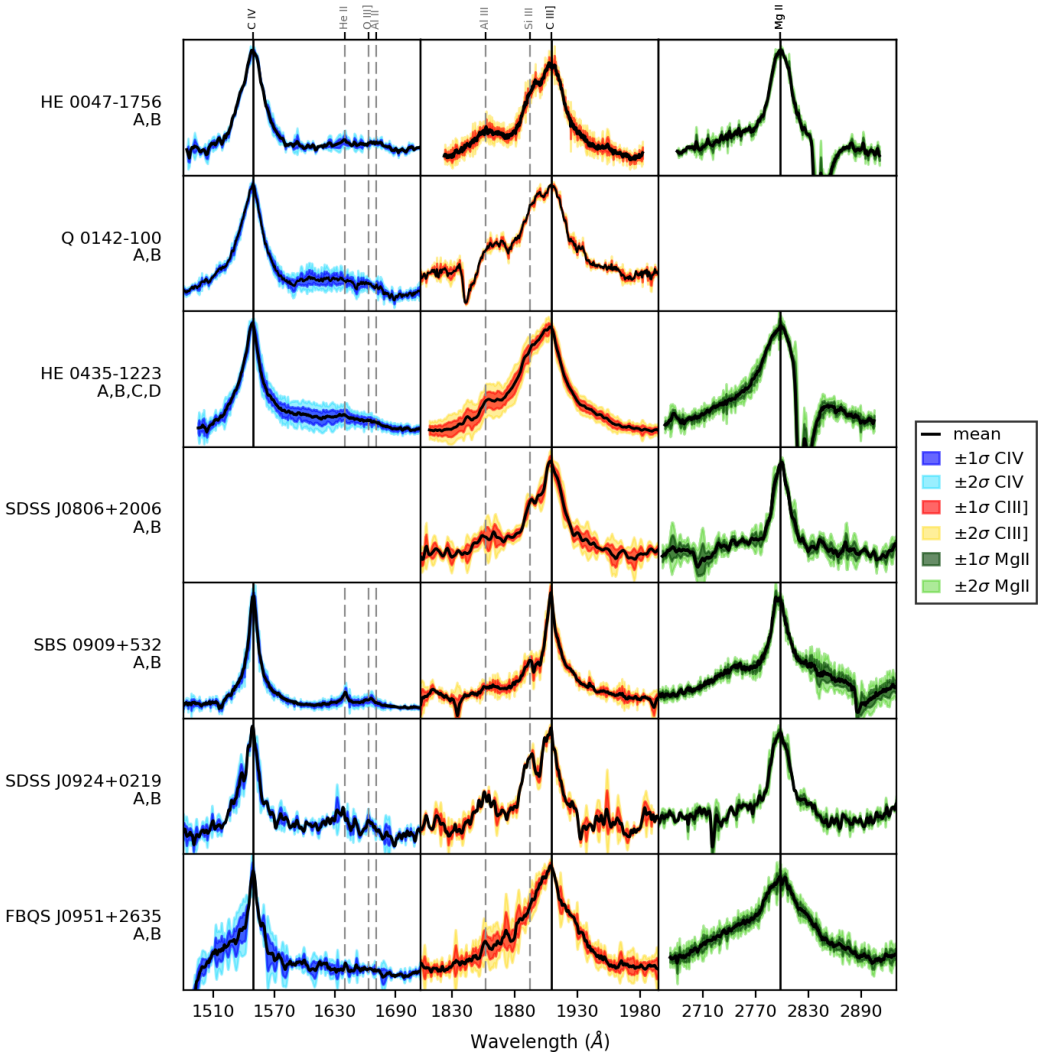

Figure 5. Average (black) spectra for the C IV, C III] and Mg II emission lines with one (dark blue/red/green) and two (light blue/red/green) sigma intervals. The y-axis is in arbitrary units of flux.

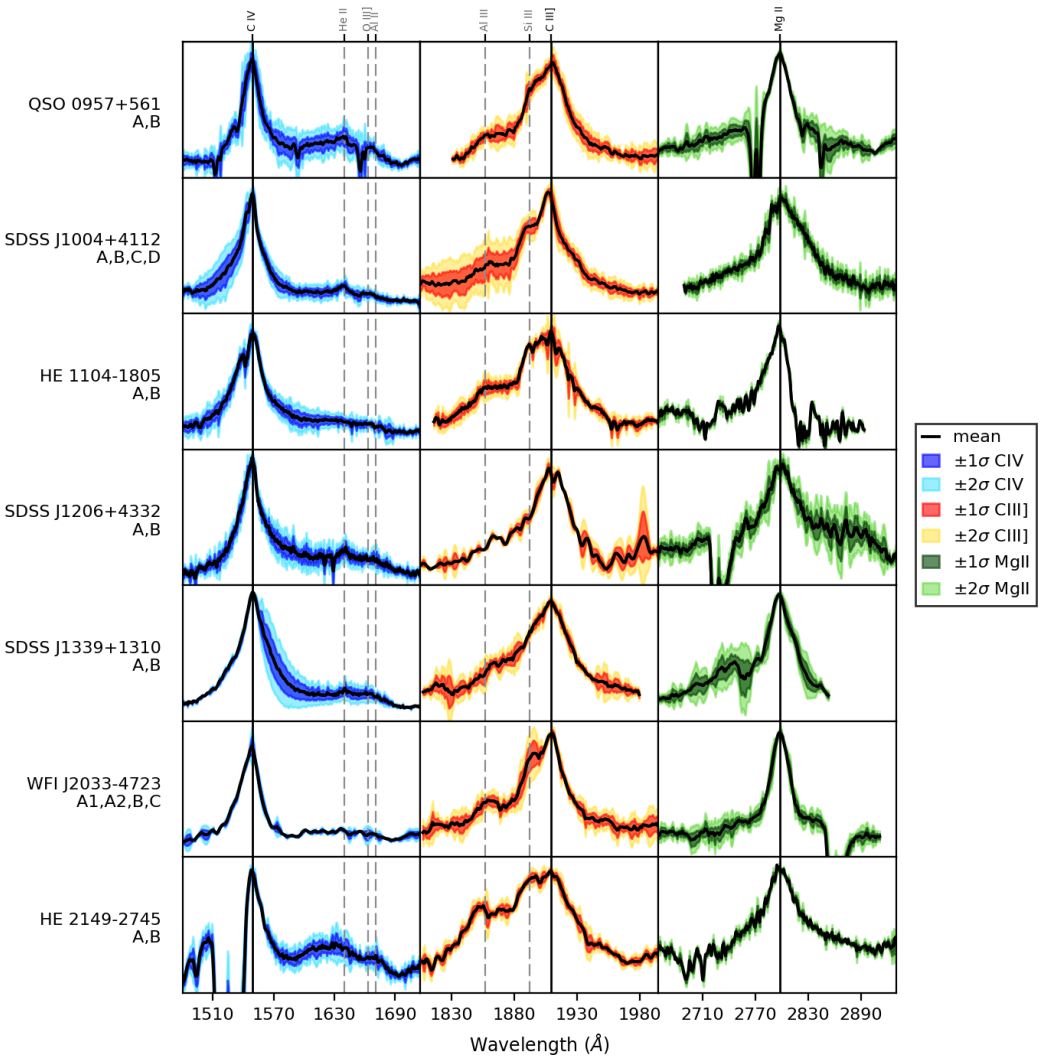

Figure 6. Continuation of Figure 6.

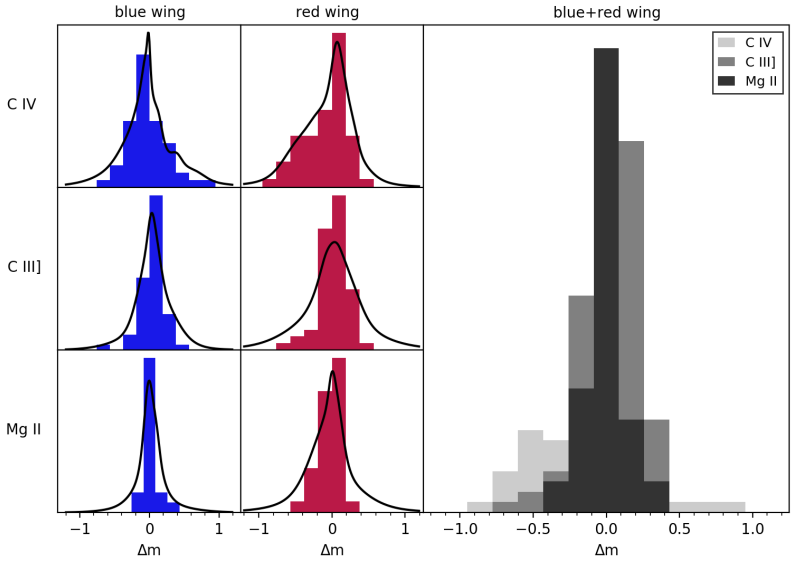

Figure 7. Histograms of microlensing magnification difference between image pairs (in the same epoch) in the blue and red wings of C IV, C III] and Mg II. Black curves show the corresponding Gaussian kernel density estimates of the PDFs.

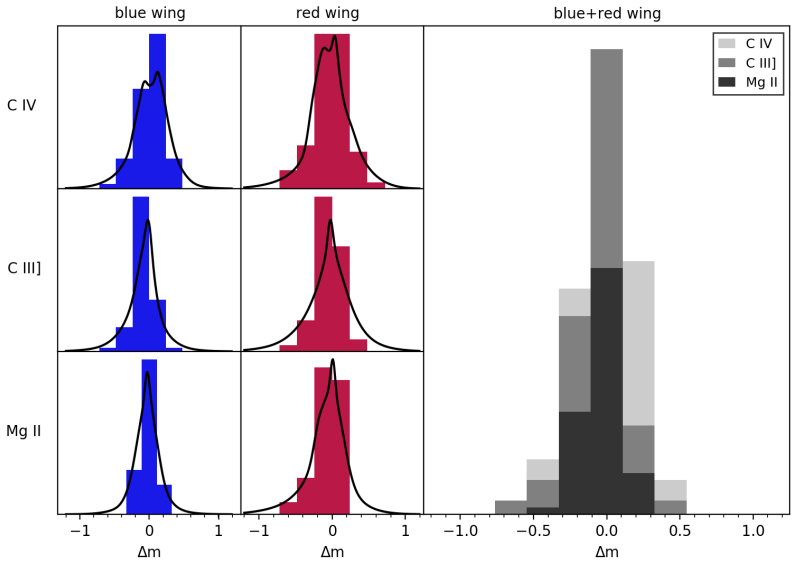

Figure 8. Histograms of magnitude difference for the same image at different epochs in the blue and red wings of C IV, C III] and Mg II. Black curves show the corresponding Gaussian kernel density estimates of the PDFs.

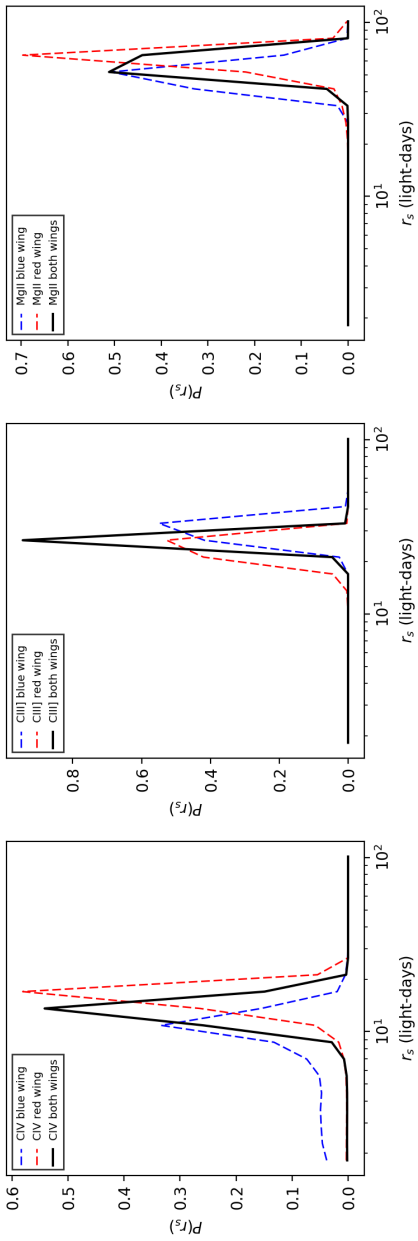

Figure 9. Joint Likelihood (solid black line) for C IV (left panel), C III] (middle panel) and Mg II (right panel). Dashed lines show the Joint Likelihood functions for the red and blue wing, respectively.

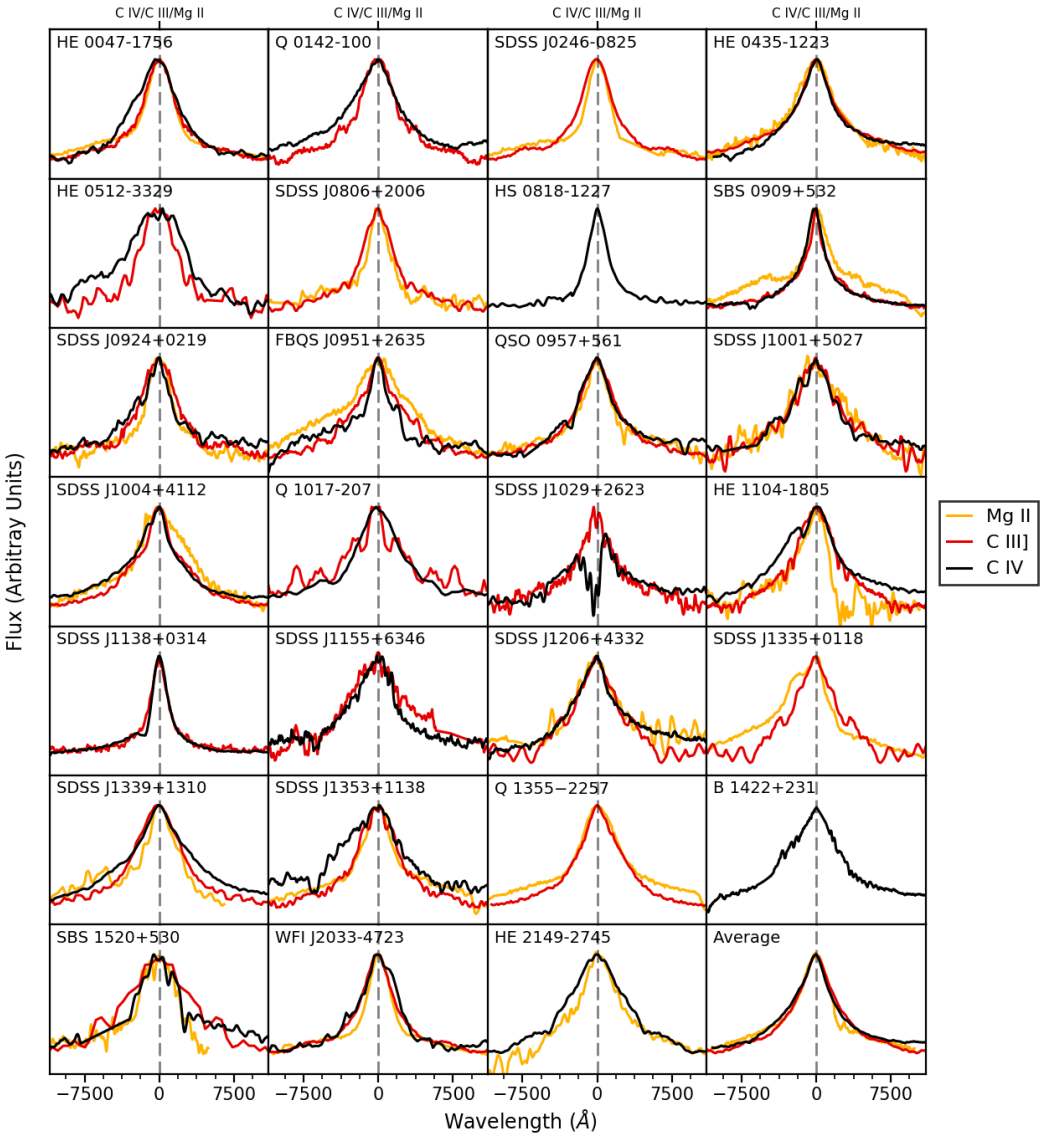

Figure 10. Line profiles of C IV (black), C III] (red) and Mg II (yellow) as a function of velocity.

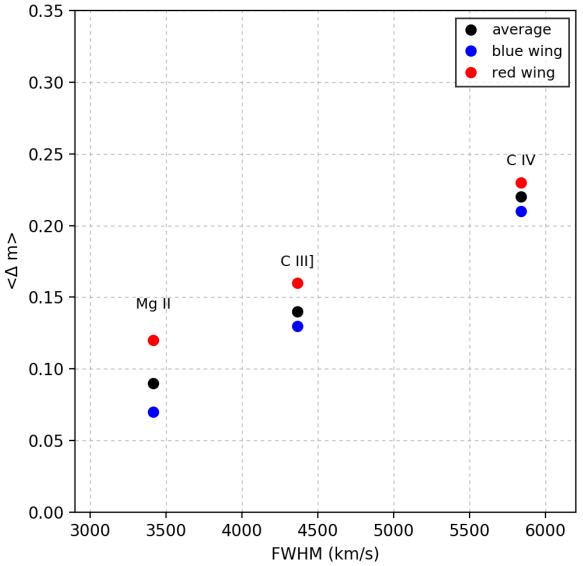

Figure 11. Average amplitude of microlensing between images as a function of the line broadening for C IV, C III] and Mg II.

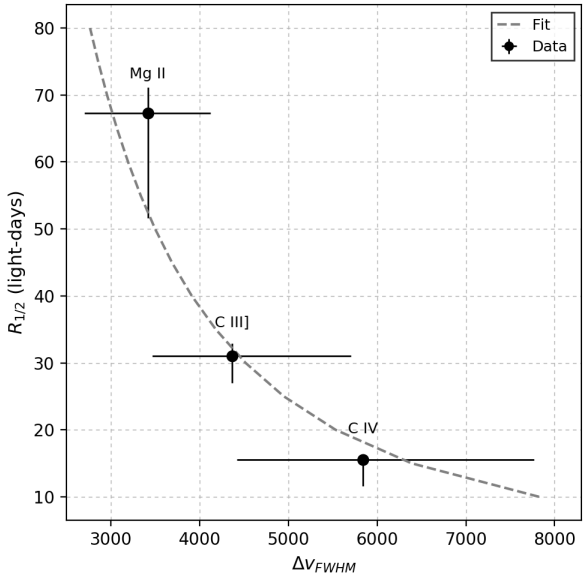

Figure 12. Average emission region size as a function of the line broadening for C IV, C III] and Mg II. The line of best fit according to Eq. 5 is shown as gray dashed line.

Table 1. Database of Lensed Quasar Spectra

Object	Image	Epoch	Date	C IV	C III]	Mg II	Facilities	Reference
HE 0047-1756	A,B	I	2002 Sep 04	x	x	-	Magellan	Wisotzki et al. 2004
		II	2005 Jul 18	-	x	x	VLT	Sluse et al. 2012
		III	2008 Jan 13	-	x	x	Magellan	Rojas et al. 2014
Q 0142-100	A,B	I	2006 Aug 15	x	x	-	VLT	Sluse et al. 2012
		II	2008 Jan 12	x	-	-	MMT	Motta (private communication)
SDSS J0246-0825	A,B	I	2006 Aug 22	-	x	x	VLT	Sluse et al. 2012
HE 0435-1223	A,B	I	2002 Sep 05	x	x	-	CAO	Wisotzki et al. 2003
	B,D	II	2004 Oct-Nov	-	x	x	VLT	Eigenbrod et al. 2007
	A,C,D	III	2007 Dec 10	x	x	x	Magellan	Motta et al. 2017
	A,B,C,D	IV	2008 Jan 12	x	x	x	MMT	Motta et al. 2012
HE 0512-3329	A,B	I	2001 Aug 13	x	x	-	HST	Wucknitz et al. 2003
SDSS J0806+2006	A,B	I	2005 Apr 12	-	x	x	APO	Inada et al. 2006
		II	2006 Apr 22	-	x	x	VLT	Sluse et al. 2012
HS 0818-1227	A,B	I	2008 Jan 12	x	-	-	MMT	Motta et al. 2012
SBS 0909+532	A,B	I	2003 Mar 07	x	x	x	HST	Mediavilla et al. 2005
		II	2016 Mar 17	x	x	x	WHT	Fian
SDSS J0924+0219	A,B	I	2005 Jan 14	-	x	x	VLT	Eigenbrod et al. 2006
		II	2016 Mar 17	x	x	x	WHT	Fian
FBQ 0951+2635	A,B	I	1997 Feb 14	-	-	x	Keck	Schechter et al. 1998
		II	2006 Mar 31	-	-	x	VLT	Sluse et al. 2012
		III	2016 Mar 17	x	x	x	WHT	Fian
Q 0957+561	A	I	1999 Apr 15	x	x	x	HST	Goicoechea et al. 2005
	B	I	2000 Jun 2	x	x	x	HST	Goicoechea et al. 2005
	A,B	II	2008 Jan 12	x	x	x	MMT	Motta et al. 2012
		III	2016 Mar 12	x	x	x	WHT	Mediavilla, Jimenez-Vicente, Fian
SDSS J1001+5027	A,B	I	2003 Nov 20	x	x	x	APO	Oguri et al. 2005
SDSS 1004+4112	A,B,C,D	I	2003 May 31	x	x	x	APO	Richards et al. 2004
	A,B	II	2004 Jan 19	x	x	-	WHT	Gómez-Álvarez et al. 2006
		III	2008 Jan 12	x	x	x	MMT	Motta et al. 2012
		IV	2016 Mar 11	x	x	x	WHT	Mediavilla, Jimenez-Vicente, Fian
Q 1017-207	A,B	I	1996 Oct 28	x	x	-	HST	Surdej et al. 1997
SDSS J1029+2623	A,B	I	2008 Jan 12	x	x	-	MMT	Motta et al. 2012
		II	2016 Mar 12	x	x	-	WHT	Mediavilla, Jimenez-Vicente, Fian
HE 1104-1805	A,B	I	1993 May 11	x	x	-	NTT	Wisotzki et al. 1993
		II	1994 Nov 29	x	-	-	ESO 3.6m	Wisotzki et al. 1995
		III	2008 Jan 11	x	-	-	MMT	Motta et al. 2012
		IV	2008 Apr 07	x	x	x	VLT	Motta et al. 2012
		V	2016 Mar 12	x	x	-	WHT	Mediavilla, Jimenez-Vicente, Fian
SDSS J1138+0314	B,C	I	2005 May 10	x	x	-	VLT	Sluse et al. 2012
SDSS J1155+6346	A,B	I	2010 Sep 20	x	x	-	HST	Rojas et al. 2014
SDSS J1206+4332	A,B	I	2004 Jun 21	x	x	x	APO	Oguri et al. 2005
		II	2016 Mar 12	x	-	x	WHT	Mediavilla, Jimenez-Vicente, Fian
SDSS J1335+0118	A,B	I	2005 Feb 17	-	x	x	VLT	Sluse et al. 2012
SDSS J1339+1310	A,B	I	2013 Apr 13	x	x	x	GTC	Shalyapin & Goicoechea 2014
		II	2014 Mar 27	x	x	x	GTC	Goicoechea & Shalyapin 2016
		III	2014 May 20	x	x	-	GTC	Goicoechea & Shalyapin 2016
SDSS J1353+1138	A,B	I	2005 Apr 12	-	x	x	Keck	Inada et al. 2006
		II	2016 Mar 17	x	-	-	WHT	Fian
Q 1355-2257	A,B	I	2005 Mar 13	-	x	x	VLT	Sluse et al. 2012
B 1422+231	A,B	I	2016 Mar 17	x	-	-	WHT	Fian
SBS 1520+530	A,B	I	1996 Jun 12	x	x	-	SAO	Chavushyan et al. 1997
		II	2016 Mar 12	x	-	-	WHT	Mediavilla, Jimenez-Vicente, Fian
WFI 2033-4723	A1,A2,B,C	I	2003 Sep 15	x	x	x	Magellan	Morgan et al. 2004
	B,C	II	2005 May 13	-	x	x	VLT	Sluse et al. 2012
		III	2008 Apr 14	-	x	x	VLT	Motta et al. 2017
HE 2149-2745	A,B	I	2000 Nov 19	x	x	x	VLT	Burud et al. 2002
		II	2006 Aug 04	x	x	-	VLT	Sluse et al. 2012
		III	2008 May 07	x	x	x	VLT	Motta et al. 2017

Table 2. Differences between Images in the C IV, C III] and Mg II Lines

Emission Line	Wing	Object	Image Pair	Epoch	$\Delta m^* \pm \sigma^{**}$	$\Delta m/\sigma$	Classification
C IV	blue wing	FBQ 0951+2635	B-A	III	0.52 ± 0.25	2.1	Microlensing
		SDSS 1004+4112	B-A	I	0.56 ± 0.16	3.4	Microlensing
				III	0.39 ± 0.07	5.8	Microlensing
				IV	0.38 ± 0.14	2.8	Microlensing
			C-A	I	0.69 ± 0.14	4.8	Microlensing
			D-A	I	0.90 ± 0.36	2.5	Microlensing
			C-B	I	0.13 ± 0.06	2.2	Microlensing
		Q 1017-207	B-A	I	-0.28 ± 0.16	1.8	
		SDSS J1138+0314	C-B	I	0.13 ± 0.05	2.9	Microlensing
		SDSS J1206+4332	B-A	II	0.31 ± 0.16	2.0	Microlensing
		HE 2149-2745	B-A	III	-0.15 ± 0.07	2.1	Microlensing
	red wing	HE 0435-1223	B-A	IV	0.20 ± 0.07	2.8	Microlensing
			D-B	IV	-0.12 ± 0.08	1.5	
			D-C	I	-0.39 ± 0.27	1.5	
		HS 0818-1227	B-A	I	-0.39 ± 0.19	2.0	Microlensing
		SBS 0909+532	B-A	I	0.13 ± 0.07	1.9	
		Q 0957+561	B-A	I	-0.19 ± 0.11	1.7	
				III	-0.36 ± 0.17	2.2	Microlensing
		SDSS 1004+4112	B-A	I	0.30 ± 0.06	5.1	Microlensing
				II	-0.53 ± 0.31	1.7	
				III	-0.52 ± 0.15	3.6	Microlensing
				IV	-0.65 ± 0.22	2.9	Microlensing
			C-B	I	0.35 ± 0.10	3.5	Microlensing
			D-B	I	0.40 ± 0.26	1.6	
		SDSS J1206+4332	B-A	I	-0.27 ± 0.15	1.8	
				II	-0.46 ± 0.13	3.4	Microlensing
		SDSS J1339+1310	B-A	III	-0.62 ± 0.15	4.2	Microlensing
		SBS 1520+530	B-A	I	-0.25 ± 0.13	1.9	
C III]	blue wing	SDSS J0246-0825	B-A	I	0.13 ± 0.06	2.4	Microlensing
		SDSS 1004+4112	C-A	I	0.33 ± 0.18	1.9	
		SDSS J1155+6346	B-A	I	-0.58 ± 0.39	1.5	
		WFI 2033-4723	C-B	II	0.12 ± 0.06	2.1	Microlensing
	red wing	HE 0435-1223	B-A	I	0.29 ± 0.14	2.0	Microlensing
			C-A	I	0.29 ± 0.15	1.9	
		HE 1104-1805	B-A	II	0.21 ± 0.14	1.5	
		SDSS J1155+6346	B-A	I	-0.63 ± 0.26	2.4	Microlensing
Mg II	blue wing	HE 0435-1223	D-B	II	0.11 ± 0.04	3.0	Microlensing
		SDSS J1206+4332	B-A	II	0.23 ± 0.14	1.6	
	red wing	SDSS J1206+4332	B-A	II	0.28 ± 0.17	1.7	

*magnitude difference between pairs of images for the same epoch

**standard deviation of magnitude difference

Table 3. Differences between Epochs in the C IV, C III] and Mg II Lines

Emission Line	Wing	Object	Image	Epoch	$\Delta m^* \pm \sigma^{**}$	$\Delta m/\sigma$	Classification
C IV	blue wing	Q 0142-100	A	II-I	-0.07 ± 0.05	1.5	
		SDSS 1004+4112	A	II-I	0.28 ± 0.07	4.1	Microlensing Variability
				III-I	0.18 ± 0.04	4.2	Microlensing Variability
				IV-I	0.43 ± 0.12	3.7	Microlensing Variability
				III-II	-0.10 ± 0.06	1.5	
				IV-II	0.14 ± 0.09	1.6	
				IV-III	0.19 ± 0.08	2.2	Microlensing Variability
			B	IV-I	0.20 ± 0.12	1.7	
		HE 1104-1805	A	III-II	-0.28 ± 0.15	1.8	
				IV-III	0.14 ± 0.08	1.7	
				V-III	0.22 ± 0.08	2.9	Intrinsic Variability?
			B	III-I	-0.44 ± 0.23	1.9	
				IV-I	-0.23 ± 0.12	2.0	Intrinsic Variability?
				V-III	0.29 ± 0.15	1.9	
		SDSS J1339+1310	A	III-II	-0.18 ± 0.07	2.4	Microlensing Variability?
		HE 2149-2745	A	II-I	0.12 ± 0.03	3.7	Intrinsic Variability?
			B	III-II	-0.20 ± 0.05	3.7	Microlensing Variability
	red wing	Q 0142-100	A	II-I	-0.20 ± 0.08	2.5	Intrinsic Variability?
		HE 0435-1223	C	III-I	-0.49 ± 0.34	1.5	
		SBS 0909+532	A	II-I	-0.14 ± 0.06	2.2	Microlensing Variability?
		SDSS 1004+4112	A	III-I	0.26 ± 0.08	3.1	Microlensing Variability
				IV-I	0.52 ± 0.23	2.3	Microlensing Variability
		HE 1104-1805	A	III-II	-0.24 ± 0.06	4.2	Intrinsic Variability?
				IV-II	-0.15 ± 0.07	2.3	Intrinsic Variability?
				IV-III	0.09 ± 0.06	1.5	
			B	III-I	-0.14 ± 0.09	1.7	
				IV-I	-0.10 ± 0.05	2.0	Intrinsic Variability?
		SDSS J1339+1310	A	III-II	-0.29 ± 0.05	6.4	Microlensing Variability
			B	II-I	-0.16 ± 0.09	1.7	
		HE 2149-2745	A	II-I	0.23 ± 0.15	1.5	
				III-II	-0.24 ± 0.14	1.7	
C III]	blue wing	SDSS 1004+4112	A	IV-II	-0.26 ± 0.16	1.7	
		Q 0957+561	B	III-I	-0.24 ± 0.16	1.5	
	red wing	Q 0957+561	A	III-I	-0.46 ± 0.25	2.5	Intrinsic Variability?
			B	III-I	-0.81 ± 0.53	1.5	
Mg II	blue wing	HE 0435-1223	A	IV-III	-0.12 ± 0.08	1.5	
			D	III-II	-0.21 ± 0.11	1.9	
				IV-III	-0.20 ± 0.12	1.6	
		FBQ 0951+2635	A	II-I	-0.11 ± 0.07	1.5	
				III-I	-0.15 ± 0.09	1.7	
		WFI 2033-4723	C	III-II	0.12 ± 0.07	1.6	
	red wing	HE 0435-1223	D	IV-III	-0.37 ± 0.23	1.6	
		SDSS J1353+1138	B	II-I	0.33 ± 0.20	1.6	

*magnitude difference between epochs for the same image

**standard deviation of magnitude difference